

# SCIENTIFIC & TECHNICAL

REPORT  
**2017**

## IMPRINT

---

**Full report title** CSEM Scientific and Technical Report 2017

**Editor and publisher** CSEM SA  
[info@csem.ch](mailto:info@csem.ch)  
T +41 32 720 5111

**Publication** Frequency yearly  
Media printed and electronic  
Website [www.csem.ch/str2017](http://www.csem.ch/str2017)

**Cover page design** Contreforme  
[www.contreforme.ch](http://www.contreforme.ch)

**Printing** Imprimerie Baillod SA, Bevaix (Switzerland)

# CSEM SA

CSEM is a private, non-profit research and technology organization (RTO) and a Swiss innovation accelerator—a catalyst for the transfer of technologies and know-how from fundamental research to industry.

CSEM's extraordinary success in the field of innovation and its diffusion stems primarily from its specialization in the micro-engineering domain—a pillar of “Swissness”—as well as from the effectiveness of its applied research program. In this program, funded by the Swiss confederation, seasoned CSEM researchers develop technologies that enable the next generation of trends: the future of energy, the Internet of Things revolution, the advent of wearable technologies for wellness and medical applications, or the rendering widespread of machine-to-machine (M2M) communications, and last but not least, the advanced human–machine interactions required by Industry 4.0.

CSEM's research strategy is built around five main programs:

**Microsystems technology**—Design, integration, and packaging of devices that sense and monitor our environment and aspects of our daily lives. Use of MEMS and advanced manufacturing technologies to develop innovative, complete, and reliable microsystems solutions for industry.

**Systems**—An application-oriented interdisciplinary program with a special emphasis on how to design, implement, manufacture, maintain, repair, and manage complex engineering systems over their lifetime cycles, taking into consideration resource limitations (in terms of processing and power consumption), miniaturization, precision, reliability, production cost, and environmental conditions.

**Ultra-low-power integrated systems**—Addresses the key challenges and technologies required to build very-low-power (long autonomy), wirelessly interconnected, embedded smart systems or remote sensing nodes.

**Surface engineering**—Focuses both on the research and development of engineered surfaces and interfaces—with optimized (bio-) chemical, optical, and electrical properties leading to improved performance of the respective components—and on their “up compatible” manufacturing processes in order to bridge the gap to industrial applications.

**Photovoltaics & energy management**—An industry-driven, application-oriented program with the aim of fostering innovation and accelerating the pace of technology transfer in the fields of photovoltaics and energy storage and systems, as well as in new market segments such as energy scavenging and the Internet of Things.



# CONTENTS

## PREFACE

## MULTIDISCIPLINARY INTEGRATED PROJECTS—MIPS

- Sensorless—Reliable Low-speed Sensorless Motor Control for Safety Related Control Systems in Harsh Environments  
Wear-a-Watt3 (WAW3) e-tonomy—Autonomy for Wearables and IoT  
GWAPO2—A Highly Conformable Multipurpose Wireless Autonomous Patch  
PORGY BESS—Platform for the Optimal Regulation in Battery Energy Storage Systems  
TeraLine—Single Detector for Multicolor Terahertz (THz) Imaging  
HybSi 2017—Novel Opportunities for High-precision Mechanisms Based on the Hybridization of Silicon at the Centimeter Scale  
HECTIC—Harsh Environment Ceramic Technology Involving Silicon Carbide  
SMAC2017—Characterization of the Flat-form Factor Miniature Clock Assembly  
VitalRFsens—A Flexible FMCW RADAR Setup  
IntelliDUST—Intelligence in Silicon for Deep-ultra-low-power Sensor Technology  
PlasMOS—Integration of Plasmonic Structures in Standard CMOS  
ExoPro—Exosomes Profiling and Characterization

## MICROSYSTEMS

- Fabry-Perot MEMS Optical Filters in 2 – 20  $\mu\text{m}$  Wavelength Range  
Optical Pressure Sensor for Environments with Strong Electromagnetic Interferences  
Compact Optical MEMS Sensors for Harsh Electromagnetic Environments  
Impact of Mechanical Shock on MEMS Accelerometers  
Measurements of a MEMS UV Laser Pointing Mirror  
Metal Implantation on Elastomer Substrate for Stretchable Strain Sensors  
Enhanced Properties of Aluminum Scandium Nitride Piezoelectric Films  
Mechanical Shock Test for MEMS and MEMS Packaging  
Integration and Interconnection of MEMS Membrane into a Multiwell Plate Insert by Overmolding  
Adhesive Bonding for Harsh Environments  
Thermal Management Solutions for mid-IR Optoelectronics Packages  
3D Printing Technology for Smart Prostheses  
Multi-material and Multi-technology Printing Platform  
Mechanical Properties of 3D Printed Material

7	LEGO-like Assembly by 3D Printing	40
9	Multi-charged Ion Implantation of Nitrogen for Improved Tribological Properties of Miniaturized Mechanisms	41
	Additive Manufacturing of Ti-based Alloy for Aerospace Application	42
	3D LIGA	43
11	Surface Properties Improvement of Biocompatible Materials by Multi-charged Ion Implantation	44
	Materials Behaviour @Mesoscale	45
	<b>SURFACE ENGINEERING</b>	<b>47</b>
12	Nanostructured Thin Films for Spectroscopy and Imaging	49
13	Nanofiber-based Retarders Fabricated by Vacuum-free Electrospinning	50
14	Microlenses for Improved Space Imagers	51
15	Blazed Gratings on Convex Substrates for High Throughput Spectrographs	52
16	New Generation of Immersed Gratings for High Resolution Spectroscopy in the Near and Short IR	53
17	Very High Fill-factors Microlens Arrays	54
18	Ultra-thin-film Deposition Processes for Controlled Hydrophilicity and Hydrophobicity by Molecular Vapor Deposition	55
19	Functional Metal Oxides for Additive Manufacturing	56
20	Hierarchically Porous Thin Films for Optical Gas Sensing	57
	Healing Chronic Wounds with Blue Light	58
21	Classification of Early Stage Zebrafish Fertilization	59
22	Analysis Cartridge for Companion Diagnostics	60
	Indirect Flow-rate-metering System for a Dispensing Application	61
23	Zero Gravity Fluidic Feeding System	62
	Bringing Function to Surfaces with Modular Photo Polymerizable Chemistries	63
	Online Monitoring of Antibiotics in Treated Waste Water Matrix	64
	Glucose Monitoring in <i>in-vitro</i> Cell Culture	65
	AUTOX—Automated Fluidic Handling System for <i>in-vitro</i> Tissue Model Monitoring	66
	Diagnostics in Non-invasive Body Fluids	67
	ELIME Assay for Fast Analysis in Urine	68
	Towards Sweat-rate Monitoring with Wearable Sensors	69
	FlusiGate—Optical pH Sensor for Non-invasive Wound Monitoring	70
	Non-invasive Measurement of Oxygen and Carbon Dioxide in Microscope Biochamber	71
	Biofunctionalized Membranes for Monitoring Tissue Mechanical Properties	72
	Optical Fiber Biosensor for Wound Care Management	73
	Smart System for Cell and Tissue Culture with Integrated Electrode for TEER Measurements	74
	oxiPAD—Oxygenation Measuring and Mapping Platform	75
	Inkjet Printed Optical Waveguides	76

PRINTBAT—Printed Lithium Ion Batteries	77	Landing on Mars with a Miniaturized Flash Imaging LiDAR	110
Organic Optoelectronic Imager	78	Narrow-linewidth Low-RAM Semiconductor Lasers for Telecommunication and Metrology	111
Pressure Sensitive Robots	79	Ultra-short Laser Pulses at 10 GHz Repetition Rate from an In-fiber Microresonator	112
<b>PHOTOVOLTAICS &amp; ENERGY MANAGEMENT</b>	<b>81</b>	High-speed Line Sensor for Optical Droplet Detection and Analysis	113
Development of Record Single Junction Minimodule Devices by Laser Patterning	84	SecureFLIM—Fluorescence Lifetime Imaging for Product and Brand Protection	114
Integrated Solar Cells to Energize the Wearables and the Internet of Things	85	oBPMTM—Optical Blood Pressure Monitoring: Performance in Anesthetized Patients	115
Silicon Photovoltaics for Hydrogen Production	86	Validation of a Multi-wavelength Photoplethysmogram Sensor to Measure Blood Pressure at Chest in Anesthetized Patients	116
Light Management for Efficient Printed Tandem Solar Cells	87	ECG Quality Assessment of Dry-electrode Cooperative Sensors	117
Sputtered Molybdenum Oxide as Hole Collector for Heterojunction Technology Solar Cells	88	Demonstration of a Proprietary Chip for Dry-electrode ECG and Impedance Measurements	118
Passivating Contacts for High-efficiency Silicon Solar Cells	89	A Novel Monitoring Solution to Reduce False Alarms in Neonatal Intensive Care Unit	119
Simple Processing of Back-contacted Silicon Heterojunction Solar Cells Based on Selective-area Nanocrystalline Silicon Growth	90	A Wearable System Based on Cooperative Sensors for Multi-lead ECG Monitoring and Electrical Impedance Tomography Imaging	120
Contacting Solutions for the Measurements of Next Generation Solar Cells	91	Sleep Phase Classification and Respiration Frequency Estimation Using a Wrist-worn Photoplethysmographic System	121
A PV Encapsulant Formulation Customized for Low-temperature Lamination Process	92	Swimming Performance with Wearable Inertial Sensors	122
How Does a Substrate Plasma Pre-treatment influence electrical properties of a TCO Film?	93	Validation Lung Phantoms	123
NeuroCool—Smart Air Conditioning, Pay Less for a Better Comfort	94		
Management of District Heating and Cooling	95	<b>ULTRA-LOW-POWER INTEGRATED SYSTEMS</b>	<b>125</b>
Automated Quantification of PV Hosting Capacity	96	Remote, Contactless RF Vital Signs Sensing	127
Battery Modelling and Efficiency Estimation	97	Making Time-critical Cyber Physical Systems Energy Efficient	128
Uncertainty Reduction in Predicting the Yield of Photovoltaic Power Stations	98	Wireless Power Transfer for Wearable Applications	129
<b>SYSTEMS</b>	<b>99</b>	High Performance Low-power Wireless Network for Water Distribution	130
Robotic Platform Integrating Concurrent Manufacturing Processes for Construction of Large Multi-material Parts	101	Pre-Distortion Filter to increase Data Rate and/or Reduce Noise in Direct Frequency Synthesizer (G)FSK Modulators	131
Machine Learning Using Satellite Imaging for Agriculture and Forestry	102	A 500 µW, 0.5 V VCO and Fractional Divider for BTLE Robust over PVT Variations	132
Collaborative Robot Intuitive Teaching by Single-hand Guidance	103	Fully Integrated, Low-power FM-UWB Transceiver for Short-range, High-density Wireless Sensor Networks	133
WiseRock—Wireless Sensor Network for Monitoring Rock and Slopes	104	A Power Management Unit for ULP SoC including BLE Radio	134
A Wireless Solar Powered Pressure Pad for Aerodynamics Testing of Flexible Profiles	105	Photovoltaic Cell Antenna	135
Vision-based Detection and Classification of Particles in Fluids	106	Biowave—a Biometric Watch Activated by Veins	136
CLUPI Focus Mechanism—Close-up Imager for EXOMARS Mission	107	X-Ray Photon Counting Chip with Backside Detector	137
Innovative Mechanical Design Based on Additive Manufacturing & Topology Optimization	108	Image Sensor with Stacked Photodiode	138
Sub-picosecond Mode-locked Semiconductor Laser for Space Applications	109	FastEye—A 1 MP High-speed Camera with Multiple ROI running at up to 64'000 fps	139
		An Evaluation Tool for Standard Cell Libraries under PVT Variation: Application to Sub-threshold Design	140

SoC Estimator—A Fast Exploration Tool for Different Architectural Choices in SoCs	141
A 0.5 V Near-threshold Microcontroller Robust over PVT Variations	142
Implementation and Benchmarking of RISC-V Microprocessors	143
An Harvesting System with Adaptive Power Management Algorithm for Energy Autonomous Devices	144
Fully Integrated Low-power Bio-potential Acquisition Analog Front-end IC	145
Microelectrode Array for Neural Interface	146

## **ANNEXES**

	<b>147</b>
Publications	147
Proceedings	148
Conferences and Workshops	151
Publicly Funded Projects	153
Swiss Commission for Technology and Innovation (CTI)	155
European Commission Projects	158
European Space Agency (ESA), Swiss Space Office and CNES Projects	161
Industrial Property	162
Collaboration with Research Institutes and Universities	162
Teaching	166
Theses	166
Commissions and Committees	168
Prizes and Awards	171



# PREFACE

Dear Reader,

New technologies and innovations are reshaping our world. They increasingly influence the markets and the economy in general and even rub off on politics. They directly impact our daily lives, better our health and well-being, and even induce certain cultural changes. They definitely improve the way we do things, and change the way we think.

Microtechnologies are at the heart of current technology mutations and are the key to the digital world—miniaturized smart sensors enable physical information to be captured, digitalized, channeled, and processed with ultra-low-power consumption. This leads to Industry 4.0 levers like predictive maintenance and real-time process optimization.

This year, as always, it is a great pleasure to share with you our latest successes and technological results, so crucial for our industries. By presenting our most recent developments we hope to inspire you with new ideas for elaborating new products or improving your production processes. We also wish to pique your curiosity and to encourage you to discuss your challenges with us.

The year 2017 saw several of our developments commended by the economic and technological communities: The Zurich start-up AVA, whose fertility bracelet—based on our solutions for the monitoring of physiological parameters—was selected as the Most Promising Start-Up of the year by Venturelab (a national program for training start-ups). The family-run Bernese enterprise Witschi Electronic excelled at the Geneva High-Precision Show with its WisioScope; this joint development from Witschi and CSEM enabling the calibration of mechanical watch movements won the jury's 1st Prize. Our technology, equally, figures abroad, for example with the miniaturized Vision-in-Package system—the VIP—for facial recognition that was recognized in the United States by the magazine *Vision Systems Design*.

Not only do these examples illustrate the talent and dedication of our engineers and scientists, they also—to my mind—show the degree to which, together, our know-how and your commitment enable you as entrepreneurs to continue to design the future of industry in Switzerland.

Mario El-Khoury  
CEO, CSEM SA



# MULTIDISCIPLINARY INTEGRATED PROJECTS—MIPS

Harry Heinzelmann

Multidisciplinary Integrated Projects (MIPs) form a horizontal program that mostly builds on technologies developed in the five topical research programs **Microsystems, Surface Engineering, Systems, Ultra-low-power Integrated Systems, and Photovoltaics & Energy Management**. The goal of the MIP program is to better exploit synergies, and to create solutions by combining several of CSEM's technologies.

Every year CSEM dedicates an important part of its resources to these highly interdisciplinary projects, targeting demonstrators with a high level of maturity (high technology readiness level (TRL)) for novel applications with high market potential in relatively short development times.

Besides typical MIPs, which last 1–2 years, Feasibility MIPs have been introduced, allowing the rapid exploration of new concepts. Another project type, Technology MIPs, addresses long-term co-developments with different technologies.

The MIP program is reevaluated annually, and consists of ongoing projects and new proposals in a healthy balance, making it possible to respond quickly to newly emerging market needs. In this way, CSEM's MIPs complement its five topical research programs in an ideal way. The MIP program enables CSEM to offer its industrial clients an even richer portfolio of technologies, beyond the possibilities of its thematic research programs alone.

An overview of 2017 MIPs follows; the projects are presented in more detail in the following pages.

## Classical MIPs

### Sensorless—Sensorless Motor Control

The MIP Sensorless aims at improving existing motor control concepts based on Extended Kalman Filters (EKF) by adding a model estimator based on moving horizon estimation (MHE). This project offers a fresh approach to sensorless motor control at low speeds by using real-time embedded optimization estimation and sensor-fusion techniques.

### Wear-a-Watt3 (WaW3) e-tonomy—Autonomy for Wearables and IoT

The project WaW3 is concluding the work done during the two previous years on the development of energy scavenging solutions for wearable devices. The provision of autonomous energy is a key technology for many future applications, including distributed sensing for the Internet of Things (IoT).

The goal of the project is to measure over one year the energy harvested by 25 wearers of the wear-a-watt watch developed in 2016—energy harvested using PV cells integrated in the watch dial and the wristband. The project is helping develop the infrastructure necessary to collect and analyze the data and to establish a predictive model with which to forecast the power output of the device.

### GWAP02—Generic Wireless Autonomous Conformal Patch

During the second year of the project GWAP02, the development of a platform for thin, miniature, flexible, and rechargeable wireless interactive sensors and actuators continued. Such portable autonomous devices address a wide

range of applications and requirements, such as monitoring health-relevant body parameters. The platform combines sources of energy (e.g., PV) with sensors, electronics, displays, interactive components, and antennas.

### PORGY BESS—Regulation of Battery Energy Storage Systems

The goal of PORGY BESS is to integrate four technologies developed at CSEM to demonstrate an optimal, predictive control of battery energy storage systems. This control platform integrates the forecasting of PV production and energy demand on an hour-to-day-ahead horizon, and performance and degradation models of batteries. It is applicable to many different storage applications, and is particularly needed if hybrid systems are to compete with diesel generators and for multi-objective distributed energy storage for which there is currently no product.

### TeraLine—Multispectral CMOS-based THz Line Camera

Imaging technologies in frequency bands other than the optical wavelengths offer complementary information, and feature the ability to penetrate at different depths into the objects under study. The project TeraLine addresses THz imaging technology, which has advantages over other imaging technologies in the microwave/IR/x-ray spectral ranges. It gives good resolution, penetrates non-conductive materials, is safe to use, and at the same time can provide spectral information. Multispectral imaging can reveal features that are not present in a monochromatic image.

The main objective of this project is to develop a multispectral CMOS-based THz line camera in the 300 GHz to 500 GHz band. This camera will make use of already existing technologies from CSEM, such as a THz line sensor based on an array of THz detectors developed in the 2016 MIP TeraXplore.

### Technology MIPs

#### HybSi 2017—Hybridization of Silicon Components

The technology MIP HybSi 2017 is a continuation of the HybSi development that started in 2013, with the goal to develop technologies for the hybrid integration of silicon-based components in high precision micro-mechanisms at the macroscopic scale (macroMEMS). Given the importance of the watch industry in Switzerland and the current trend for integrating silicon components into high-end mechanical watches, the focus is on the hybridization challenges typical to that industry. Further applications of the macroMEMS technology are expected to emerge, including for the medical industry.

In 2017, HybSi mainly addressed a new concept for an integrated macroMEMS actuator, and new processes of precise additive manufacturing onto silicon.

#### HECTIC—Harsh Environment Ceramic Tech Involving Silicon Carbide

The objective of the project HECTIC is the development of novel packaging solutions for harsh environments (including high temperatures and corrosive chemicals). Current solutions are often bulky and increase costs, and are thus prohibitive when it comes to taking full advantage of sensor miniaturization.

In this project, silicon carbide (SiC) is used as a base material, with a conformal aluminum oxide ( $\text{Al}_2\text{O}_3$ ) coating made by Molecular Vapor Deposition (MVD). A miniature, reliable pressure sensor made out of SiC, with a protective  $\text{Al}_2\text{O}_3$  layer, will demonstrate the technology. The sensor is expected to operate at high temperatures, which makes it very interesting, for example for the monitoring of turbomachinery.

### **SMAC2017—Swiss Miniature Atomic Clock**

The goal of the SMAC 2017 project is to integrate and metrologically evaluate a reliable and transportable miniature atomic clock (MAC) demonstrator based the developments of earlier MIPs. This important consolidation will result in a transportable, turnkey evaluation kit based on the flat form factor miniature atomic clock physics packages developed earlier.

### **Feasibility MIPs**

#### **VitalRFsens—Vital Sign Monitoring via RF Sensing**

The goal of the project VitalRFsens is the proof-of-principle of RF sensing for vital sign monitoring. Typical parameters to be recorded include respiration and heart rate. The sensors are either in contact with the body (typically in a wristwatch configuration) or operate at a certain distance (such as in below-mattress or in-car-seat sensor placements).

The technology is based on the processing of backscattered RF signals from the human body. Heart rate, respiratory activity, and potentially blood pressure are the main parameters to be monitored. Applications in sleep analysis are particularly interesting.

#### **IntelliDUST—Intelligence in Silicon for Deep-ULP Sensor Technology**

The project IntelliDUST is helping to turn current, passive sensors into active, independent devices in the Internet of Things (IoT). The approach is to provide existing ultra-low-power sensors with an intelligent algorithmic layer, so that measurements can be processed without negatively impacting power consumption.

The concept of an intelligence layer embedded at the bare sensor level could eventually provide a solution for truly continuous monitoring systems for the Internet of Things (IoT), provided that the tiny amount of energy required by such an intelligent sensor can be easily provided by even the tiniest energy harvesting systems.

### **PlasMOS—Integration of Plasmonic Structures in Standard CMOS**

The implementation of filters (polarization, pass-band) for image sensors and cameras typically requires extra and costly processing steps. The MIP PlasMOS explores the potential of integrating plasmonic structures directly into a standard CMOS process, for example for the easy and cost-effective implementation of filters directly onto image sensors.

This project relies on CSEM's long experience in the development of CMOS image sensors and cameras, as well as in the post processing of vision sensors, to add optical functionality (e.g., microlens arrays or zero-order filters). One typical application is an inexpensive multispectral imager based on plasmonic filters at virtually no extra cost compared to conventional imagers.

#### **ExoPro—Exosome Profiling**

The feasibility project ExoPro explores the potential of existing instrumentation for the preparation and characterization of exosomes, a class of extracellular nanovesicles that can be found in most biological fluids. Exosomes have diameters from 30 to 100 nm and are of growing interest as biomarkers. In particular, magnetic susceptometry is being investigated as a promising method of detection.

# Sensorless—Reliable Low-speed Sensorless Motor Control for Safety Related Control Systems in Harsh Environments

J. Goldowsky, D. Grivon, L. Rossini, M. Boegli, E. Haenni, S. Bitterli, E. Onillon, O. Chételat, P. A. Schmid, H. F. Knapp, M. Krieger, M. Hoechmer

PMSMs (Permanent Magnet Synchronous motors) have benefits over brushed DC motors as higher speed ranges are available, lower inertia of the rotor makes the motor more agile and its brushes do not have to be maintained. However, PMSMs require more sophisticated control circuits using hall sensors, encoders or sensorless control. Typical fields of application are dental and surgery tools where highest standards with respect to reliability have to be met and tools have to be autoclavable. Hence, hall sensors and encoders are not an option. While sensorless control has become a widely used approach for high speed applications, it bears drawbacks when low-speed applications are targeted. Reliable low-speed sensorless motor control can be achieved by combination of advanced Kalman-Filter state estimation, modelling, current pulse injection (CPI), back electromagnetic force (bEMF) and direct current measurements.

CSEM has been developing sensorless motor controllers within several projects since 2009 – starting with a two year CTI followed by several industrial projects for industrialization. The technology reached a very high level and the customer plans to go to market for a subset of possible applications this year. However, sensorless control performance for low-speed applications is usually problematic for applications with strong safety requirements. Combining advanced state estimation and modelling techniques with dedicated hardware, CSEM is now able to provide reliable sensorless control also for low-speed applications.

A traditional 4-state EKF (Extended Kalman Filter) for the estimation of currents (d and q components), angular speed, and position has been augmented to include the motors torque as an additional fifth state. This improves the controller's dynamic performance [1]. Additionally – to increase the reliability of the system – available sinusoidal back EMF signals have been included as measurements to the EKF. Due to HW computation constraints, states update is obtained with  $f_{EKF} = 10 \text{ kHz}$  (Figure 1).

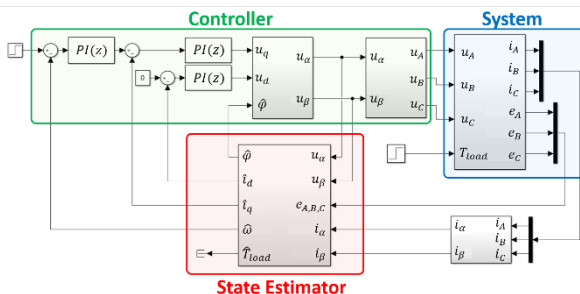


Figure 1: Block diagram of control/estimation scheme.

To verify reliable operation of the control scheme, simulations have been performed that show good results for state estimation and good system performance for critical operating conditions. Nevertheless, sensitivity to uncertain motor parameters is one of the major and well-known issues in sensorless motor control architecture [2]. The latter affects the actual control implementation and requires parameter estimation. In particular,

[1] O. Scaglione, "Iron Hysteresis and Enhanced Kalman Filtering for Sensorless Position Detection of Synchronous Motors," EPFL, Switzerland, 2013.

an external LKF (Linear Kalman Filter) for phase resistance estimation has been added to the actual control configuration (Figure 2) as proposed in [1].

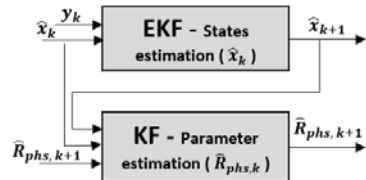


Figure 2: Block diagram of primary EKF and secondary LKF.

At present, phase resistance estimation is achieved with good results (relative error lower than 5%). Still the estimated resistance value in the primary EKF remains a critical parameter for stable operation of the controller. To meet this challenge, available information of angular position – given by back EMF zero-crossing detection – is used as further measurement to the EKF. A matrix covariance adaptation principle is also implemented to enhance the angle correction process.

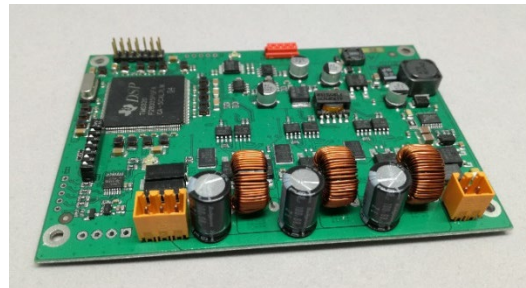


Figure 3: Next generation hardware.

For low-speed conditions current puls injection (CPI) has been utilized to guarantee stable operation even at standstill. However, CPI requires additional hardware and is not possible with all PMSMs. To push sensorless motor control without CPI towards lower drive speeds a test hardware has been developed, allowing the measurement of all required values for EKF and LKF including real verification by encoder values.

We thank MCCS, the Cantons of Central Switzerland, and the Swiss Confederation for supporting this work.

[2] B. Nahid-Mobarakeh, F. Meibody-Tabar, F. M. Sargos, "Mechanical sensorless control of PMSM with online estimation of stator resistance," IEEE Transactions on Industry Applications, vol. 40, no. 2, pp. 457–471, 2004.

## Wear-a-Watt3 (WAW3) e-tonomy—Autonomy for Wearables and IoT

J. Bailat, D. Dominé, M. Crettaz, P. Häfliiger, P. Kohler, E. Favre, N. Badel, A. Bionaz, L. Zhou, P. Liechti, R. Rusconi, N. Blondiaux, G. Cattaneo, L.-E. Perret-Aebi, J. Deng, S. Emery, P. Heinstein, S. Nicolay, R. Pugin, J. Kaufmann, M. Correvon, A.-S. Porret, J. Krauss, C. Ballif

CSEM is developing ultra-low-power solutions and flexible thin-film silicon photovoltaic cells to prepare for tomorrow's autonomous watches and other wearables. The Wear-a-Watt project demonstrator consists of a wristwatch which can measure the instant power produced by the flexible solar cells in the wristband. The evaluation platform and harvested data will be used to develop autonomous applications for the wearables.

The multidisciplinary project Wear-a-Watt builds on the strengths of CSEM in four research programs to create ultra-low-power wearable systems which can live off the energy harvested from their environment without requiring recharging or wiring. The programs involved in this project cover (i) the nano-textured flexible substrate used for the PV cells, (ii) the production and characterization of the PV cells and their optimization for low-illumination conditions, (iii) the development of an ultra-low-power chip for power management and (iv) the engineering of the complete system.

Last year a first watch prototype was realized. The project's prototype is equipped with a wristband with custom-made flexible solar cells covering a total area of 9 cm<sup>2</sup> on the watchband. The cells are connected to the measurement circuit through the watchcase. The red hand shows on the dial how much power is harvested by the PV cells in units of milliwatt on a logarithmic scale. Since this harvested energy depends indeed on the habits and the environment of the watch bearers, real life tests 'au porté' are best suited to help estimate the energy that can be collected.

The PV cells are produced onto nano-imprinted flexible polymer foils. These transparent substrates were developed in-house and up-scaled to an area of 300×300 mm. The thin-film solar cells used in this project are deposited by plasma-enhanced chemical vapour deposition for the active silicon layers and by sputtering for the front and back contacts in CSEM's new clean room facilities using processes developed in-house. Shadow masks are used to pattern these flexible solar cells to the required dimensions.

This year the integration has moved from a prototype to a real life demo. The focus was set on the integration of the PV cells into the wristband. The wristband gives mechanical stability and robustness to the cell assembly and ensures a good electrical contact of the cells to the contacting lines. The contacting lines transport the current through the watchcase by a watertight feedthrough. Ultra-low-power system for energy management and wireless communication has also been designed using in the current stage leading edge commercial off-the-shelf components. The watch can send via the low power communication protocol 'bluetooth low energy' the amount of energy harvested to a smartphone or a tablet for further data analysis.

The resulting PV cells show excellent performance even at low-illumination levels. With the first demonstrator, indoor measurements showed that a power of a few tens to hundreds of microwatts is produced. This value can reach to 10 to 15 milliwatts in the sun (indirect exposure). This is considerably more than what can be obtained with mechanical energy harvesting opening therefore new functions.



Figure 1: Demonstrator of the Wear-a-Watt project with thin-film PV cells integrated in the wristband. The cells are put on both parts of the plastic wristband and cover an area of 2.0×4.5 cm<sup>2</sup>. From indoor to outdoor the light intensity typically varies typically by 3 orders of magnitude which is why the milliwatt units are represented on a logarithmic scale on the watch dial (white and red tick marks) instead of the usual hour ticks.

In Figure 1, the advanced demonstrator is presented. 25 such demonstrators will be realized to start a 1 year long real life testing which will help us understand the different types of use case and measure the amount of energy that can be collected by different types of bearers.

In parallel, CSEM's IP blocks such as the icyTRX ultra-low-power RF transceiver, subthreshold microcontroller and a power management unit are developed and integrated. Part of a multi-project wafer, the first ICs are being tested.

This wearable test device for the Wear-a-Watt project can accommodate PV cells issued from other PV technologies provided they can fit the required dimensions and tolerances. It can therefore be used to evaluate PV cells from different technologies in real life conditions. Based on the first steps presented here, autonomous systems will further be developed. The applications will target different fields: med-tech, advanced watches, sports watches, and the broader field of the endpoints of the Internet of Things.

# GWAP02—A Highly Conformable Multipurpose Wireless Autonomous Patch

C. Hennemann, J.-D. Decotignie, B. Perrin, P.-A. Beuchat, Y. Liechti, S. Gray, D. Dominé, S. Generelli, D. Migliorelli, J. Disser, N. Glaser, F. Zanella, T. Offermans, N. Marjanović, J. Wacker

The CSEM Generic Wireless Autonomous Conformable Patch with Display (GWAP0) platform is a thin, miniature, flexible and rechargeable wireless interactive sensor system, i.e. an autonomous smart patch. It combines energy sources (e.g., PV/OPV), with pressure and temperature sensors, electronics, displays, interactive components, and antennas to create a highly comfortable multipurpose wireless autonomous patch.

To address wearable technologies such as activity trackers, hearing aids, virtual reality sensors, implementable sensors, CSEM has developed a generic, highly conformable, multipurpose, wireless patch with a display. This generic patch consists of an autonomous, flexible, and wearable platform with embedded sensors, electronics for computation, display, rechargeable battery, and renewable power source (photovoltaic), and wireless connectivity, including the antenna.



Figure 1: The generic flexible and wireless autonomous platform (left) and generic platform equipped with bigger PV cell for more autonomy.

For applications or sensors, such as a CO<sub>2</sub> sensor, where higher power is required, a second platform was designed to increase the harvested energy and to increase the charging speed of the battery (by a factor about two, Figure 1).

A comparison between the two GWAP0 PV cells is provided by Figure 2. The results show the maximum available power (P<sub>m</sub>) versus irradiance (Irr), up to 1 sun (i.e. 100 mW/cm<sup>2</sup>).

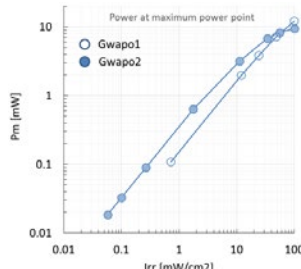


Figure 2: Power available at the maximum power point for the two thin-film silicon PV cells measured under various irradiances.

A first coating was applied to the patch in order to make it waterproof. This coating is extremely robust against tearing and bending and it is also bio-compatible.



Figure 3: Surrounding coating applied on the flexible patch.

Alternatively, a special, "conformable", ultra-thin, water-proof coating will be applied. This is done to increase the flexibility while enhancing the biocompatibility and user comfort.

GWAP0 is a generic patch/platform. Almost any type of sensor (e.g., a pH sensor) can be connected to it. As such "wearable" patch solutions are important for medical applications

(e.g., smart bandages), studies have been performed to investigate the performance of the sensor after the sterilization process (sodium hypochlorite). As shown in Figure 4, the sensors are not affected by the sterilization process.

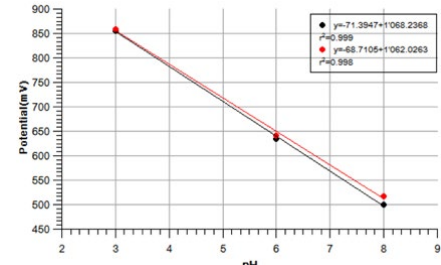


Figure 4: Calibration curve at 3 different pH before and after the sterilization.

Low-cost, printed sensors were developed for flexible, continuous and fully autonomous sensing applications. Figure 5 shows the developed pressure sensors made on PET-film with inkjet printed electrodes. The dynamic range of the sensors can be tuned with the composition of the structured-interlayer. A sensor response of more than 50 pF/mbar can be achieved.

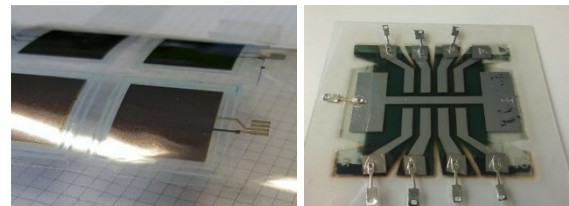


Figure 5: Printed, capacitive pressure sensors as a part of GWAP0 platform in hybrid integration approach (left) and printed, flexible solar cells as a part of GWAP0 platform in hybrid integration approach (right).

A foil-to-foil integration scheme was demonstrated in which OPV cells are integrated as standalone energy harvesting components onto the flexible PCB. The printed (blade coated), encapsulated cells (see Figure 5 right) achieved an efficiency of 4% under AM1.5 g illumination. The power output of the cells was in the range of 10-12 microwatts at 500 lux and 3-6 microwatts at 260 lux.

In a next phase, the OPV will be monolithically integrated by inkjet printing of the functional layers in the cell directly onto the flexible PCB. The inkjet-printability of the individual functional layers has been demonstrated. The next step is to inkjet-print all of the layers stacked on top of each other on the PCB in order to demonstrate a fully integrated, fully printed cell.

# PORGY BESS—Platform for the Optimal Regulation in Battery Energy Storage Systems

P.-J. Alet, M. Boegli, M. Höchmer, J. Pierer, C. Ballif

Forecasting of renewable energy production is crucial for the optimal management of distributed energy systems, especially of batteries. In this project we are developing forecasting techniques for solar photovoltaics on two time scales: on the very short term (<30 min) with full-sky imaging, and on the day-ahead scale with machine learning techniques. CSEM's forecasting techniques rank among the best available today and are ready for integration in energy management systems.

Forecasting of variable production is an essential tool to manage the power system with a large penetration of photovoltaics<sup>[1]</sup>. In particular, whereas batteries have a very short response time, they have a finite power and energy capacity, and rapid variations have an impact on their lifetime. As a result their solicitation must also be anticipated to make sure that they have the required capacity at critical times, and that their operation costs are minimized.

In the PORG BESS project we are focusing on improving short-to medium-term forecasting by building on CSEM's technologies for image processing and machine learning.

For the very short term (< 30 min), our approach is based on full-sky imaging to track the motion and nature of clouds. For development four systems have been set up in Bern (two cameras), Neuchâtel (Figure 1), and Alpnach. Furthermore a pyranometer measures the irradiance from the sun at every location. Building on the results of the Lilotrack project<sup>[2]</sup>, we have developed and deployed software for acquiring and logging images, calculating high dynamic range (HDR) images from the raw data, and analyzing them to track cloud motion.



Figure 1: Hukseflux pyranometer (front) for reference irradiance measurements and full-sky camera (back) installed on the roof of CSEM headquarters in Neuchâtel next to an operational PV system.

For medium-term (1 h to 24 h) forecasts, CSEM is focusing on a particular machine-learning approach: support-vector machine regression (SVR). This method is a nonlinear, non-parametric, kernel-based regression technique. It provides both good robustness and performance with limited training datasets. However it requires specialist know-how to formulate and tune it. Our initial developments were in Matlab and have now been

ported to Python for better integration in larger control software packages.

Inputs to the forecasting algorithm are the irradiance provided by numerical weather forecasts, and ephemerides (time-dependent elevation and azimuth of the sun). The algorithm is trained with seven-day batches of past PV production and input data, and predicts power production over a 24 h horizon. In this project we have used numerical weather forecasts with a 1 h temporal resolution and a 16 km spatial resolution. We have benchmarked our results against state-of-the-art methods (Figure 2) for a PV power plant used as reference by EURAC Research for their own work on forecasting<sup>[3]</sup>. CSEM's method came out among the best two for both root-mean-square error and mean absolute error.

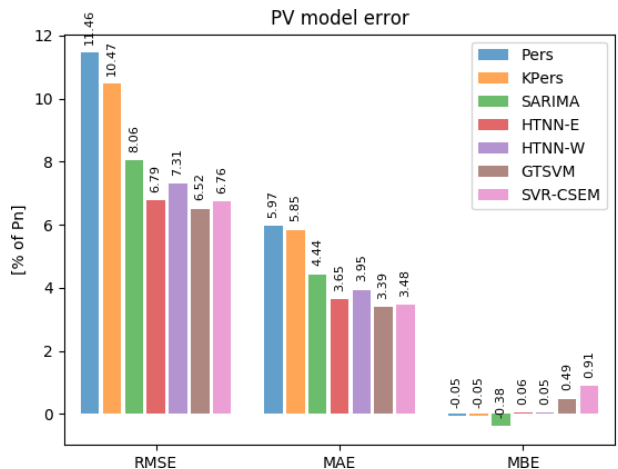


Figure 2: Benchmarking of error in PV forecasting on a 24h horizon between CSEM's method (SVR-CSEM), persistence methods (Pers and KPers), and state-of-the-art methods (autoregressive: SARIMA, multi-model based on artificial neural networks: HTNN-E, HTNN-W, and five-input support-vector machine: GTSVM).

## Acknowledgements

The development of the full-sky imaging benefits from the collaborative project SkyCam with Meteotest, which received funding from the Swiss Federal Office of Energy under grant SI/501515.

Benchmarking data were kindly provided by Marco Pierro and David Moser, from EURAC Research.

[1] P.-J. Alet, et al., "Forecasting and Observability: Critical Technologies for System Operations with High PV Penetration," in 32nd Eur. Photovolt. Sol. Energy Conf. Exhib., pp. 1444–1448, WIP Wirtschaft und Infrastruktur GmbH & Co Planungs KG, Munich (2016) doi:10.4229/EUPVSEC20162016-5DP.1.3

[2] P.-J. Alet, et al., "LiLoTrack: Short-term forecasting and storage for optimal management of PV electricity," in CSEM Sci. Tech. Rep. 2015, p. 14, CSEM SA, Neuchâtel (2016).

[3] M. Pierro, et al., "Multi-Model Ensemble for day ahead prediction of photovoltaic power generation," Sol. Energy 134, 132–146 (2016) doi:10.1016/j.solener.2016.04.040.

# TeraLine—Single Detector for Multicolor Terahertz (THz) Imaging

A. Bischof, E. Le Roux, O. Vorobyov, C. Beyer, V. Revol, G. Voyrin, J. Levrat

*Active multi-color Terahertz (THz) imaging technology has a very large potential for inspection of composite materials. The single pixel detector developed in the TeraXplore project and integrated in a 0.18  $\mu\text{m}$  CMOS process was used to build a demonstrator for THz imaging. Furthermore, a new version of the single pixel detector is currently being implemented in 55 nm CMOS technology.*

Terahertz (THz) imaging technology is increasingly being used in the fields of non-destructive material inspection (especially composites), security (people screening), medical diagnosis (skin cancer or diabetes screening) and food inspection (detection of contaminants or decayed products). THz imaging has many advantages over traditional inspection technologies like microwave, ultrasound or x-ray. For example, it penetrates electrically non-conductive materials and is safe to use. THz multispectral imaging is particularly interesting because specific materials have a precise “fingerprint” in the THz spectrum, and thus features become visible that are not present in a monochromatic image, which allow robust identification.

In this report, we present a demonstrator that was built with a THz detector obtained from last year's CSEM TeraXplore Multidisciplinary Integrated Project (MIP). The CMOS-based single point detector uses the “direct detection method”, i.e. the detector consists of an antenna and a CMOS-based RF receiver. The demonstrator setup is shown in Figure 1.

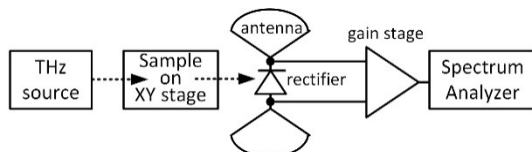


Figure 1: THz demonstrator setup.

An off-the-shelf THz source was used. The THz output can be tuned to a frequency between 325 GHz and 500 GHz. In order to reduce the impact of the rectifier's flicker noise, 200 kHz on-off keying is applied to the source signal. The measurement was done in transmittance mode, i.e. the sample is located between THz source and detector. As a single point detector is used and the sample is moved with a XY stage to enable scanning of the entire sample. The output of the detector was amplified and then observed with a spectrum analyzer, and averaged over 1 second.

Images of several different materials, such as a composites with defects, polymers and PV cells were taken with the demonstrator. Figure 2 shows a THz image of a glass fiber composite plate with 3 holes of different sizes and a metal plate attached to it. The picture was taken with a source frequency of 425 GHz and a pixel size of 0.5 mm. It can be observed that the resolution is around 1.5 – 2 mm due to the strong diffraction effects at this wavelength (0.66 mm). The different defects can be distinguished in the image (missing material, metal or polymer inserts).

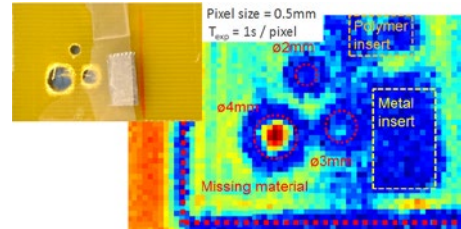


Figure 2: (left) image of glass fibre composite plate; (right) THz image.

Different detector types were developed within TeraXplore and implemented in 0.18  $\mu\text{m}$  CMOS technology. Measurements of this test chip have shown that the most promising detectors are the Poly-Gate-Separated (PGS) Schottky diode and the diode-connected MOS transistor. The optimum frequencies of operation are in line with the results of simulations. The performance of the detector is comparable to state of the art shown in Table 1.

Table 1: Detector performance vs state of the art.

	Response	NEP	Freq	Detector
Y. Zhan [1]	323 V/W	29 pW/√Hz	280 GHz	Schottky
E. Seok [2]	200 V/W	100 pW/√Hz	180 GHz	Schottky
R. Han [3]	250 V/W	33 pW/√Hz	280 GHz	Schottky
TeraXplore	158 V/W	65 pW/√Hz	425 GHz	Sch. / FET

As better performance is expected for smaller transistors [4], a new detector test chip was designed in TSMC 55 nm technology. Because of the lack of simulation models for THz frequencies, different sizes were implemented for each type of detector. As in the previous test chip, narrow-band patch antennas were integrated on the chip with the center frequencies 375 GHz, 425 GHz, and 475 GHz. This test chip will be taped out in September 2017. First measurement results are expected by the end of the year.

Work also continued on the development of a broadband antenna, which supports a frequency range from 300 GHz to 500 GHz. The first approach was 3D printing of the helix antenna, followed by electro-less deposition. However, this structure has problems with mechanical stability. Therefore a second approach was employed to print the helix in metal on the outside of a cylinder. Several samples were printed on plastic and silica rods. The metal layer of the tested silica samples was found to have good conductivity. Antenna characterization results are expected later this year.

[1] Y. Zhang, *et al.*, “Schottky diodes in CMOS for terahertz circuits and systems”, RWS IEEE Radio and Wireless Symposium (2013).

[2] E. Seok, *et al.*, “Progress and challenges towards terahertz CMOS integrated circuits”, IEEE Journal of Solid-State Circuits, 45 (2010) 1554.

[3] R. Han, *et al.*, “A 280-GHz schottky diode detector in 130-nm digital CMOS”, IEEE Journal of Solid-State Circuits, 46 (2011) 2602.

[4] A. Boukhayma, *et al.*, “A 533 pW NEP 31×31 pixel THz image sensor based on in-pixel demodulation”, ESSCIRC European Solid State Circuits Conference (2014).

# HybSi 2017—Novel Opportunities for High-precision Mechanisms Based on the Hybridization of Silicon at the Centimeter Scale

F. Barrot, F. Cosandier, G. Musy, Y. Petremand, L. Girien, S. Lani, B. Dunan, M. Dadras, E. Dominé

The high precision micro-structuration of silicon with the DRIE process opens up a new range of opportunities for the design of high precision mechanisms at the centimeter scale. Key Swiss industries such as the watch industry and scientific instrumentation can benefit from this approach. However, silicon being a brittle material, its handling and assembly with other materials is quite delicate. Combining its expertise in the domains of precision mechanisms, micro-manufacturing techniques, and high-precision 3D printing, CSEM is taking up the challenge to become the Swiss competence center for the design, manufacturing, assembly, and characterization of hybrid silicon based mechanisms.

The DRIE micro-structuration of silicon enables the design and batch production of mesoscale mechanical parts with a micrometric precision. This approach is appropriate to design and produce precision mechanisms at a scale between MEMS and classical mechatronics; such mechanisms can be found in different industrial fields such the watch industry (new watch mechanisms) or scientific instrumentation (force sensors, micro-grippers, micro-positioning stages). However, such systems are fragile, due to the brittle nature of silicon, and their assembly is a delicate task. The wafer level assembly of silicon parts, which in some cases may be combined with multi-level parts, is a way of answering this challenge<sup>[1]</sup>. When wafer level is not an option (e.g.: 3D assembly), the careful design of mechanical interfaces is then crucial to enable the safe handling and assembly of silicon parts by an operator or automation; this strategy can be implemented using the multilevel structuration of silicon (2.5D) or by using a precise 3D printing process to produce adequate mesoscale standalone mounts/interface-parts or by direct deposition of precise 3D printed interfaces on top of silicon parts.

Following this approach CSEM designed two demonstrators, each addressing a different industrial field. A first demonstrator, addressing the watch industry, consists of a linear oscillator made from the assembly of three monolithic parts comprising flexure hinges to guide oscillations without friction nor wear between parts. Its isochronism and the influence of gravity was accounted in the design. A 3D printed 5:1 scale model was produced and assembled together with a linear escapement mechanisms to check for the kinematics and dynamics of the concept (Figure 1). Then a 1:1 silicon based demonstrator was successfully produced, assembled and characterized (Figure 2). It is noteworthy that a flat, 2D stacked, version of this oscillator is conceivable

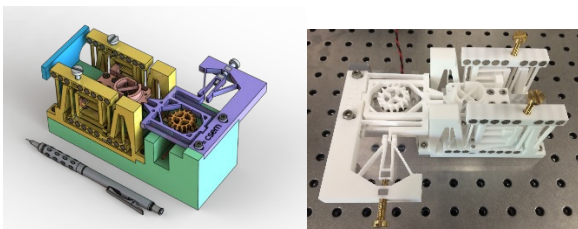


Figure 1: Linear oscillator - 5:1 scale. (left) CAD view, (right) 3D printed.

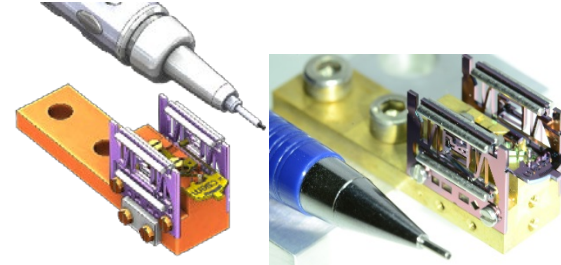


Figure 2: Linear oscillator 1:1 scale (left) CAD; (right) silicon based.

CSEM believes that high precision 3D printing is a promising approach to propose high precision mesoscale systems with enhanced functionalities and a high level of integration. In this approach, only parts requiring a very high precision are processed out of a silicon substrate with DRIE, before being assembled or combined to 3D printed parts/interfaces comprising not only mechanical but also fluidic, optical, or electrical functions. In that respect, a second demonstrator addressing the scientific instrumentation market was produced; it consists of a microfluidic system that allows the filtration of very small size particles with a "nanofilter" that can be substituted according to the filtration needs. After the concept formulation and a first version in 2016<sup>[2]</sup>, several iterations on the design were necessary, particularly for the design and implementation of the seals, to make sure that the system works without leaks and stays watertight.

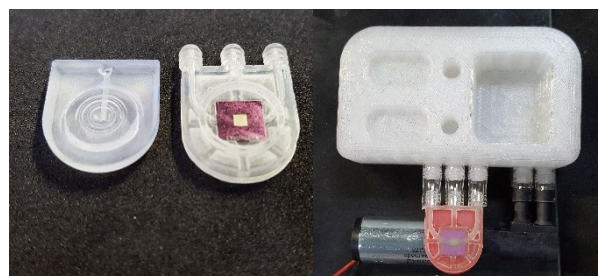


Figure 3: Microfluidic filtering system combining 3D printed parts and a high precision silicon filter. (left) Filter housing opened up, the silicon filter is the yellowish square at the center of the assembly; (right) Overall filtering system including its turbistic pump.

This work was executed in the frame of CSEM's MIP program and funded by the Canton of Neuchâtel. CSEM thanks the Canton of Neuchâtel for their support.

<sup>[1]</sup> F. Barrot, et al., "SILFEX - Hybrid Integration of Microfabricated Components", CSEM Scientific & Technical Report (2012), 15.

<sup>[2]</sup> F. Barrot, et al., "HybSi—High-precision Mechanisms at the Centimeter Scale based on Silicon Hybridization", CSEM Scientific & Technical Report (2016), 19.

# HECTIC—Harsh Environment Ceramic Technology Involving Silicon Carbide

G. Spinola Durante, A. Hoogerwerf, M. Fretz

Silicon carbide ( $\text{SiC}$ ) is a highly corrosion and temperature resistant material, which makes it the material of choice for many applications in harsh environments. CSEM is developing the key fabrication processes for  $\text{SiC}$ -based MEMS sensors and its related packaging technologies in order to fabricate fully-functional  $\text{SiC}$ -based MEMS pressure sensors and accelerometers and other sensors.

Silicon carbides ( $\text{SiC}$ ) exhibit characteristically high hardness, wear resistance, corrosion resistance, and strength — even at high temperatures. Its chemical inertness makes it biocompatible for long term medical implants [1]. Its high temperature resistance makes it useful for the monitoring of gas turbines, jet engines, oil and gas wells, and space rockets [2].

CSEM is developing the key front-end and back-end fabrication processes for  $\text{SiC}$  MEMS devices with the near term aim to fabricate fully functional pressure sensors and accelerometers. The most critical elements in fabrication that have been identified are: etching of  $\text{SiC}$ , making ohmic contacts to  $\text{SiC}$ , wirebonding chips, hermetic sealing of  $\text{SiC}$  structures to a back plate, and die-attach to a  $\text{SiC}$  submount.

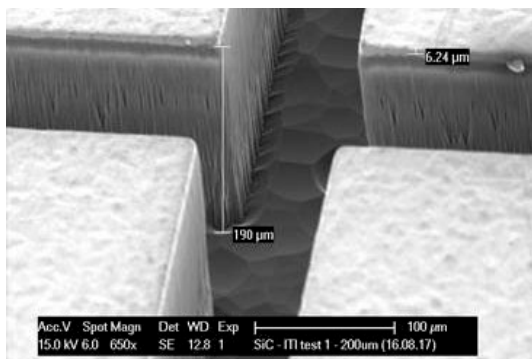


Figure 1: Picture of DRIE etched cavities in  $\text{SiC}$ .

The etching of  $\text{SiC}$  is so challenging because of its chemical inertness. Consequently  $\text{SiC}$  can only be etched with some of the most aggressive plasma etch gases. This makes it very difficult to find a material that can resist these plasma etch gases and function as a masking layer. A material has been found, which enables to obtain reproducibly a selectivity of 40:1. Figure 1 shows the results of an etch process 190  $\mu\text{m}$  deep into  $\text{SiC}$ ; depths of more than 250  $\mu\text{m}$  have already been achieved. The roughness of the bottom of the etched cavity is still being investigated, but appears to be related to the presence of micro pipes in the  $\text{SiC}$  substrate.

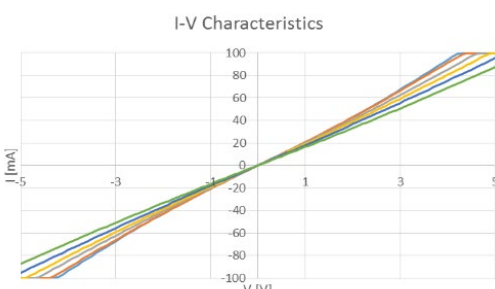


Figure 2: I-V characteristics of the metal to doped  $\text{SiC}$  contacts.

[1] S. E. Sadow, Silicon Carbide Biotechnology, Elsevier, 2016.

Electrical contacts between metal and the doped  $\text{SiC}$  layers have been made. The measured I-V characteristics show an almost perfectly linear, i.e. ohmic contact. The material choice for the contact material has been made such that the contact should be unaffected by operating temperatures of up to 600 °C. A protection layer of the interconnect metal is now being investigated to achieve this challenging requirement.

The wire-bonding of  $\text{SiC}$  chips to substrates has been achieved using platinum wire-bonds (Figure 3). The wire-bonds are expected to be resistant to temperatures of up to 600 °C and their measured bond strengths are similar to those of conventional aluminum wire-bonds. The bonding wire thickness is in the range from 25  $\mu\text{m}$  to 250  $\mu\text{m}$ , with the thicker wires having the potential for being used not only for sensors but could also ensure compatibility with high power components.

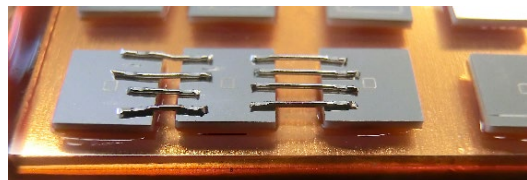


Figure 3: Picture of Pt-wirebonding with 250  $\mu\text{m}$  diameter wire.

The hermetic bonding task is ongoing and exploits results from previous projects and will enable the possibility of having an absolute pressure sensor with reference cavity (Figure 4).

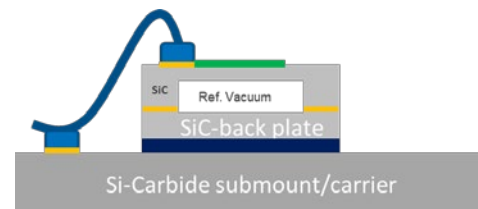


Figure 4: MEMS hermetic assembly and submount die-attach.

The key processes will then be combined in one fabrication technology aiming in the first place to make pressure and temperature sensors (Figure 4). Other sensors, such as gas sensors, force sensors, and accelerometers will be pursued at a later stage to complete CSEM's offerings in the field of applications in harsh environments.

These technology bricks will enable CSEM to position itself in the highly dynamic and innovative field and market of sensing components for harsh environments.

This work was supported by the Swiss Confederation and MCCS Micro Center Central Switzerland.

CSEM thanks them for their support.

[2] M B. J. Wijesundara, R. G. Azevedo, Silicon Carbide Microsystems for Harsh Environments, Springer 2011, pp. 1-26.

# SMAC2017—Characterization of the Flat-form Factor Miniature Clock Assembly

L. Balet, J. Haesler, S. Karlen, S. Dasen, J.-A. Porchet, D. Ruffieux, S. Lecomte

The preliminary building blocks of a miniature atomic clock (MAC) physics package (PP) with a height of less than 5 mm were presented in the past years. CSEM presents in this paper the manufacturing and functional testing of the main MAC constituents.

Last year's report presented in detail the individual components and the first assembly of a flat form miniature clock. We now report on the measurements that were performed on individual subsystems: first on the cell, then on the physics package (PP) and finally on the full system with ASIC and control electronic. Full metrological characterization of the atomic clock is challenging, as it requires months of seamless operation.

## Atomic vapor cell

The atomic vapor cell (Figure 1, left) is the core component of the MAC. Loading it with Rubidium is obtained by a proprietary process based on  $\text{RbN}_3$  solution dispensing and UV-decomposition. The cell lifetime and intrinsic frequency drift have been drastically improved thanks to protective coatings.

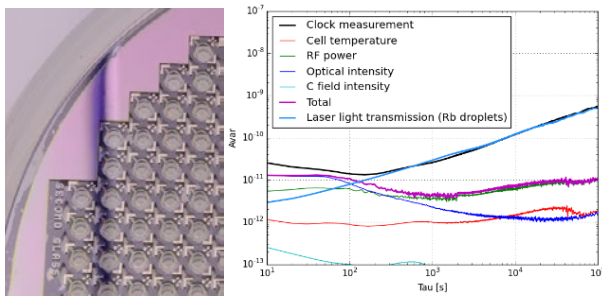


Figure 1: Metrological characterization of an atomic vapor cell and identification of the individual contributions to the frequency drift.

Metrological characterization of individual vapor cells shows that the frequency stability seems currently to be limited by the condensation of gaseous Rubidium in the form of droplets on the optical windows of the cell, thus degrading the optical field stability and causing a so-called "light shift" of the clock frequency (Figure 1, right). The engineering of condensation areas out of the cell optical path allows to minimize this effect (CSEM patent pending) and is currently under test.

## Physics package

The physics package (PP) is the miniaturized laboratory setup containing all the hardware required to operate the atomic clock, with the exception of the control electronic.

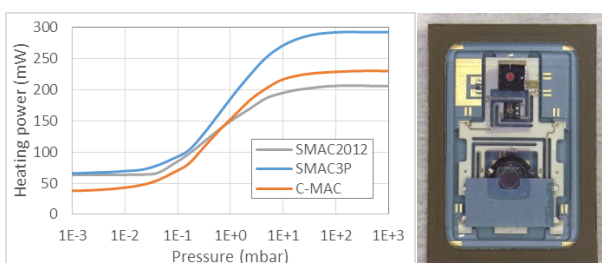


Figure 2: Total heating power for 3 different PP types as a function of the package pressure and top picture of a C-MAC PP.

The power consumption of unsealed PPs was measured in a vacuum chamber as a function of pressure. The results of the vertically stacked architecture (SMAC2012 design), flat form package with conventional electrical lines (SMAC3P) and with thin film based narrow electrical lines (C-MAC<sup>1</sup>) are compared on Figure 2. Vacuum sealing of the packages with residual pressure below  $10^{-2}$  mbar is mandatory to operate the PP below 80 mW. The thin-film technology of the C-MAC design allows further reducing the power consumption by a factor 2, slightly below 40 mW.

Vacuum sealing of the PPs was proven to be challenging for various technical reasons. Preliminary tests with thin film getters were not conclusive due to high initial pressure within the cavity (i.e. insufficient initial vacuum). Three alternative packaging solutions are thus currently being investigated.



Figure 3: (left) Short-, mid-term stability measurement of a PP interfaced with laboratory electronic via a custom test socket (right).

It was nevertheless possible to measure the C-MAC PP short-, mid-term frequency stability with the help of a laboratory electronic. An excellent fractional stability of  $7 \cdot 10^{-11}$  @ 1 s was obtained, thus validating the flat form package architecture. Improved mid-term performances (Figure 3) are certainly possible through careful tuning of the various electronic loops parameters and by reducing the "light shift".

Long-term frequency stability measurements could not be performed yet due to the systematic failure of the temperature sensors within the PP. The cause was identified and an alternative approach identified with the added benefit of being wafer level compatible and cost effective.

## Control electronic and ASIC

Several PPs were mounted on the control electronic PCB to characterize the microcontroller and the ASIC used to detect the atomic signal and lock the clock. The first three control loops used to lock the laser optical frequency, its temperature, and the temperature of the cell were tested and characterized. The RF generation was validated. However, it was not possible to characterize the locking loop due to the mentioned failure of the PP temperature sensors. Full characterization of the electronic, including the locking of the RF loop, of the magnetic field and of the laser power are planned in the near future.

[1] J. Haesler, et al., Proceeding IFCS-EFTF 2017.

# VitalRFsens—A Flexible FMCW RADAR Setup

E. Le Roux, F. Chicco

In context of the VitalRFsens MIP, a versatile test setup has been implemented in the laboratory in order to evaluate the feasibility of vital signs sensing via RF. RF offers the potential for contactless and remote sensing of vital signs. The test setup uses a real-time Frequency-Modulated Continuous Wave (FMCW) radar based on a Vector Network Analyze, combined with signal processing running on GNU Octave / Matlab®.

This report describes a flexible FMCW radar setup, which has been implemented in the laboratory at CSEM in order to evaluate the potential to monitor vital signs (e.g., heart rate) via Radio Frequency (RF) sensing. An illustration of the setup is provided by Figure 1. The goal is to provide a real-time (RT) baseband FMCW radar signal for the purposes of development of the necessary signal processing algorithms, as well as, to make emulation of potential limitations, with respect to implementation of a future low-power Integrated Circuit (IC), easy as possible. The FMCW radar setup will allow the IC specification to be validated via signal processing of the RT signal. Importantly, the setup also serves as an evaluation platform for development of antenna and product mechanics.

An FMCW radar sweeps a transmitted tone in frequency and self-mixes it with the received signal backscattered by the environment. The farther the reflector is from the transmitter, the higher the beat frequency due to the delay between transmitted tone and the received tone. The distance is proportional to the propagation speed divided by the beat frequency. A representation of the amplitude (and phase) of the reflections versus distance is provided by taking an inverse Fourier transform (iFFT) of the received signal.

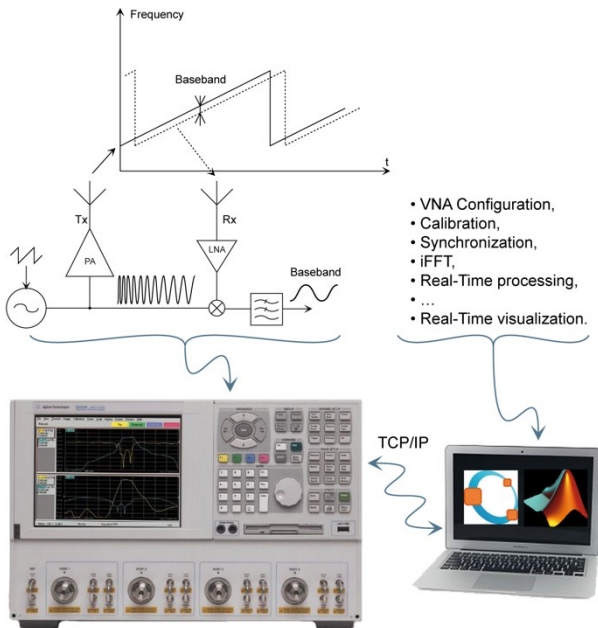


Figure 1: Setup principle.

In the setup, a Vector Network Analyser (VNA) is used to realize the RF analog processing. The remaining operation (without time-domain capability) is limited to the frequency-to-distance conversion, e.g., via an iFFT. A PC (running either Matlab® or GNU Octave) is connected to the VNA for the purposes of control and signal processing.

The flexible setup enables easy variation of the: frequency sweep (from DC to 40 GHz and, with frequency extension modules (from 50 to 75 GHz & from 75 to 110 GHz), output power, baseband bandwidth (sweep time and points per sweep) and the

topology (mono-static to bi-static or even multiple Rx channel using the 4-ports). It also enables easy emulation of close-in phase noise by driving the 10 MHz frequency reference, as well as, remote signal processing and visualization.

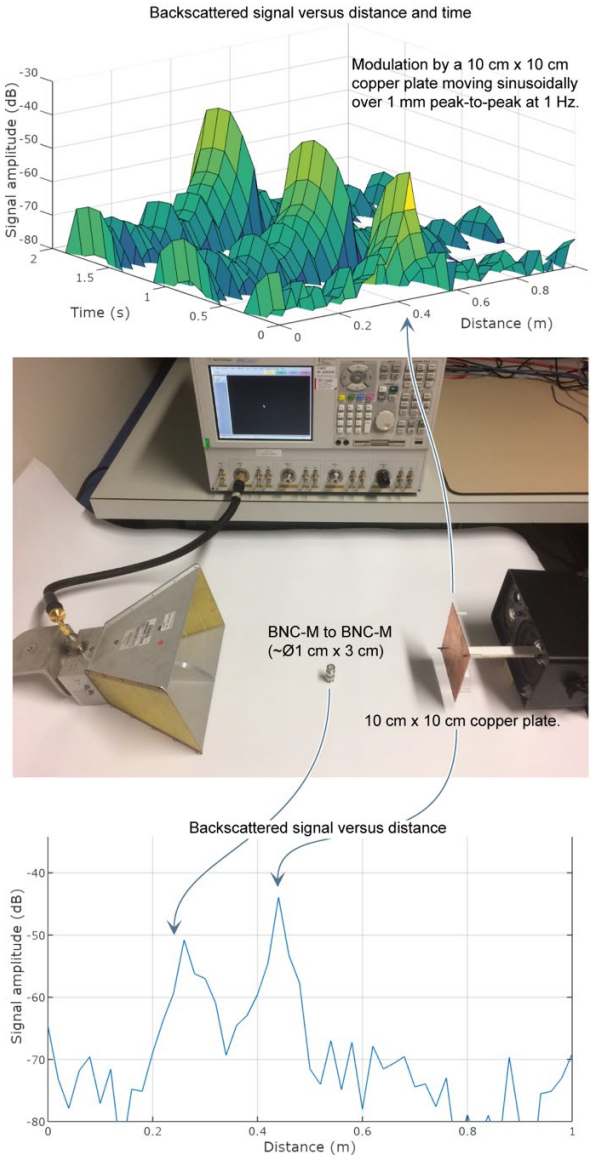


Figure 2: Real-time 10 sample/s (51 points / 10 ms sweep) running setup with 3.1-10.6 GHz (UWB) frequency sweep.

The laboratory setup, while limited in speed, is fast enough to support evaluation and development of the targeted vital signs sensing application (i.e., heart rate monitoring). In the future, the same flexible radar setup can serve as a platform for investigation and development of a variety of other applications, such as breath rate estimation, presence detection, tank level measurement and gesture recognition.

# IntelliDUST—Intelligence in Silicon for Deep-ultra-low-power Sensor Technology

E. M. Calvo, R. Cattenoz, R. Delgado-Gonzalo, P. Renevey, M. Bertschi, J.-L. Nagel, M. Pons Solé, S. Emery, J. Bailat, M. Correvon

In the era of the Internet of Things (IoT) an ever increasing amount of sensors are integrated in more devices and new applications. All these data streams need to be processed to extract features and provide value and meaning to the user. But the algorithms in charge to do this processing are becoming comparatively much hungrier in power terms than the latest ultra-low-power sensors available in the market. IntelliDUST will leverage the capabilities of sub-threshold circuits to turn "dumb" into "smart" sensors capable of providing processed signals at a fraction of the power required by the sensor.

Traditionally the processing of raw sensor data signals has taken place in the microcontroller ( $\mu$ C) with algorithms designed and targeted to the specific application. Some sensors (e.g., accelerometers) have improved up to two orders of magnitude their power consumption, rendering the algorithmic processing in the  $\mu$ C the most power hungry element in the chain. By integrating the algorithms directly in the sensor and implementing them with a dedicated sub-threshold circuit (to minimize the power required for the processing part), mass market applications in the wearables field (e.g., activity tracking, among others) could benefit from:

- Improved battery life.
- Energy harvesting becomes realistically feasible.
- Uninterrupted measurement of key parameters to fill the gaps of missing data when energy is scarce (e.g., aggregated estimations of activity parameters).
- Simplified system architecture (fast time to market).

CSEM combines expertise in signal processing and ultra-low-power design to propose an intelligent sensor system.

## Model-based activity tracking algorithm

The first stage in IntelliDUST started by converting CSEM's industry-proven algorithms related to activity tracking from C code to Simulink. This model has the advantages of being capable of generating the Hardware Description Language (HDL) code to implement an eventual chip along with extensive testing capabilities. This task has been successfully accomplished for 5 of 6 blocks (83%) composing the activity tracking algorithm (see Figure 1).

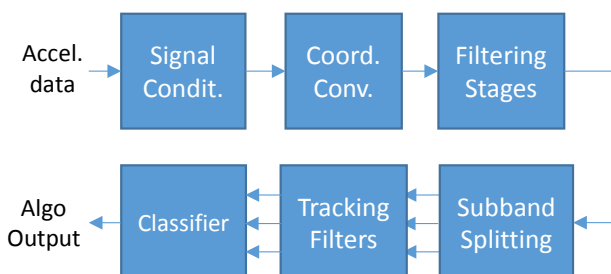


Figure 1: Block Diagram of Activity Tracker Algorithm

Optimization efforts in the model will be dedicated where deemed necessary (be it architectural or simply for better HDL generation). As a frame of reference for the comparison with the HDL implementation estimations, the activity algorithm previously

developed consumes 90 $\mu$ W when running in a Cortex-M0 (nRF51822 by Nordic Semi), while one state-of-the-art accelerometer (ADI ADXL363) requires only 4 $\mu$ W.

## Implementation assessment using sub-threshold design

Being IntelliDUST a feasibility study, a physical implementation is not sought for. However, simulation tools and previous experience allow us to accurately assess the requirements in terms of chip gates and consumption with a high degree of precision without the need for a costly tape-out. In this stage, the first four blocks of the algorithm have been synthesized to Register Transfer Level (RTL) from the HDL code generated by the Simulink model. The RTL obtained was used to evaluate complexity and power consumption.

Without loss of generality we have evaluated MIFS Deeply Depleted Channel (DDC) 55 nm technology operating at 0.5 V sub-threshold voltage already in use at CSEM. DDC choice allows the optimization of the leakage power by using advanced bulk bias setting and the reduction of the dynamic power by operating at low voltage<sup>[1]</sup>. The partial design was evaluated with real daily-life recordings of 3 channels of accelerometer data sampled at 25Hz.

## First results

The first iteration of the algorithm (4 out of 6 blocks) results in a synthesized design of around 20 kGates. See Table 1 below.

Table 1: Power consumption estimation.

Technology implementation	Power
C55DDC 0.5 V (partial algo.)	10 nW (< 0.1 nW dynamic)
Cortex-M0 $\mu$ C (complete algo.)	90 $\mu$ W
Adxl363 (sensor only, no algo.)	4 $\mu$ W

The power consumption obtained so far stays well below the consumption of the algorithm in a standard  $\mu$ C by a few orders of magnitude and we expect the final value to not be ostensibly different. The dynamic part is negligible due to low toggling activity and low frequency of operation, thus making very low leakage technologies the best fit to this application. The estimated power for the final complete implementation of the algorithm is expected to be at least one order of magnitude below the consumption for a state-of-the-art accelerometer, rendering the intelligence attached to the sensor essentially free from a power consumption perspective.

<sup>[1]</sup> K. Fujita, et al., "Advanced channel engineering achieving aggressive reduction of VT variation for ultra-low-power applications", IEDM IEEE (2011).

# PlasMOS—Integration of Plasmonic Structures in Standard CMOS

S. Emery, L. A. Dunbar, B. Gallinet

Today, the implementation of filters (e.g., polarization, pass-band etc.) for image sensors and cameras requires additional and costly processing steps. This project investigates the feasibility of directly integrating plasmonic structures in or on a standard CMOS process; such a technology could allow for easy and cost-effective implementation of filters directly in our image sensors. An immediate application is the implementation of a multispectral imager at no extra cost compared to a conventional imager.

Since the extraordinary optical transmission measured through subwavelength holes in opaque metal sheets by Ebbesen in 1998<sup>[1]</sup>, there has been some speculation as to the possible benefits of tailoring metallic nanostructures to obtain optical effects beneficial for commercial devices. Recently, detailed investigations<sup>[2]</sup> have been performed regarding the potential to excite bounded surface waves between the metal-semiconductor interface, i.e. the so-called 'plasmons'. To obtain optical emission via excitation of these delocalized surface waves, it is necessary to structure the material at the scale of the wavelength of light, i.e. 400-700 nm for visible wavelengths. These resonant structures yield filtering functions that can be tailored by changing the properties of the metal structure e.g., size of the holes, shape of the holes, period of the holes, as well as, the type and thickness of the metal used.

The challenge in this work is finding a CMOS compatible structuration that provides the desired optical filtering function. Towards this end, the PlasMOS project investigates two different options for implementing filters based on plasmonic structures i.e. the use of:

- The existing metal stack of the CMOS process.
- A post-processing step on top of the existing CMOS wafer.

The filters are designed to exhibit a transmission band that is independent of the polarization. As the main goal is to obtain a plasmonic response at visible wavelengths, we are focusing on aluminum or aluminum alloy structures (copper is unsuitable for resonant plasmonic structures due to high losses at these wavelengths).

In the case of option 1, use of the existing CMOS metallization process to fabricate the plasmonic structures limits the choice to relatively older CMOS technologies, as more recent technologies have adopted copper for most of their metal layers. A thorough comparison of technology options and design rules was performed and we concluded that simple planar structures in the dimensions available with such older technologies are not suitable for plasmonic filters in the visible range. Given this, we are now investigating more complex 3D structures that could be implemented using consecutive metal layers.

With respect to the second option, fabrication of the plasmonic filters is performed in a post-processing step: UV nanoimprint lithography is used to replicate the nanostructure from a master onto the sensor. The master consists of periodic nanostructures arranged in pixels with a different pitch. It can be fabricated once with laser interference lithography or electron beam lithography

and used numerous times, thus reducing the cost of manufacturing. After replication, an evaporation of the metal is performed on the nanostructure, thus generating an array of plasmonic nanostructures in two processing steps<sup>[3]</sup>. Each filter of the array transmits a different portion of the visible light. Specific marks are used on the corners of the sensor in order to ensure accurate alignment between the filters and the pixels.

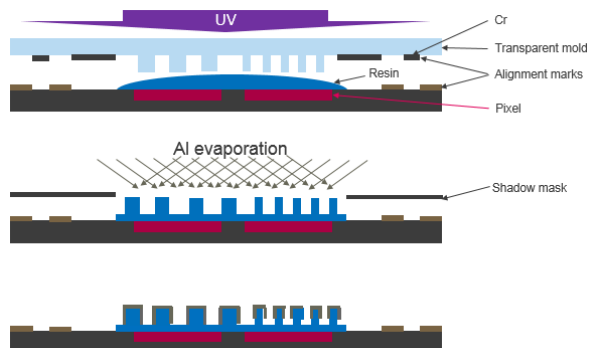


Figure 1: Fabrication of plasmonic filters in a post-processing step.

Simulations of the optical properties of the plasmonic filters fabricated via post-processing have been performed with the rigorous coupled wave analysis (Figure 2), taking into account the constraints of the process. In particular, the depth of the nanostructures and the thickness of the evaporated layer must be identical for all filters. Only the aperture dimensions and pitch can be varied.

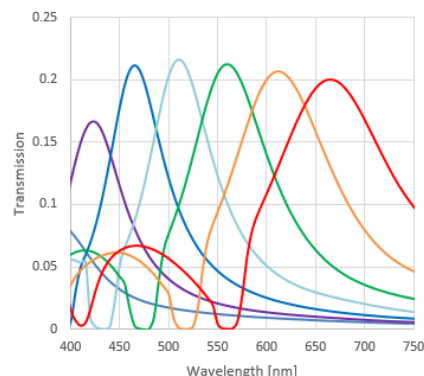


Figure 2: Simulated transmission spectrum for 6 different filters.

In a next step, the nanostructured pixels will be first fabricated in stand-alone form and their transmission characterized in order to assess the quality of the structures. In a second step, they will be replicated on top of an imager designed by CSEM.

[1] T. W. Ebbesen, *et al.*, "Extraordinary optical transmission through sub-wavelength hole arrays", *Nature*, 391 (1998) 667.

[2] F. J. Garcia-Vidal, *et al.*, "Light passing through subwavelength apertures", *Rev. Mod. Phys.*, 82 (2010) 729.

[3] F. Lütolf, O. J. F. Martin, B. Gallinet, "Fano-resonant aluminum and gold nanostructures created with a tunable up-scalable process", *Nanoscale*, 7 (2015) 18179.

# ExoPro—Exosomes Profiling and Characterization

L. Burr, H. Gao, D. Mueller, S. Paoletti, C. Beyer, R. Limacher, E. Rutz, L. Barille, L. Barbe

Exosomes are extracellular nanovesicles that can be found in most of the biological fluids. Their diameter varies from 30 to 100 nm. Exosomes have raised growing interest since they are considered as biomarkers for several diseases. Due to the vast types of extracellular vesicles (EVs) of different sizes, their different contents and different functions, there is an increasing need to develop better methods for isolation, purification and characterization of EVs.

Extracellular vesicle research spans from the diagnostic side to the therapeutic approach but in all cases, sample preparation is required to save time and to generate accurate data. Physical characterization of nanovesicles is currently carried out with techniques such as dynamic light scattering (DLS) or nanoparticle tracking analysis. Through different projects, CSEM has acquired experience in asymmetrical-flow field-flow fractionation (AF4), multi-angle light-scattering (MALS), functionalization of nanoparticles, and sample preparation.

CSEM assessed in collaboration with the Cardiocentro Ticino, the limitations on the current approaches and identified two major tracks for improvement: detection and characterization of exosomes. Regarding the first track, a novel isolation techniques of exosomes based on immuno-capture was developed and tested. Concerning the second track, AF4 was employed in combination with UV and MALS detector.

For the detection of exosomes, commercially available magnetic nanoparticles (MNP) of similar sizes (ranging from 25 to 100 nm) are functionalised with OptoDex™ technology to covalently bind antibodies specific to EVs (tetraspanin family: CD9, CD63, CD81) resulting in a system with high specificity and sensitivity. Exosomes bound to MNPs form complexes with varying hydrodynamic volumes depending on their size. Assessing the relaxation time (Brownian relation) of the suspension allows to determine the concentration and roughly the size of exosome in suspension (Figure 1).

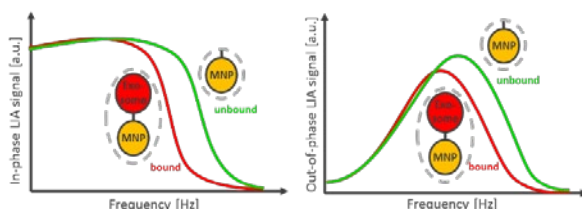


Figure 1: Changes in the hydrodynamic diameter, due to target binding to MNPs, shift the assessed measurement signal (left: in-phase, right: out-of-phase).

Following latest publications<sup>[1,2]</sup>, the optomagnetic principle (Figure 2) was chosen to measure the relaxation time due to optimal performance with respect to measurement sensitivity and system complexity. A lab setup was designed and realised for a frequency range from 10 Hz to 50 kHz and a maximum magnetic flux density of up to 3 mT.

Several studies are conducted until the end of 2017 to evaluate the sensitivity and specificity limit with respect to size and

[1] M. Donolato, et al., "Novel readout method for molecular diagnostic assays based on optical measurements of magnetic nanobead dynamics", *Analytical Chemistry* 87.3 (2015):1622-1629.

concentration of exosomes in suspension. This method can be easily extended to detect the concentration of other targets, like bisphenol A (BPA), DDT, diethylstilbestrol (DES) or heavy ions like cadmium or lead, among others<sup>[3]</sup>. A further goal will be to miniaturize the system allowing point-of-care applications.

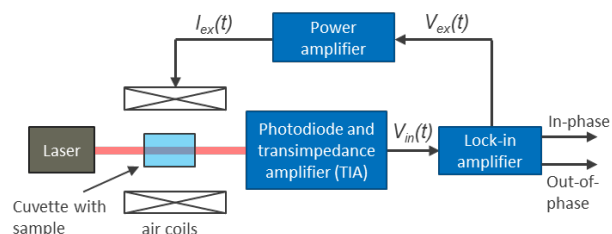


Figure 2: Schematic of the optomagnetic measurement setup<sup>[2,3]</sup>.

For the characterization of EVs, samples collected from cell culture are injected in an AF4 instrument (Figure 3) and fractions collected downstream. Size and concentration of exosome samples are determined by UV and MALS detector.

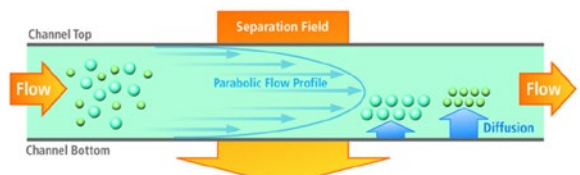


Figure 3: Principle of the size separation within an AF4 cartridge.

The effect of the membrane type and pore size (molecular cut-off) were also investigated. The fractions collected at increasing elution time provide EVs of increasing size, as shown on Figure 4 (left) with the red scattered plot. The different fractions were subsequently analysed to measure their protein content. ELISA assay allowed to specifically determine expression of membrane proteins in the different fractions. Interestingly, as shown on Figure 4 (right), smaller fractions have the highest amount of proteins.

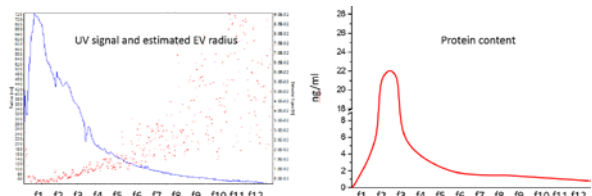


Figure 4: Size of different fractions of EVs (left) and corresponding protein content (right).

[2] J. Fock, et al., "Characterization of fine particles using optomagnetic measurements", *Physical Chemistry Chemical Physics* 19.13 (2017): 8802-8814.

[3] Xie, Lijun, et al., "Application of functionalized magnetic nanoparticles in sample preparation", *Analytical and bioanalytical chemistry* 406.2 (2014): 377-399.

# MICROSYSTEMS

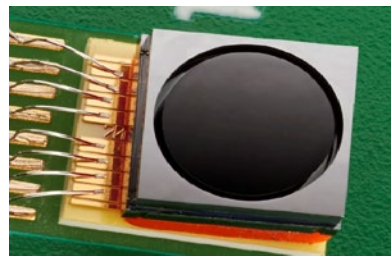
Michel Despont

The use of microsystems technology continues to grow, fueled by the need for ever smaller, lower power, smart devices. Integration of different technologies and miniaturization are at the heart of CSEM, and its MICROSYSYTEM program aims to deliver innovation through the development of new micro-manufacturing technologies, the use of MEMS technology, and the introduction of advanced packaging concepts.

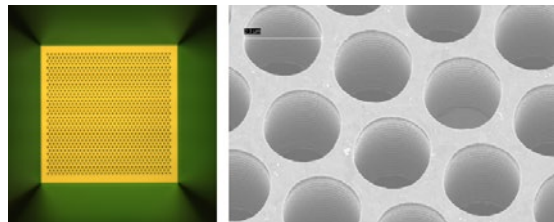
The microsystems market, according to various studies, enjoys a healthy 13–14 percent CAGR and this year is approaching a market size of 15 billion US dollars. Microsystems are used almost everywhere, in devices that sense and monitor our environment and influence our daily lives. For example, today's cars can make use of dozens of integrated sensors and actuators for monitoring and controlling engine functions as well as for safety, navigation, and passenger comfort. Similar trends can be seen in portable devices, such as smartphones, with a dozen sensors incorporated into the most recent models. Moreover, global technology trends like the Internet of Things (IoT) require the massive use of connected sensors and promise large new markets for ultra-miniaturized microsystems for applications in fields such as building automation, healthcare and the life sciences, consumer and home automation, transportation, industrial and environmental monitoring, security, and retail and logistics. All of these applications are looking for autonomous, low-power, small-form-factor, and low-cost sensor and actuator devices.

A large part of the microsystem's market is taken by large companies such as ST Microelectronics, Bosch, or Texas Instruments, which target mainly the consumer and automotive markets and make significant efforts in process standardization in order to cope with the permanent cost pressures of such applications. Beyond these mass markets, a large proportion of sensors and actuators are fabricated in moderate volumes for specialty but high-added-value markets. The fabrication of these moderate volumes of microsystem devices requires customization, and necessitates significant know-how from multiple disciplines, including fabrication technology, packaging, material science, and reliability. Hence, although the fabless model may be gaining some momentum, providers of MEMS-based microsystems are mostly relying on the Integrated Device Manufacturing (IDM) model, and use their own, dedicated, manufacturing facilities.

Swiss industry, and in particular its SMEs, has recognized the potential of developing specialty microsystem-based products as a strong differentiator and is present in many niche markets, successfully competing on a global level. For SMEs in particular, it is crucial to fill the pipeline of innovation from fundamental research to the industrialization of new technologies in order to be able to continue to offer innovative products. CSEM has a track record in bringing microsystems technologies to market, and is uniquely positioned to be an essential partner in bringing ideas to market for many Swiss high-tech SMEs active in the domain of highly miniaturized microsystems. Moreover, CSEM is looking at cross-disciplinary solutions—benefiting from nanotechnology, bioscience, and material science—in order to deliver innovations in MEMS and enable new microsystems.



Deformable micro-mirror with magnetic actuation.



Static Fabry-Pérot filter with 2 μm pores in the 10 μm thick silicon membrane.

MEMS play a major role in the MICROSYSYTEM program, and this role will be supported by increased efforts to develop advanced manufacturing and integration technologies. In particular, recent advances in digital manufacturing open up new opportunities to create and optimize MEMS devices and microsystems. CSEM strongly believes that "traditional" MEMS technologies will be augmented by these new manufacturing technologies to provide new functionalities and to deliver the versatility required for fast market introduction.

Packaging, meanwhile, no longer serves mainly as "device protection" and increasingly integrates added functionalities. These include an interface to the outside world (optical paths, electrical leads, actuators...), environmental compatibility (biocompatibility, withstand high temperatures...), or built-in sensors or quality monitoring features (antennas, pressure sensitive surface...). This makes the border between the package and the device fuzzier. Hence, it is essential to elaborate a common strategy with regard to developing—under one roof—the new processes, new devices, and new packaging that will enable the creation of novel microsystems. With its MICROSYSYTEM program, CSEM aims to create an environment that is adapted to the new challenges of microsystems and that benefits Swiss industry.

Looking back over recent years, the MICROSYSYTEM program (formerly the MEMS program) has seen significant progress related to the development of micro-components for mechanical watches and integrated optoelectronic devices. Although these topics are of great importance to Swiss industry, the technology spectrum being developed within the program must address a broad range of applications. The program has therefore, over the last few years, incorporated several new initiatives in order to diversify into new application fields, including instrumentation, aerospace, and medical devices, all of which are important markets for Swiss industry.

At CSEM, the MICROSYSTEMS strategy is oriented along several lines of action, encompassing design, microfabrication, and packaging technologies. They are:

- 1) Innovation for mechanical watches, at the crossover point of high-performance materials, advanced manufacturing, and innovative designs.
- 2) Excel in microsystems technology for harsh environments, for a broad range of applications ranging from medical to aerospace.
- 3) Develop key technologies in the field of infrared sensing and imaging.
- 4) Enhance the technology portfolio in optical MEMS and optoelectronic device assembly.
- 5) Integrate soft materials into microsystems, as better interfaces for applications in medtech and biology.

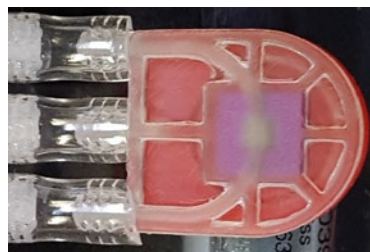
#### Long-term objectives

The global objective of the MICROSYSTEMS program is to establish MEMS device micro-fabrication and packaging technologies for CSEM's partners, and to offer to Swiss and international industries a full product-development platform from the feasibility demonstration of new device ideas to industrialized, qualified fabrication processes including the production of MEMS in small volumes. Therefore, the activities of this program are aimed at continuing to excel and to build up new competences in microsystems technology—in particular for application fields such as watch technologies, scientific instrumentation, optoelectronics, and medical device technology—with a strong focus on packaging, reliability, and cost reduction for demanding applications.

The MICROSYSTEMS program strategy has been organized into three activities—namely, (1) *MEMS Devices*, (2) *Functional Packaging*, and (3) *Advanced Micro-Manufacturing*.

The *MEMS Devices* activity deals with the development and industrialization of specific MEMS in a wide spectrum of applications. The global objective of this activity is to maintain a state-of-the-art platform capable of developing and fabricating reliable MEMS products, from prototypes to small volume production or for technology transfer. This platform, at the service of Swiss SMEs and industries, consists of a fully equipped MEMS fabrication clean room, a reliability laboratory, and an R&D infrastructure focusing on the pursuit of advanced and novel MEMS-based devices. Today, development is underway in the fields of watches and timekeeping, instrumentation and aerospace, and health, biotech, and lifestyle. These are the domains in which Swiss industry is highly successful at a global level and which have a large impact on the Swiss economy.

For industrial applications, reliability is of the utmost importance and CSEM's reliability and microstructure characterization capabilities are a powerful tool for supporting process development aiming at eliminating defect- and stress-generated failure modes and performance limitations. The continuous improvement and systematic documentation of development and production process flows within ISO-9001 ensures the successful exploitation of the technology platforms developed. This enables a systematic approach to MEMS development, from feasibility demonstration, via prototyping, to industrialization.



*LEGO-like fluidic package for silicon filtering membrane.*



*Copper coated 3D polymer antenna (1 mm height).*

The *Functional Packaging* activity focuses on (i) the development of new integration platforms for CSEM's customers, and (ii) the realization of new products based on these platforms. The chosen approach allows CSEM to serve a large number of customers in different application fields and markets. The activity's primary objectives are the integration of active MEMS dies, sensors, and actuators into prototype systems and products for different applications and markets. The activity addresses today's global packaging challenges in the fields of sensor platforms for medical and environmental monitoring, the integration of measurement solutions for harsh environments, and optoelectronics. The integration of microsystems continues to be a key element of many future high-technology application areas. Hybrid integration technologies—from embedded silicon in polymer to M(O)EMS—find broad uses in markets such as healthcare and energy. Combined with hermetic sealing and embedded self-testing, they open up additional applications for sensors in harsh environments, such as in the medical field. In addition, miniaturization in optoelectronics continues to be an innovation driver, from devices to architecture.

The goal of the *Advanced Micro-Manufacturing* activity is to answer the need of Swiss industry to fabricate small-dimension components (typically  $<1 \text{ cm}^3$ ) that can take advantage of a 3D aspect and that would not be achievable using existing technology such as clean room microfabrication (MEMS and CMOS). The envisaged solution is to develop a new combination of manufacturing technologies to improve the performance of microsystems. The core technology is based on additive manufacturing (AM), a worldwide “big trend” linked to digitalization, IoT, and Industry 4.0. This technology brings with it more flexibility and can increase the complexity of systems. However, it is still lacking user confidence, and still needs to be developed in order to achieve the small dimensions and structure quality required for its use in microsystems. The combination of its skill sets in materials, microfabrication, surface engineering, and characterization is allowing CSEM to tackle the challenge of combining different technologies and to make these new manufacturing technologies available to Swiss industry. Hence, CSEM's attention is focused on two points: (1) the process

optimization of 3D printing technology for the fabrication of small structures made of functional materials, and (2) the heterogeneous integration of 3D printing technologies with other microfabrication technologies (in particular with MEMS).



*Electrode used for successful signal generation in guinea pig cochlea  $\varnothing < 0.5$  mm.*



*Temperature-stabilized laser for gas sensing applications.*

Needless to say, the MICROSYSTEMS program will continue to work closely with the other CSEM programs (Surface Engineering, Ultra-Low-Power Microelectronics, Systems and Photovoltaics & Energy Management) to create unique solutions for our industries. One of the major USPs of CSEM, we will continue to cultivate this multidisciplinary approach to answer the needs of our customers.

### Highlights

Today's infrared (IR) filters are Bragg lattices of dielectric materials. These devices are expensive and have several drawbacks, including angular dependence, bulkiness, and incompatibility with an array arrangement. Arrays of filters with different wavelength characteristics are a key requirement for hyperspectral imaging. At CSEM, we have developed a new type of Fabry-Pérot IR filter using MEMS technology. Mirrors are made of metal films integrated onto a silicon microporous membrane. Our characterization has shown a superior optical fineness and an improved transmission as compared to commercially available filters. Moreover, the technology has the potential to come at a significantly lower cost, to be less angle dependent, and to be compatible with an array configuration. The last of these is achieved thanks to the fact that the wavelength to be filtered is defined by the geometrical design of the micro-porosity of the membrane, enabling each membrane to have a different geometry, which results in each filter having a different absorption spectrum. Hence, both a narrowband linewidth (1.5%) and a large transmission efficiency (10%) have been achieved at 10  $\mu\text{m}$  and 15  $\mu\text{m}$  wavelengths. This translates to a factor-50 improvement when compared to commercially available filters.

For over a decade, microfabrication in silicon has been a key factor in innovation for mechanical watches. The starting point was the translation of conventional micro components, such as hairsprings and gears, into silicon using microfabrication techniques. More recently, entirely new micro mechanisms have been realized thanks to the unmatched fabrication precision of

MEMS technology. In particular, advances in the state of the art of deep silicon etching have proved key for the development of an innovative mechanical oscillator based on flexure mechanisms. At CSEM, we are at the forefront of deep reactive ion etching (DRIE), which allows us to fabricate high-aspect-ratio flexures with outstanding verticality. We have achieved a verticality of  $<0.1^\circ$  on more than 600  $\mu\text{m}$  tall flexure beams that are as thin as 15  $\mu\text{m}$ .

# Fabry-Perot MEMS Optical Filters in 2 – 20 $\mu\text{m}$ Wavelength Range

B. Timotijevic, A. C. Hoogerwerf, N. Niketic

We have designed and fabricated narrow-band, infrared Fabry-Perot filters based on porous metal mirrors using simple silicon MEMS technology. The advantage of these filters is that they offer an order of magnitude better transmission and linewidth than their continuous film counterparts. They can be made in a matrix with different central wavelengths and can be finely tuned through post-processing.

There is a wide range of applications, from environmental monitoring and security to imaging and medical that require good light filtering in the infrared (IR). Gas detection using a non-dispersive IR approach is for example relatively simple and inexpensive thanks to a large variety of available IR sources and detectors, but it is still lacking cheap and versatile filters in this wavelength range. The main reason is that the commercial Fabry-Perot (FP) cavities based on continuous metal films are very lossy above 2  $\mu\text{m}$ ; a metal layer thin enough to transmit some light, would be so thin that metal could not be deposited as a continuous film. Even when the improvements are possible, a higher transmission typically comes at the cost of the bandwidth increase. Approaches where the metal mirrors are replaced by a stack of dielectrics adds to the complexity and the price of the device. Fine adjustment of the filter wavelength and making an array of filters with different wavelengths is complex, if not impossible, in a single fabrication run.

We have designed a FP IR filter, which overcomes the aforementioned constraints. Its basic element is a very thin ( $< 100 \text{ nm}$ ) porous, metal mirror (Figure 1). Its apertures (12) are engineered to provide both good transmission and reflectivity. Their size and mean distance follow simple design rules to minimize the losses through diffraction and scattering and, consequently, maximize the transmission. At the same time a good reflectivity is maintained, which is essential for a narrow linewidth of the FP cavity.

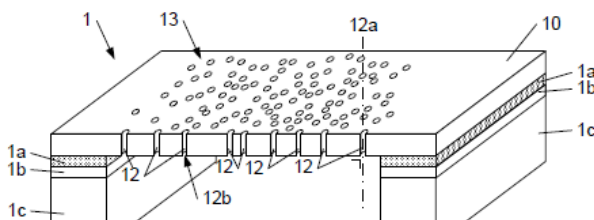


Figure 1: Porous metal mirror as a basic element of a FP filter.

To create a FP, two such mirrors are placed at a few microns distance either in air or using a sandwich layer transparent in the IR. MEMS technology turns out to be suitable to easily make the filters using a simple 2-mask process on SOI wafers. The microfabrication follows a straightforward process consisting of a photolithography, dry etching and HF release. Metallization is performed through gold evaporation, but other metals such as silver and aluminium are also compatible.

The intermediate silicon layer is practical not only as a mechanical support but it can also be slightly etched after the fabrication if a fine tuning of the filter wavelength is needed. The tuning is a result of the change of the effective refractive index when the material is removed. This approach however does not affect the linewidth of the filter since the porous mirrors (reflectivity) are not affected by the post-processing. The fine tuning is particularly useful if the spacer layer thickness is not homogenous, creating the yield problems.

Our approach also offers the possibility for making an array of filters in a single run. One option is an array of filters on a SOI wafer with a fixed device layer thickness. A mask variation of the metal apertures size and distance can provide the tuning of the wavelength up to few percent. The filter linewidth slightly varies but for certain application this is acceptable. Figure 2 shows an example of such a 7×5 array filter intended for a hyperspectral camera. The second option is a filter with a variable cavity thickness. In this case, a larger wavelength range can be covered with one filter and the linewidth is not affected by the cavity thickness variation. The only change in the process is few extra masks, for an array of 16 (4×4) filters only 4 additional photolithography masks would be needed.

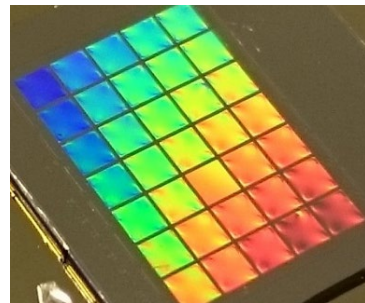


Figure 2: A 5×7 array of FP filters made from a SOI wafer with a 5  $\mu\text{m}$  device layer. 50 nm of Au is deposited on both sides of device layer.

The fabricated filters were tested preliminary in transmission using a MCT detector in a Fourier transform infrared spectrometer microscope (Bruker-Hyperion). The FP filter measured has a central silicon spacer of 5  $\mu\text{m}$ . There is a 50 nm Au layer on both sides. The opening diameters are 2  $\mu\text{m}$  and arranged in a hexagonal lattice with a period of 3.6  $\mu\text{m}$ . The two FP peaks at 10  $\mu\text{m}$  and 15  $\mu\text{m}$  have approximately 10% transmission and a 1.5% linewidth. In an ideal case, a metal-silicon-metal FP in this configuration having a similar linewidth would have a transmission of only 0.2%. We thus obtain a factor of 50 improvement. The chips from the processed SOI wafers with the device layers of 5  $\mu\text{m}$ , 7  $\mu\text{m}$  and 10  $\mu\text{m}$  are currently under inspection and will cover the filtering at other wavelengths in the target region 2 – 20  $\mu\text{m}$ .

Improved FP filters presented here have large potential in applications such as the NDIR gas sensing because the improvement of the efficiency can relax high demands from the detectors, especially for cases where only few ppm have to be detected. Furthermore, two porous mirrors described in this work can be joined in a configuration where one of the mirrors displaces through an electrostatic actuation, resulting in an efficient, continuously tunable FP IR filter.

# Optical Pressure Sensor for Environments with Strong Electromagnetic Interferences

B. Timotijevic, B. El Roustom

We have developed an optically based pulper for a pressure range 0-5 bar, suitable for environments with strong electromagnetic interferences. The sensor demonstrates precision better than 40 mbar in the given pressure range. The acquisition method allows for accuracy of 1 part in 6000.

Continuous monitoring of the harsh environments such as turbo-generators is essential. The excessive vibrations of the generator end-windings, for example, can lead to dramatic damages imposing service costs of tens of millions of CHF per day. Thus, the environmental factors such as pressure, vibrations, temperature, and humidity have to be closely observed. In addition, the monitoring often has to be several kilometers away due to a remote position of the service station. Finally, typically very strong electromagnetic (EM) fields impose the use of non-conductive devices in order to prevent the signal interference and false positives as an outcome. Metal-free, optical sensors are natural choice for such systems since they are immune to very strong EM fields and offer the possibility for delivering the signal for several kilometers without introducing significant losses using optical fibres. We have realized an optical pressure system which is compatible with such environments and provides precision of 40 mbar in a 0-5 bar pressure range.

A concept of the device is shown in Figure 1. It is consisted of an LED, a mini-spectrometer, a prism, a reference photodiode, optical fibres and a sensing element – a membrane attached to the optical fibre. The deflection of the membrane due to the pressure change causes the change of the Fabry-Perot gap formed by the fibre tip and membrane. The optical signal from Fabry-Perot cavity is analyzed using a Matlab code to determine precisely the gap and consequently the pressure. This acquisition technique allows for precision of better than 1 part in 6000 of the used Fabry-Perot cavity.

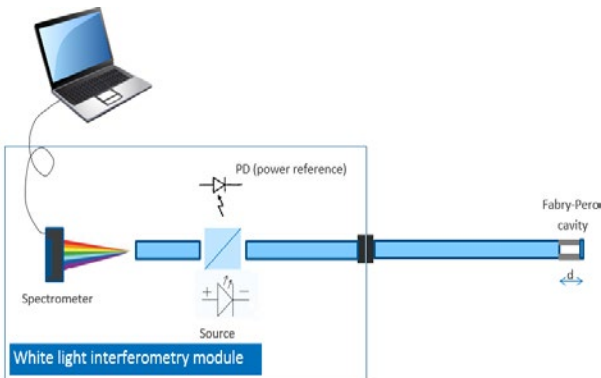


Figure 1: A concept for an optical pressure sensor.

The packaged demonstrator with the sensing element from Fiso is shown in Figure 2. The optical system was in this case developed without the reference photodiode and the prism, which are only needed to account for possible variations in the optical power coming from the source. The configuration where the entire system is always at the same pressure is often referred to as the pulper and not the pressure sensor. The demonstrator was first checked at the atmospheric pressure. The gap of the commercial Fabry-Perot sensor at the 1000 mbar is estimated to be 17.488  $\mu\text{m}$ , which is identical to the value provided by the sensor manufacturer.



Figure 2: Packaged pressure sensor with the FISO sensing element.

The same method was then used to measure and calculate the Fabry-Perot gap at different pressures in a range 0 – 5 bar. A special pressure chamber in which the sensing element and a part of the fibre were immersed was used for this purpose. The typical example of the curve gap vs. pressure obtained after several cycles is shown in Figure 3. The graph indicates an excellent linearity of the sensor with  $R^2$  value of 0.9999 with the sensitivity of  $\sim 5.3 \text{ nm/mbar}$ . The error calculated from the linear fit is within  $\pm 40 \text{ mbar}$  range. It should be noted that this is not the ultimate performance of the sensor considering that only rough steps of 0.5 bar could be used when setting up the reference chamber pressure. Similarly, the assessment of the limits of the data acquisition speed and precision requires better control of the reference pressure.

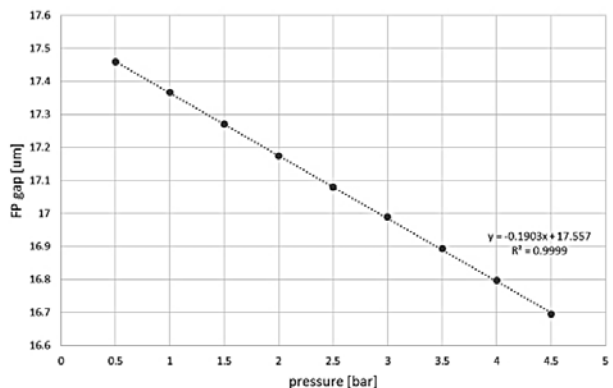


Figure 3: Fabry-Perot gap vs chamber pressure.

The approach in measuring the pressure shown here has a great potential not only because of the very precise absolute measurement in applications where EM interferences are strong, but also because it can be realized in a compact and an inexpensive way by employing the MEMS technology. The optical MEMS sensors for acceleration, temperature and inclination have already been developed and are planned to be extended for the gas, humidity, and pressure detection.

# Compact Optical MEMS Sensors for Harsh Electromagnetic Environments

B. Timotijevic, Y. Petremand, D. Z. Bayat, N. Niketic, M. Luetzelschwab

We have realized miniature optical accelerometers and temperature sensors for remote sensing of harsh environments with strong electromagnetic interferences using a common, inexpensive, silicon MEMS platform. The accelerometer has a linear error below 1% in a range 0 – 40g. The temperature sensor has precision better than 1°C in a range 20 – 150°C.

Many environments which are considered as harsh, such as: turbo-generators, tunnel mills-drives, mining sites, nuclear and chemical plants, dams and geotechnical systems require continuous monitoring of vibrations, temperature, pressure, humidity and other environmental factors in order to avoid very high, service intervention costs. In some of these environments, very strong electromagnetic fields are present that require the use of optical, metal-free sensors. Another great advantage of the optical approach is a possibility for the remote monitoring through the use of optical fibers for the signal transmission. Silicon based MEMS technology is a good approach for the fabrication of these optical sensors since it allows for cheap, compact, and robust sensing elements such as accelerometers, inclinometers, pressure and temperature sensors. In addition, the sensors can often entirely or partially share a common MEMS platform for the microfabrication. In this work we present two types of such sensors: accelerometers and temperature sensors.

The MEMS accelerometer chip uses a triangular, movable Si mirror to redirect the optical signal from an input fibre into two output fibers. The amount of the mirror displacement is directly proportional to the level of acceleration. The differential signal is collected and analyzed in a remote readout module, which, thanks to the use of low-loss fibres, can be positioned kilometers away. The MEMS temperature sensor (Figure 1) relies on a temperature dependent absorption in Si. It was designed to allow for a sufficient absorption in the Si waveguide, but also to minimize the bending losses and the losses at the coupling ends with the input / output fibres.

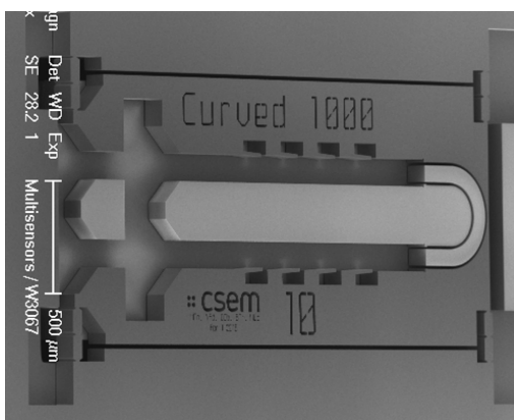


Figure 1: Example of the fabricated temperature chip. The channels are used to accommodate the input / output fibres, which guide the light to / from the curved silicon waveguide.

The frequency response measurement of the accelerometer was performed with the electrical readout which has an integrated electrical bandpass filter of 5 Hz to 1000 Hz. Between 20 Hz and 900 Hz, the non-linearity remains within +/-5%. Outside of this range, the electrical filters are attenuating the mechanical signals. The measured non-linearity meets the standards set for certain applications such as the end-winding monitoring of turbines. The dynamic range at 100 Hz is plotted in Figure 2. An excellent linearity of better than 99% is obtained up to 13g. Higher

acceleration amplitudes are not reported here due to the setup limitations, but values of up to 40 g have been verified experimentally.

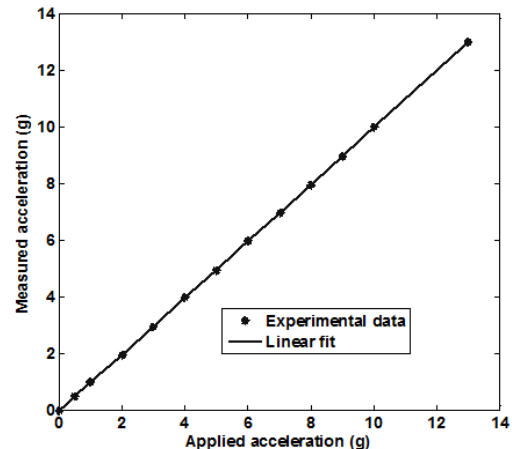


Figure 2: Performance of one specific optical MEMS accelerometer.

The temperature sensor was characterized in an oven where the temperature was controlled in a range 30°C – 150°C. The typical response of the optical temperature sensor is shown in Figure 3. The deviation from the linear fit is within 1°C, whereas if the fit to the 5th order polynomial is used, the error is within 0.8°C. The linearity can be even further improved by removing the thermal oscillations from the setup and through the thermal passivation (accelerated aging) of the chip before its characterization. The chips were also subjected to the thermal cycling at four different fixed temperatures between 20°C and 150°C and have confirmed the sensor precision within 1°C.

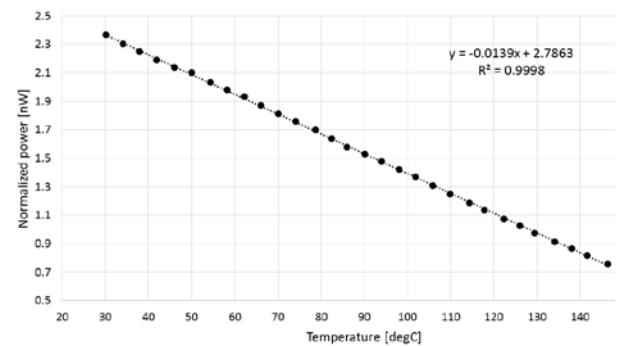


Figure 3: Performance of one specific MEMS temperature sensor.

The MEMS technology used for the sensors presented here shows a great potential for the development of other type of devices. Pressure and inclinometer sensors based on fibre-silicon Fabry-Perot cavities are currently under development.

# Impact of Mechanical Shock on MEMS Accelerometers

I. Marozau, M. Dadras, O. Sereda

Miniaturization of MEMS components and devices imposes new requirements on their reliability and, in particular, their resistance to mechanical shocks. This becomes especially important for novel potential application markets of MEMS, such as the space industry. Within the MEMS-Real project, CSEM has developed a unique two-step test procedure that was used for the evaluation of mechanical shock resistance of MEMS products. MEMS capacitive accelerometers from three different suppliers were compared in terms of their resistance to mechanical shocks. Analysis of the failure root causes allowed the identification of the critical design points that have to be optimized in order to improve the impact resistance of the MEMS devices.

CSEM has led an international consortium that aimed to develop a standardization methodology for the reliability assessment of microelectromechanical systems (MEMS) for space applications. Within this activity, special attention was given to the evaluation of the mechanical resistance of MEMS in order to identify their potential weak points and to elaborate possible optimization modifications of the current component designs. The evaluation was performed through mechanical shock testing of various MEMS accelerometers. A unique test procedure was elaborated, that consists of two steps:

- Step 1: Analysis of the failure sensitivity load in order to identify the device reliability limit(s) and define the load parameter to be applied accordingly in Step 2.
- Step 2: Acquisition of failure statistics over cycles by applying the load parameter defined in Step 1. This step involves repetitive load cycling tests at a fixed load to acquire failure statistics over the cycles.

Implementation of this two-step procedure allows not only the determination of the mechanical shock resistance of the tested components, but also the evaluation of their long-term performance when subjected to considerable loads close to their failure threshold. The later point represents the novelty of the proposed approach, allowing a more comprehensive assessment of the impact resistance of MEMS components. Using this approach, the typical failure root cause(s) were identified, allowing the elaboration of potential actions for the improvement of impact resistance.

In order to evaluate the developed testing approach, a series of tests was conducted on MEMS accelerometers from three different suppliers. The chosen devices were of the same technology (i.e. capacitive accelerometers), but featured different designs and packaging options (Figure 1).

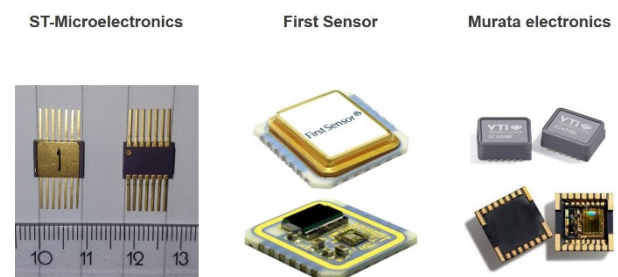


Figure 1: MEMS accelerometers from three different suppliers that were tested.

It was found that two of the three tested MEMS accelerometers can withstand high mechanical shock accelerations of 5000+ g.

However, accelerometers from the third supplier exhibited a load failure threshold of  $2750 \pm 250$  g. Statistical failure analysis over load cycles was performed using the Weibull failure distribution model<sup>[1]</sup>. Figure 2 shows a typical Weibull failure probability plot for one of the suppliers. Obtained results suggest a wearing-out behavior at 5000g (slope coefficient  $>>1$ ). This indicates that the failure rate increases fast after a certain number of shock pulses. The characteristic life and the 90% reliability limit at 5000 g are  $1360 \pm 150$  shock impacts and  $700 \pm 150$  shock impacts, respectively.

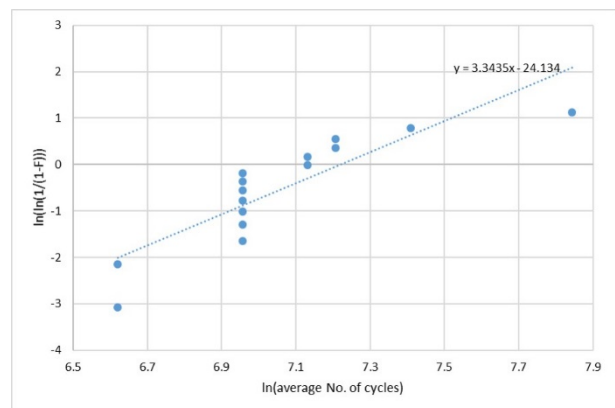


Figure 2: Weibull plot of the mechanical shock cycling test results for one of the suppliers' accelerometers at 5000 g. F is the Weibull cumulative probability function.

Analysis of the MEMS accelerometers that failed during the mechanical shock tests showed that the failure root causes are identical for all three studied devices. All analyzed failures are related to the de-bonding of wires from contact pads inside the device package (Figure 3). It can therefore be concluded that the most important parameter that influences the impact resistance is the quality of the wire-bonding. Therefore, the application of proper wire bonding techniques and procedures is necessary in order to improve the mechanical shock reliability of the MEMS. Additionally, the utilization of a gel-like polymer material to fill the package interior may also help to improve the shock resistance.



Figure 3: Examples of wire un-bonding failures occurred in MEMS accelerometer devices during mechanical shock tests.

<sup>[1]</sup> W. Weibull, J. Appl. Mech.-Trans. ASME, 18 (3): 293–297.

# Measurements of a MEMS UV Laser Pointing Mirror

A. C. Hoogerwerf, D. Z. Bayat, B. Timotijevic, V. Revol, T. Burch

The first measurements have been made on a MEMS based mirror assembly that has a mechanical actuation angle of more than +/- 15°. The large actuation angle of this mirror is well beyond commercially available MEMS mirrors and makes it useful, especially for laser pointing.

In last year's Scientific and Technical Report<sup>[1]</sup>, we reported on the manufacturing of a MEMS mirror for UV laser pointing for the atmospheric monitoring subsystem of the Extreme Universe Space Observatory mission.

The mirror assembly consists of a solid cylindrically-shaped mirror squeezed between two silicon plates. The silicon plates each have three planar spiral springs in them that are flexible for out-of-plane movements, but are rigid for in-plane movements. In the center of the springs the mirror is fixed to the two plates. When laterally moving one silicon plate with respect to the other, a torque exerts on the mirror. The mirror can accommodate this torque, by tilting in its direction. Thus, the relative X-Y movement of one silicon plate translates into a tip-tilt movement of the mirror. The mechanism is shown in Figure 1, where the silicon plate on top is significantly smaller than the other. The mirror in this structure is made of aluminum and can be seen in the center of the structure.

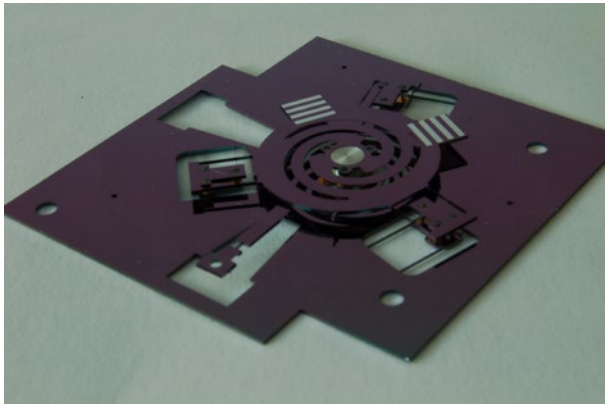


Figure 1: The first assembled MEMS mirror.

The assembled MEMS mirror has to be mounted and attached to voice coil actuators in order to be tested. It happened that the mounting process had a low yield due to the breaking of the fragile silicon beams that attached the structure to the actuators. As a result, a new fabrication run had to be undertaken and this enabled us to improve some of the design and assembly aspects. One important aspect that was improved, was to put the linear guides that were distributed over the two silicon plates on one plate. The mechanical connections that had to be made between the guides on the two plates were an important cause of yield loss and the elimination of this necessity improved the yield significantly.

The assembled and mounted mirror is shown in Figure 2 together with the voice coil actuators and encoders. The orange structures in the corners are 3D printed spacers that assure the appropriate spacing between the plates. The mounted mirror can then be tested for its functional performance. In Figure 3, the mechanical angle of the mirror with respect to the voice coil stroke is shown.

The red line in the figure shows a fitted curve based on a geometric model. As can be seen from this figure, the maximum deflection angle of the mirror is above 15°, which is the specified maximum deflection angle. The voice coil force can be derived from its actuation current. The mirror deflection angle as a function of this force is shown in Figure 4. The curve reveals a stick-slip behavior of the system. This behavior can be compensated once the full position feedback has been installed.

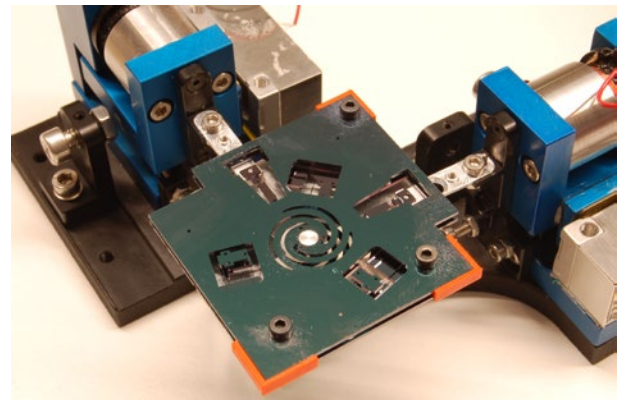


Figure 2: The mounted MEMS mirror.

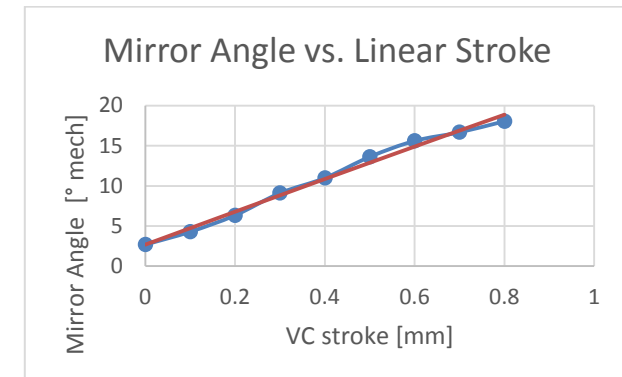


Figure 3: The measured displacement versus angle curve.

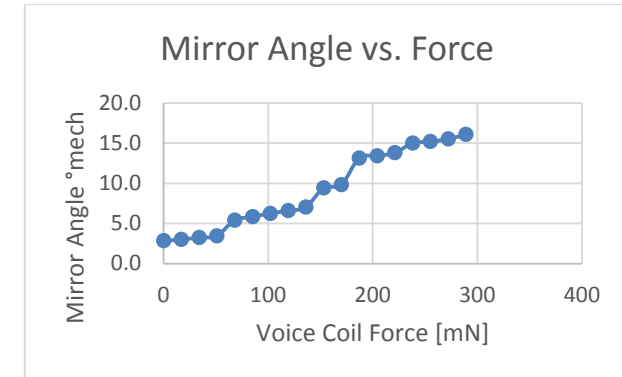


Figure 4: The measured displacement versus force curve.

<sup>[1]</sup> A. Hoogerwerf, et al., "A MEMS UV Laser Pointing Mirror for Atmosphere Monitoring", CSEM Scientific & Technical Report (2016) 25.

# Metal Implantation on Elastomer Substrate for Stretchable Strain Sensors

F. Sorba, J. Baborowski, S. Rosset •, M. Despont, H. Shea •, C. Martin-Olmos

Stretchable strain sensors hold great promise due to their broad applicability but their fabrication is still a challenge. CSEM in collaboration with EPFL has fabricated metal strain gauges through ion implantation embedded on suspended poly(dimethylsiloxane) (PDMS) membrane. This approach combines compatibility with microfabrication technology, ease of patterning and high strain sensitivity.

Strain sensors are largely used in nearly all fields of engineering. The most common way for the implementation of strain sensors are metal strain gauges through e-gun evaporation. However, the use of metal strain gauges is limited because of the small strain that can be monitored. Nowadays, soft-MEMS technology is becoming very attractive due to the combination of low stiffness substrates with stretchable materials. Consequently, there is an increasing need of stretchable conductive materials for sensing applications. Stretchable electrodes are highly desirable in field such as soft robotics or skin-like electronics requiring high strain sensing capabilities [1].

In this project, compliant electrodes on stretchable substrates are fabricated using a low-energy metal ion implantation by filtered cathodic vacuum arc (FCVA). Using implantation does not involve the formation of a continuous rigid film on the substrate. Instead, it leads to the formation of small size (2–20 nm) metallic clusters in the polymer matrix which have been shown to be approximately 50 nm inside the polymer matrix [2]. These clusters are in contact with each other allowing the formation of a conductive path, however they do not form a strong mechanical bond. In addition, this fabrication technique leads to a reduced impact on the stiffening when stretching, and therefore higher performance of the devices.

The fabrication process is shown in Figure 1, the substrates used are 10 µm thick suspended polydimethylsiloxane (PDMS) membranes. Firstly, the electrical contacts are patterned using gold sputtering through a mask. Then the implantation is performed and wires are glued to the contacts.

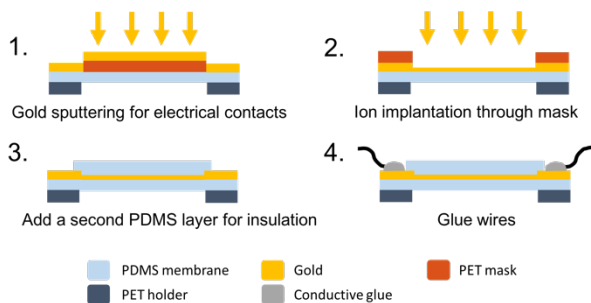


Figure 1: Process flow schematics of the implanted strain sensors on thin suspended stretchable membranes.

The implanted strain sensors can be protected using a second PDMS membrane as insulation layer. This would be interesting for the use of the device in liquid environment.

The fabricated samples have been electrically and mechanically tested on a measurement setup composed by a step-motor for in-plane stretching and a force sensor.

The change in resistance has been monitored while stretching the membrane (Figure 2). It corresponds to a gauge factor of about 25 which is one order of magnitude more sensitive than typical thin film strain gauge.

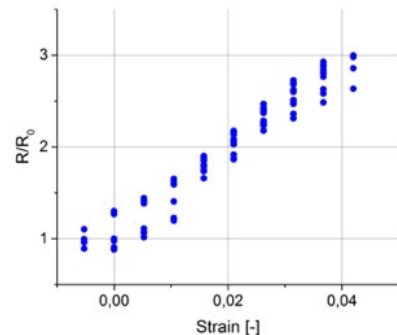


Figure 2: Change in resistance plotted versus the applied strain to the membrane resulting in a gauge factor of 2.

A 50% increase in the mechanical stiffness of the PDMS membrane has been quantified as the impact of the implanted layer. The force is measured while stretching the membrane and the Young's modulus is extracted from the stress versus strain graph (Figure 3).

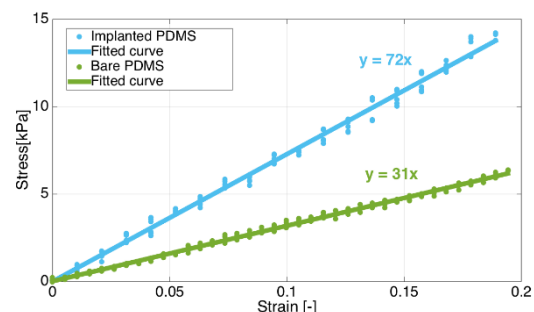


Figure 3: Stress-strain response of the bare and the gold implanted membrane shows a 50% increase in the Young's modulus.

The next step will be the calibration of the samples in liquid environment. This is possible thanks to the elastomeric insulation layer protecting the strain sensors.

The development of these stretchable strain sensors would allow advancements in sensing in soft-MEMS interfaced with liquid environment with high potential for biological applications.

Financial support by the Swiss National Science Foundation (SNF) is gratefully acknowledged (project No 205321\_153365).

• Microsystems Space Technologies Laboratory, EPFL, Neuchâtel  
[1] A. P. Gerratt, H. O. Michaud, S. P. Lacour, "Elastomeric electronic skin for prosthetic tactile sensation." Advanced Functional Materials 25.15 (2015): 2287-2295.

[2] S. Rosset, et al., "Metal ion implantation for the fabrication of stretchable electrodes on elastomers", Advanced Functional Materials 19.3 (2009): 470-478.

# Enhanced Properties of Aluminum Scandium Nitride Piezoelectric Films

M. Dubois, K. Vaideeswaran, G. Christmann, S. Nicolay

The introduction of scandium into the aluminum nitride lattice allows for a significant increase of the piezoelectric properties of this material, opening new opportunities in the sensor and actuator fields, where superior sensitivity or displacement are required..

Aluminum nitride piezoelectric thin film sputtering is a very mature technology, as it is used to manufacture the many front-end RF filters and duplexers found in each mobile phone produced today. This success is due to the unique material properties of AlN, such as its low dielectric constant and low loss in the GHz range, its very high sound velocity, and its very stable piezoelectric behavior. Despite these excellent properties, this material has some limitations when it is to be used in actuator applications where large displacements or forces are required, or for sensors with superior sensitivity. Indeed, moderate piezoelectric coefficients are the main drawback of aluminum nitride.

The partial substitution of Al atoms by Sc has been shown to increase significantly the piezoelectric properties of the material, due in particular to a softening of the lattice. Thin films with Sc content lower than 10% have already been industrialized: they bring a real advantage to RF applications since the continuous increase of performances required by the latest generations of mobile phones becomes hard to meet by regular AlN. In this context, as the incorporation of a few percent of Sc enlarges the piezoelectric coupling while keeping all the other properties nearly constant, aluminum scandium nitride is expected to become the material of choice for high-performance applications.

The use of larger Sc contents to further enhance the piezoelectric response is however much more challenging in terms of technology and integration. In collaboration with Evatec AG and EPFL-LC, CSEM has started to develop processes to deposit high performance AlScN piezoelectric thin films containing up to 40% scandium. Two approaches exist for the sputter deposition of these films: The target can be a compound target made of an alloy of Al and Sc in the proportion aimed at in the final piezoelectric film. As an alternative, two smaller individual targets of pure Al and Sc can be sputtered simultaneously the Al/Sc ratio being controlled by the power delivered to each magnetron source. In both case nitrogen gas is used in the plasma to react with the metal and form the AlScN. The compound target is considered as the most promising method for industrial applications, as the deposition rate and uniformity are much higher thanks to the use of a single large diameter target. However, the manufacturing of such a target is extremely challenging for high scandium contents and even though this problem is being investigated by a few suppliers in the world, targets are currently not yet available. The second option with two smaller targets is thus the one applied at CSEM. The film uniformity is enhanced by rotating the substrate in front of the two magnetron sources. Despite the moderate deposition rate, this method has the advantage of permitting the tuning of the film composition, up to very large Sc contents.

As an example, Figure 1 shows the X-ray diffraction rocking curve measured around the (002) peak of an AlScN film containing 40% Sc. The curve is very narrow and thus corresponds to a very good crystalline quality.

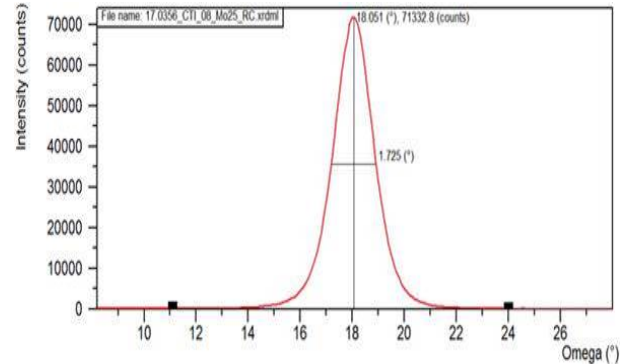


Figure 1: XRD rocking curve measured on a film with 40% scandium content.

Figure 2 displays the transverse piezoelectric coefficient  $e_{31f}$  measured on AlScN thin films as a function of the Sc content. It confirms that the piezoelectric properties of these films are drastically improved by the addition of scandium in the lattice.

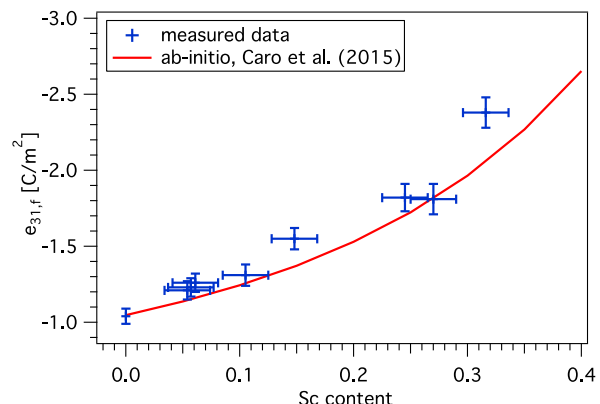


Figure 2: Transverse piezoelectric coefficient of AlScN films as a function of the scandium content.

This improvement makes aluminum scandium nitride films a real alternative to PZT as a piezoelectric material for large stroke or high sensitivity applications, especially since the integration of such films into MEMS is easier than that of PZT, due to a lower deposition temperature and a larger possible choice for the electrode material.

The research leading to these results has been funded in part by CTI, under grant 18616.1 PFNM-NM. Evatec AG and EPFL-LC are gratefully acknowledged for the fruitful collaboration.

# Mechanical Shock Test for MEMS and MEMS Packaging

K. Vaideeswaran, M. Despont, M. Dadras, O. Sereda

The reliability of MEMS resonators in terms of hermeticity of the MEMS packaging and MEMS functioning has to be ensured under harsh conditions such as seen in applications like automotive or aeronautic. This study determine the mechanical shock load limit, at which devices fail over a low number of load cycles as a result of suddenly applied forces or abrupt changes in motion produced by rough handling, transportation, or operation. The secondary purpose of the tests was to evaluate the devices performance for the large number of load cycles of a fixed shock acceleration.

The ESA's founded project WAFer Level Encapsulation for micro-Systems PLUS (WALES-PLUS) aims at providing a wafer level L0-MEMS packaging platform suited for the needs of the European Space Agency (ESA) and the space community at large. A common platform was developed between CSEM and VTT (Finland) for the process compatibilities between the two facilities for a L0-packaging on a 6" wafer including seamless process sharing. As test vehicle, MEMS resonators (Figure 1) has been fabricated and characterization has been pursued for their functioning as well as for their behavior under various harsh environmental conditions such as temperature and shock cycling.

At CSEM, the resonators were subject to reliability tests based on their resistance to mechanical shocks. The primary purpose of these tests was to determine the mechanical shock load limit, at which devices fail over a low number of load cycles as a result of suddenly applied forces or abrupt changes in motion produced by rough handling, transportation, or operation. The secondary purpose of these tests was to evaluate the devices performance for the large number of load cycles of a fixed shock acceleration.

The shock-testing apparatus (PST-300 from Shimadzu Corporation) at CSEM is capable of providing shock pulses of the half-sine waveform with the following specified characteristics:

- Peak acceleration: 200 – 2000 g; pulse duration: 0.5 ms.
- Peak acceleration: 800 – 5000 g; pulse duration: 0.2 ms.

Through electrical measurements carried out before the test and during each step of the test, the failure of the device is detected. In the current study, this was achieved by the measurement of the electrical resistance of the devices. The resistance was measured using micromanipulator probes with a DC source. Since the contact of the micromanipulators with the probes varies between different trials, a small dispersion in the measurement (of the order of a few ohms) is expected. Nevertheless, since failure of the device entails a change in the resistance of the device over many orders of magnitude, this dispersion may be ignored.

The tests consisted of two parts:

- 1) Determination of the device failure threshold for the increased acceleration shock pulses.

The measured values of the resistance of the three resonators A1, A2, and A3 with varying shock accelerations are charted in Figure 2. At the end of the trial, none of the resonators had failed up to shock accelerations of 5000 g. It is concluded that the device failure threshold exceeds 5000 g.

- 2) Evaluation of the failure statistics over cycles at a fixed shock acceleration.

Figure 3 summarises the measured resistances for the three resonators with increasing pulses of mechanical shocks with acceleration of 5000 g. Similar to the study concerning the determination of the failure threshold, a small dispersion in the measured resistance (from the contact between the manipulator

and the contact pad) is observed and neglected. At the end of 3000 cycles, the resistance of the three resonators is relatively unchanged, leading to the conclusion that the devices survive at least 3000 shock pulses of 5000 g peak acceleration.

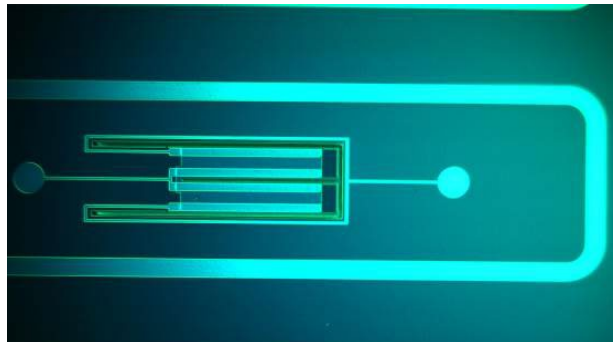


Figure 1: Piezoelectric MEMS resonator before encapsulation.

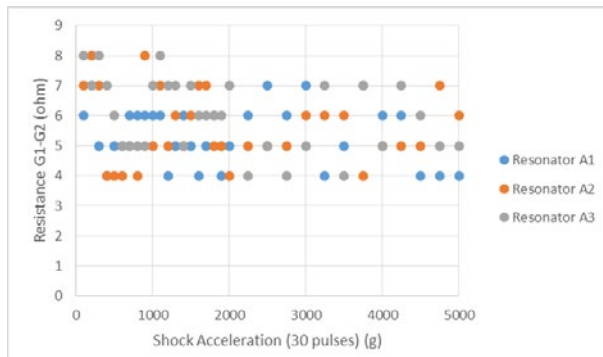


Figure 2: Summary of mechanical shock tests conducted on resonators A1, A2, and A3, for the determination of the failure threshold. From the negligible variation in the resistance, it may be concluded that the device failure threshold exceeds 5000 g.

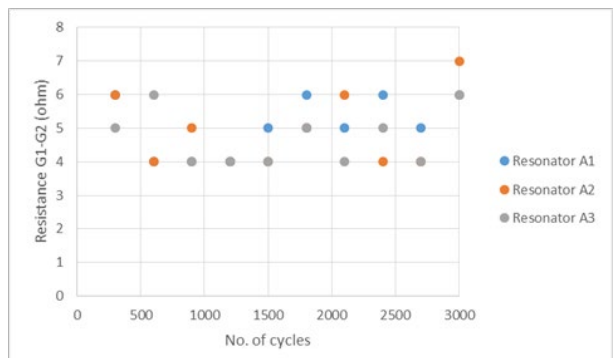


Figure 3: Summary of mechanical shock tests conducted on resonators A1, A2, and A3, for the determination of the failure statistics over cycles. Since no evident variation in the resistance of the resonators is observed, it may be concluded that none of the three resonators failed even after 3000 shock pulses of 5000 g acceleration.

# Integration and Interconnection of MEMS Membrane into a Multiwell Plate Insert by Overmolding

G. Voirin, R. Ischer, T. Overstolz, O. Dubochet, B. Oudot <sup>•</sup>, E. Marguet <sup>••</sup>, S. Angeloni \*

*With MEMS technology, a thin and porous membrane was fabricated, it is adapted for the characterization of biological barrier cell culture. The electrodes for transepithelial electrical resistance (TEER) measurements were incorporated on the membranes. Injection molding was used to integrate the MEMS membrane in a smart insert that can be used in a multiwell plate for automated high quality continuous TEER measurement.*

In the frame of the European project Smarter-SI [1], a system has been developed for the characterization of biological barriers model. The electrical resistance of a cell layer is one parameter of choice for the qualification of the biological barrier function. The electrical resistance is measured between both sides of a cell monolayer grown on a semipermeable membrane integrated in a plastic insert. The inserts are placed in a 12 wellplate. Electrode are integrated on the membrane and connected to the top of the insert with electrical leads attached to the wall of the insert. A specific PCB with adapted contacts connects the inserts electrical leads to a flexible part of the PCB that is connected to the electronic module that process and store the TEER measurements of each connected well.

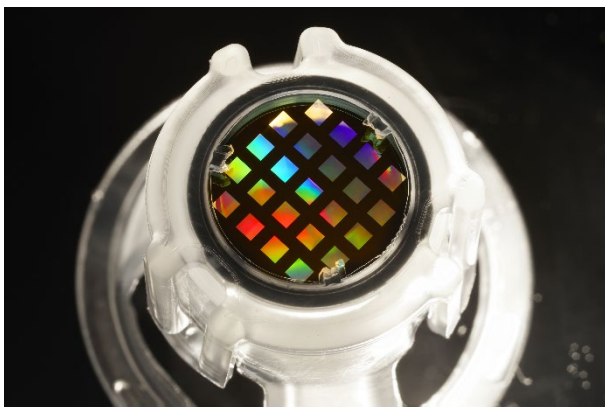


Figure 1: Plastic insert with ceramic membrane with submicronic pores.

The membranes are made with MEMS technology on silicon wafer. The membrane thickness is given by a silicon nitride low stress layer. The pores are defined by submicronic photolithography and etched in the silicon nitride layer. Submicrometer pore diameter can be achieved. Pore diameter down to 400 nm have been fabricated using stepper photolithography, pore diameter down to 80 nm can be achieved using a specific nanolithography. The membrane are obtained by etching the silicon wafer up to silicon nitride membrane from the back side after protection of the front side (Figure 2). Electrodes are defined by photolithography followed by metal deposition.

In order to ease the use of the silicon/silicon nitride membrane for cell culture support and for TEER measurement [2], the MEMS membranes are package in plastic supports made by injection

molding. The assembly is done either by clipping or directly during plastic injection [3], this insures the sealing between the plastic insert and the silicon/silicon nitride membrane.

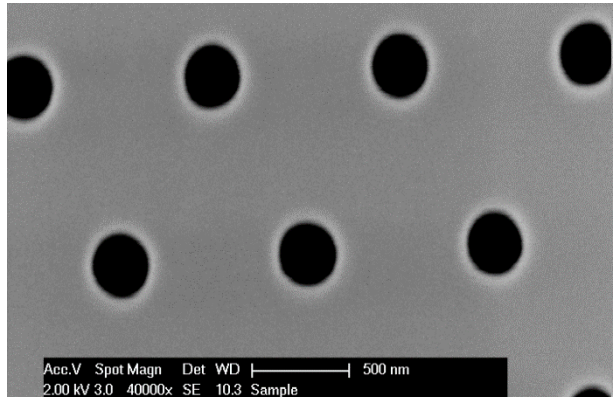


Figure 2: SEM picture of the 400 nm pores in silicon nitride layer.

The contact with the electrodes for TEER measurement is done by introducing electrical leads during the injection (Figure 3).



Figure 3: Design of the smart insert with overmolded electrical leads and silicon nitride membrane (a, b) and details of the interconnection of the electrodes on the membrane with the electrical leads (c).

By combining MEMS technology and injection molding, it was possible to develop a smart insert adapted for the characterization of biological barriers function by TEER measurements.

The Innovation Action Smarter-SI has received funding from the European Community's Programme HORIZON 2020 under GA No. 644596, and from the Swiss State Secretariat for Education, Research and Innovation (SERI) under contract number 15.0085. The valorization and successive industrialization of the developed technology will be performed in collaboration with start-up SiMPLInext SA.

• dna-plasturgie Sàrl, Biel-Bienne, Switzerland  
•• Gravity.swiss sa, Le Cerneux Pequignot, Switzerland  
\* SiMPLInext SA, Neuchâtel, Switzerland  
[1] <https://www.smart-systems-integration.org/smarter-si/>,

[2] G. Voirin, et al., "Smart System for Cell and Tissue Culture with Integrated Electrode for TEER Measurements", in this report, page 74.

[3] Patent application WO2016180836

# Adhesive Bonding for Harsh Environments

G. Spinola Durante, M. Fretz, R. Jose James, T. Stadelmann, M. Auchlin, M. Dadras

Specifications in data sheets are good indications for a first selection of candidate adhesives in a specific application. However, they cannot replace thorough testing of a fabricated bond, since information like adhesion on specific substrates is not always available. Often also missing from suppliers is data on adhesion stability during mechanical or chemical testing. CSEM has the experience and the equipment to test adhesives to their limits.

Compared to other bonding methods (e.g., soldering, welding, mechanical fastening), adhesive bonding has following advantages: low temperature bonding, ability to join a wide variety of dissimilar materials, absorbing stresses in the joint, resistance to corrosion and many chemicals and acids, no special atmosphere required when curing, clean and optically appealing. In addition to standard bonding of two components, adhesives may be used to provide protection for electrical components from mechanical stress and the environment, usually referred to as glob topping and potting.

Furthermore, electrically conductive adhesives may replace solders to provide a conduction path, underfiller materials help improve the reliability of flip chip assemblies, and thermally conductive adhesives act as heat conducts.

CSEM has the know-how and equipment to utilize adhesives in many specific customer applications. Our expertise builds on know-how in working with a variety of adhesives from different manufacturers:

- Designing adhesive joints (geometry, thickness, material).
- Surface cleaning / activation (plasma / silanization).
- Dispensing processes (time-pressure, volumetric, jetting).
- Curing profiles.
- Electrical testing (2-probe / 4-probe impedance measure).
- Mechanical destructive/non-destructive testing (shear-testing, pull-testing, shock-testing, etc.).
- Environmental testing (temperature cycling, high-temp. storage, temperature and moisture exposure etc.).

Thorough testing of the bond joint becomes particularly important if the device is exposed to harsh environments. We are equipped and trained to conduct extensive testing and FMEA to characterize with analytical tools the resulting failures. Common procedures are 85°C / 85% RH exposure, temperature cycling (according to MIL-STD or JEDEC), immersion tests in warm deionized water, shear tests of the bond in combination with above environmental tests or custom designed procedures.

As one example, we investigated whether electrically conductive adhesives could replace solders in SMD-attach processes on PCBs. Test vehicles were designed to characterize the electrical resistance of glued joints on gold and tin surfaces. The graphs in Figure 1 show the electrical resistance of Ohmic contacts made on five samples with an electrically conductive adhesives on tin-plated PCBs. Differences can clearly be spotted on the long-term resistance decline.

In another second example, adhesives are compared before and after immersion for 4.5 days in DI-water at 60°C. The shear values are expressed in MPa in Figure 2. A threshold line of 10 MPa is also drawn consistent to the limit compatible to the specific application. The values represented in Figure 2 are

related to five different adhesive materials with and without silanization on the substrates.

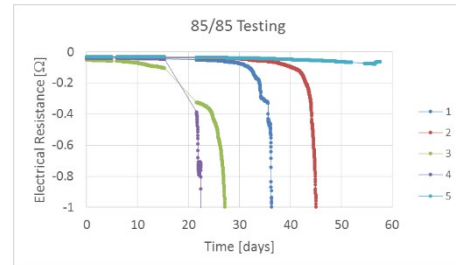


Figure 1: Electrical resistance measurements for five samples bonded with an electrically conductive adhesives on a tin-plated PCB.

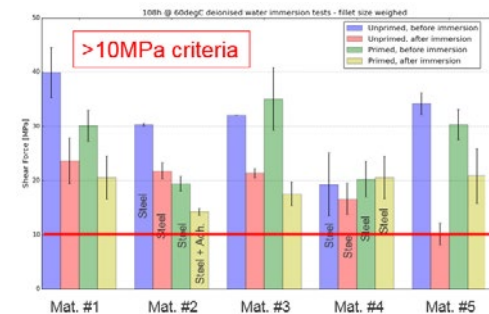


Figure 2: Comparison of shearforce stress values before and after immersion in DI-water at 60°C for 4.5 days.

Aside from adhesive process development, new testing equipment upgrades are being developed to permit simultaneously reliability testing at high temperature and high acceleration (shock). The system will permit to simulate simultaneously high temperature and shock resistance of MEMS. The development is focused on the temperature of 350°C and acceleration shock up to 1000 g. Figure 3 presents schematically the designed high temperature fixture adapted to the shock machine.



Figure 3: Shock-tester with 350°C capable fixture upgrade.

CSEM is active in both process development and upgrading of test capabilities. Both activities provide CSEM with a broad portfolio of expertise and know-how, thus enabling our customers to acquire innovative and challenging process developments in the field of adhesive joining.

This work was supported by the Swiss federation and MCCS Micro Center Central Switzerland. CSEM thanks them for their support.

# Thermal Management Solutions for mid-IR Optoelectronics Packages

G. Spinola Durante, J. Pierer, K. Krasnapski, M. Lützelschwab, J. Kaufmann

Applications of mid-infrared photonic technologies are fueled by innovative advances in quantum cascade lasers, and other key optical components like MEMS gratings and fiber-optics. The integration of devices into optoelectronic packages for stable operation at high powers poses challenges in terms of thermal management. We present here a Comsol model fully coupled with a thermo-electric-cooler (TEC). Benefit of the simulations is to optimize for lowest laser temperature operation to ensure longest system reliability and lifetime.

New sensing applications are expected to drive the mid-IR laser market in the next few years. A wide array of sensing applications are envisaged, from industrial process controls and environmental monitors to hazardous chemical detection and new medical diagnostics. IR-light sources for use in spectroscopic applications need to be very accurate and stable over time with respect to spectral performance. Temperature holds a key to a stable operation at high power for QCL and other optoelectronics components. In Figure 1 is shown a Kovar package with IR-window, thermo-electric-cooler and laser on a submount.

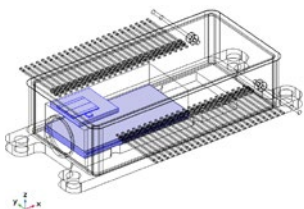


Figure 1: CAD Model of a mid-IR laser package including thermoelectric cooler (TEC), and laser on a submount.

In Figure 2 is shown the mesh of the full package model. The model amounts to 5.4 MDoF (Degrees of Freedom) due to the high element density in the region of the thermoelectric pellets.

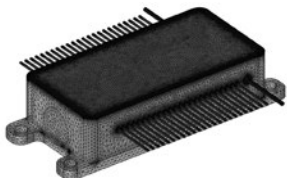


Figure 2: Meshed CAD Model of a mid-IR laser package (Comsol multiphysics modeling).

The simulation is intended to help define the package elements thickness, position and choice of material. For this purpose a parametric study is set-up to find the optimal and lowest laser stationary operating temperature. Transient analyses are also conducted to derive the time until warm-up and to avoid excessive instability in the temperature profile that could lead to serious laser device damage. The thermal model includes not only thermal conduction physics, but also convective effects due to air surrounding the components inside the package and the package exterior surfaces. The contribution from radiation is also taken into account for the external surface of the package to ensure no artificial hot-spot comes out from the simulation results ( $\sim T^4$  dependence). The second aspect of the thermal model is that it requires also the embedding of a TEC model available from Comsol. The model in itself couples thermal-electric physics. The specific thermo-electric pellets material data have been applied

according to measured data from the TEC supplier. The simulation of this full package model is therefore quite complex from both the geometry and the multi-physics aspects. The model was also tested against TEC analytical formula and was proven correct.

The full package model, including all bond interfaces simulated with FEM methods yields the chance to analyze in detail temperature profiles, as can be seen in Figure 3.

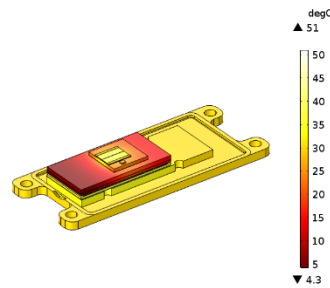


Figure 3: Comsol thermal simulation results (Kovar frame hidden).

The main benefit of simulating the full package is to find out by parametric analysis, which factor plays a major role to reduce the laser temperature and to estimate the overall operating conditions and set a worst-case limit to it. This scenario estimation is much less cumbersome, if compared to the effort to actual assemble and test including the cost for material. The simulation time is also relatively short and can take in this example around 2-3 days for a full parametric analysis.

Many details are also available for further investigation from the model as can be seen in Figure 4, by observing the thermal gradient at the TEC level. TEC optimization could also be further improved together with the supplier.

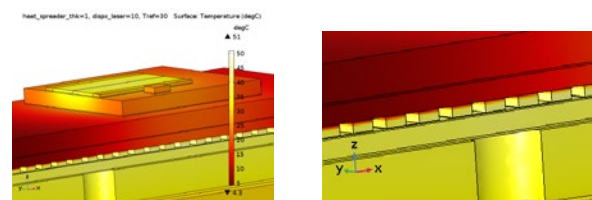


Figure 4: (a) Comsol results on TEC pellets; (b) zoom.

Optimization activities on thermal management for mid-IR devices at CSEM cover a broad range of topics including CAD design, package design for manufacturing, simulation and testing. This expertise can be tailored according to the system's specific requirements.

CSEM has conducted these investigation partially in the framework of the EU-consortium MIRPHAB<sup>[1]</sup>.

[1] MIRPHAB is an all-services integrated Pilot Line for the development of MID-IR photonics sensors in Europe.  
<http://www.mirphab.eu/>.

# 3D Printing Technology for Smart Prostheses

O. Chandran, B. Dunan, P. Morand, S. Lani

3D-printed prosthetics has served as the poster boy for 3D printing in medicine for quite some time. With the actual digital revolution, it is one of the best example of personalized care giving the possibility to produce prosthesis as the exact needed scale and geometry. Within this development basic technological building blocks were developed, more particular the first stone to manufacture sensors on 3D printed components.

Digital manufacturing is actually at the heart of the actual industrial revolution, particularly additive manufacturing (AM) also known as 3D printing with opposition to more traditional subtractive technology like CNC milling. Surprisingly, most of all AM technologies are not recent comparing to the original patent for each technologies (Fused Deposition Modelling FDM, Stereolithography SLA Selective Laser Sintering SLS, and Selective Laser Melting SLM) having more than 25 years old. In fact, patent falls have allowed a new dynamism into the development of AM technologies which were mainly limited to rapid prototyping. Competition has pushed to the development of new system with improved performances and now capable of being competitive for low volume production. For the same cost, the technology is also offering freedom of design (customized shape, mass reduction) without adding cost.

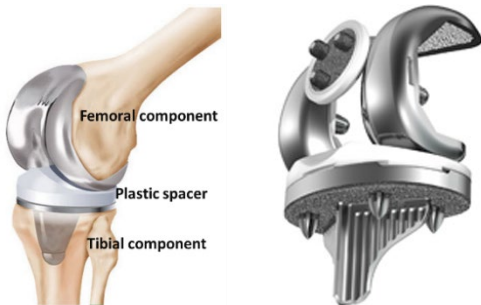


Figure 1: (left) Knee prosthesis with its components (source: <http://surgicalwatch.com/knee-replacements/>); (right) 3D printed prosthesis example from Stryker.

One interesting application for AM technologies is the realization of personalized prosthesis or implant, perfectly fitting patient morphology thanks to CT-scans and image reconstruction. First real application was performed in 2011 by Xilloc. Each year more and more devices are getting approved by FDA, like for example spinal cage, hip acetabular cup or jaws. Not all devices are currently FDA approval because of the actual regulation excluding production volume lower than 5 of the same pieces per year. Figure 1 is describing a knee prosthesis in its traditional and printed version.

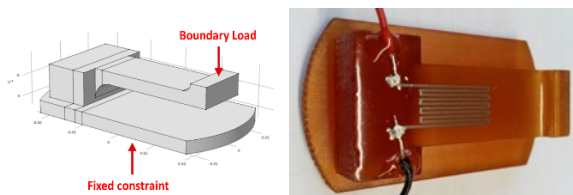


Figure 2: (left) Testing structure design for resistive sensor; (center) FEA simulation of the structure; (right) fabricated testing structure with design sensor N°2 (CLIP2).

Within this development, the objective was to develop key building blocks for the integration of force sensors on medical implant or prosthesis which could be used for components qualification or during its lifetime operation: post-operative recovery improvement, patient motion monitoring or failure

detection. First envisaged force sensors is a resistive sensor based on the variation of its conductivity with an applied load.

Key building technologies necessary for their applications to prosthesis were:

- Optimization of the deposition technic of a conductive material (Au or Ag) by aerosol jet printing.
- Evaluation of sintering method and parameters (photonic curing, oven curing).
- Optimization of the substrate fabrication by FDM and SLA and surface post-processing when required.

So far, only tests with silver sintered under oven curing and a SLA substrate (cyanate ester – CLIP®) have permitted to measure a resistance variation when applying a load (Figure 2). Resistance measured for 2 different designs and deposition process (CLIP1 and CLIP2) are presented in Table 1 and compared to the bulk value. Values are compared to the Ag bulk value and are higher than expected compared to similar coating on a glass substrate (2-10x bulk value at 90 min annealing) and is attributed to surface defects (roughness, defects) of the 3D printed components. Sensors drift is below 0.1% of variation of 30 min measurement time, showing a very good stability of the sensor. Gauge factor (GF) is estimated around 0.6, value that could be improved with more additional process optimization as typical metal conductors are having a GF around 2.

Table 1: Resistance value with respect to curing time at 150°C.

Sample	30 min	60 min	90 min
CLIP1	569.7 Ω (223×Bulk)	111.5 Ω (48×Bulk)	82.2 Ω (33×Bulk)
CLIP2	4578.7 Ω (652×Bulk)	2129.7 Ω (303× Bulk)	1259.6 Ω (179×Bulk)

This work has demonstrated the feasibility to print sensors on a 3D printed object like an implant or a prosthesis. Future works will be carried on improving manufacturing processes and to develop wireless sensors (LC-circuits) for battery less integration.

This work has been carried in collaboration Dr. Danick Briand from EPFL-LMTS laboratory.

# Multi-material and Multi-technology Printing Platform

O. Chandran, B. Dunan, P. Morand, M. Wittwer, A. Bionaz, S. Lani

*Within this development, the possibility to fabricate by 3D printing a component or device made from different materials was investigated. More particularly it was evaluated within the same printing machine to deposit rigid or flexible material, conductive material, sensors or actuators.*

For over 5 years, additive manufacturing or also called 3D printing is an important topic in technology development and an important part within the actual industrial revolution: Advanced Manufacturing, combination of different fabrication technologies including 3D printing. Thus, AM is more than 30 years old and known for rapid prototyping, it is only recently that system performances have only changed since the opening to the market to new actors bringing many novelties. Still eyes are focused on Selective Laser Melting (SLM) of metal for industrial applications and of Fused Filament fabrication (FFF or FDM) for home applications or in between UV stereolithography (SLA). Now these technologies are capable of either being for rapid prototyping or for parts production. But so far, most of the machines are single material or eventually 2 materials for FFF. Recently, the company Aether<sup>©</sup> has started the development of a printing system combining different printing technologies and materials. Standard features of the machine are:

- 2 FFF hot-end filament extruders.
- 8 syringe extruders.
- 14 microvalve droplet jet extruders.
- UV LED lamp.
- Laser engraver.
- Small CNC drill.
- Heated glass syringe extruder.
- Microscope and vision system for fine printing calibration.

The mounting of head was made modular giving the opportunity to adapt many more potential technologies and so with more custom solutions.



Figure 1: View of the generic printing heads of the Aether 1 system.

Aether<sup>©</sup> and CSEM have entered into a collaboration phase on to develop and promote this technology and to give a unique position to CSEM in advanced manufacturing and the capability to manufacture components with improved properties. Some examples of envisaged developments are:

- Flexible substrate with embedded conductors or electrodes for wearables applications.
- Integration of actuators and/or sensors on a 3D component.
- Improved pre surgical model based to reproduce hard and soft tissues (actually only hard tissues e.g., bones are reproduced).

As the system is a "beta" unit, a large part of the development was to adjust the different features and to adapt the G-code post processing unit to the need. One example of development in progress was to develop the printing of a silicon based flexible material, PDMS, and conductive materials (Silver and Carbon based paste). An example of carbon based conductive printing is given in Figure 2 and compared to the CAD file. Typical resistance of the structures are from 88 to 200  $\Omega$  depending of the curing process, respectively from 175°C during 5 min to room temperature (overnight). This is allowing to be applied to a very broad kind of polymer, even PLA polymer deposited by FDM printing. Preliminary tests on same structures with silver ink led to a resistance lower than 1  $\Omega$ .

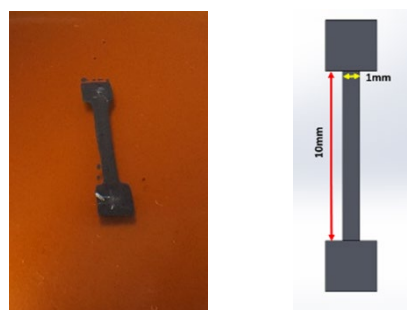


Figure 2: (left) 3D printed carbon based conductive test structure; (right) Corresponding CAD structure.

Future developments will be on the combination of rigid polymer, elastomer (PDMS) and conductive materials to form advanced 3D printed components, e.g., containing actuator and/or sensors and/or any active layer for example light.

# Mechanical Properties of 3D Printed Material

M. Hashmi, B. Dunan, S. Zabihzadeh, M. Auchlin, M. Dadras, S. Lani

Most of the 3D printed materials are presenting different mechanical properties than bulk material. To understand if a material can be used for prototyping or also for production, or for knowing for which application, we have evaluated the properties of several materials obtained by UV stereolithography.

Except "big player" of UV stereolithography (3D Systems, Stratasys, EnvisionTEC) for which the material is only available for their own printing system, most of the available resin materials are delivered without specification of their mechanical properties after curing. To optimize manufacturing process and to define applications cases like rapid prototyping or, product, biocompatibility, chemical compatibility, operating environment, it is necessary to have the access to thermal and mechanical properties as well environment compatibility and reliability.

In this work, we have focused on the evaluation of mechanical properties of material fabricated by UV stereolithography (SLA) technology relying on the photo-hardening of a liquid resin by the projection of a 2D light pattern. All the materials are commercially available but without available measured properties.

Characterization of materials have been carried out according to ASTM standards for tensile test (D638), bending test (D790) and hardness (D2240). Samples geometry used was ASTM D638 type V for tensile testing.

Process parameters evaluated were:

- Raw material – Actually, 4 different materials have been evaluated: high accuracy resin, flexible resin and 2 ceramic composites resins.
- UV exposure duration – it determines the level of curing per layer and printing time and the geometry accuracy. At least 3 values per material were evaluated.
- Thermal annealing – UV exposure can be not sufficient to reach 100% curing level. A thermal annealing might be necessary within the range of 85 to 200°C.
- Printing orientation – 2 different orientations were evaluated for the realization of the testing components, printed bottom-up with layer perpendicular to the pull direction and printed flat with layer parallel to the pull direction as presented in Figure 1.

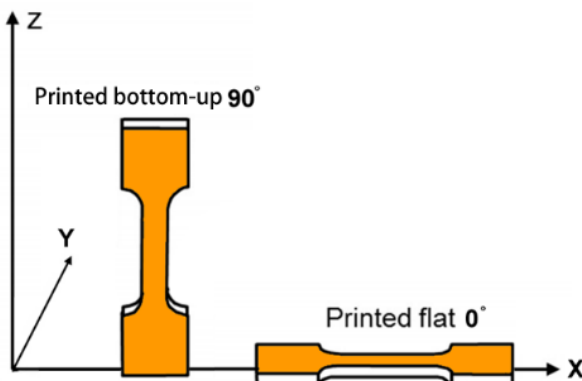


Figure 1: Definition of printing/pull testing orientation.

An example of results is given in Figure 2 showing the impact of UV post curing time on tensile Young's modulus (average of 3 measurements). Similar behavior are achieved for bending test but with a modulus reduced by about 35%. As expected, flat orientation gives higher modulus and strength values compared

to bottom up orientation. For this resin, a hardness of 80 Shore D was measured.

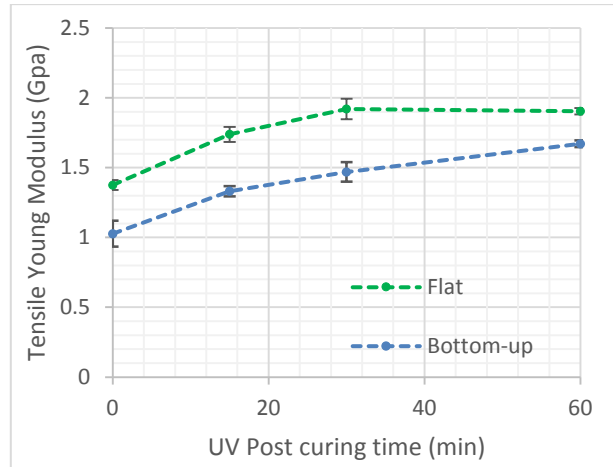


Figure 2: Average tensile modulus for different UV post-cure time and building orientation.

Flexible material was also measured. A tensile strength was measured at 9.5 MPa both for flat and bottom up building orientation and 11 MPa for thermal additional curing, all for optimum layer dose and UV post curing values. A Shore-A hardness of 84 was measured.

All measurements have been performed according to ASTM, but a typical printed part contains hollow or lattice structures to reduce printing time, consumption of material or weight. As UV post curing is requested to reach higher cross linking level, it would be interesting to also evaluate the performances of these structures on the resulting performances of the material. This will be the next tasks within this evaluation. An example of sphere with lattice structures is given in Figure 3.

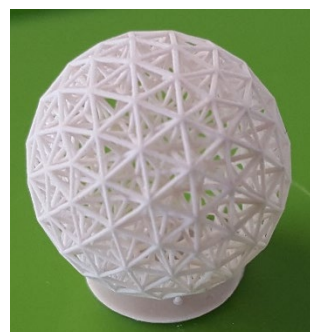


Figure 3: Example of lattice structure.

# LEGO-like Assembly by 3D Printing

B. Dunan, A. Bionaz, F. Cosandier, F. Barrot, S. Lani

Within this development, it was evaluated the possibility to use additive manufacturing to add fluidic functionalities on a silicon or glass based device. To do so, different approaches were evaluated: direct printing and LEGO-like encapsulation. This second approach was presenting the advantage to be reversible. It is relying on the fabrication of 2 components with alignment features and structures similar to a LEGO® brick to hold the pieces together.

Nowadays most of the microfluidic systems in academic or industrial world is performed in "2D" meaning all the integration and functionalities are in the same place. With the development of additive manufacturing, thinking microfluidic in 3D became possible, particularly for 3D channels or passive elements.

In 2016 we have reported the realization of structure directly on glass or silicon substrate to form hybrid fluidic systems<sup>[1]</sup>. In this development, we have evaluated the possibility to connect 3D channels for microfluidic applications with silicon device in a reversible way. The proposed concept rely on two 3D printed components enclosing a microfabricated silicon device with a microporous Si<sub>3</sub>N<sub>4</sub> membrane for application in filtration. To achieve liquid tightness, the parts shall integrated deformable part acting as sealing (chip to AM part, 1st AM part with 2nd AM part) and clamping structures (1st AM part with 2nd AM part), that could be assimilated to a LEGO bricks, with pins and holes. The proposed solution do not require any screw or additional clamping to ensure liquid tightness.

Different designs were evaluated both to evaluate the sealing (O-ring like function) and mechanical clamping (force required to maintain the different parts in intimate contact). Most efficient structures are presented in Figure 2, all containing 1 inlet channel and 2 outlets channels with the result of the filtration. Testing setup is composed of the 2 presented printed parts, 1 silicon chip with a SiN microporous membrane (pore size of about 1 µm), a micropump (CSEM Turbisc pump), and a 3D printed system by Fused Filament Fabrication (FFF) with reservoirs and distributing channel. All fluidic connections are so far realized with flexible tubes which could be removed in the future by printing the reservoir with a flexible material and allowing direct connection of the pump and filtering part.

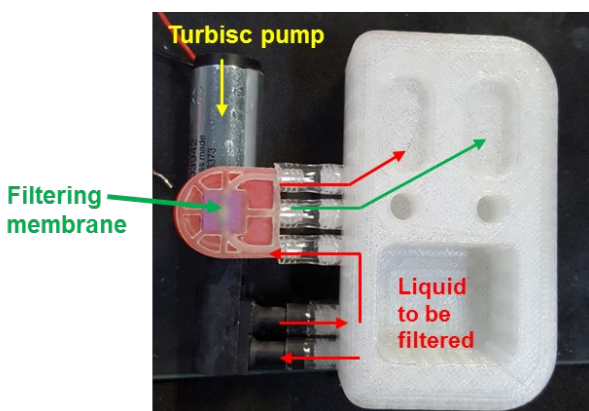


Figure 1: Fluidic setup for liquid filtering.

The fabrication of the different parts for holding the silicon membrane was made by UV stereolithography (SLA) offering a channel size down to 0.25 mm diameter and a maximum size of 80×45×70 mm<sup>3</sup>. SLA is a 3D printing technology for which a liquid resin is hardened thanks to a projection of a patterned UV

light. Different acrylate based resins were evaluated and best tightness results were achieved by combining a rigid polymer (hardness shore-D 80) and a soft polymer (hardness Shore-A 85) instead of pure LEGO-like of 2 rigid parts.

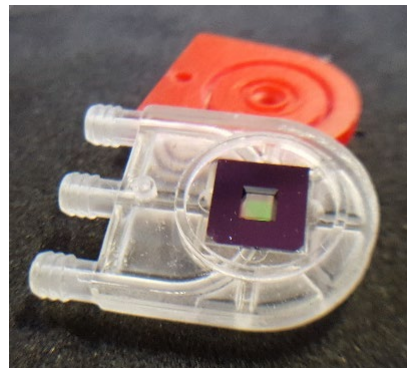


Figure 2: Rigid transparent and red flexible structures used to package a silicon porous membrane.

The performance evaluation was performed by injecting a water on the inlet channel of an assembled device with a silicon device without holes. The absence of leak on the package side or in the outlet corresponding to the filtrate is sufficient to demonstrate the liquid tightness and compatibility of the mechanical clamping mechanism.

Experiments with colored polystyrene micro beads (blue particles of 0.5 µm and red particles of 1 µm) have been performed. Blue color particles were dominating on the red particles and the membrane pores get obstructed before having fully filtered the blue particles as red particles have a diameter close to the pore size.

In conclusion, results are sufficient to validate the 3D printed packaging method and could be applied to more complex microfluidic and more concrete applications.

Others types of devices insertion will also be investigated in the future, for example a socket like structure as presented in Figure 3 or direct printing on a silicon chip, the ultimate goal of the development.

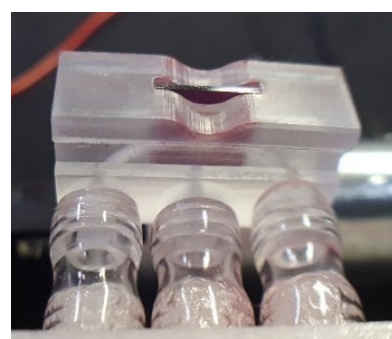


Figure 3: Socket like design with embedded top and bottom channels.

[1] S. Lani, A. Bionaz, "3D Printing for Advanced Manufacturing", Scientific & Technical Report (2016) 26.

# Multi-charged Ion Implantation of Nitrogen for Improved Tribological Properties of Miniaturized Mechanisms

K. Vaideeswaran, O. Sereda, C. Yamahata <sup>•</sup>, M. Auchlin, S. Biselli, D. Z. Bayat, C. Spoerl <sup>•</sup>, M. Dadras

*Multi-charged Ion Implantation (MCII) enables the simultaneous implantation of ions having different charges (e.g., N<sup>+</sup>, N<sup>2+</sup>, N<sup>3+</sup> and N<sup>4+</sup> in the case of nitrogen) and hence, of different energy levels, resulting in a uniform penetration of ions over a wide range of depths<sup>[1]</sup>. Ion implantation is well known for significantly improving surface properties of materials<sup>[2,3]</sup> such as aluminum alloys, iron based alloys, titanium alloys (e.g., for medical applications), and brass alloys (e.g., for the watchmaking industry), making it a technology of high interest in applications where wear and friction are of concern. The effects of ion implantation in brass are relatively less studied. This study aims at improving the tribological properties of brass parts through MCII process. The project will help idonus to master the MCII process, and ultimately put turnkey MCII machines on the market.*

The project aims at reducing the coefficient of friction (COF) of free machining brass through surface modification of a brass alloy of composition CuZn39Pb3 by MCII using ions of nitrogen. Microstructural investigation of the as-received brass alloy showed the presence of three phases: α FCC phase which is a solid solution of Zn in Cu, β BCC phase of the solid solution richer in Zn and Pb particles in cubic phase.

Simulations were carried out to determine the penetration depth of ions, which yielded a maximum penetration of ions to a depth of 50 nm for an implantation carried out at 35 kV. Based on the simulations, and with agreement with technical limitation of the machine, the implantation bias was fixed at 35 kV. The implantation dose was varied from 1E17 to 4E17 ions/cm<sup>2</sup>.

After ion implantation, as observed through Scanning Electron Microscopy (SEM), the roughness of the surface was seen to have increased and some nano-sized pores are formed additionally on the surface (see Figure 1, left). Grazing-Incidence X-Ray Diffraction (GI-XRD) studies after implantation showed diffraction peaks corresponding to the three principal phases: α-FCC brass, β-BCC brass, and Pb. No additional peaks corresponding to any crystalline precipitates in form of nitrides were observed in the implanted sample. These results corroborate well with other studies<sup>[4]</sup> on implantation of Cu- and Cu-based alloys. Transmission Electron Microscopy (TEM) micrographs and elemental analysis of an implanted sample (35 kV, 4E17 ions/cm<sup>2</sup>) was also undertaken, showing a microstructure modification over the distance of about 70 nm from the surface (see Figure 1, right). Two distinguished modified layers are clearly observed (named "a" and "b"). Presence of N was detected only in inner layer (named "b"), while no N is detected on layer "a". This can be explained by deep penetration of N depending on acceleration energy. No additional phases were detected in the implanted layer.

The tribological evaluation of the samples showed that up to an applied force of 25 mN, the benefit of ion implantation was clearly demonstrated through an at least 2-fold decrease in the COF at the surface for the implanted sample, in comparison to the non-implanted sample. Additionally, for an applied force of 5 mN over long sliding distances, while for the non-implanted sample the COF increases almost immediately to above 0.6, the implanted sample shows a very stable and low COF (<0.3) for up to more

than 36 m of sliding, clearly demonstrating that the improved COF is stable over the long sliding distances (see Figure 2). A remarkable reduction in the debris in the implanted sample following long distance sliding experiments was also rendered evident.

The change in the microstructure of the material (as observed through electron microscopy) as well as the remarkable improvement in the tribological properties (lowering of COF and reduction in wear) has been observed and show the potential of the MCII technology for improving surface-related mechanical properties. Future efforts will be oriented on studying the influence of acceleration energy on microstructure and surface properties.

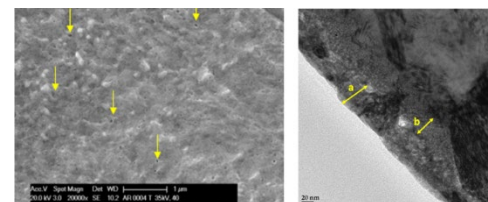


Figure 1: Electron microscopy of implanted sample (35 kV, 4E17 ions/cm<sup>2</sup>): (left) SEM micrograph showing nanopores (marked by yellow arrows) after implantation; (right) TEM micrograph showing modification of microstructure over a distance of up to 70 nm from the surface, with two distinguishable modified layers (named "a" and "b").

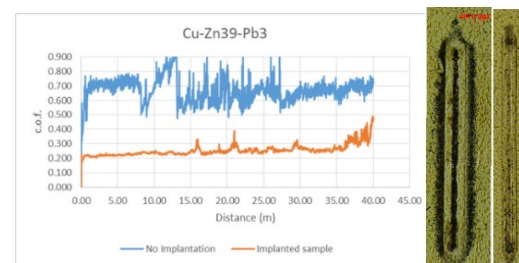


Figure 2: For an applied force of 5 mN over a sliding distance of 40 m, while the unimplanted sample (blue curve) has a high COF right from the beginning, the implanted sample (orange curve) shows signs of increasing COF (>0.3) only after ~36 m of sliding. The drastic reduction in the debris is also observed between the sliding traces of the non-implanted (image, left) vs. the implanted sample (image, right).

This project was funded by the Swiss Commission for Technology and Innovation (CTI) under the project number CTI No.25480.1 PFNM-NM.

<sup>•</sup> IDONUS Sarl, Rouges-Terres 61, 2068 Hauterive, Switzerland

<sup>[1]</sup> D.M. Gordin, J. Mat. Sc.: Mat. in Med., 2012, 2953-2966.

<sup>[2]</sup> S. Thibault, PhD Thesis, Caen Univ. (France), 2009.

<sup>[3]</sup> C. Pierret, PhD Thesis, Caen Univ. (France), 2012.

<sup>[4]</sup> M. Cavallier, PhD Thesis, Caen Univ. (France), 2014.

# Additive Manufacturing of Ti-based Alloy for Aerospace Application

S. Zabihzadeh, V. Pejchal, S. Biselli, G. Perruchoud, F. Reinert<sup>•</sup>, A. Burn<sup>••</sup>, V. Romano<sup>••</sup>, H. Najafi<sup>••</sup>, M. Dadras, O. Sereda

Additive manufacturing (AM) by selective laser melting (SLM) enables fabrication of near-net-shape metallic components with complex geometries. As such AM offers unrivaled flexibility in design topology and is particularly interesting for aerospace industry as it can offer economy in weight with maintaining or even improving functionality of components. Titanium-based alloy Ti6Al4V is an attractive material for aerospace structures as it possess a higher strength to weight ratio as well as higher operational temperatures than aluminum. In 2017 CSEM launched a two-year joint project with the company ProtoShape (Biel) and Bern University of Applied Sciences (BFH) with the objective of developing an end-to-end production process of Ti6Al4V alloy for the aerospace market.

Although AM-SLM is a powerful technique for fabrication of complex metallic components, it is also challenging to master the fabrication process. The main limiting factors of the SLM technique is introduction of defects such as pores, regions with unmelted or only partially melted particles, high surface roughness, and microcracks<sup>[1]</sup>. Anisotropy in physical and mechanical properties due to the additive layer-by-layer fabrication process, and high tensile residual stresses are among other limiting factors. The presence of defects and the residual stress has significant effect on the mechanical properties, particularly the strength and ductility of the metal which severely limits its use for aerospace applications. Process optimization including SLM manufacturing and post-processing is the main goal of this project for achieving the mechanical properties comparable to the bulk commercialized material.

Initially, as-received powders for the SLM process were characterized in terms of flowability, size distribution, residual humidity, chemical composition, and bulk density to select the best candidate powder. SLM parameters such as laser speed, power, spot size, and hatch size were optimized in order to decrease the porosity, microcracking, and the surface roughness of the samples based on microstructural observations of preliminary samples.

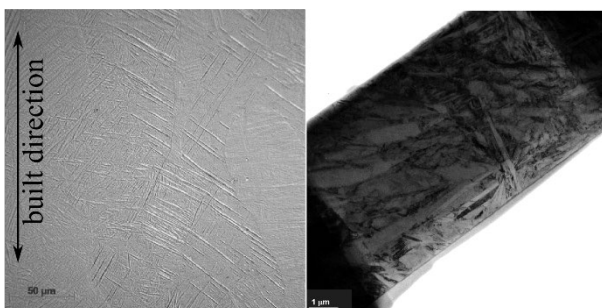


Figure 1: Optical micrograph and TEM of the AM-SLM as-built Ti6Al4V sample exhibiting predominantly very fine acicular martensitic  $\alpha'$  grains in transformed beta grains typical for quenched Ti6Al4V.

Following the initial microstructural observations more detailed investigation of the as-built material was performed by means of optical and electron microscopy (both TEM and SEM) and X-ray diffraction (XRD). Samples were produced on industrial SLM machines at ProtoShape using reference parameters defined by

ProtoShape and BFH. The investigations done at CSEM revealed that the as-built material consists predominantly of primary beta grains elongated along the building direction transformed to acicular hexagonal  $\alpha'$  grains (see Figure 1); this is a typical footprint of the rapid solidification for the Ti6Al4V alloy. Microhardness measurements of fabricated samples yielded values near 400 HV which is consistent with microhardness values of the quenched conventional Ti6Al4V exhibiting similar microstructure.

In general, the microstructural observations confirmed that AM-SLM process leads to nearly full-dense Ti6Al4V with the microstructure indistinguishable from conventional Ti6Al4V with similar heat-treatment history.

Besides participating in process optimization, CSEM asseses the best application of the technology to demonstrate the advantages of AM manufactured Ti6Al4V. A novel design and topology of the bracket for fixation of the zoom apparatus of the ExoMars camera was developed (Figure 2). An optimized design of the bracket obtained using topology optimization (TO) as well as the successfully built demonstrator of the optimized part with complex geometry is shown in the right-hand side of the figure.

CLUPI (ExoMars Focus Mechanism) bracket example :

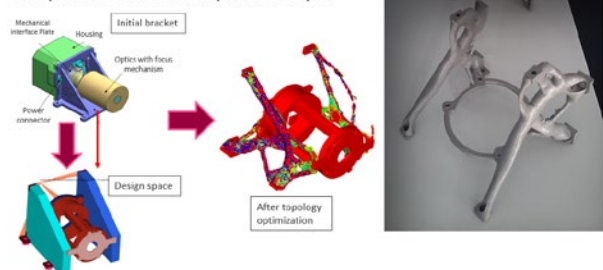


Figure 2: Design of the bracket for ExoMars camera zoom mechanism via topology optimization and the complex part successfully built using AM-SLM.

The future development will consist of investigation of suitable post-processing parameters and investigation of the material tensile properties to achieve mechanical properties that will meet demands of the aerospace industry.

Commission for Technology and Innovation (CTI) is acknowledged for its partial financial support.

• ProtoShape GmbH  
•• Bern University of Applied Sciences

[1] Chunlei Qiu, et al., "Microstructure and Tensile Properties of Selectively Laser-Melted and of HIPed Laser-Melted Ti-6Al-4V," Materials Science and Engineering: A 578 (August 20, 2013): 230-39, doi:10.1016/j.msea.2013.04.099.

# 3D LIGA

B. Dunan, G. Voirin, A. Bionaz, F. Cardot, S. Lani

A new method to form metal millimeter scale components has been developed that benefits from the use of a digital based manufacturing technology (UV stereolithography) to build freeform molds for metal electroplating. This method presents the advantage of easy modification through mask design and is an essential element for creating complex metal parts on the millimeter scale.

Lithographie, Galvanoformung, Abformung (lithography, electroplating, and molding) known as LIGA is a fabrication technology used to create high-aspect-ratio microstructures. More specifically, UV LIGA was developed in 1990s for realizing molds in SU8 resin with UV photolithography (resolution typically of about 1–2 µm in plane and aspect ratio of 10) to fabricate watch components<sup>[1]</sup>, as well as various other parts, after electrodeposition of nickel based material. By introducing a step of planarization after metal plating, it is possible to form parts composed of several layers. Increasing the complexity allows for multipart and intricate components like microtools for surgery to be built (MICA freeform metal components<sup>[2]</sup>). Combining 3D printing for mold fabrication and metal electroplating is opening the door for the realization of highly complex structures at a reasonable price. The most interesting additive manufacturing technology for fabricating molds for "3D LIGA" is UV stereolithography, which is an accurate technology with acceptable throughput thanks to 2D UV light projection. The envisioned process flow consists of the following:

- Starting from a conductive surface, which can be a CMOS, a MEMS, a metal coated surface, or a metal substrate. Depending on the conductive material and the resin used in the 3D process, an adequate surface processing step (water removal, silanization...) may be required.
- Alignment of the 3D printer with reference structures on the substrate. Alignment features have been added to a conventional 3D printer.
- 3D printing of the mold with an actual minimum feature size of 0.2 mm for channels or 0.1 mm for vertical structures.
- Electroplating of the metal material using a MEMS electroplating process.
- Planarization of the metal to remove the excess material using chemical mechanical planarization (CMP) or diamond turning.
- Removal of the mold either by chemical or plasma etching, or thermal degradation, depending on the metal material and compatibility of the stripping process.
- Cleaning of the part and, if needed, removal from the substrate. For example, in case of processing a CMOS for making 3D electrodes or antennas, only the conductive layer between structures would need to be removed, for instance, by ion beam etching.

To date, the development has consisted of evaluating each processing steps. In a first stage, the development of a silane based chemical treatment of the conductive surfaces to improve the adhesion of the polymer mold was demonstrated. The shear strength of the silane process was about 400 g/mm<sup>2</sup>, which is expected to be sufficient for the desired application. In a second stage, the resistance of the mold to chemical baths of Cu and NiP was evaluated, and no impact on the mold was observed. Finally, the possibility to achieve electroplating through the mold was evaluated. Particular attention was given to the cleaning process to remove the residual resin from the seed conductive layer due to partial polymerization at the surface as well as a foot effect at the substrate interface due to the over exposure needed to start the polymerisation of the first layers.

The building of the first layers on the substrate is critical as the substrate surface position has to be well calibrated. Optimization of the printing parameters and of the resins composition was necessary to avoid a foot effect at the substrate interface.

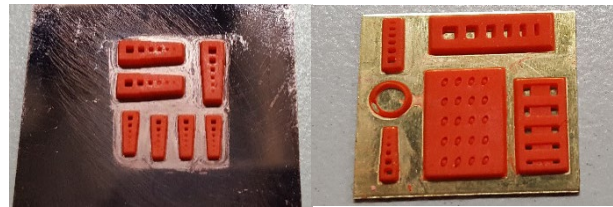


Figure 1: 3D printed mold on substrate.

Figure 1 presents a test mold fabricated on a Cu coated silicon substrate (left) or a brass substrate (right). Different test structures have been printed such as cylinders, spirals, and solenoids with different sizes. Up to this point, removing non polymerized resins from channels with diameters less than 0.5 mm remains challenging. Figure 2 presents a result of a plating experiment of Cu on a 3D mold.

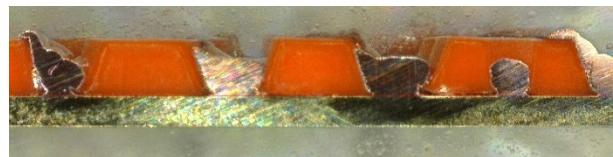


Figure 2: Cross-section of brass substrate with Cu plating.

In summary, the feasibility of using a 3D printed mold fabricated by UV stereolithography for electroplating metal components has been demonstrated. Future development will focus on the optimization of the resin composition to reduce its hardness so that higher aspect ratio features can be fabricated without the risk of delamination.

<sup>[1]</sup> H. Lorentz (1998) Nouvelles Technologies de microstructuration de type UV-LIGA et fabrication de composants micromécaniques. (Thèse doctorale inédite) EPFL, Suisse.

<sup>[2]</sup> <http://www.microfabrica.com/>

# Surface Properties Improvement of Biocompatible Materials by Multi-charged Ion Implantation

A. Böhlen, K. Vaideeswaran, C. Yamahata, S. Biselli, C. Spoerl<sup>•</sup>, O. Sereda, M. Dadras

Surface properties of biocompatible polymers (e.g., PEEK) play an extremely important role in their functionality. In the case of implants, the tribological properties of such materials including the coefficient of friction (COF) and their resistance to wear are crucial, since they influence heavily the application lifetime. Multi-charged Ion Implantation (MCII) enables the simultaneous implantation of ions resulting in a uniform penetration of ions over a wide range of depth. In this project, the surface microstructure of PEEK is engineered through MCII, and the variation in the surface properties accompanying such modifications is analyzed.

Biocompatible materials are extremely surface sensitive; with their interactions with the environment being heavily influenced by their surface properties. The main objective of this study is to improve the tribological properties of biocompatible materials, specifically polyether ether ketone (PEEK), by Multi-charge Ion Implantation (MCII), using Helium ions.

Using Monte Carlo simulations, an estimation of the penetration depth for He ions was calculated. For a dose of  $0.1\text{E}16$  ions/cm<sup>2</sup> accelerated at 20 kV, the maximum concentration of ions was calculated at  $\sim 280$  nm from the surface with a full width half maximum (FWHM) of  $\sim 130$  nm. Using this information as a guidance, implantation was carried out at 10 kV and 20 kV, with doses of  $0.05\text{E}16$  and  $0.1\text{E}16$  ions/cm<sup>2</sup>.

The effect of He implantation on the PEEK surfaces was analyzed through the measurement of surface roughness and the wetting angle. Figure 1 summarizes the results obtained from these analyses. It has been observed that the implantation has no detrimental effect either on the surface roughness or on the wettability. All surfaces remain distinctly hydrophilic (contact angle  $>65^\circ$ ) even after the ion implantation.

Tribological analyses on the surfaces were carried out on the reference and implanted surfaces. A 2 mm diameter quenched steel ball was used for the experiments and the applied loads were limited to 5 mN, corresponding to expected values of contact pressure in implant applications ( $\sim 10$  MPa). As shown in Figure 2, after 0.2 m of sliding, no significant difference in the coefficient of friction (COF,  $\sim 0.6$ ) was observed between the reference and the implanted ( $0.1\text{E}16$  ions/cm<sup>2</sup>, 20 kV) samples.

In order to observe the wear resistance of the surfaces, the same load (5 mN) was applied over a sliding distance of 40 m. While the sliding trace was distinctly visible in the reference sample, it was hardly distinguishable in the implanted sample (see Figure 3). On the other hand, a clear wear of the steel ball was observed for the implanted sample, while the steel ball sliding against the reference sample remained unaffected (insets in Figure 3). This shows a marked increase in the hardness and the resistance to wear of the PEEK surface following implantation. The increase in the hardness is possibly related to the formation of a highly cross-linked carbon rich surface layer, as shown in previous studies<sup>[1]</sup>.

Based on these results, further analyses aimed at demonstrating the change in the surface functionalization, hardness, and the wear rate are being currently undertaken.

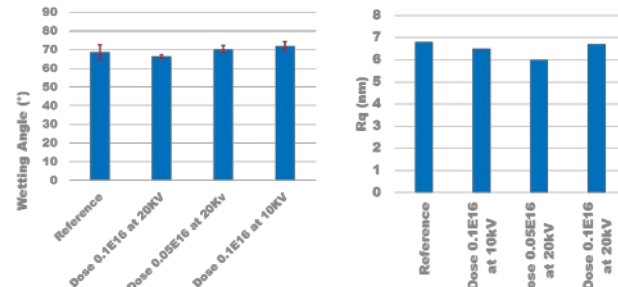


Figure 1: Variation in the wetting angle (left) and the surface roughness (right) of PEEK before implantation (reference) and with different implantation parameters for He ions (all doses in ions/cm<sup>2</sup>). No degradation of the wettability or surface roughness was observed.

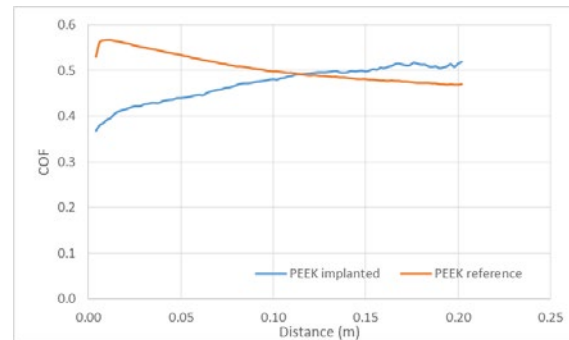


Figure 2: Surface COF measured for an applied normal force of 5 mN for a PEEK sample before implantation (reference) and after implantation ( $0.1\text{E}16$  ions/cm<sup>2</sup> at 20 kV). At the end of 0.2 m of sliding, there is no drastic change in the COF before and after implantation.

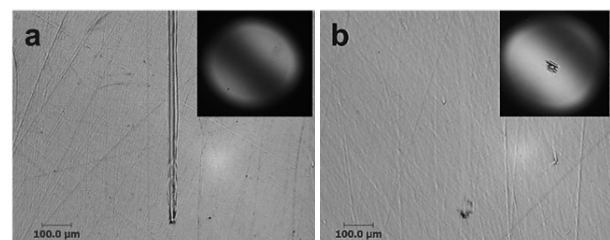


Figure 3: For a sliding distance of 40 m (at 5 mN), the non-implanted PEEK surface (a) shows a clear sliding trace on the surface, but after He implantation (b),  $0.1\text{E}16$  ions/cm<sup>2</sup> at 20 kV) the trace is hardly distinguishable. On the other hand, the surface of the steel ball (shown in insets) shows no wear against the non-implanted sample, while a clear wear of the steel ball is observed for the implanted surface.

• IDONUS Sarl, Rouges-Terres 61, 2068 Hauterive, Switzerland

[1] Gopal R. Rao, et al., J. of Mat. Res., 11.10 (1996): 2661-2667.

# Materials Behaviour @Mesoscale

M. Dadras, D. Z. Bayat, O. Sereda

In material science, mesoscale is a domain between microscopic-atomic scale and the macroscopic one. It is defined between millimeter and hundreds of micrometres. At this scale different structures, such as crystal grains, surface roughness, voids, grain boundaries, play an important role in macroscopic material properties. Characterization at mesoscale needs the appropriate know-how and adapted tools. CSEM broadened its activities in this field by seamlessly embracing tools development, characterization and modelling. The aim is to be able to measure and understand the material behaviour at mesoscale for improving the design and fabrication.

Generally mesoscale is defined as the link between microscopic and macroscopic worlds. There are significant differences between microscopic objects (at atomic scale) and macroscopic ones (functional bulk parts at millimeters scale) in terms of dimensions and functionality. The gap between this two domains (@atomic and @millimeter scales) is joined by the intermediate phenomena at mesoscale, which can be not only understood theoretically, but also observed analytically<sup>[1]</sup>. One of the important point at mesoscale is the size effect which can influence the behavior of developed bodies. As an example, the surface roughness does not influence the mechanical properties at the same manner if we talk about bulk materials at millimeter scale or about mesoscale one. Figure 1 presents schematically the mesoscale domain<sup>[2]</sup>.

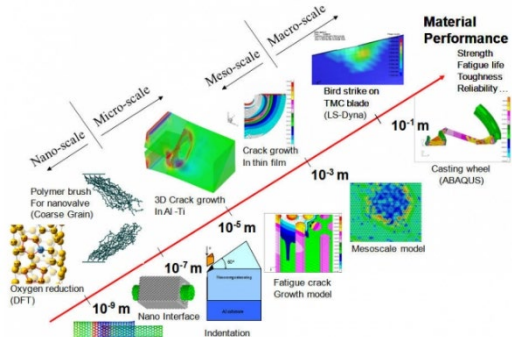


Figure 1: Mesoscale domain<sup>[2]</sup>.

CSEM by its mission is involved in development and investigation at mesoscale for several years. MEMS, MOEMS and recently Macro-MEMS are among several examples which have been already presented in the previous reports (Figure 2)<sup>[3]</sup>.



Figure 2: Monolithic balance wheel comprising a spring function implemented with silicon flexure hinges. The inertia is set with a gold ring assembled manually (8 mm diameter)<sup>[3]</sup>.

The new activity established at CSEM is focused more precisely on investigation and characterization followed by understanding the properties and phenomena at mesoscale. Three main activities cover mesoscale investigations: Development of new

[1] <https://mesoscale.llnl.gov/>

[2] Zhenhai Xia, Department of Materials Science and Engineering, University of Texas (<http://materials.engineering.unt.edu/xiagroup>).

instruments, Characterization and Modelling, followed by improvement of mechanical properties (Figure 3).

By developing the mesoscale activity, CSEM envisaged to be able to answer the demand of industries especially for improving the design, performances and understanding the behaviour of mesoscale objects.

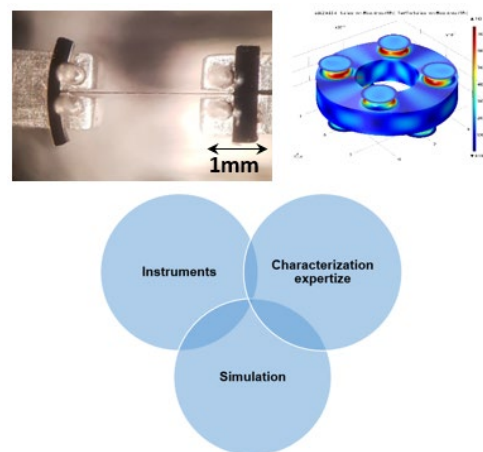


Figure 3: CSEM's mesoscale activity covering simulation, development new instruments and characterization.

Figure 4 presents the developed system capable of combined tensile and in-situ stress level tests at the same time covering the force range of 1 mN to 2 N.

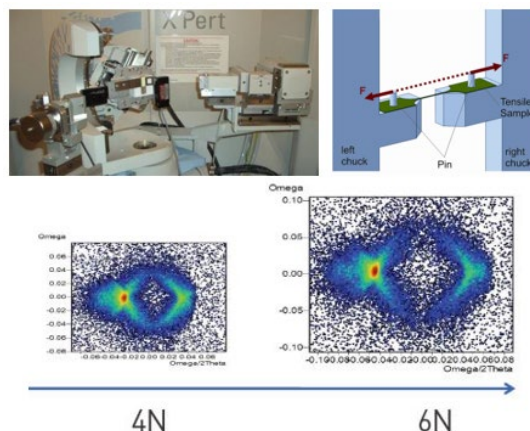


Figure 4: Developed system for mechanical properties measurement of samples with cross section of roughly  $30 \mu\text{m}^2$ . Force precision is 0.01 mN and displacement precision of 0.1  $\mu\text{m}$ .

Combination of mesoscale development materials and their characterization by in-situ micro and nanostructural investigation will provide knowledge and an understanding applicable to real functional conditions.

[3] F. Barrot, et al., "HySi – Hybridization of Silicon Micro-components", CSEM Scientific & Technical Report (2014), 13.



# SURFACE ENGINEERING

Harry Heinzelmann

The structural and chemical composition of surfaces strongly influences many components' properties. This becomes even more true with increasing miniaturization, when surfaces represent an even larger part of the components' volume, and start to dominate their behavior. Surface topographical and chemical properties determine a wide range of effects, such as surface adhesion and friction, optical reflectivity and color, electrical conductivity, and (bio-) chemical affinity. The determination, understanding, and controlled modification of surface topography and chemistry are therefore of great importance for the development of small components and devices, and the ability to fabricate nano-engineered surfaces on large scales and at a competitive cost is a key competence that supports industrial applications.

Some of the most important areas with regard to controlling surface properties deal with the topographical structure and the chemical composition. CSEM's SURFACE ENGINEERING program addresses the understanding of how these surface properties influence micro- and macroscopic behavior, and the development of corresponding manufacturing technologies. The *Nanosurface Engineering* activity concentrates on the development and fabrication of nano-structured surfaces and nano-porous films with added functionality, as well as on the design and realization of nano-optical components based on nano-engineered surfaces. The *Biosurface Engineering* activity addresses the biochemical functionalization of surfaces that are developed for use in (affinity) sensors and as cell and tissue support substrates, and includes microfluidics and sample-handling instrumentation. Finally, the *Printable Electronics* activity deals with printing processes for both organic and inorganic electrical circuits, the design and testing of electronic components, and the higher-level integration of printed electronics components for flexible solutions.

The SURFACE ENGINEERING program not only addresses questions at the material and process levels, it also aims to develop manufacturing methods and higher-level integration pathways that enable CSEM to offer attractive solutions to industry. The program hence develops scientific knowledge in the design, modelling, generation, and understanding of functional surfaces, alongside technological expertise in the development and stabilization of up-scalable fabrication methods, characterization, and integration.

The program's mission is therefore to "research and develop engineered surfaces and interfaces by controlling their (nano-) structured topography and their surface material composition using processes compatible with large-scale manufacturing, in order to design and optimize predominantly their (bio-) chemical, optical, and electrical properties, and to improve the performance of the respective components."

## Long-term objectives

The global, long-term objectives of the SURFACE ENGINEERING program are twofold. On the one hand, it is important to strengthen CSEM's technology position in those areas where CSEM can offer unique and valuable solutions to industry. These include the development of well-designed

surfaces with novel optical and chemical properties, and corresponding fabrication methods that allow competitively priced manufacturing, the conception of lab automation equipment for use in cell sorting and tissue preparation environments, and the further development of printed electronics solutions on flexible substrates, for example for the fabrication of printed electrochemical sensors that are biochemically functionalized for their specific applications. On the other hand, it is a long-term objective of the program to continue to provide both a state-of-the-art understanding of optimizing surfaces and the corresponding methods that are necessary to leverage key CSEM technologies originating in other technological programs. Examples of this supporting role include the direct writing of microscale structures onto image sensors for improved positioning based on shadow mask imaging, or the deposition of conformal protective layers onto sensors for harsh environments.

The long-term objectives in *Nanosurface Engineering* are the continued development of methods of originating nanoscale surface structures, such as nanoparticle and molecular self-assembly and sol-gel processes, with a particular emphasis in the coming years on providing appropriate manufacturing techniques and processes that are compatible with production in industrial environments. In micro-/nano-photonics engineering, the potential of printing optical components will be further explored, both for the quasi-2-D printing of filter structures and the 3-D printing of free-form optical components. The aim is to continue to provide novel and price-competitive solutions for applications including sensing, imaging, and illumination.

In *Biosurface Engineering*, the long-term objectives are to develop those technologies critical to the support, handling, and measurement of biological materials. These include the necessary interfaces found at the heart of bioreactors and instruments, appropriate sensors for stand-alone use or integration, and the liquid- and sample-handling technology based on micro-fluidics that allows the development of complete solutions for handling cells and microorganisms under optical and other sensory control.

The long-term objectives in *Printable Electronics* are to provide the key elements for maintaining a flexible technology platform in printed electronics, including the identification and characterization of suitable materials and the optimization of processes. A special emphasis is being put on the hybrid integration of standard components with printed components, and on the printing of electronic structures on top of prefabricated components such as MEMS sensors.

The research carried out in this program is concentrated on the following activities:

- *Nanosurface Engineering*, specifically addressing micro-/nano-manufacturing technologies, functional nanocoatings, and nanophotonics engineering.
- *Biosurface Engineering*, specifically addressing bio-interfacing, biosensors, and bioinstrumentation
- *Printable Electronics*, specifically addressing printable electronic processes and components; design, modelling, and testing; and application and hybrid integration.

The **Nanosurface Engineering** activity concentrates on the development and fabrication of nano-structured surfaces and nano-porous films with added functionality, as well as on the design and realization of nano-optical components based on nano-engineered surfaces. This includes novel methods of nano-structure origination; replication methods for nanoscale structures; tooling (e.g., for embossing and injection molding); coatings from sol-gel films with tunable nano-porosity and their application-specific functionalization (e.g., by introducing guest materials for sensing or optical amplification); and the modelling of optical properties and the design and realization of related optical components and devices, with methods that have recently expanded to include (3-D) printing techniques.

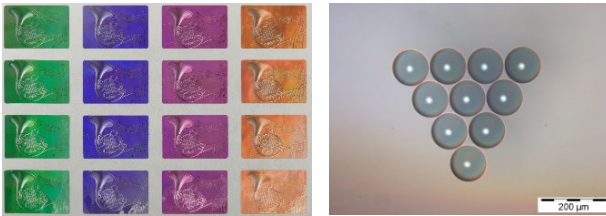


Figure 1: Optical effects generated by microstructures for security (left); optical microstructures made by printing (right).

The **Biosurface Engineering** activity addresses the biochemical functionalization of surfaces that are developed for use in (affinity) sensors and as cell and tissue support substrates, and microfluidics and sample-handling instrumentation. This includes surface grafting with specific biomolecules showing the desired affinities, for both electrochemical and optical sensing, and the development of adapted optical reader instrumentation; the design of novel cell supports such as beads and bioreactors, for 3-dim cell cultures, for example for cell-based (ex vivo) toxicology studies; and the development of microsystems and instrumentation for the handling of biological samples.



Figure 2: Demox oxygen reader in the form factor of a microscope objective (left); prototype instrumentation for sorting and handling of biological samples (right).

The **Printable Electronics** activity deals with printing processes for electrical circuits, the design and testing of electronic components, and the higher-level integration of printed electronics components for flexible solutions. This includes high-resolution, exploratory printing processes such as Aerosol Jet Printing (AJP); the printing of electronic components and circuits on flexible substrates, as well as encapsulation and packaging; the modelling of higher integrated components such as light-management solutions for organic light-emitting diodes and photodetectors; and printing processes for large arrays of electrochemical sensors and other electronic circuits.



Figure 3: Roll-to-roll printing of electronic circuits (left); printed resistive pressure sensor (e.g., for robotics applications) ("SmartSkin") (right).

The three activities of the program have strong mutual synergies, for example in the development of printed electrochemical sensors that are specifically functionalized for applications in environmental or biochemical sensing, in the development of cell culture supports with optimized surface topography and chemistry with integrated electrochemical sensors for monitoring, and in plasmonic sensing for high-sensitivity, label-free analytics.

### Highlights

Numerous developments have generated significant interest, both among industry partners and in the peer community. The Demox reader platform for oxygen can be widely applied and has led to interest in the detection of other substances. For security, a range of new optical effects have been developed that include multiple color changes upon rotation. Pressure sensors printed onto flexible substrates allow a wide range of applications, such as the use as "artificial skin" for robots. The project "SmartSkin", carried out in collaboration with an industrial partner, enables machines to detect obstacles upon the slightest contact, and thus to become safe to operate in the vicinity of humans.

The SURFACE ENGINEERING program is an important part of CSEM's global research program and has numerous synergies with the four other thematic research programs. It thus supports the further development of a range of core technologies, as well as their transfer to industry.

# Nanostructured Thin Films for Spectroscopy and Imaging

G. Quaranta, F. Geister, F. Lütolf, L. Dümpelmann, M. Stalder, B. Gallinet, R. Ferrini

*Nanostructured thin films requires a minimal amount of optics, which is an asset in the development and integration of miniature spectrometric or imaging systems. Plasmonic nanostructures were used as a polarization-tunable filter to provide color input to a black & white camera. In addition, a miniature photo-spectrometer based on dielectric nanostructures was fabricated, calibrated and successfully characterized with a green LED light.*

In the last years, the need for miniature photo-spectrometers ( $< 250 \text{ cm}^3$ ) has significantly increased. The main drivers are: reduced time for results, in situ analysis, decreased costs and increased ease-of-use of systems for non experts<sup>[1]</sup>. A promising application of such miniature spectrometers was recently reported as non-destructive testing of fruit ripeness<sup>[2]</sup>. In this framework, nanostructured thin films have the advantage to require a minimal amount of optics, which is an asset in the development and integration of miniature spectrometric or imaging systems.

A plasmonic nanostructure has been fabricated with UV nanoimprint lithography and thin layer metallization. A plasmonic resonance can be observed in transmission in the visible range for the polarization across the grating lines, thus generating a given color at a broad range of viewing angles. If the plasmonic nanostructure is inserted between an input polarizer at  $45^\circ$  and an analyzing polarizer, such as shown in Figure 1(a), four different colors can be observed in transmission<sup>[3]</sup>.

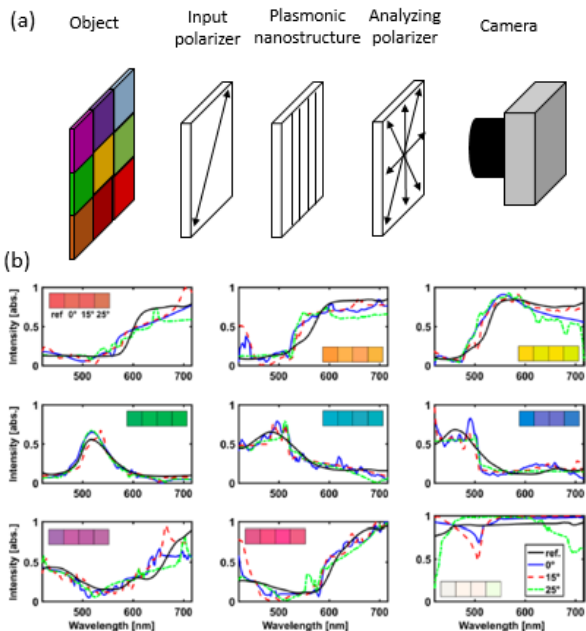


Figure 1: a) Plasmonic nanostructures used as tunable filters for imaging; b) Reconstruction of color spectra from colored patches (Macbeth ColorChecker) recorded with a conventional spectrometer (ref.) and the imaging system at tilt angles of 0, 15, and  $25^\circ$ .

[1] C. Bouyé, B. d'Humières, TEMATYS Report 15, 12 (2016).

[2] A.J. Das, A. Wahid, I. Kothari, R. Raskar, Scientific Report 6, 32504 (2016).

[3] L. Dümpelmann, B. Gallinet, L. Novotny, ACS Photonics 4, 236–241 (2017).

This system has been used as a tunable filter for a camera, where the transmitted color is actuated by a rotation of the analyzing polarizer. In Figure 1b, the reflectance spectra from various colored patches (Macbeth ColorChecker) have been reconstructed using the tunable plasmonic filter in front of a black & white camera<sup>[4]</sup>. A reasonable agreement with the reference is observed, which shows that color information can be obtained on a camera without the loss in resolution inherent to the use of a matrix of standard absorbing filters. The reconstruction of the spectrum is relatively stable with a field of view of at least  $25^\circ$ .

Dielectric nanostructures can also be used as filters in photo-spectrometers. Figure 2 shows a miniature photo-spectrometer fabricated using a nanostructured film as optical filtering element.

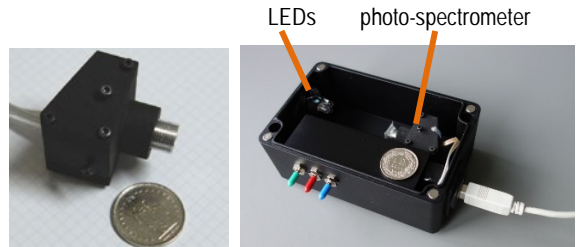


Figure 2: The fabricated miniature photo-spectrometer (left), a suitable housing including LEDs and USB connector (right).

The miniature photo-spectrometer was mounted in a housing together with RGB LEDs for illumination and a USB connection for data processing on a computer. The measured data are acquired with a miniature CMOS sensor of  $4.3 \times 5.7 \text{ mm}^2$ . A measurement for the green LED light together with the exact reference spectrum is shown in Figure 3. A promising agreement between the measured and the green LED reference spectrum is found using compressing sensing.

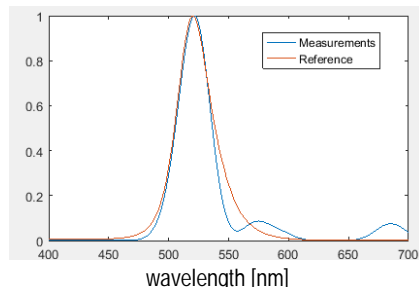


Figure 3: Miniature photo-spectrometer measurement of a green LED, exact spectrum (reference, in red) and measured spectrum (in blue).

[4] L. Dümpelmann, A. Luu-Dinh, B. Gallinet, L. Novotny, ACS Photonics 3, 190–196 (2016).

# Nanofiber-based Retarders Fabricated by Vacuum-free Electrospinning

M. Stalder, F. Geister, R. Ferrini, C. T. Bormann •, R. Oehrlein •, A. Hafner •, Y. Grether ••, M. Waser ••, U. Pieles ••

Today most optical instrumentation is based on thin optical films, which act as interference filters, color beam splitters etc. The majority of these components are manufactured by vacuum processes like magnetron sputtering or physical vapor deposition. Because of their large technical demand, vacuum free methods are very much appreciated. Electrospinning is a vacuum-free versatile method to deposit nano-fibrous materials, originally used for the production of non-woven fabrics for applications in filtration, textile, and medtech industries. The goal of this project is to use electrospinning for depositing highly oriented nano-fibrous layers of dielectric materials on planar substrates (e.g., glass or thin polymer sheets) in order to fabricate optical components. In this report the fabrication of optical retarders based on electrospun polymer nano-fiber layers is presented.

Manufacturing of sub-micron fibers or nano-fibers by electrospinning has attracted a lot of interest in the past years, as it is simple and economic<sup>[1]</sup>. The deposition of highly oriented nano-fibrous layers of optical materials is a new approach for the production of optical anisotropic films such as retarders or waveplates. Retarders are used to modify the state of polarization of light e.g., in liquid crystal displays, projectors or novel brand protection devices.

Preliminary electrospinning tests were carried out with non-oriented nanofibers (Figure 1 left). The main focus was however on electrospinning of oriented nano-fibers by electrospinning onto a rotating cylinder recipient<sup>[2]</sup> (see Figure 1, right).

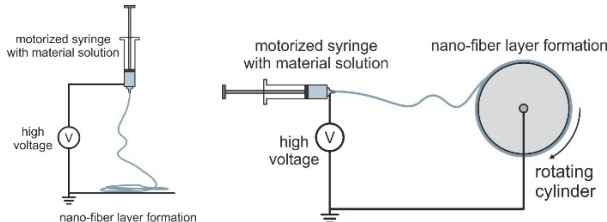


Figure 1: set-ups of the used electrospinning machines for the generation of non-oriented (left) and oriented (right) nano-fiber layers.

For the generation of retarders based on nano-fibers, two concepts were tested: a) nanofibers with a fiber diameter significantly smaller than 100 nm leading to birefringence<sup>[3]</sup>, and b) nano-fibers with intrinsic birefringence.

Commercial polymer materials were used for electrospinning, including: polyimide P84 (PI), polypyrrolidone (PVP), poly(vinyl alcohol) (PVA), polyethylene oxide (PEO), polystyrene (PS). Moreover, a high index of refraction polymer synthesized by BASF Schweiz AG was also tested. The experiments showed that the diameter of the electrospun fibers remains larger than approx. 100 nm, thus generating a strong light scattering.

In order to minimize light scattering, the polymer fibers were encapsulated in a material with a index of refraction close to that of the fibers. Once the light scattering is minimized, the intrinsic birefringence of the nano-fibers can be observed. The analysis of the fabricated samples showed that PS is the polymer with the best parallel aligned nano-fibers and the highest birefringence,

thus it was chosen as reference for further studies. Figure 2 shows scanning electron microscopy (SEM) images of perfectly aligned PS nano-fibers from a 6% and a 1.5% solution.

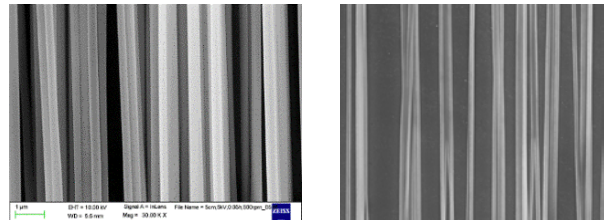


Figure 2: Perfectly oriented PS nano-fibers generated with a 6% solution (left) and with a 1.5% solution (right).

PS nano-fiber based retarders were fabricated, encapsulated and spectroscopically characterized by measuring the transmission spectrum of the devices between crossed polarizers with a diagonal orientation of the nano-fibers of 45° with respect to the polarizer. The best nano-fiber based retarder (from the 6% solution) showed a retardation of approximatively 1/8 wave for green light (500 nm). By placing the retarder on a mirror the retardation is doubled, thus acting as a quarter wave plate. The measurement set-up is illustrated in Figure 3 (left). Figure 3 shows images of the nano-fiber retarder between crossed polarizers (retarder area approximatively 8×8 mm<sup>2</sup>).

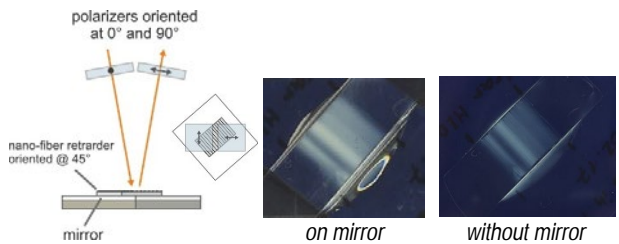


Figure 3: Optical set-up, side and top view (left) and fiber-based retarder between crossed polarizers (middle and right).

In conclusion, the fabrication of a quarter wave plate retarder based on electrospun PS nano-fibers was successfully demonstrated.

This work was supported by the Nanoargovia (Swiss Nanoscience Institute, University of Basel) in the project NF-Optics A11.12. CSEM thanks them for their support.

- BASF Schweiz AG
- Fachhochschule Nordwestschweiz (FHNW), Life Sciences
- [1] A. Greiner, J. H. Wendorff, "Elektrospinnen - eine faszinierende Methode zur Präparation ultradünner Fasern", Angew. Chem. 119 5770 (2007).

[2] Z. M. Huang, Y.Z. Zhangb, M. Kotakic, S. Ramakrishnab, "A review on polymer nanofibers by electrospinning and their applications in nanocomposites" Comp. Sci. Tech. 63 2223 (2003).

[3] C. Gu, P. Yeh "Form birefringence dispersion in periodic layered media", Optics Letters 21 504 (1996).

# Microlenses for Improved Space Imagers

F. Zanella, G. Basset, C. Schneider, A. Luu-Dinh, F. Herzog, F. Lütolf, J. Schleuniger, O. Fernández, S. Fricke, M. Schnieper

*Microlenses are widely used within consumer imaging products, not only in order to compensate for non 100% fill factor but also in view of improving the Modulation Transfer Function (MTF) and cross-talk between adjacent pixels. Such microlenses are manufactured within the standard flow of CMOS foundries and are directed at consumer electronics imagers with pixel pitch in the 1 to 5  $\mu\text{m}$  range. They rarely address the requirements of typical space imagers with pitch from about 5 to 100  $\mu\text{m}$ . However, there is a clear need for performance improvement of space CMOS imagers enabled by microlenses. CSEM was mandated by the European Space Agency (ESA) to lead an activity with the objective to design, manufacture and test the application of microlenses on a back thinned and back illuminated CMOS image sensor (BI-CIS) under space environment conditions.*

CSEM has a long track-record in the fabrication and deposition of custom microlens arrays on various type of imagers. Microlens arrays can increase the sensitivity of imager sensors, reduce their angular dependency and vignetting or improve their resolution by maximizing their MTF and minimizing their parasitic light sensitivity.

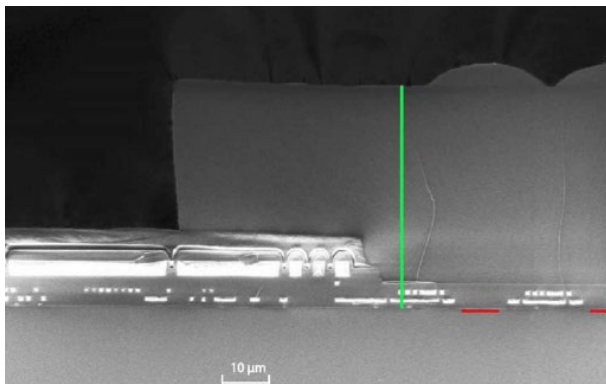


Figure 1: Scanning Electronic Microscope cross-section view of an image sensor covered by microlenses produced by CSEM. Red horizontal segments (bottom-right corner): sensitive areas of the imager. White: metal contacts and interconnects<sup>[1]</sup>.

Designing and manufacturing microlens arrays requires an excellent understanding of the imager pixel geometry, an accurate ray-tracing simulations for the tolerancing and a perfect design for manufacturability optimization. And also all the information about the light incidence distribution.

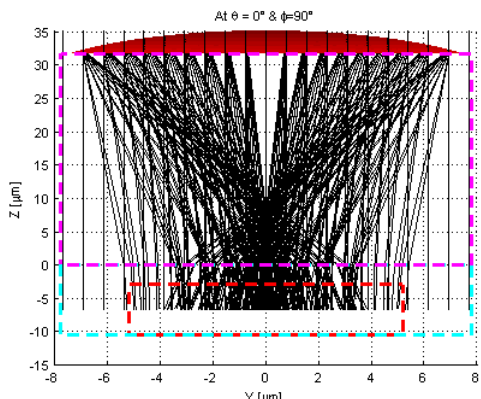


Figure 2: Ray-tracing (Matlab<sup>®</sup>) cross-section of a single BI-CIS pixel covered with a square microlens at normal light incidence. X & Y scales in microns,  $\lambda = 530 \text{ nm}$ . The red dashed rectangle (centered bottom one) highlights the sensitive volume of the pixel.

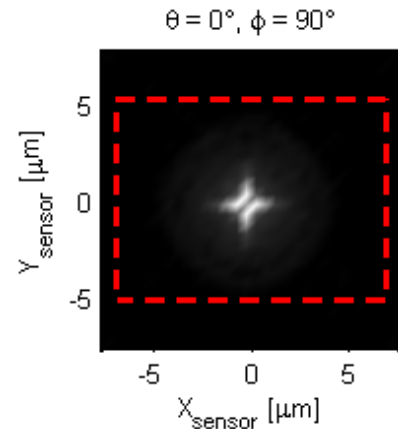


Figure 3: Result of the ray tracing from Figure 2 showing the light distribution on the pixel. The red dashed rectangle highlights the sensitive area of the pixel.

Manufacturing microlens arrays for state-of-the-art imagers to be used in space environments requires various testing and validations to ensure the robustness of the microlenses and their material e.g., to thermal shock and cycles, to vibrations and to UV and other (protons etc.) irradiations.

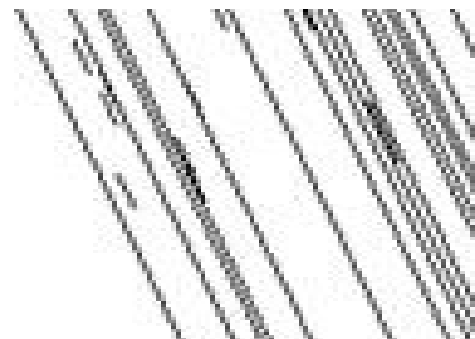


Figure 4: Ray-tracing (LightTools<sup>®</sup>) of a 3x3 pixel BI-CIS array covered with square microlenses at normal light incidence. The blue rectangles at the bottom highlight the sensitive area of the pixels.

In the scope of the ESA activity EXPRO+ AO/1-8624/16/NL/PS/gp, CSEM is designing microlens arrays and their complete space proof testing in order to address the needs of the space industry.

Higher resolution imagers will translate in better imaging systems in satellite and space probes. This will enable a higher accuracy in Earth observations and deep space scientific missions imaging.

<sup>[1]</sup> J. M. Pavia, M. Wolf, E. Charbon, "Measurement and modeling of microlenses fabricated on single-photon avalanche diode arrays for fill factor recovery." Optics express 22.4 (2014): 4202-4213.

# Blazed Gratings on Convex Substrates for High Throughput Spectrographs

I. Zhurinsky, C. Schneider, S. Fricke, M. Schnieper, F. Lütolf

*Blazed grating with a period of 3300 nm, 5.1° left facet angle, and 298 nm height has been fabricated on a convex surface in a sol-gel material and also transferred directly into substrate. This blazed grating will be applied in the Galileo telescope.*

Convex grating is one of the key element of the compact spectrograph designed to disperse light<sup>[1]</sup>. This two-arm instrument provides in parallel imaging and spectroscopic capabilities. In order to optimize the spectrograph efficiency, this convex grating must be blazed at the right angle for maximizing the light in the first order of a diffraction. This spectrograph is a part of the Digital-Micromirror-Device-based MOS instrument, under development and should be mounted on the Galileo telescope.

The blazed gratings on a convex substrates will be tested in such a spectrograph, it turned out to become one of the key elements of telescopes with applications as well as on Earth as in space for investigation of the formation and evolution of galaxies. Within the BLAZEDGRATSPHER project a blazed grating has been fabricated on a convex substrate.

A reflective blazed grating optimized for the 1st order of diffraction, with a period of 3300 nm and a blaze angle of 5.1° (Figure 1), was fabricated onto and into convex substrates surfaces. The substrates had a radius of curvature of 225 mm and a footprint diameter of 63.5 mm. The blaze was optimized for the center wavelength of 580 nm for a total spectral range of 400 – 800 nm.

In a first step a master of the blazed grating structure needed to be originated. This was made on a flat substrate starting from a rectangular grating with a period of 3300 nm. The rectangular grating was UV replicated twice to keep the respective grating profile polarity using Sol-Gel material and subsequently converted into a blazed shape by an angular Ar ion etching process. The desired blazed grating parameters like; depth and blaze angle, have been reached by adjusting the initial grating depth in Sol-Gel as well as the etching angle and duration.

Two approaches have been studied to transfer the blazed grating from a flat surface onto a convex substrate.

In the first approach, a flexible stamp was generated by an UV replication of the master blazed grating, using a flexible nanoimprint material. The flexible stamp was then used to emboss Sol-Gel spin-coated on the convex substrate. In this approach the final component is a convex substrate with a Sol-Gel layer carrying the grating structure.

In the second approach, nanoimprint material was used as a masking layer for a Reactive Ion Etching of the convex substrate.

Again, a flexible stamp was used to emboss a thin layer of nanoimprint material spin-coated on the convex surface. After curing, the structure was transferred into the quartz substrate by a dry etching process. With this second approach, the final component is a convex quartz substrate with the grating structure etched into the volume.

SEM characterizations of the blazed grating onto/into the convex substrates showed a homogeneous profile in the middle and on the edges of the sample.

The blazed grating transferred directly into the convex substrate is more preferable (the 2nd approach), since it will not suffer from any possible aging issues related to adhesion of the Sol-Gel grating to the substrate. In addition, issues arising from thermal mismatch between substrate and Sol-Gel are also avoided, which is an asset for future space applications well known for strong varying operational temperatures.

The following technologies have been developed in the frame of the project:

- Fabrication of a specific blazed grating on a flat substrate based on an initial rectangular grating.
- Transfer of this blazed grating from a flat to a convex substrate by using two processes, first a UV casting of Sol-Gel material and second, a dry etching process.

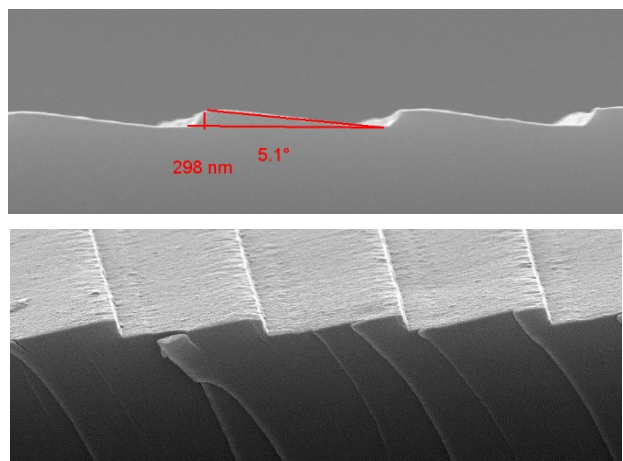


Figure 1: SEMs of the blazed grating on a convex substrate: profile (top) and general view (bottom).

<sup>[1]</sup> F. Zamkotsian, et al., "Building BATMAN: a new generation spectro-imager on TNG telescope", Proc. SPIE 9908, (2016).

# New Generation of Immersed Gratings for High Resolution Spectroscopy in the Near and Short IR

R. Krähenbühl, F. Lütolf, S. Fricke

Spaceborne remote sensing of the chemical composition of the earth atmosphere is an important monitoring tool for scientists studying the influence of gases on the climatic changes and the weather. The requirements of diffraction gratings used in such spaceborne spectrometers are permanently increasing in complexity. Using conventional diffraction gratings would result in larger gratings, and consequently in bulkier instruments. Immersed gratings and especially immersed gratings in transmission are technical solutions to achieve higher performance and more compact instrument configurations simultaneously. Within two ESA projects the important technology building blocks for the successful realization of fused silica (NIR) and Si (SWIR) immersed gratings in reflection and transmission are being developed and demonstrated.

The realization of immersed gratings started with an analytical study to optimize performance and fabrication tolerances of the grating using RCWA (Rigorous Coupled Wave Analysis), FDTD (Finite Difference Time Domain) and raytracing methods. Parameters such as groove shape, period, duty cycle, depth, and incidence angle were screened in respect to diffraction efficiency, polarization sensitivity, dispersion resolution and manufacturability. In the end, gratings with rectangular grooves of high aspect ratios were chosen, because they yield the best performances (efficiency >90%, polarization sensitivity <2%, dispersion 0.2°/nm), and they enable optical contact to a planar surface thanks to their flat top.

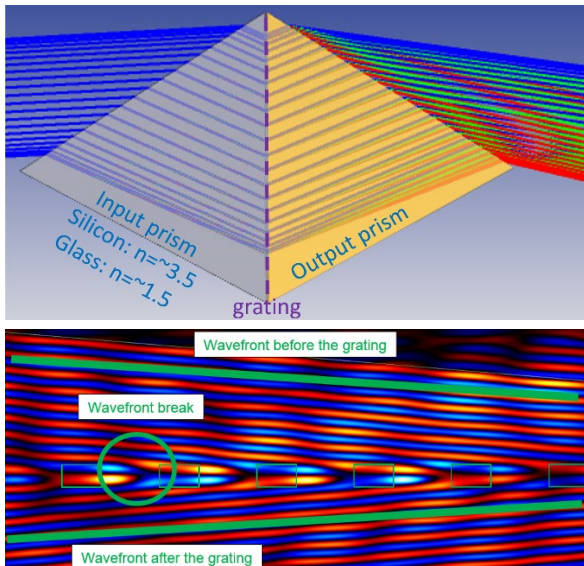


Figure 1: Proposed and simulated immersed grating in transmission using raytracing (top) and FDTD (bottom).

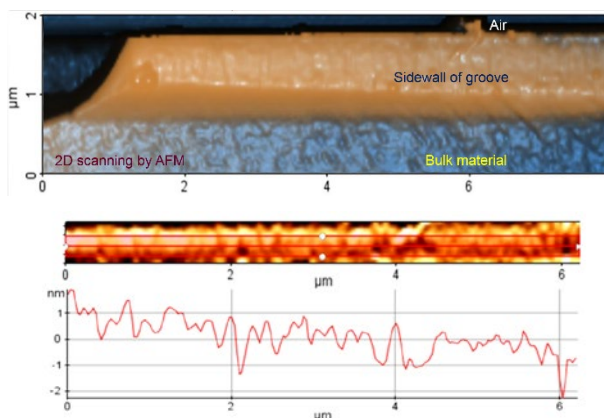


Figure 2: Fabricated grating with ultra-smooth sidewalls.

In a next step, technology developments for the chosen binary gratings with high aspect ratio were carried out. To obtain the required depth, while reaching very low straylight values, special efforts targeted ultra-smooth grating sidewalls. Thereby, special efforts were devoted to the development of an advanced new two-step reactive dry etching process, as well as an additional smoothening step of the holographically structured photoresist.

Silicon, as well as fused silica glass gratings were then bonded to silicon and fused silica surfaces, respectively. This step was performed by our partner WZW, who introduced special polishing and cleaning procedures to achieve surfaces with low roughness and cleanliness required for successful contacting.

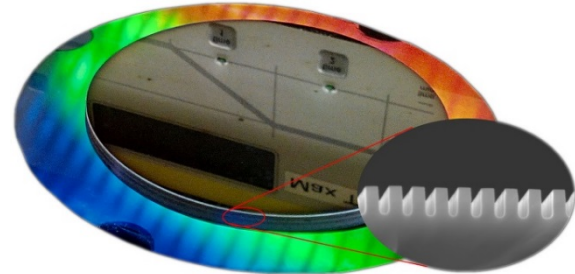


Figure 3: Bonded Si-grating to plane Si-substrate.

Lastly, the final immersed gratings are tested and characterized using metrology, modelling and interpretation of the optical measurements. First measurements carried out by our partner Micos on the fabricated gratings showed straylight (BTDF, bidirectional transmittance distribution function) below the measurement sensitivity.

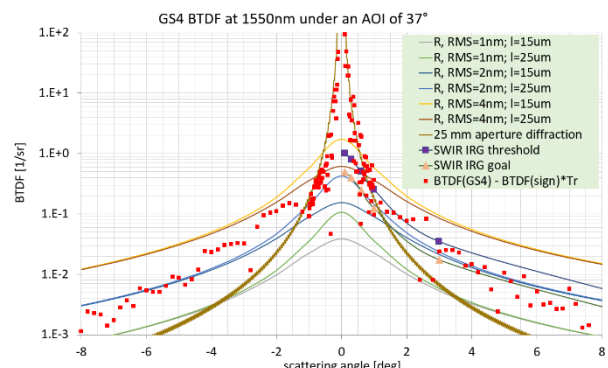


Figure 4: Grating BTDF below measurement sensitivity.

These technology developments will enable the realization of new generation SWIR & NIR immersed gratings with unprecedented performances.

# Very High Fill-factors Microlens Arrays

G. Basset, C. Schneider, A. Luu-Dinh, F. Zanella, F. Herzog, S. Fricke, M. Schnieper

*Microlens arrays are optical components used in many optical systems. They allow homogenizing light beams, splitting beams in multiple beamlets, performing beam shaping or coupling light beams in and out of optical fibers. The successful high quality fabrication of microlens arrays made them key components and an enabling technology in many systems such as steppers and scanners used in semiconductor manufacturing or in optical fiber networks, the backbone of the internet. Producing microlens arrays with more densely packed microlenses, providing a so-called higher fill-factor, generates better performances for the various systems relying on them.*

High quality microlens arrays are nowadays commonly manufactured using a thermal reflow of positive photoresist pillars followed in a second step by a transfer of the microlens arrays into various materials using dry etching reactors<sup>[1]</sup>.

The first step, called the microlens master fabrication, starts with coating a glass or silicon wafer with an organic photoresist layer. This photoresist material is then exposed through a photomask by UV light creating a patterned exposure. This pattern is revealed in the photoresist material in a development bath, completing the photolithography process.

The resulting arrays of micro-pillars contain the material required for the array of microlenses, while having flat-tops. The microlens array master fabrication continues with a thermal reflow in which the photoresist pillars are melted and take spherical or aspherical shapes due to the surface tension of the melted resist. Producing consecutively very dense microlens arrays required an excellent control of all mastering steps.

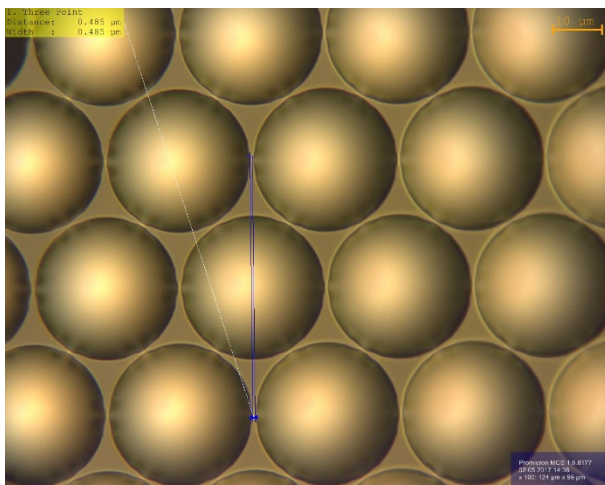


Figure 1: Optical microscope view of a very high density circular microlens array arranged in a honeycomb layout. The microlens master in photoresist is produced at Süss Micro-Optics following an optimized process transferred from CSEM.

After performing optical metrology and inspection, the second step consists in transferring the microlens array into the wafer material using reactive ion etching. This process conserves the microlens array layout, but allows to finely tune the profile of the microlenses. Aspherical microlenses can be produced from a spherical shape microlens master by continuously optimizing the plasma composition during this reactive ion etching transfer.

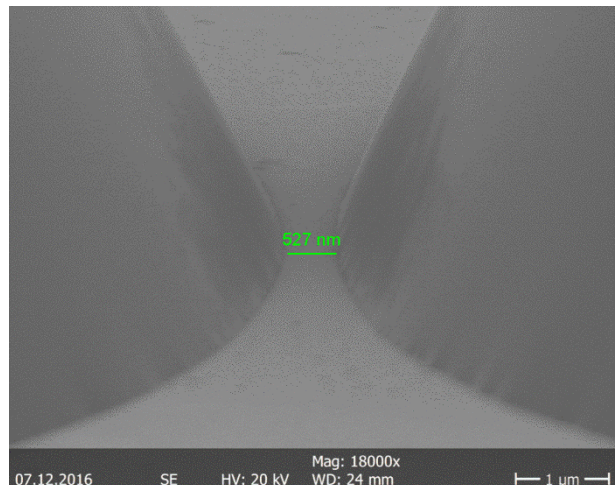


Figure 2: Scanning Electronic Microscope detailed view on a subwavelength gap between adjacent photoresist microlenses.

Süss Micro-Optics, a leader in delivering high quality micro-optics such as microlens arrays, and CSEM partnered to address this challenge with the support of the Swiss Commission for Technology and Innovation.

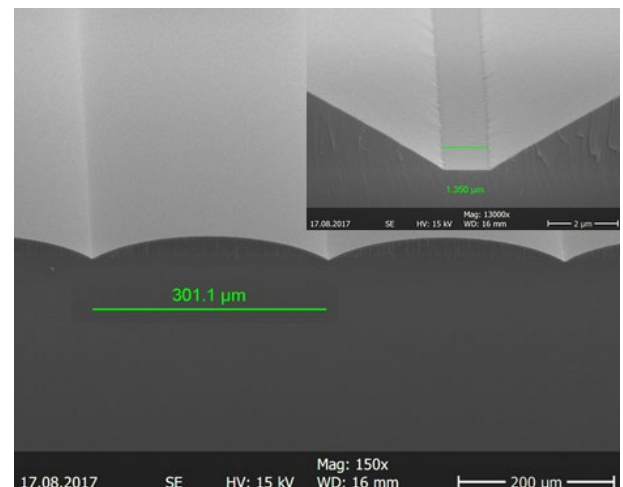


Figure 3: Scanning Electronic Microscope overview of a photoresist master of 300 μm pitch cylindrical microlenses, and detailed view (top right) of a 1.35 μm inter-lens gap. The fill-factor is measured above 99.5%.

The various steps of the mastering, from the photolithography and mask design to the flow control during the thermal melting of the photoresist, are improved to reliably deliver very dense microlens arrays of any shape and size.

<sup>[1]</sup> H. Ottevaere, et al., "Comparing glass and plastic refractive microlenses fabricated with different technologies." Journal of Optics A: Pure and Applied Optics 8.7 (2006): S407.

# Ultra-thin-film Deposition Processes for Controlled Hydrophilicity and Hydrophobicity by Molecular Vapor Deposition

G. Andreatta, L. Fanni, A. Bionaz, N. Blondiaux, J. Déglon •, R. Pugin

Molecular Vapor Deposition (MVD®) replaces traditional liquid coating processes with a highly reproducible vapor deposition alternative that is ideal for manufacturing applications. The deposited thin films can be used as lubricative, protective, hydrophobic, hydrophilic, biocompatible, or reactive coatings. A precise control of wetting properties can be achieved on a variety of materials and over intricate features with high aspect ratios. Anti-stiction films are created by deposition of fluorocarbon materials and will benefit various MEMS devices including displays, sensors, actuators, RF switches, inkjets, and data storage devices. For biological MEMS, excellent wetting control can be achieved on micro-fluidics (lab-on-a-chip, microplates). MVD® is also used for commercial applications requiring moisture barriers, anti-corrosion coatings, or release layers for imprinting.

The MVD® technology was developed to deposit ultra-thin, functionalized, both organic and inorganic films with higher yields and better cost efficiencies than traditional liquid deposition techniques. Such films serve as lubricative, protective, hydrophobic, hydrophilic, biocompatible, or reactive coatings. We have described elsewhere examples of the unique properties obtained by MVD® coatings at CSEM e.g., barrier layers for miniature atomic clocks<sup>[1]</sup>, apolar monolayers for MEMS gas chromatograph<sup>[2]</sup>, and ice-phobic coatings<sup>[3]</sup>.

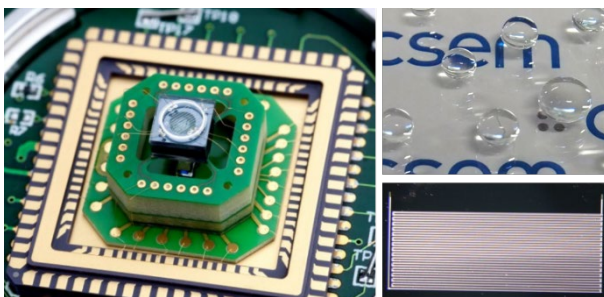


Figure 1: Applications of MVD® thin films at CSEM. Clockwise from left: Miniaturized atomic clock; Nanostructured, transparent and super-hydrophobic surfaces; apolar column structures for MEMS chromatograph.

Amongst other properties, MVD® coatings are particularly appropriate as means of controlling the wetting properties or functionality of the surfaces. Therefore, the surface energy of several type of chemistries deposited by the MVD® technology was characterized and results are shown in Figure 2.

Moreover, we have shown that the wetting properties of dense layers are mainly controlled by the molecular chemistry. Dependency of the density, thickness, and properties of the coatings on the depositing parameters was fully characterized and the coating processes were optimized for each application.

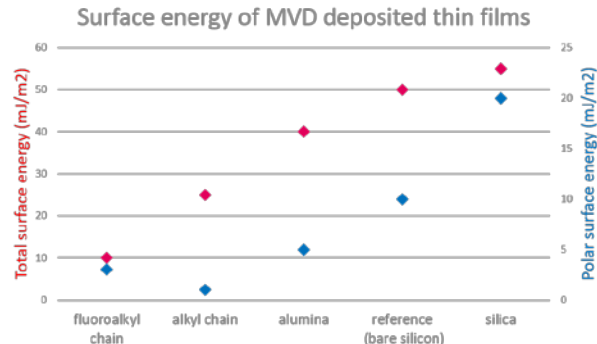


Figure 2: Total surface energy (red) and polar surface energy.

Biotech devices in the field of lab-on-a-chip MEMS and microfluidics rely heavily on the wetting properties and surface functionality of intricate shapes and channels. In collaboration with DBS System SA, producer of HemaXis™ devices, we developed unique hydrophilic coatings to improve blood collection in dried blood sampling system. The coatings are conformal on high aspect ratio structures such as plastic micro-channels and allow for easier and faster blood transport through the devices.



Figure 3: HemaXis™ blood collection sampler includes microchannels covered with a highly conformal hydrophilic MVD® coating.

Controlling the wetting properties of surfaces is critical for numerous applications such as biomedical systems, aeronautics, watchmaking, or MEMS devices. MVD® technology provides a method for reproducibly coating complex high-aspect-ratio structures in a wide range of materials in a manner which is highly compatible with industrial applications.

• DBS System SA, Gland, Switzerland

<sup>[1]</sup> T. Overstolz, *et al.*, "Improved Lifetime of Miniaturized Vapor Cells in Atomic Clocks", CSEM Scientific & Technical Report (2016), 34.

<sup>[2]</sup> A. Hoogerwerf, "Design of a MEMS Gas Chromatograph", CSEM Scientific & Technical Report (2015), 26.

<sup>[3]</sup> E. Scolan, *et al.*, "Icephobic Coating Associated with Low-power Electromechanical De-icers", CSEM Scientific & Technical Report (2015), 44.

# Functional Metal Oxides for Additive Manufacturing

N. Hendricks, S. Lani, R. Pugin

Additive Manufacturing (AM) has numerous advantages over traditional manufacturing techniques such as reduced material waste, on demand fabrication times, and ease of customization, but there is a lack of new and advanced materials to further extend AM's capabilities. To address AM's material capabilities, CSEM is developing and expanding nanoparticle based materials which are capable of being processed with current AM techniques, such as Aerosol Jet Printing (AJP) and Stereolithography (SLA). Specifically, the use of functional metal oxide nanoparticles are of interest due to the broad range of applications such as sensors, photovoltaics, photonics, flexible electronics, and catalysts as well as the availability of such materials.

Additive Manufacturing (AM) is becoming more and more common today as a tool for researchers and companies that require rapid optimization and enhanced flexibility, specifically in the fast-paced research and start-up environments. At CSEM, there are several AM techniques readily available which includes Aerosol Jet Printing (AJP) and Stereolithography (SLA). To increase the value of AJP and SLA, inks and resins are being investigated that integrate the functional properties of metal oxide nanoparticles directly into 2D and 3D printed patterns, which will exploit the full potential of the functional metal oxide material.

Current materials for AJP, which are readily available, are based on conductors and organic dielectrics where the functionality is limited to electrical properties. Recently, the AJP community has been making efforts to print solvents for etching as well as other polymeric materials such as Teflon (poly(tetrafluoroethylene)) and Kapton (polyimide). For SLA, the common materials used are based on organic materials capable of undergoing photopolymerization with ultraviolet (UV) light to create photo-harden polymers. As SLA has matured over the last three decades, the materials being utilized in SLA are expanding to include ceramics, various types of polymers, composites, and biomaterials.

By utilizing pre-synthesized, commercially available nanoparticle powders and highly concentrated nanoparticle solutions as starting materials, inks have been formulated specifically for use with the AJP system. Through optimized formulation, crack-free microstructures constructed from nanoparticle inks have been successfully patterned; as an example, stannic oxide patterns are shown in Figure 1. Other materials that have been printed crack-free with the AJP technique include titanium dioxide, aluminum dioxide, copper oxide, and iron oxide.

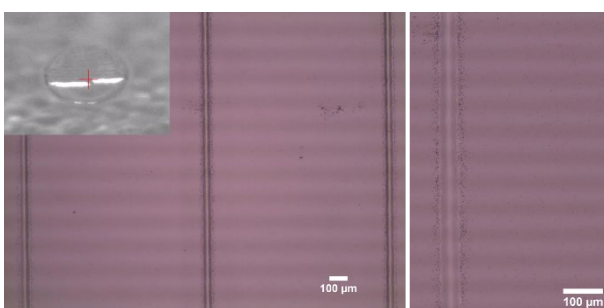


Figure 1: Crack-free microstructures from stannic oxide NPs.

Silicon dioxide nanoparticles have also been printed with AJP into photonic crystal structures with unique optical properties in the visible spectrum. Figure 2 is an example of silicon dioxide nanoparticles patterned into a monolayer structure. Such silicon dioxide nanoparticle inks have also been deposited on graphite electrodes for use as a sensing scaffold for detecting analytes in liquid solutions.

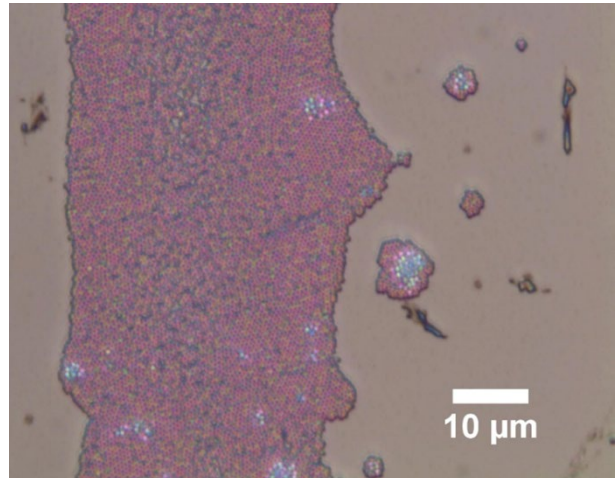


Figure 2: Photonic crystal structure from silicon dioxide NPs.

With SLA, the effort has been to create composite materials from pre-synthesized nanoparticles and commercially available resins. Through specific resin formulation and dispersion techniques, composites with functionality, such as piezoelectric or magnetic properties, have been realized. One such example of functional composite resins for SLA, shown in Figure 3, is with barium titanate nanoparticles and a commercially available resin. The concentration of the barium titanate nanoparticles in the composite can be tuned to adjust the piezoelectric response while also maintaining a high quality dispersion.



Figure 3: SLA printed structures from a barium titanate NP based composite resin.

In summary, strategies are in place to quickly print functional metal oxide nanoparticles, as inks for AJP or as resins for SLA, for a large range of applications. This provides a material platform for common AM techniques here at CSEM that is unique and flexible.

# Hierarchically Porous Thin Films for Optical Gas Sensing

X. Bulliard, A. Grivel, G. Weder, R. Ischer, G. Voirin, R. Smadja, R. Pugin

Silica-based porous thin films are used as support to photosensitive materials applied to the optical detection of gas. Porosity control is key to increase the sensitivity and the dynamic response of the sensing layer. In this work, a patented dual hierarchical porosity is created by combining a mesoporous layer based on silica nanoparticles with a microporous sol-gel layer containing photosensitive materials. The obtained thin film is used for gas detection by choosing photosensitive materials that are responsive to oxygen or carbon dioxide. When mounted on custom-made sensing architecture, the sensor response to gas pressure is significantly improved with the introduced dual range of porosity.

Nano-porous layers are very useful matrixes for the immobilization of biomolecules in biodiagnostics, as semi-permeable membranes or as gas sensors.<sup>[1]</sup> The sensor response is usually measured electrochemically or optically depending on its architecture. In this work, we chose the mode of optical detection by measuring either absorption phase change or fluorescence quenching of photoresponsive dyes in the presence of either carbon dioxide or oxygen. The total concentration as well as the distribution of dyes within the nanoporous layer are critical parameters to obtain high sensing performances.

To get an accurate control of the distribution of the dyes within the porous thin film, we developed a patented technology at CSEM for the production of thin films with a dual range of porosity.<sup>[2]</sup> The hierarchical porosity facilitates the access of the gas within the layer and maximizes the surface contact area between the dye and the gas. A first range of porosity is obtained by depositing a mesoporous layer made of silica nanoparticles. The pore size and surface area are controlled by the diameter of the nanoparticles. A second type of porosity was then generated by depositing a sol-gel solution in which the photosensitive dye was dissolved. A curing step allows for the development of micropores within the sol-gel layer embedded in the first mesoporous layer. A Scanning Electron Microscope (SEM) image of the layer cross-section is represented in Figure 1a.

The hierarchically porous layer can be processed on a wide range of different substrates, including plastics, metal or metal-oxides through different wet coating deposition techniques. Figure 1b gives an example of the hierarchically porous layer deposited on an A4-sized plastic substrate for applications to oxygen sensing. In this specific example, the fluorescence lifetime of a Ruthenium (Ru) dye is measured against oxygen pressure. When comparing with a microporous layer containing a single range of porosity, the dual porosity of the hierarchical layer led to a more linear response as shown in Figure 1c. Similar experiments were reiterated for the detection of carbon dioxide by measuring the absorption change of another type of dyes.

The A4 plastic substrate coated with the sensing hierarchical layer are then straightforwardly integrated in custom-made sensing architectures. Figure 1d shows one example of such architecture for applications in oxygen sensing in cell cultures (Figure 1e). In this case, the A4 layer was subdivided into smaller patches. The reader format is similar to that of a microscope objective and the reader can be directly affixed on an inverted

microscope and routinely used for biological applications. The microscope facilitates alignment between sensor and reader while ensuring a stable and constant optical environment for reliability.

Noticeably, this technology finds applications not only in the biological fields, but also in aerospace, for example for the production of pressure sensitive paints (PSP) used to measure aerodynamics of airplanes models.

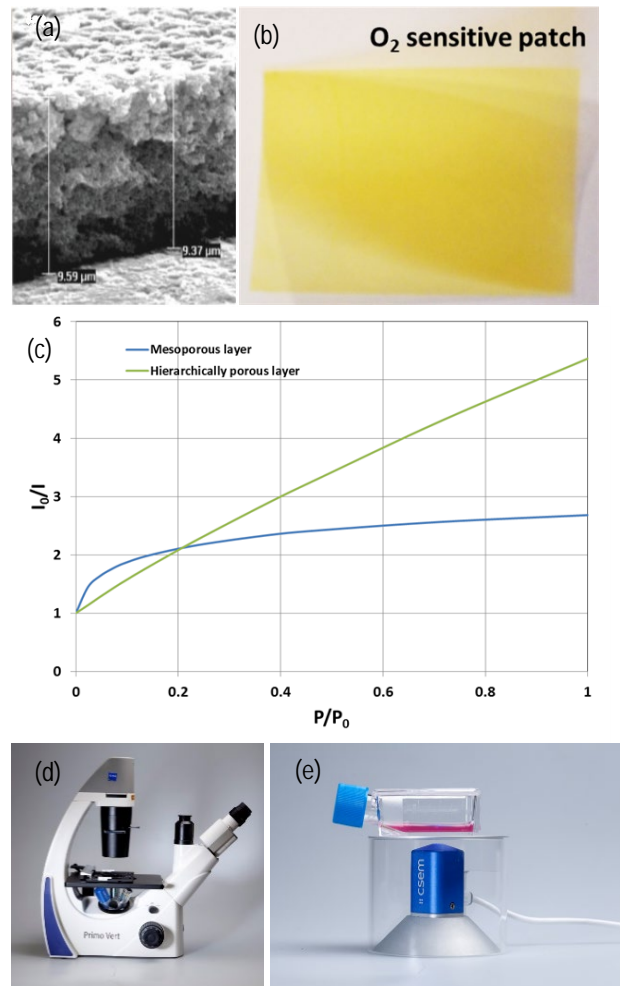


Figure 1: a) Nano-porous layer with hierarchical porosity; b) sensing layer deposited on plastic substrate; c) comparison of the sensing layer response between a single range of porosity and a dual porosity; d) sensing layer patches mounted on an optical microscope; e) sensing architecture integrated into a custom-made sensing architecture for oxygen sensing in cell cultures.

[1] O. Pérez-Anguiano, *et al.*, "Transparent and robust silica coatings with dual range porosity for enzyme-based optical biosensing", *Adv. Funct. Mater.* 27 (2017) 1606385.

[2] E. Scolan, *et al.*, "Optical sensor for detecting a chemical species" US Patent 20170176332.

# Healing Chronic Wounds with Blue Light

D. Kallweit, O. Fernandez, F. Geister, R. Ferrini

In 2017 CSEM continued its development work within the European project MEDILIGHT. The project aims to develop an intelligent and highly integrated phototherapy band-aid for the healing and monitoring of chronic wounds. Within the project a smart medical device for professional wound care is developed. The device uses recently proven therapeutic effects of visible light to enhance the self-healing process and monitor the status and history of the wound during the therapy.

The MEDILIGHT wound care system consists of a small non-disposable electronic module and a thin and flexible sheet with LEDs and integrated sensors for the monitoring of temperature and blood oxygenation at the wound.

Blue light is known for its anti-microbial, anti-proliferative and anti-inflammatory effects without damaging the tissue. Key biological effects of blue light on bacteria, keratinocytes and fibroblasts have been demonstrated with the lighting system developed by CSEM. In-vitro studies treating different bacterial strains with blue light revealed bacteriostatic and even bactericidal effects.

The developed thin LED illumination system is shown in Figure 1. The mechanically very flexible LED foil is able to provide a high luminous intensity of over 25 mW/cm<sup>2</sup> at a very high degree of illumination homogeneity (Figure 2).

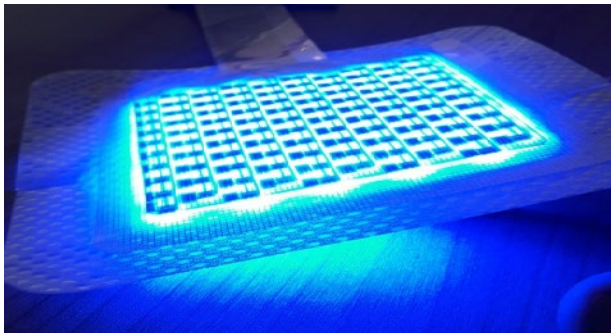


Figure 1: Photograph of the flexible LED foil with sensors.

In order to keep the wound dressing with the lighting system thin and flexible a thin double layer diffusor foil was implemented, which provides a homogenous light distribution at the wound, at a distance of only a few millimeters.

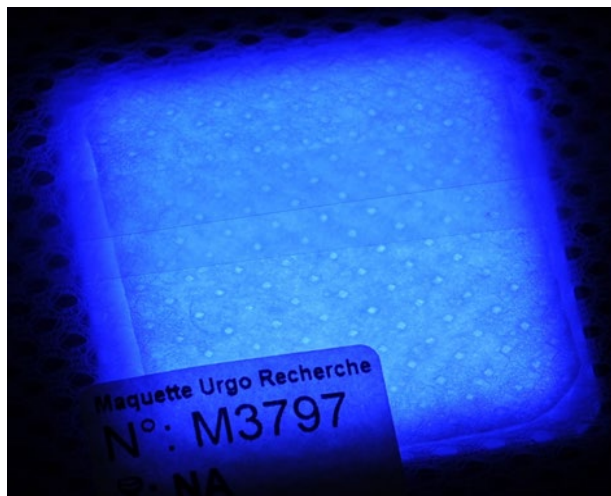


Figure 2: Flexible LED lighting system with wound dressing.

In order to increase the optical efficacy of the lighting system the flexible LED foil was also equipped with a highly reflecting, flexible back reflector foil. Light which is not transmitted but reflected at the diffusor and consequently would be lost, is thus

efficiently redirected towards the wound. The back reflector provides an efficiency of 98% and is as mechanically flexible, self-adhesive, and can be easily cut according to the actual design of the LED foil with its sensors for temperature and blood oxygenation.

The first prototype of the MEDILIGHT system is shown below in Figures 3 and 4. The MEDILIGHT system is intended to be applied to diabetic foot ulcers (on the sole) and venous leg ulcers (on the sides of the lower leg). The size of the flexible illumination system will be varied between 4×4 cm and 10×10 cm.



Figure 3: MEDILIGHT demo with electronic box and flexible LED foil.



Figure 4: MEDILIGHT demo applied on the foot.

The project MEDILIGHT is funded by the European Commission (grant agreement no. 644267) and builds on the competencies of the following partners: Technical University of Berlin (TUB, Germany); Laboratoires URGO (France); Ruprecht-Karls-University Heidelberg (Germany); CSEM (Switzerland); SignalGeneriX Ltd (Cyprus); Microsemi Semiconductor Limited (United Kingdom); and AMIRES s.r.o. (Czech Republic).

# Classification of Early Stage Zebrafish Fertilization

S. F. Graf, M. Höchemer, I. Kastanis, H. Dong, D. Kohli

The demand for zebrafish egg assays to perform toxicity test is still increasing. However, one remaining bottleneck is the early stage classification of fertilized zebrafish eggs. Current systems can only distinguish between fertilized and coagulated (unfertilized) eggs after 24h. In many cases this is too late and therefore the selection is still done manually. For this reason our CellFactor technology was further developed to use deep learning to classify eggs into an unfertilized or a fertilized class for subsequent sorting into multi well-plates.

The zebrafish is considered as one of the most suitable model organisms to test toxicity of compounds mainly because of its transparency, the large number of eggs available and the fact that they share 70% of genes with humans. Therefore, in the last years' popularity of the zebrafish model increased rapidly for such toxicity test. Today's trend is towards high throughputs while a remaining bottleneck is still the preparation of eggs into multi well-plates after which they are processed with high throughput machinery.

To address this bottleneck, CSEM has developed the imaging-based CellFactor (see Figure 1) in the past years with its patented transport system<sup>[1]</sup> based on viscosity drag force and delivery on demand system. Furthermore, a deep learning classifier was implemented to distinguish fertilized eggs from coagulated eggs after about 24h. However new protocols ask for earlier classification of fertilized eggs, preferably in the first hours.



Figure 1: CellFactor 2nd generation.

Therefore the latest development for the CellFactor is the deep learning based classification of cell-stages in two classes as shown in Figure 2. The first class named U covers the potentially unfertilized cell stages (0- and 1-cell stage). The second class named C currently includes the 2-, 4- and 8-cell stages of which the 2-cell stage might still be the result of a spontaneous cell division of unfertilized eggs.

The patented transport system brings a huge advantage to other imaging systems, since the egg is rotating over the length of the imaging area. This allows to view the egg from different sides. Furthermore, in case no decision could be made, the egg remains in the sorter and a few seconds later the same egg can be inspected with different views. As an example in Figure 3 a series of frames of a zebrafish egg passing the imaging system is shown. The classifier starts to recognize the egg as fertilized (class C) in the last two frames when it has rotated enough for classification.

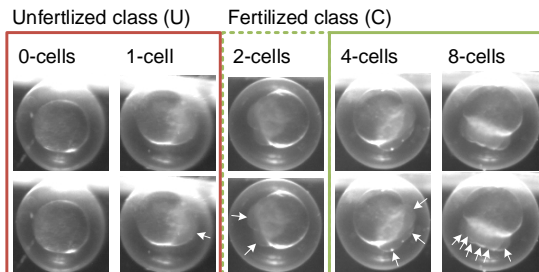


Figure 2: Images of 0- to 8-cell stage zebrafish eggs taken in the CellFactor, whereof the 4- and 8-cell stages represent fertilized eggs and 2-cell stages might also contain some unfertilized eggs which could have undergone some spontaneous cell division. (top row) original image; (bottom row) top row images with arrows indicating the individual cells of the egg - not every cell might be visible.

The required time to identify and classify eggs with our deep learning algorithm takes about 8 ms which allows to run the CellFactor with frame rates of more than 80 frames per second.

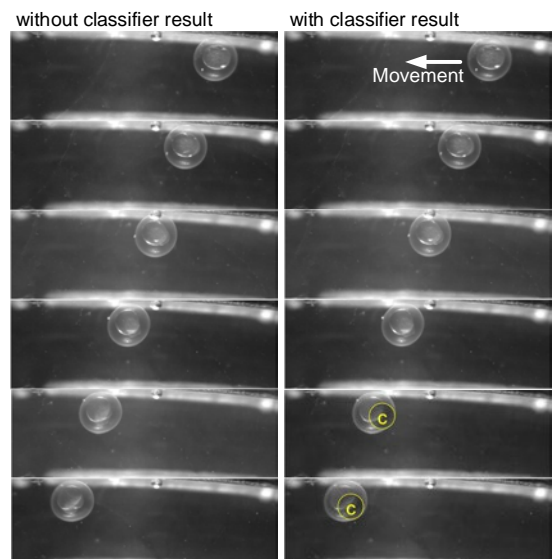


Figure 3: Frames (32 ms in-between) of an egg rolling along the image area when passing the camera system of the CellFactor. The classifier correctly identifies the egg in the last two frames when the cells start to be visible as fertilized egg of the class C.

With this latest development, the scientist can make sure to have fertilized zebrafish eggs for their toxicity test within the first hours post fertilization. With additional teaching data it should be possible to teach the classifier to also distinguish between individual cell stages of the fertilized eggs.

This work was supported by the Swiss federation and MCCS Micro Center Central Switzerland. CSEM thanks them for their support.

<sup>[1]</sup> Graf, et al., (2011) Journal of Laboratory Automation, 16(2), 105-111.

# Analysis Cartridge for Companion Diagnostics

S. F. Graf, T. Volden, S. Berchtold, J. Goldowsky, N. Schmid, V. Revol, H. F. Knapp

The most viable defense against cancer morbidity is to be able to detect the cancer early enough and then treat it adequately. For this purpose Point-of-Care (PoC) devices are required which deliver reliable, accurate and fast results. Together with a consortium CSEM is developing such a PoC device to detect and monitor cancer-based on specific proteins. For this purpose a disposable analysis cartridge with integrated whole blood filter and bio-functionalized optical chip is being developed. The cartridge design addresses the requirements such as user friendliness, low-sample volume, highly reproducible flow, avoidance of air bubbles on the sensing area, and the compatibility for mass production.

In the medical diagnostics industry, there is an ever-increasing need for the development of robust, reliable, accurate and fast devices for early diagnosis, screening and monitoring of diseases allowing for the emerging paradigm shift of Personalized Medicine and Companion Diagnostics. There is a special interest in cancer. According to the World Health Organization (WHO), many cancers can be reduced, and patients have a high chance to be cured if cancer is detected early and treated adequately.



Figure 1: Mock-up representation of the PoC device develops in the project BioCDx for early diagnostics and monitoring of cancer.

The European project BIOCDx<sup>[1]</sup> aims to develop a miniaturized, ultra-sensitive and reliable Point-of-Care (PoC) device with disposable microfluidic cartridge for early detection and monitoring of cancer biomarkers in whole blood samples (see Figure 1).

The disposable cartridge is represented in Figure 2. The integrated blood filter retains red and white blood cells and platelets, while letting the blood plasma pass through. The plasma is then transferred to a label-free bio-functionalized optical detection chip based on up to eight Mach Zehnder Interferometers developed by Lionix International. Additionally, nanoparticles will be used to increase the signal strength and gain a higher sensitivity. Only active areas of the optical chip will be functionalized with antibodies while the remaining area will be coated with an anti-fouling layer. Moreover, the signals of the eight interferometers will be multiplexed to reduce the number of photodiodes required.

The design of the microfluidic cartridge was done at CSEM and aimed to achieve the following properties:

First, accurate measurements require a wide range of flow rates from 4 to 40  $\mu\text{l}/\text{min}$  with minimal flow pulsation. This was realized by integrating three syringes on the cartridge to store the dedicated buffers to drive the flow. Furthermore, the use of these syringes allow the instrument to control the flow according to a specific protocol.

Secondly, air bubbles on the optical detection area disturb the measurement. Thus, the cartridge includes an air bubble removal mechanism, which allows to detect air bubbles in the liquid and to redirect them to the bypass waste by switching an on-cartridge valve.

Finally, the cartridge is designed for low-cost replication with fast prototyping such as micromilling or 3D printing for small series and injection molding for larger lot sizes.

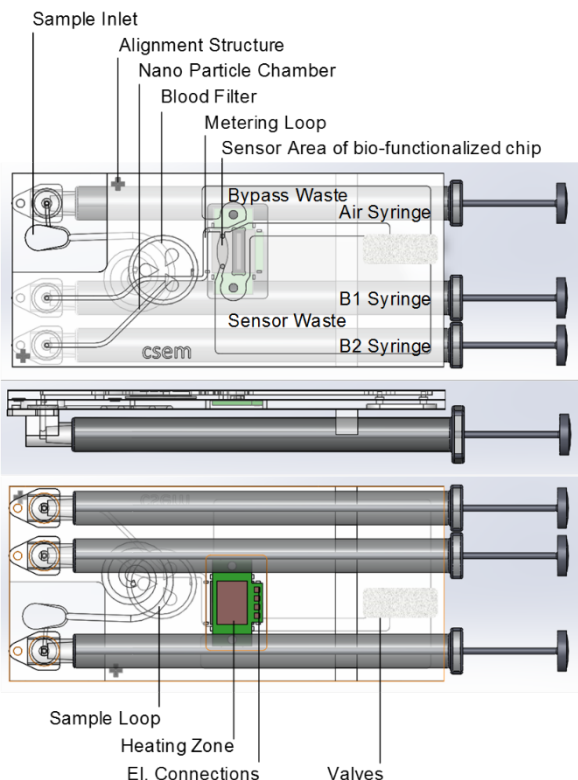


Figure 2: CAD drawing of the analysis cartridge, where whole blood is separated to blood plasma and eventually analyzed for specific proteins using a bio-functionalized chip based Mach Zehnder Interferometer.

Future work will involve the manufacturing and testing the microfluidic cartridge. Furthermore a breadboard setup will be developed to control the complete fluid handling by actuating the syringes and switching the valves which eventually will lead to the integrated PoC device. Other project partners will focus on the bio-functionalization and optimization of the optical chip.

This work was supported by the Swiss federation, MCCS Micro Center Central Switzerland, and the European Commission (H2020-732309 BIOCDx). CSEM thanks them for their support.

[1] <http://biocdx.eu/>

# Indirect Flow-rate-metering System for a Dispensing Application

J. Goldowsky, N. Schmid, V. Revol

Metering in dispensing applications is a challenging field, which requires often application customized solutions due to incompatibilities of the sensors with the dispensed liquids. Some reoccurring problems are aggressive liquids that would damage the sensor, sterile liquids while the sensor cannot be sterilized, or media that can clog the sensor channels. Hence, CSEM is exploring novel techniques of metering liquids in contact-less manners. While a controlled pressure-driven approach has been described earlier<sup>[1]</sup>, here an approach is described utilizing the balancing flow of gas into an arbitrary stiff container from which liquid is dispensed. One major advantage of this technique is that the sensor output is fully independent of the liquid dispensed and therefore the system does not have to be calibrated for the liquid in use, cannot be damaged by or contaminate the liquid as it is not in contact. Dispensing volumes down to 4  $\mu\text{l}$  have been tested and the technologies bear the possibilities to decrease this volume by factors, when scaling the internal volumes of the dispensing apparatus.

There are in general three types of systems in physics, isolated, closed and open systems. While isolated systems do not allow the exchange of mass and energy, closed systems can exchange energy, and open systems energy and mass with its surroundings. When a small volume is dispensed from a containment the closed gas phase system will respond with a pressure drop. This has been shown to be usable for metering applications<sup>[1]</sup>.

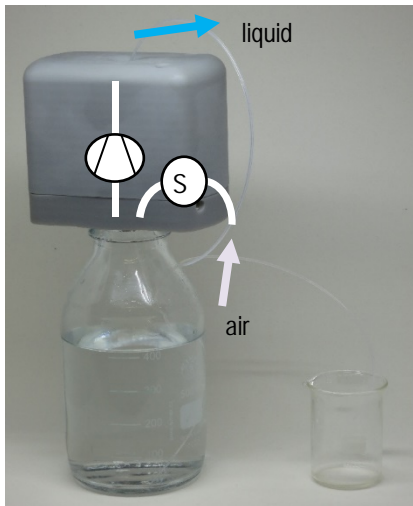


Figure 1: Bottle with integrated pump and flow-rate-sensor.

Within an open gas phase system (Figure 1), a slight pressure drop induces an air flow to restore pressure equilibrium between the system and its surroundings. By inserting a flow sensor into this gas flow path, information can be obtained related to the dispensed volume, the encapsulated gas volume and thereby the fill-level of the containment.

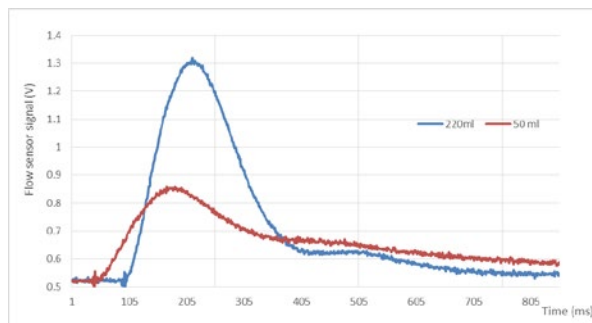


Figure 2: Flow-rate signal depending on filling level (250 ml bottle).

<sup>[1]</sup> J. Goldowsky, et al., "Sequential Actuation of Fluids for a Food Quality Monitoring System", CSEM Scientific & Technical Report (2015), 48.

The dependency of the sensor signal from the fill-level of the bottle is shown in Figure 2. As one can see, the peak value of inflow into the containment varies with its fill level. Additionally, for smaller fill-levels (i.e. greater gas volumes) the time to reach equilibrium to the surroundings is greater. However, as one would expect, the integral value of the sensor system is independent from the fill level and only dependent on the dispensed liquid volume.

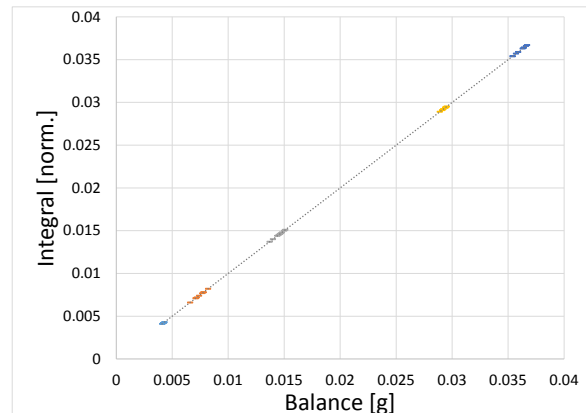


Figure 3: Air flow measurement (by sensor signal integration and normalized to weight scale measurement) when dispensing 4-40  $\mu\text{l}$  from a containment with a gas volume of 100 ml compared to high precision weight scale measurement. The colors represent (1, 2, 4, 8, and 10 strokes of the pump).

Figure 3 shows measurement results obtained by integration of the flow-sensor signal lasting from the moment of dispensing until the system reaches a steady state. It can be seen that the variance of the pump is much greater than the measurement error of the indirect flow metering sensor. As this sensor application is only dependent on the properties of the inflowing gas it can be of great value in all applications where a sensor in contact to the medium is problematic. Additionally, utilizing this measurement approach, no calibration of the sensor to the dispensing liquids is required.

Ongoing work is the comparison of the closed and open system approaches for small volume dispensing (nano-liter to micro-liter range).

This work was supported by the Swiss federation and MCCS Micro Center Central Switzerland. CSEM thanks them for their support.

# Zero Gravity Fluidic Feeding System

S. Berchtold, J. Goldowsy, K. Krasnopouloski, C. Giger •, F. Ille •, V. Revol, H. F. Knapp, M. Egli •

In this project a microfluidic feeding system for intervertebral disc (IVD) degeneration model in zero gravity is developed. The experimental setup will allow deeper insight into mechanical loading effects on degenerating IVDs. The model will be of interest for research groups, companies developing IVD replacement products and could provide knowledge for long-duration space mission like the one to Mars.

Age related lower back pain due to intervertebral disc (IVD) degeneration is developing into a considerable economic and societal burden. Astronauts experience accelerated disc degeneration induced by mechanical unloading during space flight. Mechanical unloading by simulated microgravity to isolated bovine IVDs represents a new model to investigate degeneration processes.

Mechanical unloading can be achieved by using Random Positioning Machines (RPMs), known to simulate microgravity through the principle of gravity vector averaging. This procedure has demonstrated good correlation to space experiments on several mammalian cell types already. A newly developed bioreactor that fits inside an incubator on the RPM ensures stable cultivation conditions for isolated IVDs. In order to mimic physiological conditions, the reactor features a mechanical loading system that induces different loading/unloading pattern. To ensure stable nutrition, a fluidic system for medium exchange was incorporated (Figure 1).

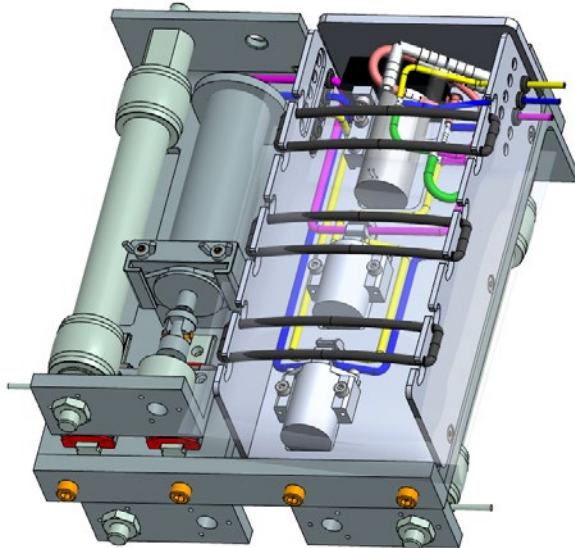


Figure 1: CAD model of fluidic feeding system including three mechanical loading systems.

Three mechanical loading systems with IVDs and the fluidic system can be mounted into the incubator. Also medium and waste container have to be incorporated to ensure a few days of continuous testing. To ensure biocompatibility the integrated

materials in the fluidic feeding system in contact with the liquid are all autoclavable. A small peristaltic pump is used to transport the standard medium to the IVDs.

The valves incorporated in the fluidic system can be used to feed every IVD individually with the needed medium during the test duration. This ensures stable conditions for the IVDs.



Figure 2: Front view of experimental setup placed into incubator.

The experimental setup (Figure 2) will allow deeper insights into mechanical loading effect on degenerating IVDs. Its use will provide valuable knowledge for physiotherapy, rehabilitation and preventive medicine. This tool will be of interest for research groups mainly but may also serve as test bed for IVD replacement product development by companies. It will also be interesting for space agencies concerning the health of astronauts when sending them out for long-duration space mission like the one to Mars.

This work was supported by the Swiss federation and MCCS Micro Center Central Switzerland. CSEM thanks them for their support.

• HSLU Lucerne University of Applied Sciences and Arts, CC Bioscience and Medical Engineering

# Bringing Function to Surfaces with Modular Photo Polymerizable Chemistries

H. Chai-Gao, L. Mühlbach, S. Generelli

CSEM's patented linker polymer OptoDex® and related surface functionalization technologies cover a large scope of applications. A series of photolinkers based on the organic polymer, are developed. As a complementary technology, organic polymer-based linking polymer are resistant to the biodegradation and maintains the advantages of OptoDex® and increase the strength, hydrophilicity, lubricity and stability of coating, thereby to expand the applications of the technology.

OptoDex technology is a uniform and well-developed platform for surface bioengineering. Photolinker polymers serve to immobilize probe (bio-) molecules on material surfaces. Light activation of photolinker polymers leads to the generation of highly reactive intermediates, in particular photogenerated carbenes, which form covalent bonds with (bio)molecules on any type of material. However OptoDex still could not satisfy for some kinds of material surface coating, e.g., Teflon, medical implant devices, catheters and textiles, because of its degradable polysaccharides chain. Two novel organic polymer-based non-degradable photolinker polymers (OptoBOD and OptoPEG) are considered to develop. It will maintain the advantages of OptoDex and increase the strength, hydrophilicity, lubricity and stability of coating, thereby to expand the applications of the technology.

The photopolymerizable chemistries using ultraviolet light at a 350 nm wavelength differ from other surface bioengineering approaches with regard to:

- the unique chemistry and its versatility.
- the technological flexibility allowing many differing applications in the fields of biomedical and material science.
- beneficial overall cost projections.

In this study, two organic polymers, polyethylenimine (BOD) and polyethylene glycol (PEG), were selected to synthesize photolinker polymers, respectively. Polyethylenimine (BOD) finds many successes in the field of surface coating, CO<sub>2</sub> capturing and polymeric transfection due to its high adhesion and adsorption, high cationic and high reactivity. Polyethylene glycol (PEG) is a polyether compound with widely applications from industrial manufacturing to medicine.

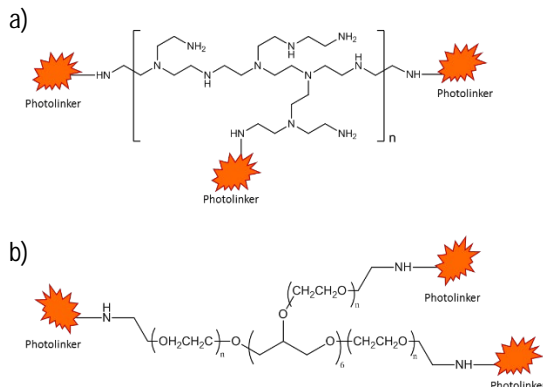


Figure 1: Schematic of molecular structure. The red-labelled groups (TRIMID) process the photo-reactive function. a) OptoBOD®, a polyethylenimine-based photolinker polymer; b) OptoPEG, a polyethylene glycol-based photolinker polymer.

Characterization of photolinkers includes the determination of photoreactivity, binding efficiency, biocompatibility, surface property and stability. The UV spectra of OptoBOD or OptoPEG are recorded before and after irradiation to detect the

photoreactivity, respectively. The decreasing of specific adsorption at 365 nm indicated that the polymer labelled with photoreactive groups could be active by UV light, thereby generate carbene radicals for covalent crosslinking (Figure 2).

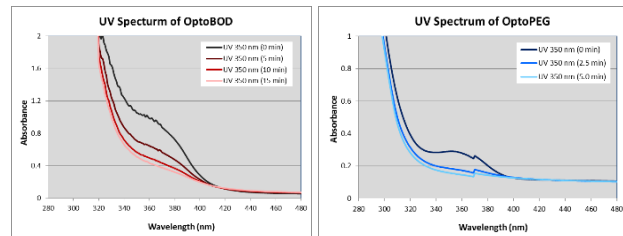


Figure 2: The UV spectra of OptoBOD (left) and OptoPEG (right) before and after irradiation, decreasing the adsorption at 365 nm where the specific wavelength of photoreactive groups is.

The binding efficiency and biocompatibility of photolinker polymers were evaluated by two tests: i) Photoimmobilization of peroxidase on polystyrene (microtiter plate) and determination of remained enzymatic activity; ii) Photoimmobilization of monoclonal anti-peroxidase antibody onto polystyrene (microtiter plate), formation of immuno-complex by binding of peroxidase, and determination of enzymatic activity. The results of both tests conclude that the light-dependent covalent binding of biomolecules works well and remains biological activity of immobilized molecules. Obviously, the higher cation contained in the photolinker polymer, the higher background appears because of the enriched positive charges on the surfaces. (Figure 3).

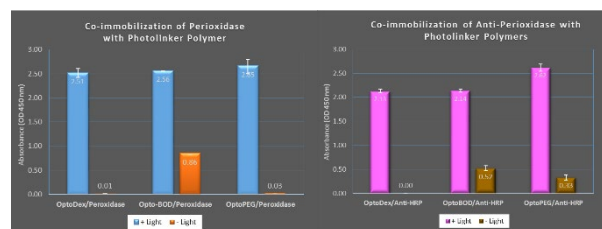


Figure 3: Photoimmobilization of peroxidase (left) or anti-peroxidase (right) on polystyrene (microtiter plate) and determination of remained enzymatic activity directly or after immuno-complex formation. Set-up non-irradiated samples as controls.

The next works will be to characterize the hydrophilicity and lubricity of material surfaces coated with photolinker polymers and evaluate the stability of coating.

# Online Monitoring of Antibiotics in Treated Waste Water Matrix

H. Chai-Gao, S. Cattaneo

This work shows that detection and quantification of antibiotics residues in waste water is feasible using the waveguide-interrogated optical biosensor (WIOS) platform. The platform allows robust, fast and specific contaminant analytics at low cost. Furthermore, considerable efforts are made to develop antibiotics assays which are compatible with automated fluidics in treated waste water matrices. Towards this end, the assay technologies rely on covalently bonded, multicomponent sensor arrays which allow repetitive array regeneration.

Antibiotics are among the most successful group of pharmaceuticals used for human and veterinary therapy. However, large amounts of antibiotics are released into municipal wastewater due to incomplete metabolism in humans or due to disposal of unused antibiotics, which finally find their ways into different natural environmental compartments. Once antibiotics enter the ecosystems, they can affect the ecological function of the water ecosystem. Thus, concerns have been raised about the potential impact of antibiotic remnants in the aquatic environment. Apart from chemical pollution caused by antibiotics themselves, the use of antibiotics may induce the development of antibiotic resistant bacteria (ARB) and antibiotic resistant genes (ARGs), which comprise health risks to humans and animals. Reliable online monitoring of antibiotic residues in the final effluents of wastewater treatment plants can help to evaluate the success of antibiotic treatments and to reduce a serious threat to global public health.

Reliable online detection of several antibiotics simultaneously in treated waste water needs a system with the following characteristics:

- Sensitivities within the regulatory scope, and time to result of less than 1 hour.
- Cost efficiency concerning instrumentation as well as consumables.
- Extremely user-friendly, featuring a high degree of automation and operation autonomy combined with robustness of operation. The detection platform has to be operated by personnel not specially trained in executing bioassays.

The wavelength-interrogated optical sensing platform (WIOS) developed by CSEM could fulfil such requirements. The sensitivity of the instrument was shown to be below  $10^{-6}$  refractive index units for bulk refractometry and the limit of detection for the adsorption of small molecules corresponded to a surface coverage of  $0.3 \text{ pg/mm}^2$ . A further advantage is the possibility to measure eight channels (pads) simultaneously, allowing the parallel detection of several antibiotics (Figure 1).

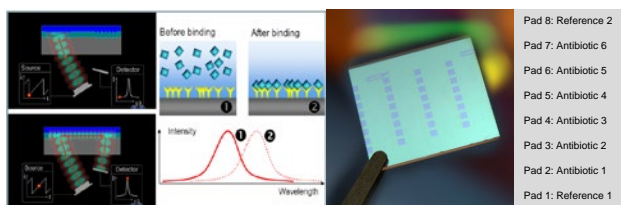


Figure 1: WIOS principle and chip layout.

In this study, we focused on developing methods to accurately determine antibiotics in pure water and treated waste water. Diclofenac, a nonsteroidal anti-inflammatory drug, was selected as an example to set up the competitive immunoassay assay (Figure 2). The biosensing surface plays a crucial role and the surface functionalization technology of CSEM can offer a unique

covalent binding of hapten-conjugate (with antibiotic) sensor surfaces. The advantages are, (i) robust immobilization via multiple photobonding sites (mesh-like linking), (ii) well designable surface properties (e.g., density of capture molecules) (iii) suppression of non-specific binding due to the dextran basis of both, capture and cross-linker (OptoDex™) molecules and (iv) the range and sensitivity of measurement are designable.

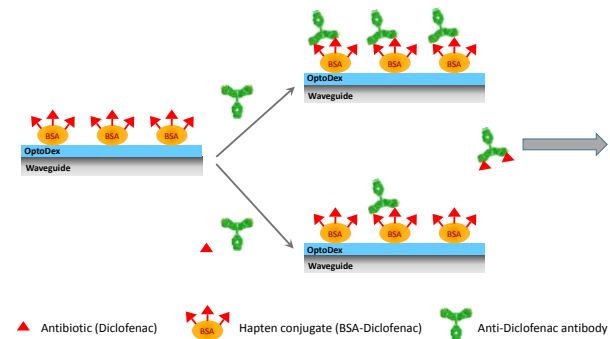


Figure 2: Schematic of the bioassay principle (competitive immuno-assay).

To test the performance of the immunoassays and of the WIOS detection platform, diclofenac was spiked into pure water or treated waste water matrix (provided by Eawag) at indicated concentrations, respectively. Figure 3 shows the obtained dose response curves.

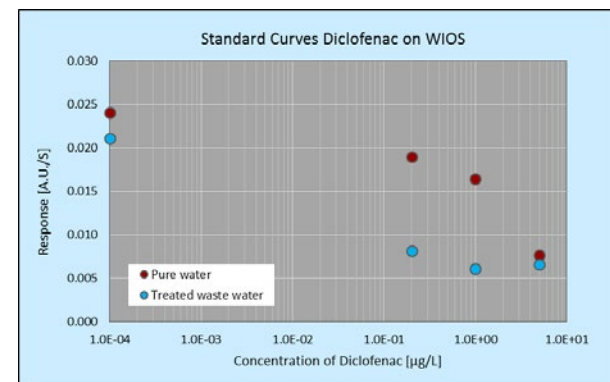


Figure 3: Diclofenac dose response curves, in pure water (red) and in treated waste water (blue). In general, the sample contains 90% of pure water or treated waste water and 10% of concentrated PBS buffer (10x).

We can summarize that the system of online monitoring antibiotics in treated waste water has following properties:

- Label-free sensing with WIOS.
- Competitive immunoassay with detection limit of  $0.2 \mu\text{g/l}$ .
- Available for multi-components analyses.

# Glucose Monitoring in *in-vitro* Cell Culture

H. Chai-Gao, M. Viviani, L. Mühlbach, R. Junozovic, S. Generelli

Screen-printed glucose sensors are in general used as single-test devices. Within this work we tested the possibility of use of the same type of technology for continuous monitoring of complex media as cell culture with the same low-cost sensors, without adding on costs of the fabrication. The sensors can be used up to 24 hours after contact with media, providing a potential interesting solution for monitoring of complex media with a low-cost, disposable solution.

CSEM's in house screen-printed disposable sensors could be the solution to an easy and cost-effective glucose monitoring in bioprocesses. The target we are aiming at is to develop sensors that are extremely simple and cost-effective to produce, and optimize their long-term response when used for continuous monitoring. The characterization and long-term continuous performance of the sensors were investigated in cell culture medium DMEM (Dulbecco's Modified Eagle Medium) supplemented with 10% FCS (Fetal Calf Serum). Two different functionalization protocols (glutaraldehyde-induced polymerization and photo-polymerizable dextran-based polymer) for the low-cost glucose sensors were applied. The two functionalization protocols used two different matrices for the immobilization of the enzyme, one based on glutaraldehyde-induced polymerization (GS), another using photo-polymerizable dextran-based polymer (GX).

The goal of the carried out stability tests presented here is to achieve long-term stability of glucose sensors in order to monitor bioprocesses. Classical bioprocesses accomplished with the protein expression hosts mammalian cells, bacterial cells and yeast are performed on a range of times spanning from 2 to 20 days, typically. The longest lasting processes to assess sensor stability are carried out with mammalian cells. The temperature for growth is typically 37°C and the process duration is up to 3 weeks as the cells duplicate once in 24 h typically. This process was chosen to test (long-term and continuous) performance of the CSEM glucose sensors.

Each of these processes uses different media, which represents a varying sample matrix for a biosensor. These sample media are complex in composition and will determine the background signal for the biosensor. For each biosensor, the measurement in a different sample matrix has to be validated.

The results showed that both glucose sensor sets have a linear range in DMEM + 10% FCS in the range of 0.2 mM to 2 mM glucose, with sensitivity up to >5 mM (see Figure 1). Similar results have been obtained with other cell culture media, such as RPMI or other custom-made cell culture media, formulated for *in-vitro* tissue model maintenance.

The storage lifetime tested was limited to 3 months. Sensors present the same sensitivity and linear range after a storage time (4°C, dark, under vacuum) of 85 days, which indicates the possibility of longer storage times (Figure 1).

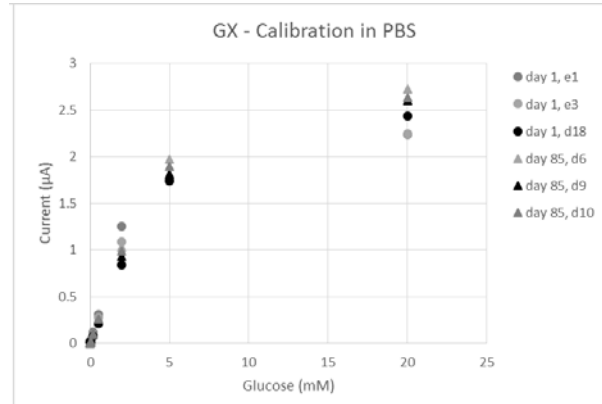


Figure 1: Calibration curves in PBS (Phosphate-buffered saline) of GX sensors at day 1 (dots) and day 85 (triangles) of storage.

The GS series showed a significant drop of sensitivity within 3 h of immersion in cell culture medium (37°C, 5% CO<sub>2</sub>, H<sub>2</sub>O-saturated). The GX series maintained its sensitivity until 24 h of continuous contact with cell culture medium (37°C, 5% CO<sub>2</sub>, H<sub>2</sub>O-saturated), gaining a factor 8 in lifetime. The functional lifetime may be improved by further optimization, packaging and screening, at the cost - however - of a more complicated, multi steps and costly fabrication technique. Within the present study the costs of fabrication have been kept to a minimum, to provide an interesting solution for monitoring of complex media with a low-cost, disposable solution.



Figure 2: The sensors, based on screen printing, are designed and fabricated to be low cost. The optimization performed in this work has the aim to optimize the ratio of cost to functional lifetime.

# AUTOX—Automated Fluidic Handling System for *in-vitro* Tissue Model Monitoring

D. Schmid, M. Viviani, S. Generelli, N. Tscharner, E. Accastelli •

*Multi-Organ-Chip (MOC) and in-vitro tissue model monitoring technologies are alternatives to animal testing in pharmaceutical, cosmetics and chemical industries. An important performance criterion is the ability to measure in-process controls online. CSEM developed AUTOX, an at-line monitoring system for cell culture handling. The solution addresses a strong market need to optimize pharma drug discovery process with better ROI and will contribute to the development of know-how and competencies in Europe to drive regenerative therapies in the future.*

A shift from traditional bioprocesses in large scale steel bioreactors to disposable cell culture platforms occurred in the last decades. Novel technologies such as individualized cell therapy or drug screening with body-on-a-chip systems have emerged. This trend has influenced bioprocess development; therefore innovative analytical solutions to control bioprocesses are required<sup>[1]</sup>. Process parameter monitoring is especially crucial for multi-organ chip platforms. Traditionally, repeated manual sample extraction has to be conducted from these platforms for offline analysis in different analytical instrument.

CSEM developed AUTOX, an at-line monitoring system, based on automated electrochemical sensing, enabled by an 8-channel amperometric/potentiometric monitoring system with pneumatic (pressure/vacuum) fluid flow control. A fluidic system allows for automated calibration, sample extraction, mixing (where needed), incubation and introduction of the liquid into the parallel multiparameter sensing unit. With CSEM's electrochemical sensors, monitoring of pH, glucose, lactate, LDH (lactated dehydrogenase), glutamate, ALT (alanine transaminase) and different ions (K, Na, ...) is possible. The versatile sensor and fluidics control unit allows for system extension and adaption (control of additional pumps, valves and external sensors).

The control unit ( $18 \times 20 \times 15 \text{ cm}^3$ ) can be connected to a host laptop and runs with a LabVIEW user control software. Its pneumatic system can supply up to 300 mbar pressurized air and -300 mbar vacuum suction and control 32 individual channels for latching or non-latching valves. The amperometric sensing unit feature a resolution of 0.3 nA at 0-10  $\mu\text{A}$  dynamic range or 30 nA at 0-1 mA (16-bit ADC).

The fluidic sample prep unit ( $5.5 \times 13 \times 2 \text{ cm}^3$ ) can process samples down to 200  $\mu\text{l}$  and perform calibration, dilution, mixing, measuring and cleaning functions. Up to 8 electrochemical sensors can be connected in parallel for potentiometric and amperometric measurements.

## Main system specifications

- +/-300 mbar pressure/vacuum supply.
- 32 individual channels for valves control.
- 8 individual channels for amperometric measurements.

• Tissuse GmbH, Berlin (D)

[1] M. Rios, "Analytics for Modern Bioprocess Development", BioProcess International, March 2014,

- 0-1'000  $\mu\text{l}/\text{min}$  flow rates.
- Integrated calibration, dilution, mixing, incubation, measurement and cleaning functions.
- Glucose, lactate, enzymes, ions and pH monitoring.
- Quantitative results in <2 minutes.

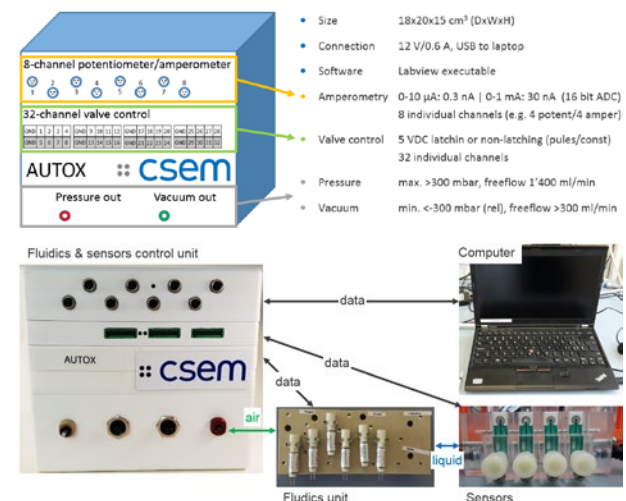


Figure 1: (Top) Schematic representation of the automated fluidics and sensing control system with specifications; (Bottom) Realized all-in-one demonstrator control system and schematic connection diagram.

The control of bioprocesses is crucial in order to achieve optimized production, product folding and/or secretion from fully viable cells which results in enhanced product quality and higher product titers. CSEM's small-scale analytical platform is a step towards an inexpensive monitoring technology fulfilling the future industrial need.

This work has been funded within the H2020 gateone-project in the Information and Communications Technologies call of the European Commission (Project ID: 644856). The goal of gateone is to lower the adoption barrier of bio related technologies thanks to smart systems, and the developed system will further contribute to the value proposition of existing cell culture handling platforms by demonstrating the benefits of process automation.

# Diagnostics in Non-invasive Body Fluids

S. Paoletti, S. Generelli

*Health self-monitoring is the future of medical devices. With the aging of the population and the raising of incidence of chronic illnesses the issue of giving tools to populations at risk that insure a comfortable and safe life, while maintaining a certain autonomy will be helping in maintaining a high quality of life.*

Today, most routine health assessment techniques rely on blood-based analysis, involving invasive tools to extract, prepare and analyze samples. Over the last decade there has been a move towards the use of “freely accessible” body fluids like saliva, tears, urine, breath, and sweat. However, even though several tests based on these body fluids are already accepted and implemented in clinical test, there is a lack of technologies adapted to bring non-invasive health monitoring to a larger panel of users. Furthermore, the panel of recognized health markers present in these matrices is still limited.

At CSEM development of different sensors and solutions for non-invasive monitoring is ongoing since several years, with the aim to provide simple and robust solutions for non-invasive point of care diagnostics and therapy monitoring devices. Big part of our work is focused on the usability of the new device:

- By untrained personnel.
- In clinically challenging situations – from individuals from whom sampling blood would be difficult to perform.
- In remote areas.



Figure 1: Miniaturized electronics and wireless communication are interfacing with low-cost printed sensors.

CSEM has been developing different technologies that could be used on a modular approach for diagnostics:

- a) Sample collection and preparation: based on different microfluidics designs, that allow to collect, sample, load and process different body fluids as blood, urine, saliva and sweat. Simple pre-concentration solutions have been successfully tested. One example is illustrated in the present report<sup>[1]</sup>.
- b) Detection unit: according to specific targets and requirements, CSEM developed optical, fluorescent or electrochemical sensors that are integrated in different cost-effective solutions. An

example of transducer is described in<sup>[2]</sup>, and an example of compact custom-made fluorescent reader is given in<sup>[3]</sup>.

c) Data acquisition, storage and exchange: together with the detection unit, CSEM is working also at the necessary electronics, power requirement and data management tools to realize a full integrated system.

As mentioned, a limited number of health assessment tests based on biomarkers found in non-invasive body fluids is already available and clinically recognized as valid. However, in general relatively limited data are available on the study of the relationship of several biomarkers present in these body fluids and their metabolic relevance. This is especially true for sweat, where a very limited number of studies can be found on the thorough tests of the clinical relevance of biomarkers. Additionally sweat could be an ideal candidate for completely non-invasive health monitoring self-check.

The lack of data can be partially explained by the lack of adequate technical solutions to ensure a correct and simple collection of sample and its subsequent analysis. CSEM works at the development of more sensitive, easier to use simpler systems, or as well novel integration concepts to bring new tools to be able to test and explore new possibilities in the health domain. Some examples are the sweat monitoring device (disposable patch depicted in Figure 2) or the novel sensing system based on nano-porous membranes.

Always based on the principle of the exploration of new technologies, CSEM is in the process of testing some tools and developing processes for the extraction and fractionation of exosomes from complex matrices<sup>[4]</sup>.

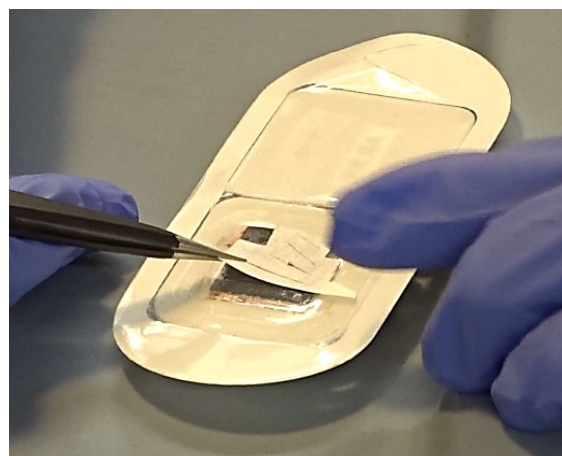


Figure 2: Disposable patch for sweat ions monitoring.

<sup>[1]</sup> D. Migliorelli, *et al.*, “ELIME Assay for Fast Analysis in Urine”, in this report page 22.

<sup>[2]</sup> D. Schmid, *et al.*, “Towards Sweat-rate Monitoring with Wearable Sensors”, in this report, page 69.

<sup>[3]</sup> C. Hofer, *et al.*, “FluSiGate—Optical pH Sensor for Non-invasive Wound Monitoring”, in this report, page 70.

<sup>[4]</sup> L. Burr, *et al.*, “ExoPro—Exosomes Profiling and Characterisation”, in this report, page 22.

# ELIME Assay for Fast Analysis in Urine

D. Migliorelli, H. Chai-Gao, L. Mühlbach, R. Junuzovic, S. Generelli

In the recent years the efforts and investments in researching rapid, 'point-of-care' diagnostics are significantly increased. Urine has been identified as a favourable alternative biological sample due to the ease of obtaining samples from patients, the ease of laboratory handling and processing, and the lower risk of nosocomial transmission to healthcare and laboratory workers. We report on a process for urine diagnostics using Screen Printed Electrodes (SPEs) in combination with functionalized magnetic particles.

Globally, people living with HIV are 26 times more likely to develop tuberculosis (TB) disease than those who are HIV-negative. Diagnosis of HIV-associated TB (HIV-TB) remains challenging due to non-specific clinical features, early dissemination beyond the lungs, the relatively low mycobacterial burden within sputum samples, and a substantial proportion of these patients have extrapulmonary TB without pulmonary TB. This makes the urine-based testing a promising diagnostic tool, since, compared with the sputum, it is easy to collect and store and lack the infection control risks associated to the sputum-testing.

Tests based on the detection of mycobacterial lipoarabinomannan (LAM) antigen in urine have emerged as potential point-of-care-tests for tuberculosis. This antigen is predominately present only in people with active TB disease. There are already some strips commercially available, based on the lateral flow immunoassay principle, but they still lack in sensitivity.

CSEM has developed an Enzyme-Linked-Immuno-Magnetic-Electrochemical (ELIME) assay, for saliva diagnostics using Screen Printed Electrodes (SPEs) (Figure 1).

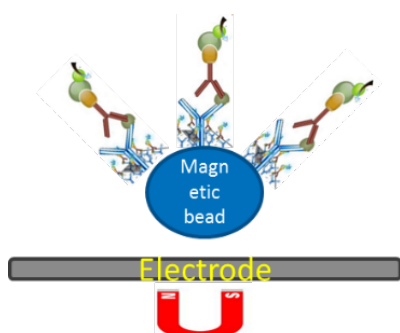


Figure 1: Scheme of the ELIME immunoassay where the magnetic beads are used as a support and the screen printed electrodes as transducer.

The process consists mainly of two steps: a 'pre-concentration' step in order to collect the biomarkers of interest in a simple preparation procedure using functionalized magnetic particles, and of a 'detection' step, where the SPEs will be used as the platform to perform and quantify sandwich-type immunoassay. The two 'pre-concentration' and 'detection' steps can be used in concomitance with each other, or used separately. For example, the 'pre-concentration' step may be used as a pre-clearance and 'pre-concentration' step for the subsequent detection using commercially available ELISA detection kits or lateral flow immuno-chromatographic assays.

A similar approach could be used for diagnostics on other body fluids as sputum and urine. On this purpose CSEM has developed an ELIME assay for the detection of LAM in urine.

Shortly the magnetic beads have been coated with the capture anti-LAM antibody and the immuno-activity of the functionalized magnetic beads characterized by sandwich immunoassay.

The capacity of the antibody-coated magnetic beads to pre-concentrate the samples was tested. Free LAM was spiked into urine matrix; subsequently the detection limit of ELISA assays were determined with and without the 'pre-concentration' step. Results of this test are reported in Figure 2.

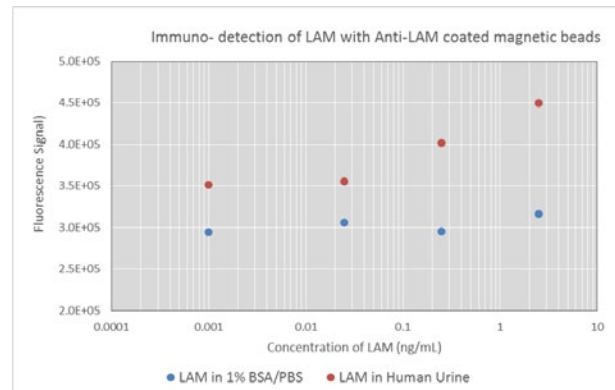


Figure 2: ELISA detection of spiked LAM with the use of 'pre-concentration' step, using anti-LAM antibody functionalized magnetic beads (red dots) and without pre-concentration (blue dots).

Figure 2 indicates that anti-LAM capture antibody coated magnetic beads can lower the LAM detection limit in human urine down to 0.025 ng/ml.

According to the results obtained with the optical reader, a preliminary test has been done in order to evaluate the screen printed electrodes as detection platform for the immunoassay described above (Figure 3).

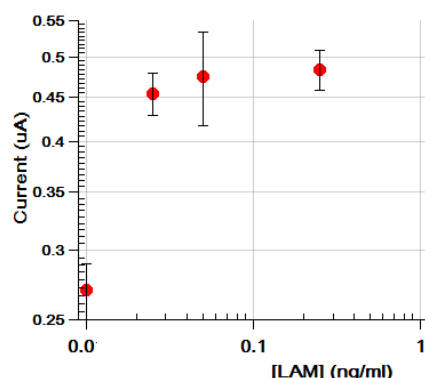


Figure 3: ELIME amperometric measurements of different concentrations of LAM in urine.

The system is certainly able to detect the presence of LAM in saliva with potentially lower detection limit than the optical ELISA system. To achieve a quantification of LAM needs of further optimizations.

# Towards Sweat-rate Monitoring with Wearable Sensors

D. Schmid, S. Generelli, F. Pereira, M. Viviani, R. Junuzovic

Sweat plays a major role in our body's ability to regulate its temperature. Sweat rate measurements are necessary to have a clear understanding of the hydration state of a person and set up a personalized hydration plan. We report on a new method for on-body sweat-rate measurements based on calorimetric forced evaporation, featuring a robust, simple and reliable design. Future applications include sports monitoring, work safety, and medical monitoring.

On-body vital signs monitoring with dry electronic and wet electro-chemical sensors are key technologies of CSEM and biochemical sweat analysis is seen as a future game-changer in the wearable market. Biochemical sweat sensors provide information about chemical composition and analyte concentration, but for many applications the absolute amount of an analyte is needed. This requires a measurement of the sweat volume or sweat rate. Sweat rate is also the key marker for hydration monitoring, which is more and more requested by sport, professional performance related activities, and rehabilitation.

For real-time sweat-rate measurement, there is yet no commercial reliable and accurate solution available<sup>[1]</sup>. The most widely accepted measurement method for the assessment of individual sweat rate of athletes is still based on the loss of body mass that occurs over a define period of time<sup>[2]</sup>. All of the current approaches for sweat rate monitoring lack either reliability and robustness, real-time readout capability or simplicity – drawbacks that so far hindered successful integration into commercial wearable monitors.

To circumvent this problems, CSEM started the development of a sweat-rate sensor that works reliably also during intense movement and at high relative humidity (Figure 1).

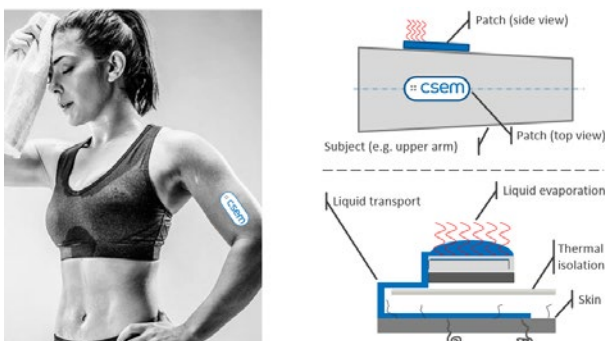


Figure 1: Left: visualization of sweat rate sensor as skin patch. Right: working principle with sweat collection and calorimetric sweat rate measurement by forced evaporation.

CSEM's novel approach for sweat rate measurements is based on continuous calorimetric liquid volume measurement by forced evaporation (patent pending). The method was originally developed for measurement of small liquid volumes in lab

<sup>[1]</sup> M. Villiger, R. Stoop, T. Vetsch, E. Hohenauer, M. Pini, P. Clarys, F. Pereira, R. Clijsen, "Evaluation and review of body fluids saliva, sweat and tear compared to biochemical hydration assessment markers within blood and urine", European Journal of Clinical Nutrition (2017), 1-8.

automation applications. For sweat rate measurements, sweat is collected at the skin surface and passively transported to an evaporation stage. The sweat rate can be calculated from the electrical power needed for evaporation and the known thermal properties of sweat. With this approach, dynamic changes in the sweat rate can be monitored more accurately due to the fact that sweat is continuously evaporated and thus removed (no reservoir needed). The sensor principle has been demonstrated with a lab setup using artificial sweat (Figure 2). Energy consumption has been shown to be acceptable with an efficient heating concept and for a limited sweat collection area (1 cm<sup>2</sup>)<sup>[2]</sup>.

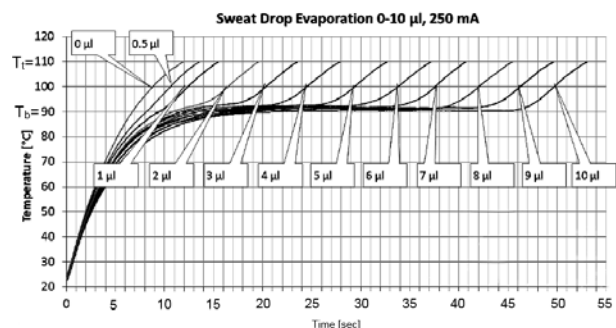


Figure 2: Lab setup demonstration of calorimetric sweat volume measurement based on forced evaporation. A precision of 1.4% CV in the range of 0-10 μl was obtained.

Next, the concept will be adapted to develop a wearable sweat rate sensor in a robust patch with passive fluidics that can be directly attached to the skin, and integrated electronics based on CSEM's well-proven electronics platforms for sensor control and wireless communication.

In combination with biochemical sweat analysis sensors (e.g., pH, glucose and lactate) this sensor will allow a more accurate understanding of the body chemistry and hydration state of a person. Robust and reliable wearable sweat sensors are expected to be used in sports (training optimization, efficient hydration), work safety (fire fighters, workers in hot environment) and medical healthcare (elderly monitoring for sufficient hydration, diabetes early indicator for hypoglycemia). The sensor can however be applied also in other fields, where cost-efficient, highly precise and parallel measurements of small liquid volumes are required.

<sup>[2]</sup> L. F. Aragon-Vargas, "Workshop: Sweat rate measurement in athletes", in proceedings, XXXI FIMS Sports Medicine World Congress, San Juan, Puerto Rico, May 2010.

# FlusiGate—Optical pH Sensor for Non-invasive Wound Monitoring

C. Hofer, S. Cattaneo, L. Boesel •, A. Osypova •, G. Panzarasa •

The pH value is a clinically relevant factor to assess and monitor the healing progression of wounds. Together with our project partner Empa, we developed a solution for non-invasive wound monitoring, consisting of wound pads with integrated pH-sensitive fluorescent spots, and a compact, stand-alone reader for high-sensitivity fluorescence intensity measurements. The portable size, low cost, and ease of use of the reader show potential for a variety of applications based on monitoring fluorescence intensity.

The aim of the project FlusiGate was to develop an optical pH sensor for the non-invasive monitoring of the healing process in chronic wounds. The system consists of pH-sensitive fluorescent spots integrated in wound pads, developed by Empa, and a cost effective, hand-held fluorescence intensity reader developed by CSEM.

The pH value has been shown to be a crucial factor to determine the state of wounds. The relevant pH range for wound monitoring was identified between pH = 6 and 8. Within this range, wounds show a distinguishable pH profile depending on their healing status, allowing an early detection of acute and chronic wounds and a consequent adaptation of the wound treatment at an early stage. Various types of fluorescent pH sensors were developed by our partner Empa and were coupled to polymeric gel pads (Figure 1).

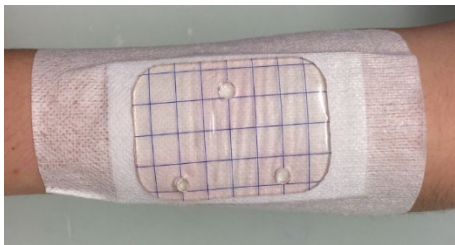


Figure 1: Polymeric wound pad with fluorescently labeled sensing spots developed by Empa.

The fluorescent response of the chemicals sensors was measured with a hand-held fluorescence intensity reader developed by CSEM (Figure 2).

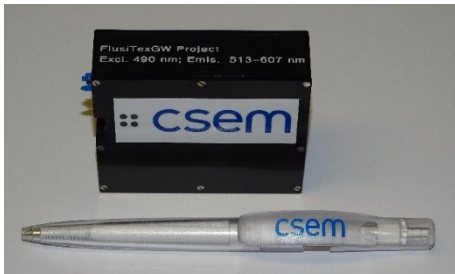


Figure 2: Compact, stand-alone sensor for real-time high-sensitivity fluorescence intensity measurements.

The prototype reader allows high-sensitivity fluorescence intensity measurements in reflection mode (epi-fluorescence configuration). A combination of a short-pass excitation filter, a dichroic mirror and a long-pass emission filter is used to separate the fluorescent signal from the excitation light. As a light source,

a cyan LED emitting at 490 nm was selected. The detection range was set to 510–610 nm, following Empa's requirements. A second photodiode is used as a reference to monitor the LED intensity and correct for possible fluctuations. The prototype was enclosed in a plastic housing (dimensions 75×60×22 mm) for easier handling and to shield it from ambient light.

The reader is connected to a laptop for instrument control, data collection and analysis. A LabVIEW graphical user interface (GUI) was developed for controlling the prototype and recording the fluorescence intensity. The GUI allows adjusting the LED intensity and the signal amplification, depending on the strength of the fluorescence emission from the sample. Furthermore the user can perform a reference measurement on the polymeric pad outside the sensing areas, to correct for possible background signals arising from scattering or auto-fluorescence from the polymeric pad.

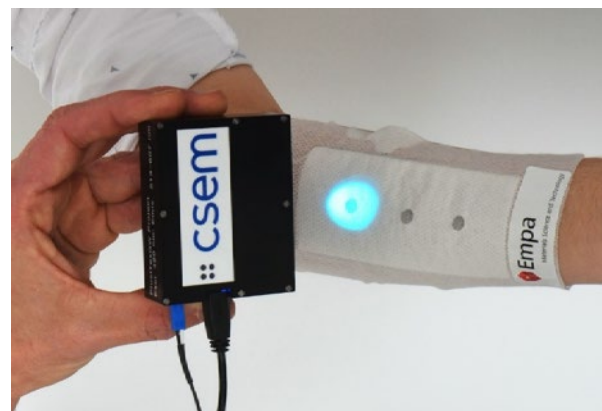


Figure 3: Complete FlusiGate system for optical pH monitoring on wound pads.

The performance of the prototype and the chemical sensors was evaluated in buffer solutions and artificial wound exudate. The performance of the CSEM prototype was essentially on par with high-end fluorescence systems, despite a considerably reduced size and cost, allowing accurate pH measurements in the range pH = 6–8.

Current applications of the FlusiGate system are in the field of wound monitoring and chemical sensing (pH, oxygen), but other applications in the nondestructive analysis of fluorescent probes (medical diagnostics, food analysis, anti-counterfeiting, etc.) can be envisaged.

The work was supported by Nano-Tera (projects FlusiTex and FlusiGate). We would like to thank them for their financial support.

• Empa St. Gallen

# Non-invasive Measurement of Oxygen and Carbon Dioxide in Microscope Biochamber

S. Heub, M. Jungo, R. Ischer, G. Weder, A. Grivel, R. Smajda, X. Bulliard, R. Pugin, M. Despont

Contactless gas sensing is essential for both monitoring and understanding a variety of phenomena from research to industry. CSEM has developed a new generation of non-invasive optical oxygen and carbon dioxide sensors showing high accuracy and precision in specific environments in the life sciences. The combination of their disposability or long-term use with a small footprint is of particular interest for incubation biochambers.

Oxygen ( $O_2$ ) and carbon dioxide ( $CO_2$ ) are involved wherever there is life. Monitoring of both gasses is critical for the study of biological processes. Optical sensor technologies enable non-invasive sensing as the reader is separated from the sensing part. One big challenge for gas sensing in the life sciences is related to the environmental conditions. They have to maintain efficiency and reliability over physiological conditions such as given temperature range, high humidity conditions, or salty solutions. By combining such sensors with miniaturized readers, it is possible to address the requirements of applications such as small biochambers. The CSEM has developed innovative biocompatible, and non-invasive optical gas sensor with integrated readers, providing an outstanding solution for  $O_2$  and  $CO_2$  monitoring for medicine.

CSEM's patented sensing technology consists of a thin mesoporous silica-based film that is functionalized with a sol-gel network encapsulating a luminescent-reactive dye. The high porosity of the films provides a high optical density and results in fast response time, high stability to aqueous solutions, and high sensitivity. These sensitive layers are printed onto the substrate in an automated procedure (Figure 1), and the process is adapted to industrialization for large-scale production. These sensors are biocompatible, sterilizable, and disposable although they can be used for long-term gas monitoring over several months.

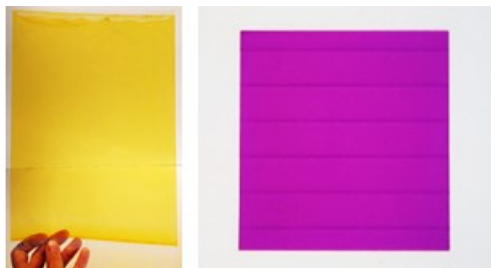


Figure 1:  $O_2$  sensor (yellow) printed by Slot Die, and  $CO_2$  sensor (purple) sensor printed by inkjet.

Sensors performances are summarized in Table 1. The oxygen sensors show a high accuracy of 0.1% and a precision better than 0.3% over the whole working range from 0% to 21%  $O_2$  concentration. They are stable in highly humid and liquid environments, and over a wide temperature range that typically suits applications in biology. CSEM's sensors meet all the requirements for a reliable local monitoring of gas concentration in small environments for biological applications.

Table 1: Performances of  $O_2$  and  $CO_2$  sensors in gas phase.

	Oxygen	Carbon dioxide
Optimal measuring range	0 – 21%	3 – 12%
Accuracy	0.1% at 2% $O_2$ -0.2% at 20.9% $O_2$	0.2% at 5% $CO_2$ 0.1% at 10% $CO_2$
Precision	≤ 0.3% at 2% $O_2$ ≤ 0.3% at 20.9% $O_2$	≤ 0.7% at 5% $CO_2$ ≤ 1% at 10% $CO_2$

Strong from the successful development of the microscope objective-like reader Demox<sup>[1]</sup>, CSEM has pushed further the challenge of miniaturized integration. The  $O_2$  and  $CO_2$  sensors can now be combined with other monitoring tools (e.g., temperature & humidity sensors) for the implementation of a small incubator on a microscope stage with a total control of environmental parameters (Figure 2). The luminescent measurement is performed using reflective mode and is achieved non-invasively through the wall of the biochamber, thus avoiding any contamination of the sample in the chamber. The source and reflected light are guided through an optical fiber from and to the integrated reader, limiting its footprint on the microscope area.

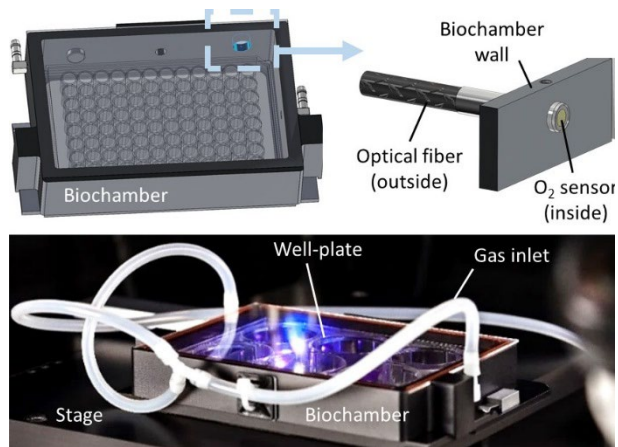


Figure 2: Integration of  $O_2$  sensing in a commercial product, a stage-top biochamber.

The gas sensors presented here have been developed to monitor  $O_2$  and  $CO_2$  in real time in a microscope stage-top biochamber, but they enable similar types of measurements for many other applications in life sciences. They can be used for example for monitoring in bioreactors, process control of food and beverages, or quality control of air and water. CSEM gas sensing solutions are highly customizable in terms of power supply, wireless communication, or e-reading on mobile devices.

<sup>[1]</sup> G. Weder, et al., "DEMOX - a Miniature Non-invasive Optical Oxygen Sensor", CSEM Scientific & Technical Report (2015), 47.

# Biofunctionalized Membranes for Monitoring Tissue Mechanical Properties

F. Sorba, A. Poulin •, M. Despont, H. Shea •, C. Martin-Olmos

CSEM is working in collaboration with EPFL to develop soft-MEMS based measurement platforms to study the mechanical properties of cell monolayers. Cell monolayers are recently in the spotlight for their use in studying the mechanical properties transition from single cell to tissue. For advancements in this field, a reliable and repeatable protocol to pattern a cell monolayer on soft thin elastomeric membranes has been established.

Discoveries in mechanobiology suggest that changes in cell mechanics contribute to the development of many diseases, like cardiomyopathies, glaucoma, premature aging and cancer<sup>[1]</sup>. There is an increasing demand in soft-MEMS based measurement platforms with high throughput and easy operation for this new field of science. A crucial part of this research deals with the need of more realistic *in-vitro* models mimicking the *in-vivo* physiological conditions and its integration within a measurement device. The materials used in the device should ideally be as soft as the cell layer to ensure accurate measurements. However, very soft substrates are known to hinder cell adhesion and proliferation. To overcome this, a biofunctionalization protocol to selectively grow a layer of cells on low stiffness substrates has been established. This method allows to have a uniform and repeatable layer of cells.

The current approach uses soft (30 kPa), thin (10 µm) suspended polydimethylsiloxane (PDMS) membrane. Generally, cells favour adherence to surfaces that are hydrophilic or contain functional groups such as – NH<sub>2</sub>. Therefore, the established protocol makes use of polydopamine-based functionalization of PDMS followed by a secondary reaction with biomolecules containing amine groups<sup>[2]</sup>.

First the polydopamine solution is incubated on top of the suspended elastomeric membrane. Then a Mylar mask is placed on the membrane and fibronectin solution, a well-known protein to promote cell adhesion, is incubated on top. After removing the mask and washing the surface, a pluronic solution is incubated to obtain an antifouling effect on the surface not functionalized with fibronectin. A schematic of the full protocol is showed in Figure 1.

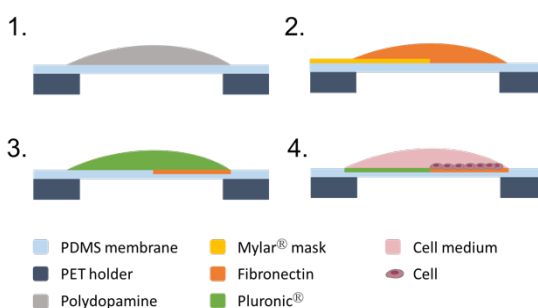


Figure 1: Schematic drawing of the protocol for selective covalent adhesion of cell on thin suspended PDMS membrane.

• Microsystems Space Technologies Laboratory, EPFL, Neuchâtel

<sup>[1]</sup> D. E. Jaalouk, J. Lammerding (2009), "Mechanotransduction gone awry", Nat Rev Mol Cell Biol 10(1): 63-73.

A first series of membranes have been functionalized using this protocol and Sarcoma Osteogenic (SaOS2) cells have been cultured to confluence (Figure 2). The selective adhesion of cells has been proven to be highly repeatable and stable over time. Cells could be cultured on these substrates for more than 1 week which is highly desirable to be able to monitor their properties over time.

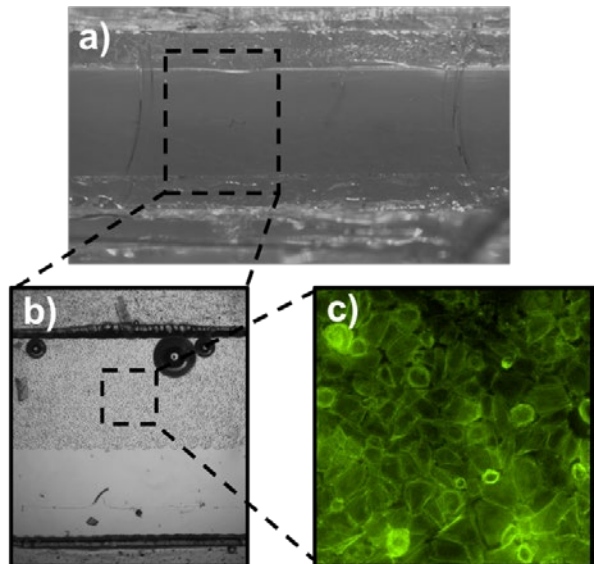


Figure 2: a) Soft membrane used for measurement of cell mechanical properties; b) Cells cultured on top of the membrane for 24 hours form a monolayer only in the selected region thanks to the patterning protocol; c) Fluorescence image of the actin filament forming the cell cytoskeleton shows that cells are well adhering on the surface.

Currently, the tests of the device are in progress together with the design of a method to calibrate the platform for stiffness measurement.

Thanks to the possibility to culture uniform monolayer of cells on very soft and thin substrates, the presented approach is very convenient to study the mechanical response of cells with soft-MEMS. Progress in this field has great potential to lead to better diagnosis and treatment of several pathologies.

Financial support by the Swiss National Science Foundation (SNF) is gratefully acknowledged (project No 205321\_153365).

<sup>[2]</sup> M. Perikamana, S. Kumar, et al., "Materials from mussel-inspired chemistry for cell and tissue engineering applications", Biomacromolecules 16.9 (2015): 2541-2555.

# Optical Fiber Biosensor for Wound Care Management

R. Smajda, G. Voirin, R. Ischer, M. Correvon, G. Dudnik

A system to deliver negative pressure therapy on patients suffering from diabetic foot ulcer and venous leg ulcer was developed and was tested in clinical environment on 15 patients for the monitoring of pH and temperature in wound and for the estimation of matrix metalloproteinase level in wound exudate.

For some chronic diseases, therapy could be better exploited if several parameters could be monitored to follow the evolution of the disease during the treatment at hospital or even better at home. The objective of the European project SWAN-iCare [1] was to develop a negative pressure therapy system equipped with sensors and actuators to be able to monitor patients and allow physician to remotely take action for the wellbeing of his patients. The system was developed to monitor patients with diabetic foot and venous leg ulcer. It was tested on several patients with three sensors, pH, temperature and Matrix Metalloproteinases (MMP).

The negative pressure therapy consists to apply a negative pressure on the wound using a sealed dressing to enhance blood circulation and remove wound fluids. The negative pressure is generated with a pump worn by the patient, while the wound fluid is collected in a canister attached to the pumping system. The system (Figure 1) that was built was not only able to generate the negative pressure but was also able to monitor therapy parameters, collect data from sensors integrated in the wound, in the dressing or in the tubing, it was also able to store the collected data and send them on demand to the information technology system of the hospital and therefore be available via a web application to the health responsible (nurse and physician).



Figure 1: Scheme of the complete system.

[1] [www.swan-icare.eu](http://www.swan-icare.eu)

CSEM was in charge of the electronics of the system including sensor interface and one of the final sensor (MMP). The electronics is composed of two main parts, the part integrated with the pump that controls the pumping system with its sensors and user interface. It has a Bluetooth Low Energy (BLE) interface for collection of sensor data and a GPRS interface to communicate with the information system of the hospital; the second part is the sensor interface that is placed close to the wound and is connected to the sensors located in the wound (pH, temperature) and in the tubing (MMP). The sensor interface transmits the sensor data to the pumping system using the BLE connection.

The MMP sensor consists of an optical fiber sensor. A portion of the optical fiber is modified to be sensitive to MMP. The sensitive part is made with a gelatin layer stained with chlorophyllin. The gelatinase MMP digest the gelatin and the transmission of the fiber increases. By recording the transmitted power at a wavelength absorbed by the chlorophyllin (630 nm), comparing it with the transmitted power at a wavelength not affected by chlorophyllin (850 nm) and analyzing the signal with time the MMP-9 concentration of the solution in contact with the sensor can be evaluated. The sensor was located in the negative pressure tubing close to the wound.

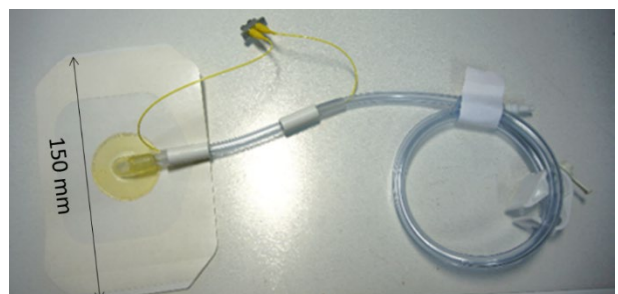


Figure 2: MMP optical fiber sensor integrated in the tubing of the negative pressure therapy system.

The complete system was tested in clinical environment on several patients suffering from diabetic foot ulcer and venous leg ulcer at the University Hospital of Pisa. Main result of this study is that the system is mature enough to go in clinical environment and that it was possible to monitor the temperature and pH in the wound, and to estimate the MMP content of wound exudate on 15 patients.

This work is supported by the EU-funded FP7 ICT-317894 SWAN-iCare project.

# Smart System for Cell and Tissue Culture with Integrated Electrode for TEER Measurements

G. Voirin, R. Ischer, T. Overstolz, B. El Roustom, K. Mayora •, M. Belcastro ••, M. Meloni \*, S. Angeloni \*\*

In the frame of the European project Smarter-SI a smart TEER measurement system for the characterization of model biological barrier cultivated on semipermeable membranes is being developed. This development will help two SMEs to broaden their portfolio and to expand their services based on cell culture analysis.

In the field of cell and tissue culture, it is important to control or monitor the quality of the function achieved by the cell or tissue culture. For biological barrier such as intestine, lungs, skin, blood-brain barrier, its function can be monitored by measuring the TransEpithelial Electrical Resistance (TEER), which is a recognized indicator of the integrity of the cellular barrier. Classical measurement scheme consist of a cellular layer cultured on a semipermeable filter insert that define two compartments (Figure 1). Measurement of the resistance takes place between electrodes placed in each compartment with the cellular layer in between. In order to protect the cell layer and the electrodes, the measurement is made with an alternate current. One reference and commercially available TEER measurement system is the Epithelial Voltohmmeter (EVOM from WPI, Sarasota, USA).

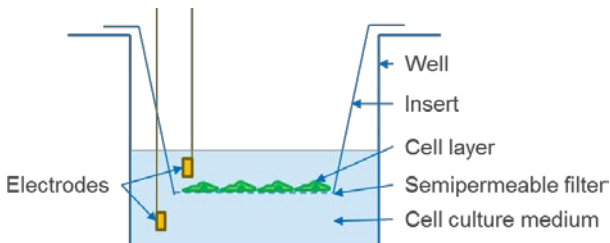


Figure 1: Scheme of TEER measurement.

In the frame of the European project SMARTER-SI<sup>[1]</sup>, a smart TEER measurement system is being developed. It will be able to monitor continuously the TEER in 12 inserts of a wellplate. The system will operate inside an incubator where optimal conditions for the growth of cell and tissue culture are applied. The cell culture insert contains a smart microfabricated microporous silicon nitride permeable support, 400 nm thick with high density of submicron pores. It constitutes an excellent epithelium/endothelium support with good capacity to enable transport through the thin supporting membrane, without interfering with the barrier function expressed by the tissue. The measurement's electrodes are integrated on each side of the

membrane insert. The electrodes are connected with electrical leads integrated in the insert up to the top of the well<sup>[2]</sup>. A hard/flexible PCB is used to contact all the inserts of the wellplate (Figure 2). The flexible part connects to the electronic module. Like this, the TEER signal is carried out of the cell growth support (insert), passes through the PCB towards the electronics module that performs sequentially the measurement in each well. The electronic module is able to do standard TEER measurement at a fixed low frequency similarly to the Epithelial Voltohmmeter and to do impedance measurement over a large frequency range. The electronic module collects data automatically and the data are available via USB connection for analysis.

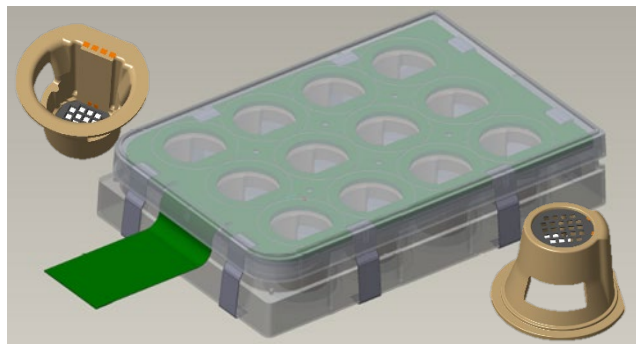


Figure 2: View of the smart 12 wellplate and of the inserts with thin ceramic membrane and electrodes.

The Smarter-SI project with its Cooperative Foundry Model allows to support the development of industrial prototypes for the benefit of SMEs. In the specific case of smart TEER measurement system, two SMEs will benefit, SiMPInext will broaden its product portfolio with the automated TEER measurement system and VitroScreen will expand its services in complex cell and tissue culture analysis.

The Innovation Action Smarter-SI has received funding from the European Community's Programme HORIZON 2020 under GA No. 644596, and from the Swiss State Secretariat for Education, Research and Innovation (SERI) under contract number 15.0085.

• IK4-Ikerlan, Arrasate-Mondragon, Spain  
• Tyndall National Institute, UCC, Cork, Ireland  
\* VitroScreen S.r.L., Milano, Italy  
\*\* SiMPInext SA, Neuchâtel, Switzerland

[1] <https://www.smart-systems-integration.org/smarter-si/>

[2] G. Voirin, et al., "Integration and Interconnection of MEMS Membrane into a Multiwell Plate Insert by Overmolding", in this report, page 34.

# oxiPAD—Oxygenation Measuring and Mapping Platform

N. Marjanović, J. Disser, F. Zanella, B. Gallinet, O. Fernández, R. Ferrini

The oxi-PAD project aims to develop a mobile, flexible, easy to handle Peripheral Artery Disease (PAD) monitoring oxygenation sensor/platform for in-and out-patient usage. Once realized the oxi-PAD will allow early detection of PAD, assessment of early interventions (like drug treatment), real-time assessment of surgical interventions, monitoring after surgical interventions and possibly homecare monitoring. The oxi-PAD will be applied on the skin of the patient and acquire data continuously while the patient moves or walks. Overall, the oxi-PAD sensor can be integrated into a CSEM's breakthrough wearable monitoring / diagnostic system i.e. re-usable sensor and processing systems for e.g., cardiovascular monitoring of the vessels.

The CSEM's oxi-PAD concept consists of a re-usable wireless oxygen sensor and processing system (for PAD diagnosis / continuous monitoring) packaged in a compact wearable device. The currently used ankle-brachial-index (ABI) method has several drawbacks: it is not applicable to patients with arterial calcification (hardening of the arteries), renal patients and diabetics, thus resulting in false negative results. As such, more than 50% of all patients, especially suffering from mild PAD are not diagnosed and are thus not treated in time.

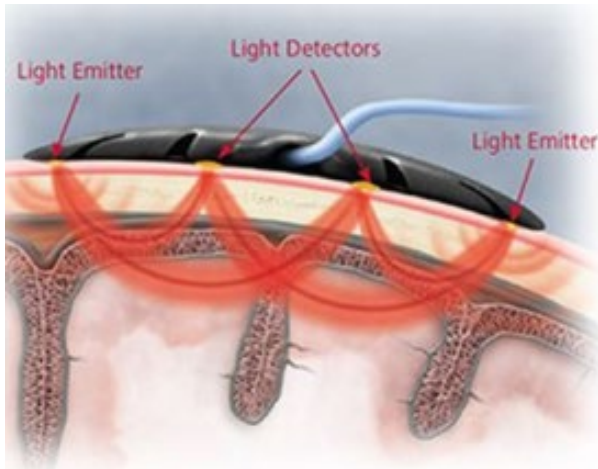


Figure 1: Principles of the proposed oxygenation sensor.

The key enabling advantage of CSEM's oxi-PAD is the possibility to acquire data continuously while the patient moves or walks. The parameter "pain when walking" often used in the diagnosis of PAD is very subjective. In contrast quantified oxygenation would allow a better classification of PAD since the walking distance of a patient can then be correlated with muscle oxygenation. The proposed oxi-PAD data acquisition system is a non-invasive device wrapped around the patient leg. Alternatively the oxi-PAD could successfully collect data when wrapped around the patient arm as well.

The oxi-PAD consists of arrays of Light Emitting Diodes (LEDs) and Photo Diodes (PDs) on a flexible foil. Two predominant wavelength bands are selected 750 nm (red) and 850 nm (infrared). Depending on the distance between the PDs and the LEDs the light propagates through deeper tissue/muscle layers. The ratio of red to infrared transmitted light gives a measure of the oxygen saturation of the blood or muscle and thus an indicator for tissue oxygenation (Figure 1). Such light propagation could be simulated in LightTools® in order to position the PDs with respect to the LEDs.

The layout of the proposed oxi-PAD device is shown in Figure 2 (first generation).

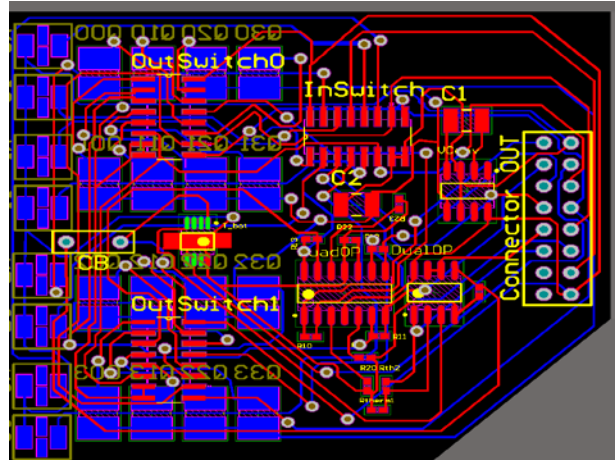


Figure 2: CSEM's oxi-PAD – layout of the first generation with 4 sensing channels.

In addition to the array of LEDs and PDs, the oxi-PAD allows embedding electronic components, such as temperature sensor, sweat sensor, battery, micro-controller, and GPS for measuring walking distances. This enables autonomous data acquisition while the patient walks/moves. The acquired data will be transmitted wirelessly to a computer or smartphone, and stored in order to track the PAD history.

The main novelties of the CSEM's oxi-PAD (Figure 2) are listed below:

- Flexible / wearable device.
- Smart packaging and proper skin fixation.
- Smart device i.e. algorithms for oxygenation mapping and quantification.
- Continuous monitoring with warning and alarm functions when critical data are collected.

The main oxi-PAD use case is by general practitioners during the regular check-up. The user-friendly oxi-PAD will further revolutionize in- and out-patient PAD diagnostics and enable real-time monitoring, and patient monitoring after surgical interventions.

Once realized the oxi-PAD will replace the currently used expensive and non-accurate PAD identification techniques.

# Inkjet Printed Optical Waveguides

F. Lütolf, P. Theiler, R. Ferrini

Optical waveguide structures have been inkjet-printed with a special technique relying on the formation of capillary bridges. The optical losses amounted to 0.61 dB/cm on average with the best waveguides performing at 0.2 dB/cm, highlighting the precision with which the features were deposited. Besides waveguide-based applications like sensing or data transfer, the developed printing technique could also easily be adapted to other structures or materials to enable rapid prototyping and actual production alike.

Additive manufacturing has received a lot of attention recently as it is a material-efficient, low-temperature, and vacuum-free process. Non-contact printing is a highly customizable technology amongst this family of techniques due to the different inks and hence functionalities available. Inkjet printers usually also only require a simple digital blueprint. It is therefore no surprise that huge efforts have been undertaken to apply inkjet printing outside of classical color generation and use it for writing electrical circuits, optical microstructures or microfluidic channels. Unfortunately, basic microscopic geometries such as (high aspect ratio) lines are for example inherently unstable and prone to bulging due to the surface tension of the deposited ink. For this reason, smooth and tall lines comparable to photolithographically patterned waveguides have been very difficult to print up to now.

We recently developed an approach that turns the formerly problematic surface energies into the driving forces for structure generation. The technique relies on the deposition of pinning caps, which can subsequently be connected with self-aligning capillary bridges (Figure 1).

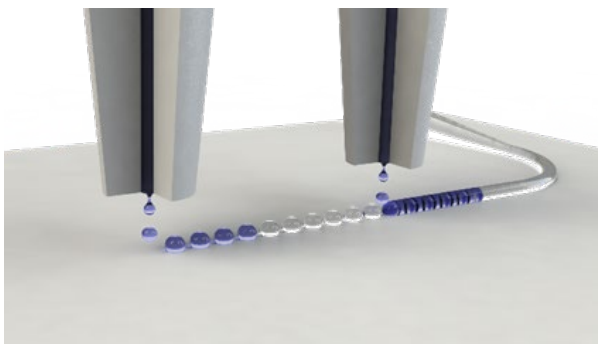


Figure 1: Sketch of the specially developed printing process.

This very simple method allowed us to accurately print a variety of continuous structures including curved waveguides or optical splitters (Figure 2). These are examples for features that would be nearly impossible to print through classical droplet deposition, as the cohesive forces in the liquid would force the material into round blobs instead of thin, connected lines.

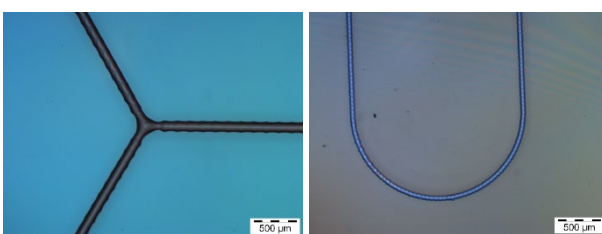


Figure 2: Printed optical waveguide geometries.

To compare the performance of the printed structure, a series of tapered, curved waveguides was printed and optical losses were measured with red laser light and a photodiode (Figure 3). Our average loss measurements of 0.61 dB/cm on a batch of waveguides are to our knowledge the first ones to date for inkjet printed waveguides. The best performing waveguides in the batch showed losses down to 0.2 dB/cm, which is comparable to

lithographically patterned ones. In this context, we also demonstrated the importance of minimizing any line roughness (and especially preventing bulge formation) in order to achieve such high quality waveguides.

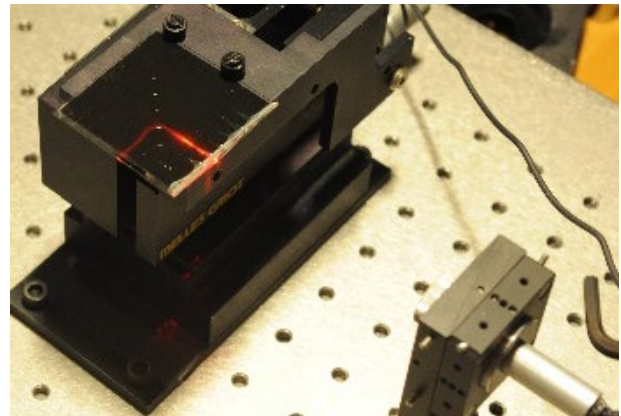


Figure 3: Optical characterization setup excluding the photodiode.

In general, the replacement of standard optical components by micro-optical elements has often proven advantageous. Rather frequently though, several elements must be combined and aligned with respect to each other, which is particularly challenging in the context of miniaturization. The use of inkjet printed capillary bridges here also allows for flexible yet simple designs to connect or align waveguides with other components, which is a clear advantage over common photolithographic techniques.

In summary, the capillary-bridge printing technique reported circumvents the severe problems inkjet printing previously experienced in attempts to print linear or complex features on low energy surfaces. Besides rapid prototyping, which traditionally relies on additive manufacturing techniques, the present technique also facilitates industrial fabrication since inkjet printing is a very mature process that can even be included in roll-to-roll lines. It may not only pave the way towards flexible waveguide design, but can also be applied for new solutions in the broader domain known as free-form optics, where removing constraints on symmetry can offer considerable savings both in space and weight. Consequently, lab-scale as well as industrial applications ranging from lab on a chip over optical sensors to lighting can profit from these developments.

# PRINTBAT—Printed Lithium Ion Batteries

O. El Baradai, J. Schleuniger

The PRINTBAT project aims the development of fabrication processes for flexible printed lithium ion batteries using large-scale and versatile manufacturing techniques such as screen printing which gives rise by free-form factors to new emerging markets such as flexible electronic.

This report describes the manufacturing of lithium-ion batteries by screen printing, starting from positive and negative electrodes to the assembly of full cells. Moreover, a reduced environmental impact is achieved by replacing conventional fluorine based-binders and toxic solvents with bio-sourced and aqueous components. Firstly rheological results are presented for the formulated inks. Secondly the inks, printed onto the cellulosic-based separator according the technique described by El Baradai, *et al.*<sup>[1]</sup>, are characterized electrochemically for anode and cathode performance. Subsequently the performances of a full cell is presented. The last part is dedicated to the analysis of bending deformation on the physical properties of the materials.

Inks in the optimal rheological range for screen printing have been formulated by variation of content ratios. A rheological study has been performed on the influence of carboxymethyl (CMC) and microfibrillated (MFC) cellulose components used as a disperser and binder respectively. Because of its electrical conductivity, graphite component (GP) was maximized to ensure a good conductivity of inks. Moreover, an analysis has been performed to investigate the impact of carbon black (CB) and carbon nanotube (CNT) particles as a rheological and electrical enhancer. A steady state analysis has been performed to analyze the response of the ink to shear rate increment. The ink viscosity has been characterized by measuring rheological properties in a shear rate ramp ranging from 1 to 1000 s<sup>-1</sup> (orange curve) and 1000 to 1 s<sup>-1</sup> (blue curve). 1000 s<sup>-1</sup> has been selected as maximum shear rate, because it is the highest shear value typically reached in a screen printing process. As an example the rheological behavior of the ink formulated for the positive electrode is shown in Figure 1a.

The electrodes have been characterized in half cell configuration to investigate their electrochemical performances. As shown in Figure 1b, the negative electrode exhibits the characteristic oxidation and reduction peaks of graphite based electrodes. The first voltammetry cycle (blue curve) shows the classical profile of a first activation of the electrode with the formation of a solid electrolyte interphase (SEI) layer on graphite based electrodes.

For the assembly of full cells, the positive and negative electrodes have been printed onto the separator in order to use it not only as physical barrier avoiding potential short circuit between the electrodes, but also as a substrate to print the components of the cell. A full printed cell has been tested and the chrono-potentiogram in Figure 1c reveals that side reactions are completely avoided during the charging of the cell. Even after a charge and discharge cycle of the cell, the open circuit voltage (OCV) is 3.15 V, in line with the expected value for lithium ion technology.

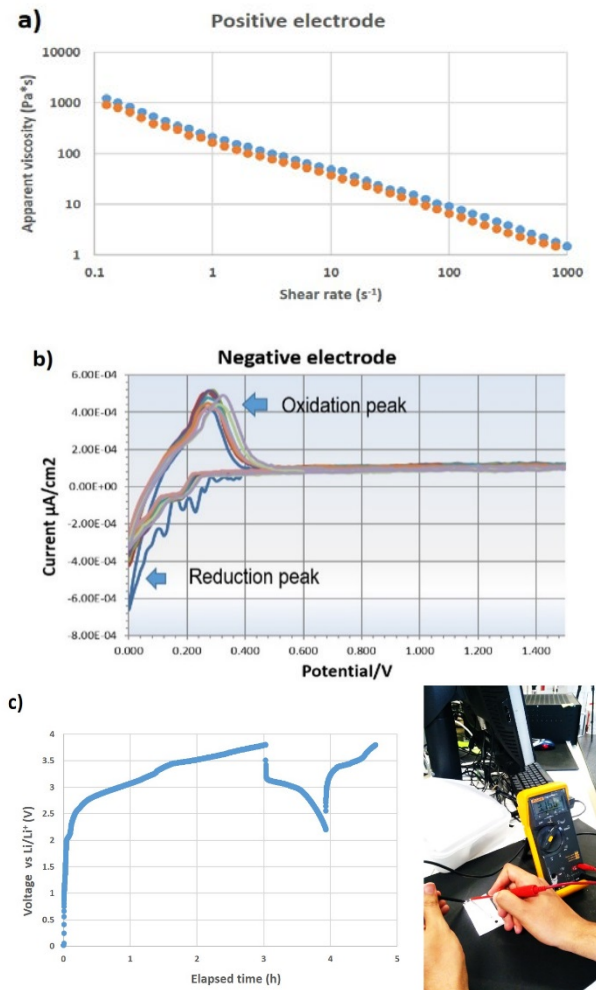


Figure 1: a) Steady flow measurement of the ink for the elaboration of the positive electrode; b) Voltammetry of the negative electrode; c) Chrono-potentiogram of a full printed cell and OCV after charge cycle.

The mechanical properties of the electrodes have been tested by stress – strain and bendability test. The formation of cracking due to repetitive bending impacts the electrical conductivity of the electrodes. For this reason the evolution of the electrical conductivity as function of the number of bending has been investigated. The positive electrode showed a reduction of 14% in electrical conductivity after 600 bending cycles at a bending radius of 1.5 cm, which requires further optimization. However, owing to the elastic properties of the graphite the electrical conductivity of the negative electrode is not affected by the number of bending cycles.

<sup>[1]</sup> O. El Baradai, *et al.*, "Up-scaling of microfibrillated cellulose based positive electrodes for lithium ion batteries by roll-to-roll printing process," Int. J. Eng. Innov. Technol., vol. 5 (2015).

# Organic Optoelectronic Imager

N. Marjanović, J. Disser, F. Zanella, M. Chrapa, J. Schleuniger, A. Mustaccio, R. Ferrini, M. Schnieper

The objective of the EU FP7 INGRESS project was to develop and evaluate innovative technologies for fingerprint live scanners that support the examination of additional biometrics associated with the finger. INGRESS proposes the development of different technologies to address the issue of very bad fingerprint images obtained from fingers with superficial skin disorders and therefore ensure that citizens are not inconvenienced, through no fault of their own, by the inability to use biometric technology as foreseen by policy directives. CSEM contributed to this project with the design, the development and fabrication of mock-ups of organic optoelectronic imagers based on printed Organic PhotoDiode (OPD) arrays coupled with an Organic Light Emitting Diode (OLED) as backlight. The combination is driven with standard electronic components. The optical imager with an OPD array of 128×128 was demonstrated. The 512×512 organic imager is fabricated but still under evaluation.

Within the EU FP7 INGRESS project CSEM was developing the surface fingerprint reader using Printed Organic Electronics (POE).

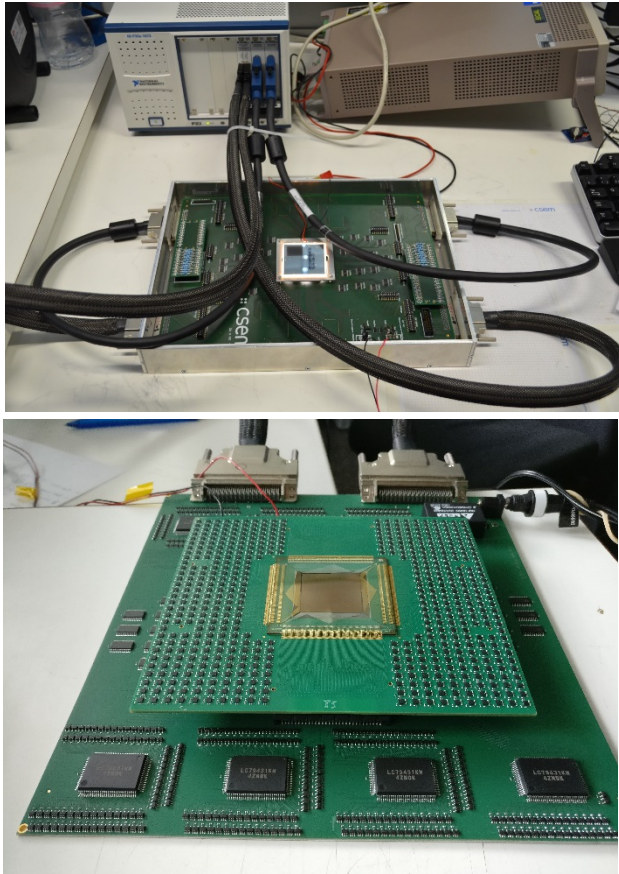


Figure 1: Hybrid optoelectronic platform – first generation (top) and second generation (bottom). A 512×512 organic imager at 512 dpi based on Organic Photo Diodes is visible in the bottom picture.

The reading / driving platform for the image acquisition was designed using best performing and cost-effective silicon electronic parts, while the passive organic imager part is based on an array of printed organic photodiodes (OPDs)<sup>[1]</sup>. For the light source an organic light emitting diode (OLED) was used. The system integration is done in a hybrid manner i.e. OPDs and OLED were coupled with the in-house designed and developed acquisition platform embedding standard silicon-based electronic components. Several generations of mock-ups were

continuously developed during the project while upgrading the OPDs and electronics reading platform, e.g., hardware and software (Figure 1).

The POE imager part includes a 2" flat and uniform light source (OLED) for the illumination of the user finger this through a glass substrate. The light reflected from the finger is then detected by the printed organic photodiodes array (OPDs) which comprise, from front to back: a transparent electrode (TCO), the active material converting the absorbed photons into charge carriers and a non-transparent electrode. Since ridges of the finger touch the front sensor surface and the valleys do not, the amount of reflected light to the OPD will vary, thus allowing an optical representation of the fingerprint pattern.

The first generation of the driving platform was designed in house as a learning platform. It is bi-directional and allows reading in & out signals of various resolutions (according to the roadmap) or driving displays. The in-house developed software of the driving platform was continuously updated, to finally reduce the acquisition time down to 20 s. The second generation of the driving platform (Figure 1) could only read out imagers but has an optimized analog front end and driving scheme.

Operational imagers were demonstrated under different uniform illumination conditions in order to exhibit different grey scale levels. Imaging tests were conducted with chessboards patterns of different resolutions. From those tests, the limitations of the 128×128 POE sensor at 128 dpi were identified and the path toward 512 dpi POE sensors was paved from the lessons learnt.

The main outcome of the INGRESS project is the fabrication of the POE i.e. the design and development of organic/printed electronic imagers with the resolution of 128 dpi and 512 dpi.

CSEM will use the developed POE organic imager concept to upgrade it in terms of:

- Flexibility (currently on glass substrate).
- Larger area (currently 2 inches substrate with 1 inch imager).
- Further increasing the cost effectiveness.

The developed concept can be applied in mobile detectors, smart phones, tablets and devices for object recognition or privacy protection.

<sup>[1]</sup> G. Maiellaro, et al., IEEE Transactions on Circuits and Systems I, Vol. 61, p. 1036-1043, 2014.

# Pressure Sensitive Robots

J. Disser, F. Zanella, A. Mustaccio, N. Glaser, N. Marjanović

A SmartSkin demonstrator based on a hybrid integration approach was developed for an artificial robot's haptic experience. Within the gateone-project, printed pressure sensors on flexible/stretchable foil were placed under the robot skin enabling the robot to "feel the environment" and to interact with humans once touched. A security feature, i.e. emergency function, was implemented whereas teaching/learning features are also enabled.

Robots have been working in the industrial production for decades, however they have been doing this in an isolated environment i.e. with no humans around. In recent years, the field of collaborative robotics has gained a lot of attention and robots started working alongside their human co-workers. This change demands the robots to be aware of their surroundings in a much more comprehensive way.

The Swiss SME F&P Robotics AG<sup>[1]</sup> has been aware of this challenge in their customers' industry and is producing intelligent robots which can safely collaborate with their co-workers in industries such as food production and packaging as well as medical assistance. Through the integration of flexible pressure sensors into their soft robot skin, they want to improve their products further.

The realized SmartSkin demonstrator is shown in Figure 1. It consists of a 2×3 pressure sensor array which is printed on a flexible and stretchable foil.

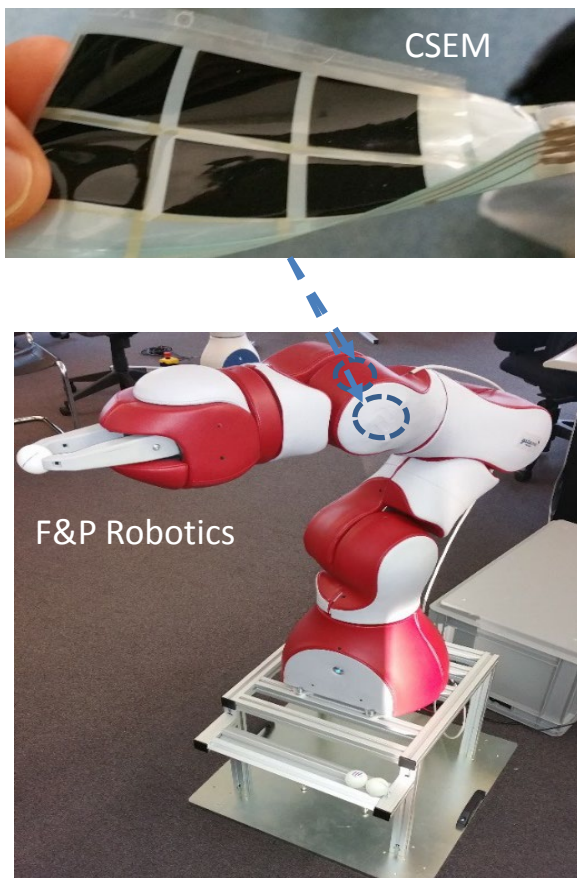


Figure 1: SmartSkin demonstrator.

[1] [www.fp-robotics.com](http://www.fp-robotics.com)

[2] French version: <http://future.arte.tv/fr/innovations-medicales/des-robots-sensibles-au-service-de-lhomme>

CSEM conducted the design of the sensors, their fabrication by screen printing and their characterization. The resulting pressure sensor is thin (between 300 and 400 µm), flexible, easy to customize and has a sufficiently large active area in order to provide pressure mapping information (i.e. position of the pressure stimulus) over the surface of the robot arm. The sensor was placed under the robot external leather "skin" and was interfaced with the robot electronic hardware. In this configuration the sensor is sensitive to pressures between 0.1 kPa and 10 kPa, as shown in Figure 2.

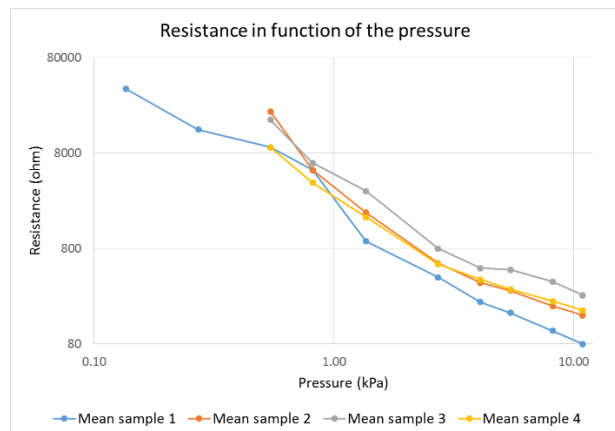


Figure 2: Mean resistance measured vs pressure. Both axes in logarithmic scale.

An emergency stop based on these sensors has been implemented by F&P Robotics AG. The demonstrator was highlighted in an ARTE-RTS report<sup>[2]</sup>.

The novel technology will allow F&P Robotics AG to become a game changer in this industry by providing robots equipped with cost-effective and large area printed pressure sensors which add sensing functionalities, manipulating and correction capabilities. These demonstrators will open new market opportunities for the collaborative robot from F&P Robotics AG, especially in the human environment and food handling segments.

This work was funded by the European Commission H2020-ICT-2014-1 under the grant 644856 (gateone-project).

German version: <http://future.arte.tv/de/medizinische-innovationen/empfindsame-roboter>



# PHOTOVOLTAICS & ENERGY MANAGEMENT

Christophe Ballif

The past year was marked by contrasting news: US presidential actions with regard to the climate and the environment showed that climate skepticism is not yet fully extinct. Indeed, the global trend regarding active policies that support an energy transition is far too moderate—in other words, the Paris climate agreement is yet to be implemented. On the other hand, there was also the first popular vote in a country—Switzerland—via which a new strategic approach to that very transition was accepted, and with a strong mandate of 58 percent of the votes cast. In Europe, the low price of CO<sub>2</sub> emissions certificates means that coal-powered plants can continue to operate, and thus prevent a faster substitution of fossil fuels by renewable energy sources when it comes to electricity generation. In the US, the substitution of coal by gas allows a reduction in US CO<sub>2</sub> emissions. In Asia, India's moratorium on new coal-powered plants, and a reduction in the number of coal-powered plants planned for construction in China, have both been triggered by the falling costs of photovoltaics and wind. Indeed, for new power production capacity, solar is now the lowest cost electricity source with power-purchase agreements down to 2.5 cts/kWh in some places where the electrical distribution system is compatible. A fact that more and more countries are becoming aware of. This explains the continued growth in the volume of installed PV modules: 70 GW in 2016 and likely to rise to 85–90 GW in 2017. This volume should soon reach 100 GWs of annual production. A recent paper in *Science*<sup>[1]</sup> even shows that, depending on the scenarios, the annual production capacity of photovoltaics could reach up to 600 GW/year in 2030, which is indeed what is required, at least, to be serious about limiting global warming to 2°C (which would anyway still be accompanied by already huge consequences). Noticeably though, the margins in the PV sectors along the full value chain, down to and including solar park contractors, are extremely low if not negative, creating quality, financial, and innovation risks.

Another ongoing revolution is linked to mobility. With several countries announcing the future prohibition of combustion engines, with the push for electric cars in China (also triggered by direct pollution problems), fuel-cell cars in Japan, and the installation of more hydrogen stations in countries such as Germany, it can safely be predicted that a huge system change is ongoing. In particular, Li-ion battery packs at prices down to USD 125/kWh are now being predicted for 2018 (i.e., USD 6000 for a battery that allows 400 km of autonomy, down from USD 20,000 five years ago), with a further cost reduction potential with future increased volumes. This "silent" revolution will further continue to transform the electricity and energy market, and will also have a huge impact on the tax system in countries where fuel taxes are high. In Switzerland, for example, 1 kWh for an electrical car would have to be taxed at around 50 cts if it had to compensate for the loss of taxes currently imposed on petroleum products. Along with transportation, energy efficiency in the construction market is receiving more and more attention. Combining these aspects with heating and cooling, electricity, mobility, solar, and other sources, this translates into more and more market and integration complexity. Working on apps, hardware, and on the general intelligence necessary to address

energy management at the household, district, city, or national level becomes, hence, crucial.

With its dense network of established companies, its start-ups, its network of universities and higher education institutions that receive topical public funding, and its people's vote in support of a new energy strategy, Switzerland continues to hold a good hand, as it can develop, test, and implement solutions leading to economical and environmental value. In the field of pure photovoltaic cells, despite a shift in production to Asia, Swiss exports—in the shape of both equipment and know-how—continue to play an important role. We see this, e.g., in both European (Enel/3Sun) and Russian industrial investment in heterojunction solar cell technology, based on Swiss innovation.

In this context, the CSEM PHOTOVOLTAICS & ENERGY MANAGEMENT (PV&E) program's vision for Switzerland is to continue developing innovative process technologies, device concepts, and new high-tech solutions to better serve the Swiss and global renewable energy industry. More generally, the PV&E program targets the following objectives:

- To provide cutting-edge innovation in the field of photovoltaic devices, realizing the best devices with a high potential for industrialization, from advanced crystalline silicon to multi-junction solar cells.
- To design and develop highly reliable modules, for the power market, for the transportation sector, or with the highest potential for adoption by the public in the built environment.
- To support the development of next-generation equipment and metrology systems, all along the value chain of photovoltaics, creating a sustainable cleantech value for existing and future CSEM customers.
- To provide new solutions for specialized devices, coatings, or materials with higher added value, and for PV components with enhanced functionalities.
- To bring solutions to the energy/electricity management field as we transition toward a society essentially powered by renewables, in which energy efficiency and management will be realized through intelligent hardware and algorithms.

Solutions to these challenges are brought to market either by partner companies or via the creation of start-ups. To meet these objectives and to support the transition to an energy system in which solar will play an essential role, CSEM collaborates closely with the EPFL PV-Lab, with Swiss universities and ETH entities (EMPA and EPFL), as well as with universities of applied sciences (HSR, FHL, and ZAHW)—in particular SUPSI (accreditation and powerplants) and BFH (the BFH-CSEM energy storage center). CSEM also collaborates with multiple local and international organizations or agencies.

## General situation

In 2017, CSEM was able to further develop and extend its activities related to the PV&E program through the addition of a new sector dealing with energy systems. The overall program employed around 57 FTEs at the end of 2017 through both industrial collaboration with close to 40 companies and competitive public funding from CTI, EU H2020, SNF, SFOE, among others. The overall organization of the

program is summarized in Figure 1. The available technology infrastructure platforms are complemented by additional software/hardware in laboratories (e.g., simulation platforms for electrical grids, for plasma modelling, micro-grid hardware). Below, we describe the program's three activities with some highlights from 2017.

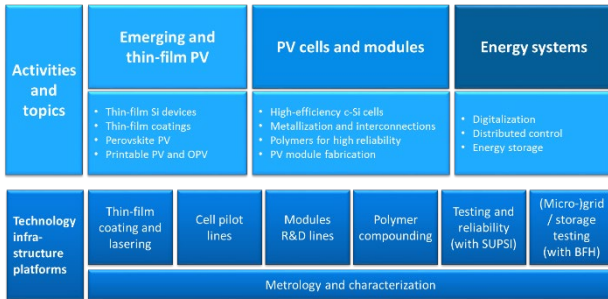


Figure 1: Schematic of the activities in the PV & ENERGY MANAGEMENT program. Top part—activities; bottom part—technology infrastructure platforms.

In the **Emerging and thin-film PV** activity, CSEM provides the industry with a high level of expertise regarding customized PV cells for product integration. It also makes available its know-how regarding coatings for optoelectronics applications for the solution of diverse industrial challenges. The multidisciplinary team applies laser patterning, thin-film deposition, printing methods, and device technology to design and produce cells that meet the most challenging demands, thanks to top-level facilities and latest-generation equipment.

At the same time, CSEM is preparing for the future of PV with new materials and cell architectures from the forefront of academic research. To this end, CSEM is exploring more efficient and cheaper solar cells in collaboration with world-leading institutes and universities. This includes modules and multiple junction devices based on perovskite device structures.

These two parts of the activity tackle challenges in the following fields:

#### Customized PV

- Series production of customized solar cells.
- Development of flexible solar cells (based on OPV and thin-film silicon technologies).
- Integration of PV cells into final products (thin-film, III-V, crystalline silicon, and OPV).
- Development of complete energy harvesting systems.
- Benchmarking of cell technologies for various applications.

#### Thin-film coatings and patterning

- State-of-the-art transparent, conductive coatings and electrodes for smart sensing and detection.
- Light management through microstructured substrates, films, and foils.
- Materials and processes for optoelectronics (LED, OLED, TFT, sensors, smart windows, and PV).
- Multifunctional coatings and layers for decorative, lubricating, and/or electronic applications.

#### Emerging PV

- Development of advanced cell concepts and PV materials with printable PV.
- High-efficiency perovskite solar cells, IR transparent perovskites, and components for multi-junction cells.

Our applications have been demonstrated in the field of energy harvesting, for different applications ranging from watches to smart farming. The activity is complemented by a network of CSEM professionals who combine energy-harvesting solutions with ultra-low-power designs to make the Internet of Things and wearables fully autonomous. In CSEM, customers find a one-stop-shop for their most demanding projects.

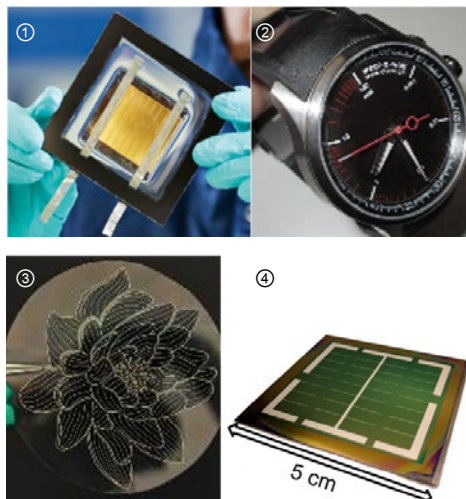


Figure 2: (1) Encapsulated perovskite solar cell modules reaching up to 16% solar conversion efficiency (aperture area) (IEEE JPV 2017). (2) PV dial and band with strong low-illumination and indoor performance. (3) OPV 9-segment modules. (4) First "large-area" tandem perovskite on silicon solar cells (together with the EPFL PV-Lab).

In its **PV Cells and Modules** activity, CSEM develops and matures materials, processes, and technologies for the cost-effective manufacturing of reliable and high-efficiency PV cells and modules, as well as for the optimum integration of PV products into dedicated applications (building integration, mobility, and energy harvesting).

Within its flexible, high-end R&D platforms, CSEM is mastering high-performance silicon solar cell manufacturing over the full processing chain. This includes everything from wafer texturing to reliability testing allowing us to deliver high cell efficiency and maximum module outdoor performance at controlled costs. CSEM demonstrates key expertise and a high-efficiency track-record in the fabrication of crystalline silicon heterojunction solar cells, back-contacted heterojunction solar cells, high-temperature passivating contacts, and technologies for advanced PERX concepts, as well as next generation multi-junction devices: perovskite/silicon and III-V/silicon tandem solar cells.

As part of this broad mandate, CSEM is actively developing materials, processes, and technologies necessary for metallization, cell interconnection, and module integration with goal of achieving maximum module performance, reduced PV electricity costs, and long module lifetimes. To this end, we have developed broad expertise in fine-line printing using screen, stencil, and inkjet printing, as well as in the full process flow for the copper plating of heterojunction solar cells. In addition, CSEM develops advanced interconnection technologies, such as multi-wire and shingling technologies, and possesses a unique and flexible R&D polymer

platform for customized polymer compounding, extrusion, and processes, for long-term reliability.

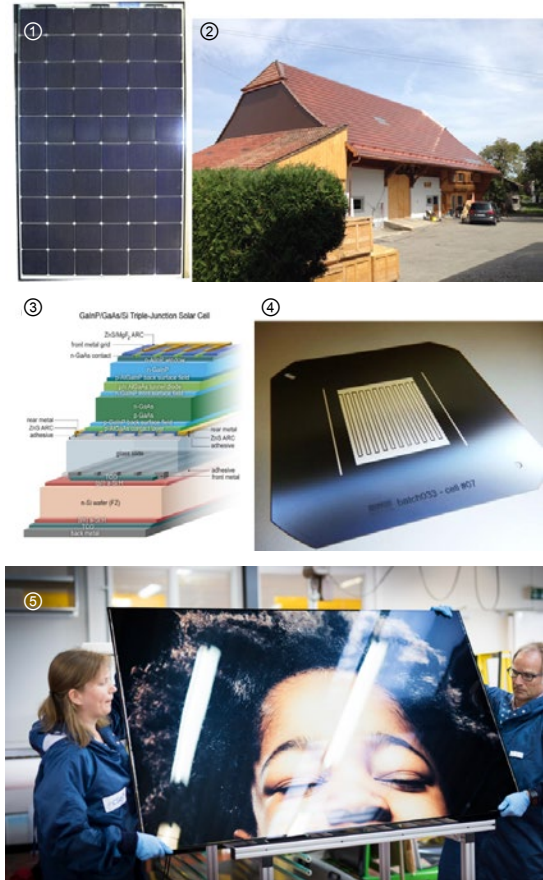


**Figure 3: PV-Si cells and modules.** (1) 335 W record efficiency contribution of CSEM to 335 W power output on a multi-wire modules of Meyer Burger with Indium free interconnects, certified by TUV for bifacial heterojunction technologies. (2) “Terra-Cotta” c-Si modules prepared by ISSOL with the support of CSEM. (3) World record 1 Sun tandem devices with up to 32.8% efficiency by CSEM, EPFL, and NREL (*Nature Energy* 2017). (4) Novel IBC patterning process with up to 23.6% efficiency (*Nature Energy* 2017). (5) First high-resolution PV integrated photos (with the support of the BCN).

The speed and scale at which PV products are being deployed are accompanied by a broadening of the integration of PV devices and elements. In the targeted applications, PV products must meet performance and reliability requirements while delivering the required aesthetics, color, shape, weight, and system specifications. We have significant expertise in PV product integration with a focus on innovative solutions for BIPV application with various solutions for modifying the color and esthetic aspects of modules. In addition, customized PV solutions have been developed for specific applications in the field of mobility, from the stratosphere to land and sea.

For all these activities, CSEM is developing extensive know-how, high-end equipment, and processes for PV metrology characterization. All of which can be readily developed for or transferred to its industrial partners.

[1] N. M. Haegel, *et al.*, *Science*, 14 (2017) 141.

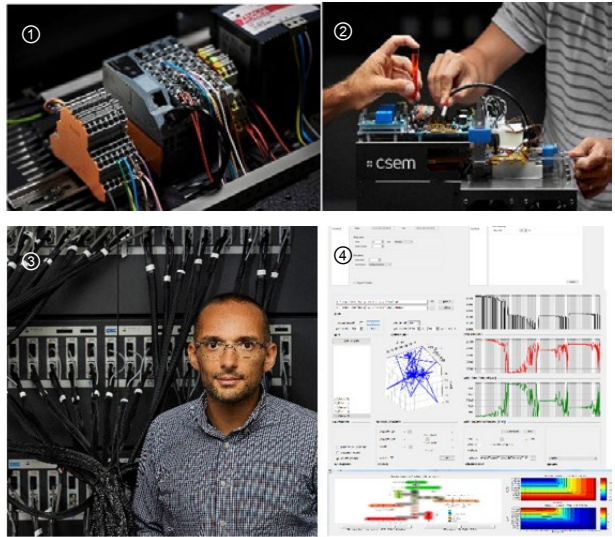


**Figure 4: Energy systems.** (1) Prosumerlab, prototyping platform for building energy management systems. (2) Hyperbat, development of a hybrid electricity storage system based on supercapacitors and batteries. (3) ESReC, test benches for the characterization of battery cells under charge and discharge cycles. (4) Sabina, calculating PV hosting capacity with CSEM’s plugin for DlgSILENT PowerFactory.

Within its **Energy Systems** activity, CSEM develops solutions to build and manage an efficient, sustainable-energy world based on distributed renewable power generation. A multidisciplinary team brings together a wide skill base including power engineering, power electronics, signal processing, machine learning, optimization and control, and systems engineering, to engineer this new world.

We provide services and technologies in three main areas:

**Digitalization**—We apply artificial intelligence techniques to generate value from energy data. This includes forecasting energy production and consumption on multiple time scales, and tracking individual appliances from aggregate power measurements.

**Decentralized control**—We develop multi-level control from the device level to grid-interactive functions. Our solutions increase the local consumption of renewable energy, system flexibility, and power quality. We focus on single- or multi-vector microgrids operating at scales ranging from single buildings to cities. With our thermal-control technologies, the energy consumption of existing buildings can be reduced while maintaining or improving user comfort.

**Electricity storage in supercapacitors and batteries**—We develop characterization methods and dynamic models to predict the performance of storage devices in complex operating conditions. With these models, we can also optimize the design and control of storage systems.

Applications of CSEM technologies have already been demonstrated on inverters, in direct current (DC) microgrids, and in energy management systems for residential and commercial buildings. We work with component vendors, system integrators, and utilities to turn these technologies into successful products.

# Development of Record Single Junction Minimodule Devices by Laser Patterning

A. Walter, S.-J. Moon, B. Kamino, S. Nicolay

In the framework of the European Horizon 2020 project CHEOPS (low Cost and Highly Efficient phOtoVoltaic Perovskite Solar cells), CSEM is taking an active part in the upscaling of the emerging perovskite solar cells. In particular, laser patterning techniques developed for thin film silicon photovoltaics devices have been adapted and successfully applied to perovskite minimodules. These development led to record efficiency perovskite devices of increased size.

In recent years, a new class of thin film PV absorber – the organic-inorganic halide perovskite (PK) – has attracted a strong interest, leading to an unprecedented rise in efficiency<sup>[1]</sup>. However, despite the great efforts put into the race to reach record efficiencies, most of the reported results so far were obtained on devices with a scale significantly smaller than 1 cm<sup>2</sup><sup>[2,3]</sup>. Therefore, one goal of CHEOPS' is to demonstrate the upscaling of this promising technology towards devices of industry-relevant scale.

CSEM had previously made the demonstration of the first PK minimodule using a fully laser-based patterning scheme as depicted in Figure 1. This allowed to strongly reduce the fraction of dead area of the module (down to 16%) which led to an aperture area efficiency of 5.52% on 6 cm<sup>2</sup><sup>[4]</sup>. However, these early modules suffered from current losses due to back contact delamination originating from the laser patterning of the P3 interconnection line. Moreover, a high front TCO sheet resistance coupled to highly resistive P2 contacts strongly limited the fill factor (FF) of the full module.

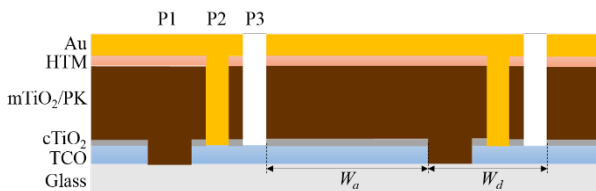


Figure 1: Typical architecture of a PK minimodule and interconnections (P1-P2-P3 scribing lines) defining the active ( $W_a$ ) and dead ( $W_d$ ) area width.

Building on this previous knowledge, specific actions have been taken in order to mitigate the losses. First of all, by switching the side from which the P3 scribing was performed (i.e. by shooting the laser beam directly on the metal layer rather than through the glass) it was possible to strongly reduce the delamination of the metallic back contact. Then, by reducing the mesoporous TiO<sub>2</sub> (mTiO<sub>2</sub>, used as electron transport layer in conjunction with the corresponding compact layer) layer thickness, the ablation of said layer through the P2 process was made easier. Together

with the choice of a less resistive TCO and the reduction of the dead area width, this led to increased FF. Indeed, it has been shown at CSEM that the laser patterning of the interconnections allowed dead area width as low as 400 µm, exceeding CHEOPS' goal of 500 µm.

In parallel, a careful choice of perovskite material and deposition process allowed the deposition of highly uniform layers by spin-coating on 5×5 cm<sup>2</sup> substrates. This improved uniformity of the active layer led to very small current density variation over the whole area of the module. In conjunction with the improved laser patterning steps with a reduced dead area, CSEM has been able to demonstrate a module aperture area (14 cm<sup>2</sup>) efficiency as high as 16%. To the best of authors' knowledge this is the highest reported efficiency for this kind of perovskite and on modules of that size. Moreover this exceeded the project's requirement for a 12% module.

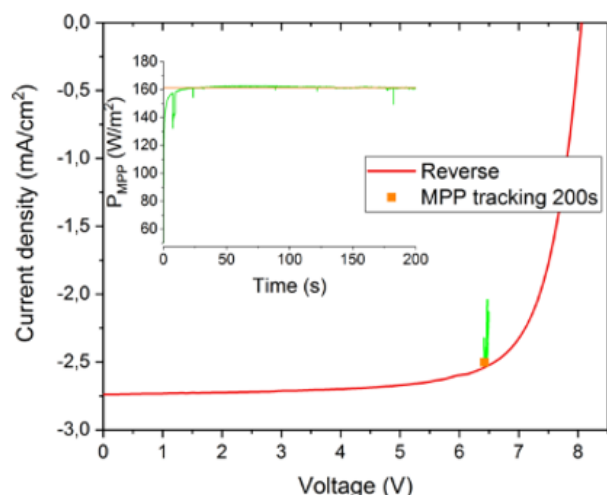


Figure 2: IV measurement of the champion module device. The device has a  $V_{oc}$  of 8 V, a  $J_{sc}$  of 2.74 mA/cm<sup>2</sup> and a FF of 75% for an efficiency of 16.55%. The inset shows the maximum power point tracking over time, demonstrating how the efficiency stabilizes at 16%.

CSEM is therefore paving the way for high efficiency large area perovskite solar devices.

[1] NREL, "NREL Efficiency Chart," 2 December 2016. [Online]. [http://www.nrel.gov/pv/assets/images/efficiency\\_chart.jpg](http://www.nrel.gov/pv/assets/images/efficiency_chart.jpg)

[2] W. S. Yang, J. H. Noh, N. J. Jeon, Y. C. Kim, S. Ryu, J. Seo, S. I. Seok, "High-performance photovoltaic perovskite layers fabricated through intramolecular exchange," *Science*, vol. 348, no. 6240, pp. 1234-1237, 2015.

[3] S. S. Shin, E. J. Yeom, W. S. Yang, S. Hur, M. G. Kim, J. Im, J. H. Noh, S. I. Seok, "Colloidally prepared La-doped BaSnO<sub>3</sub> electrodes for efficient, photostable perovskite solar cells," *Science*, vol. 356, no. 6334, pp. 167-171, 2017.

[4] S.-J. Moon, J.-H. Yum, L. Löfgren, A. Walter, L. Sansonnens, M. Benkhaira, S. Nicolay, J. Bailat, C. Ballif, "Laser-Scribing Patterning for the Production of Organometallic Halide Perovskite Solar Modules," *IEEE Journal of Photovoltaics*, vol. 5, no. 4, pp. 1087-1092, 2015.

# Integrated Solar Cells to Energize the Wearables and the Internet of Things

P. Häfliger, E. Favre, D. Dominé, J. Brossard, J. Bailat, M. Crettaz, L. Zhou, J.-M. Koller, P. Liechti, N. Blondiaux, A. Bionaz, W. Fantin, B. El Roustom

*Flexible solar cells with a decorative pattern in the form of the heidi.com logo have been realized and integrated into a back-pack. An integrated data-logger measures the power produced and a transmission system broadcasts the data through a smartphone to the cloud. The data harvested help us figure out what applications can be powered with this technology and pave the way for autonomous wearable devices. Heidi.com and CSEM presented their innovation at the Swiss Pavilion during the EXPO 2017 in Astana, which served as a real life testing of this solution.*

When considering connected accessories and smart clothes, producers and designers face the problem of the seamless integration of new technologies into their products. What is more, providing energy to these devices is a recurring problem. Photovoltaic cells are often considered to supplement and extend the battery lifetime, however existing solutions are not aesthetically acceptable. In fashion and clothing – design matters. The requirement of the industry is that there should be no visible difference between smart clothes and regular products offered.

In this project, the industrial partner Heidi.com wanted to have a technology integrated in its clothes that is not visible to the wearer and fits perfectly the existing design of the brand. Within the European 'gateone-project', Heidi.com and CSEM partnered to integrate PV cells as power source in the textiles and also in the Heidi.com logo tag.

The main markets for smart textiles are the sports and fitness markets but also less function driven markets such as luxury and consumer goods where elements of gamification can be added – i.e. elements which engage the customer.



Figure 1: Examples of the realization of the back-pack for the staff of the Swiss Pavilion at the ASTANA EXPO with a PV powered heidi.com logo in green on the back packpack.

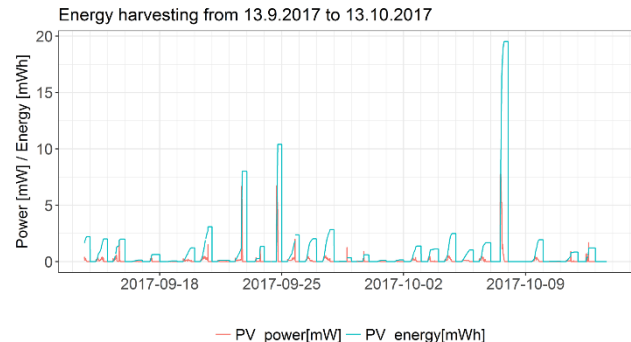


Figure 2: Several days acquisition of the energy produced by the PV label heidi.com on a back-pack.

A data-logging system has been developed to monitor the power produced by the integrated solar cells. The importance of such real-life use case study is paramount since it can help dimension the PV cell to power the targeted application. In Figure 2, daily energy production during a month for the backpack (from Figure 1) is shown.

The energy production depends a lot on the use case of the back pack. The energy production reaches only micro watt hours when the back pack is not used or when it stays the whole day indoors.

In contrast almost 20 mWh can be produced on a sunny day, by spending a couple of hours outdoor at the lakeside with the cell facing the sun. On normal days the energy production reaches up to 3.5mWh and the average energy production is around 1.5 mWh. The total energy production of the month showed in the diagram (Figure 2) is 71 mWh.

Depending on the color, the loss due to the aesthetic decoration of the cell is around 70%. So with no, partial or optimized decoration even more energy could be produced. By combining the cell with a battery and benefiting from the high production days, enough energy is produced to power different types of applications.

These can be purely new functions but also help engage customers through notifications and games. Typical new functions consists of powering sensors to send the user information on his environment: UV exposure, air pollution or noise level. Typical games on the other hand are useful in the context of the personalization of objects which in creative industries – advertising, marketing and design – can help engage the customers. This added energy can help power applications which provide the customers a rewarding experience, providing useful feedbacks, reminders or encouragements.

This project was funded by an EU-grant under the Project ID 644856 H2020-ICT-2014-1.

# Silicon Photovoltaics for Hydrogen Production

J.-W. Schüttauf, D. Dominé, A. Faes, M. Despeisse, C. Ballif, J. Bailat

The SHINE Nano-Tera.ch project aims at the realization of a fully integrated solar-to-hydrogen system using silicon solar cells. By using shingled modules based on silicon heterojunction solar cells, both extensively studied at CSEM, we have managed to obtain a solar-to-hydrogen conversion efficiency of 14.2%, which currently represents the highest efficiency for a design fully based on silicon solar cells.

Due to the intermittent nature of renewable energy technologies such as wind and solar, their large-scale implementation requires solving current challenges related to energy storage. A possible solution to elegantly store energy from sunlight in chemical bonds is the direct production of hydrogen using solar cells and water. The multidisciplinary Nano-Tera.ch project SHINE involves several research groups within different relevant fields<sup>[1]</sup>. CSEM is in charge of developing and optimizing the photovoltaic components of the system.

Thin-film silicon triple-junction devices have been developed to be coupled to electrolysis units. At one sun illumination, a power density of 11.3 mW/cm<sup>2</sup> has been obtained, leading to a potential water splitting efficiency of 8.1%<sup>[2]</sup>.

As reported last year, more straightforward solutions using silicon solar cells have also been studied (see Figure 1), such as a serial connection of silicon heterojunction solar cells using the shingling method (see Figure 2). With this approach, that is still rather novel in module fabrication, and predominantly developed at CSEM, cell-to-module losses for our devices that were tested in water splitting experiments were found to be as low as 0.2% absolute (around 1% relative). Furthermore, these modules have withstood thermocycling tests of 400 cycles ranging from -40°C to +85°C.

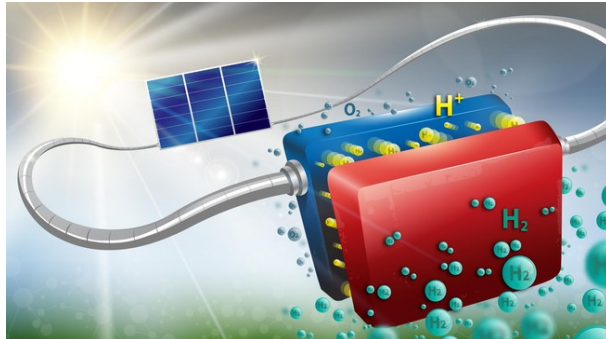


Figure 1: Artistic impression of our record solar-driven water splitting system<sup>[3]</sup>.

With our shingled modules, we have obtained a stable (> 100 h) solar-to-hydrogen conversion efficiency of 14.2% without DC/DC conversion, both with commercially available proton exchange membrane (PEM)-based electrolyzers, as well as with electrolyzers fully relying on and earth-abundant electrocatalysts<sup>[4]</sup>. This value currently represents the highest reported efficiency worldwide for solar-driven water splitting

based on silicon photovoltaics<sup>[3, 5]</sup>, surpassing the previous highest efficiency (9.8%) by over 40% relative.

Moreover, contrary to many other approaches presented in the literature, this solution also provides an excellent stability. Efficiencies up to 17% should be practically possible on the short term following our approach by intelligently connecting already existing products.



Figure 2: Shingled silicon heterojunction module of three cells connected in series. Due to the excellent alignment of adjacent cells, no space is lost, and aesthetics are improved.

As the components in the presented system are commercially viable, easily scalable and have long lifetimes, these devices have the potential to open a fast avenue towards the industrialization and deployment of cost effective solar-fuel production systems. As an example, a 12-14 m<sup>2</sup> system installed in Switzerland would allow the generation and storage of enough hydrogen to power a fuel cell car over 10'000 km every year. The approach should nowadays already allow for large-scale hydrogen production at a cost of ~CHF 3/kg, which is not yet compatible though with hydrogen production by steam reforming (which is currently the most common method to produce hydrogen, and which is based on fossil fuels). Further developments, increasing oil prices and climate policies could help to close this gap.

CSEM thanks Nano-Tera.ch for its financial support received in the framework of the RTD project SHINE.

[1] <http://www.nano-tera.ch/projects/367.php>

[2] D. Dominé, *et al.*, Proc. of WC PEC 6, Kyoto, Japan (2014).

[3] <https://actu.epfl.ch/news/an-effective-and-low-cost-solution-for-storing-sol/>

[4] J.-W. Schüttauf, M. A. Modestino, E. Chinello, D. Lambelet, A. Delfino, D. Dominé, A. Faes, M. Despeisse, J. Bailat, D. Psaltis, C. Moser, C. Ballif, *J. Electrochem. Soc.* 163, F1177 (2016).

[5] J. W. Ager, M. Shaner, K. Walczak, I. D. Sharp, S. Ardo, *Energy Environ. Sci.* 8, 2811 (2015).

# Light Management for Efficient Printed Tandem Solar Cells

T. Offermans, J. Mayer, M. Chrappa, G. Nisato, R. Ferrini

The activity on micro & nano optics at CSEM addresses the design and fabrication of light management structures for a variety of applications. Applying light management on the outer surface of thin film PV is a favorable method for efficiency enhancement, especially for already highly optimized PV stacks. The fabrication of such light management structures is compatible with roll-to-roll production techniques such as hot-embossing or UV NIL (Ultra-Violet Nano Imprint Lithography), thus making them an optimal cost-effective solution for thin film PV.

Light management has always been a crucial topic for thin film photovoltaics, where the thickness of the absorbing layer is smaller than the wavelength of the incident light preventing the full absorption of the incident sun light. Tandem solar cells are solar cells with two (or more) thin absorbing layers. Tandem solar cells are already highly optimized structures, both optically and electrically. The front and the back sub-cell in the tandem generally absorb complementary parts of the solar spectrum, which puts a constraint to the range of possible material combinations. Since their electrical characteristics have to be carefully matched as well, an additional constraint is imposed to their layer thicknesses. Therefore, further enhancement of the tandem cells efficiency may only come from external light management structures.

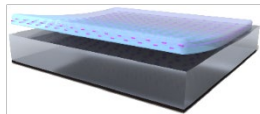


Figure 1: The external light management concept.

The use of additional optical structures on the surface of organic solar cells can give rise to a further increase of the cell efficiency originating from the redirection of incident light into steep propagation angles. As we have reported before<sup>[1,2]</sup>, thin film interferences caused by light at high propagation angles can lead to an enhanced efficiency in thin film PV devices. The redirection of the incident light can be realized by implementing a diffractive structure at the cell outer surface. Consequently our approach is not dependent on the absorption spectrum of the organic semiconductor but only linked to the device architecture, i.e. the tandem stack.

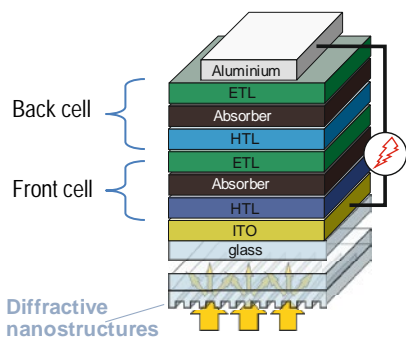


Figure 2: Stack of the tandem cell with additional light management structure.

Tandem cells were printed with the same photoactive absorber in the front and back sub-cell (Figure 2). Because of the low

charge mobility of the particular absorber used, the absorber layer thickness was limited to <150 nm. As a consequence a thicker single junction cell with this absorber material would be outperformed by a tandem stack in which two thin single junctions are stacked serially.

Optical simulations were performed to calculate the absorption as a function of the light propagation angle in the substrate (Figure 3). It can be observed that the angle dependent absorption for large diffraction angles is beneficial in different wavelength regions for the two sub-cells: whereas the back cell absorption can be enhanced moderately in a broad range 550-800 nm, by up to 50% enhancement is revealed in the range of 420-600 nm for the front cell.

Therefore, a light management nanostructure can be optimized such, that its diffraction pattern distributes the light in a best compromise of the two sub-cells. By these means an overall gain can be obtained, if the wavelength integrated absorption is considered. Optical simulations predict an enhancement of up to 9% with the nanostructure attached to the device surface.

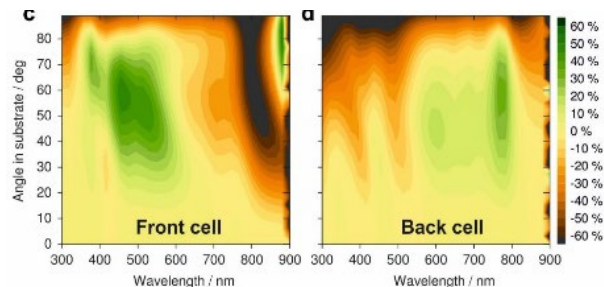


Figure 3: Absorption in-/decrease for redirected light for the front cell and for the back sub-cell with respect to straight incidence.

The nanostructure was fabricated on glass and attached to a glass-encapsulated tandem device. The device efficiency was improved by 9% (i.e. from 8.7% to 9.5%) in line with the simulated enhancement.

In conclusion, the use of diffractive nanostructures for light incoupling provides a solution that avoids electronic losses as it leaves the PV stack intact and is compatible with mass manufacturability. The approach thus offers a platform for various thin film photovoltaic technologies and applications and can therefore provoke increased research activity and interest from thin film PV producers.

CSEM gratefully acknowledges support from the EU project Sunflower (Nr. 287594) and the Canton of Baselland.

[1] J. Mayer, B. Gallinet, T. Offermans, R. Ferrini, "Diffractive nanostructures for enhanced light-harvesting in organic photovoltaic devices", Opt. Express 24, A358–A373 (2016).

[2] J. Mayer, B. Gallinet, T. Offermans, I. Zhurinsky, R. Ferrini, Sol. Energy, "Self-Contained Optical Enhancement Film for Printed Photovoltaics", Mat. Sol. Cells 163, 51–57 (2017).

# Sputtered Molybdenum Oxide as Hole Collector for Heterojunction Technology Solar Cells

G. Christmann, A. Descoedres, L. Barraud, N. Badel, M. Despeisse, S. Nicolay, C. Ballif

Heterojunction technology solar cells offer the highest reported efficiencies for crystalline silicon wafer-based devices. Despite their excellent performance, in particular a very high open circuit voltage, these devices exhibit some parasitic light absorption due to the use of doped amorphous silicon layers. Recently, it has been proposed to replace p-type amorphous silicon layers with high work-function transition metal oxides to improve solar cell performance. This project explores the use of molybdenum oxide deposited by sputtering as a hole selective contact within an industry compatible process.

Continuous improvement of crystalline silicon solar cells have brought them closer and closer to their theoretical maximum efficiency of about 29%. Indeed, their highest reported efficiency is currently 26.6%<sup>[1]</sup>. This record cell uses the heterojunction technology (HJT), which offers particularly high levels of passivation and thus high open circuit voltages. These devices nevertheless show some amount of parasitic light absorption due to the use of hydrogenated doped amorphous silicon (a-Si:H) layers to form the charge separation junction. As an illustration the record cell uses a back contacted scheme in order to reduce as much as possible front side light absorption losses. However, such technique requires costly and complicated patterning steps. It is therefore highly desirable to find a transparent selective contact for HJT solar cells that could "simply" replace the doped a-Si layers.

In this context, molybdenum oxide (MoOx) was recently proposed as an efficient hole contact for HJT solar cells, demonstrating above 22% efficiency<sup>[2]</sup> and improved short circuit current compared to a reference cell using p-type a-Si:H. The result was however obtained with non-industry standard techniques, namely thermal evaporation for MoOx deposition and copper electroplating for the grid. In this project, we explore the possibility to use a MoOx hole collector deposited by sputtering in a standard screen printed solar cell structure. In addition to the above-mentioned advantages, sputtering deposition of MoOx would be a less costly and less time consuming process than the deposition of p-type a-Si:H by plasma enhanced chemical vapor deposition.

In order to explore the potential of MoOx, it was included in a variety of structures:

- MoOx layer added to a standard i/p a-Si:H stack.
- MoOx layer added to an i/p a-Si:H stack with only one third of the nominal p thickness.
- MoOx layer added to an i a-Si:H layer for complete replacement of the p type a-Si:H layer.

By using these three configurations, we can observe the behavior of MoOx in gradually more and more constraining structures: the first one will allow to see if such layer creates electrical problems such as added series resistance, the two following ones will test the selectivity of the material for partial and total replacement of the p type layer.

Device results are presented, each time comparing a reference structure without MoOx to one with the MoOx layer. Regarding the structures with a standard i/p a-Si:H stack, it is seen that the

addition of a MoOx layer has nearly no effect on the power conversion efficiency (PCE). When reducing the p layer thickness, the reference device exhibit a very significant drop in PCE: the thinned down p layer is no longer selective enough, as a consequence, the open circuit voltage ( $V_{oc}$ ) is strongly reduced (not shown here). When adding the MoOx layer we see that the cell PCE is fully recovered to the standard cell level: this layer provides the extra selectivity. However, when fully removing the p type layer, the PCE dramatically drops as expected, and despite a significant increase with the addition of a MoOx layer, the efficiency remains very low, and not usable for a commercial device. Despite a clear effect on the selectivity ( $V_{oc}$  goes from below 300 mV to nearly 500 mV), we were unable to reproduce the results of evaporated MoOx with PVD MoOx in the absence of a p a-Si:H layer. However, an encouraging result is that we were able to deposit MoOx without sputtering damage, meaning that optimizing of the MoOx/i a-Si:H layer combination can lead to better devices.

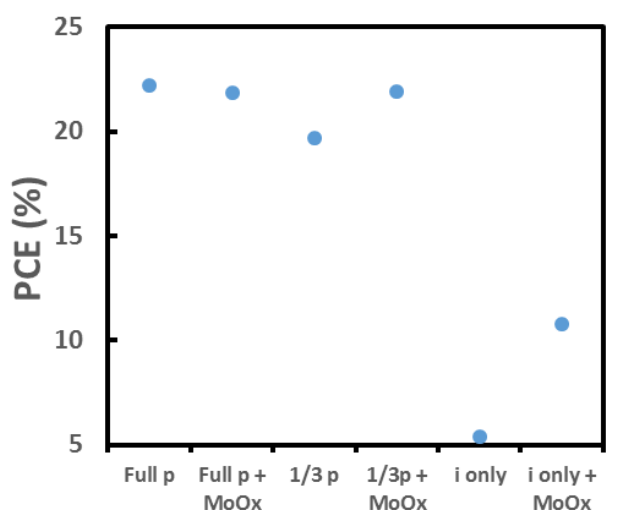


Figure 1: Power conversion efficiency (PCE) of the various structures tested during the project.

In conclusion, sputtered MoOx shows properties of a hole collecting material, and can be used to partially replace the p type a-Si:H layer in HJT solar cells. This can lead to reduced processing time and cost. It was however not possible to fully replace the p type a-Si:H layer, which is the ultimate goal and would have a great impact on the solar cell process flow and performance. Future developments will aim at optimizing the i-a-Si:H/MoOx stack as whole.

<sup>[1]</sup> <https://www.nrel.gov/pv/assets/images/efficiency-chart.png>

<sup>[2]</sup> J. Geissbühler, et al., Applied Physics Letters **107**, 081601 (2015).

# Passivating Contacts for High-efficiency Silicon Solar Cells

M. Despeisse, A. Descoedres, C. Allebé, N. Badel, L. Barraud, J. Champliaud, F. Debrot, A. Faes, A. Lachowicz, J. Levrat, B. Paviet-Salomon, L. L. Senaud, J. Horzel, G. Christmann, L. Ding, S. Nicolay, A. Ingenito<sup>•</sup>, G. Nogay<sup>•</sup>, P. Loeper<sup>•</sup>, C. Ballif

CSEM has set up a complete R&D platform for the fabrication and the characterization of high efficiency silicon solar cells. Innovative and industry-relevant solutions are developed for the improvement of all cell processing steps, aiming for high conversion efficiencies at competitive costs. Strong emphasis is set in CSEM and EPFL laboratories on jointly developing passivating contacts to minimize recombination losses between silicon and metallization, following two approaches: a first one is based on hydrogenated amorphous silicon (low-temperature hetero-contact as used in heterojunction solar cells), while a second one is based on a thin oxide layer topped by silicon layer (high temperature passivating contact). High passivation levels are achieved with both approaches, translated into up to 23.9% cell efficiency for both-sides contacted silicon heterojunction solar cell fabricated in CSEM R&D platform, and into promising high temperature contacts achieved by EPFL.

CSEM brings to maturity materials, processes and technologies for the definition of next generation high performance and cost effective crystalline silicon (c-Si) solar cells. The main limitations in conversion efficiency of standard c-Si solar cells originate from the recombination losses between the silicon and the metallization. To limit these losses, CSEM develops so-called passivating contacts, enabling to achieve increased operating voltages, following two different technological routes.

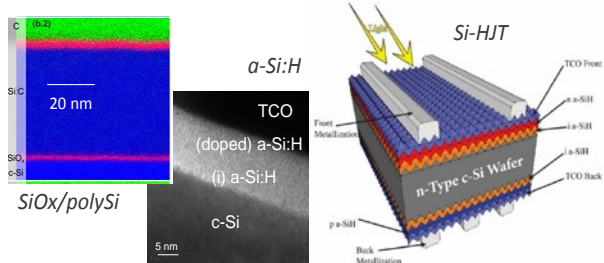


Figure 1: TEM images of high temperature passivating contact based on oxide/polySi structure (left) and of an a-Si:H based passivating contact (middle). Schematic of a Si-HJT solar cell architecture (right).

First, a strong focus is set on hydrogenated amorphous silicon (a-Si:H) based passivating contacts. Intrinsic a-Si:H layers are deposited on the silicon wafer surfaces, providing excellent chemical passivation: carrier lifetime >30 ms could be achieved with CSEM a-Si:H layers on 250  $\mu\text{m}$  thick Fz wafers (resistivity of 4 Ohm·cm). Then, doped-a-Si:H layers allow for the selective collection of carriers, with p-type doped layer acting as hole selective contact, and n-type doped layer as electron selective contact. Transparent conductive oxide layers are further deposited on both-sides of the wafer on top of the a-Si:H layers, and must demonstrate excellent trade-off between optical and electrical performance. CSEM developed high mobility layers based on a large variety of materials (ITO, IZO, IWO, ICO, AZO...), with highest mobility achieved with IO:H up to  $120 \text{ cm}^2/(\text{V}\cdot\text{s})$ . Low-temperature metallization is finally applied to complete the passivating hetero-contacts, and CSEM developed full processes and strong expertise for fine-line Ag printing (printing down to 20-30  $\mu\text{m}$  openings) and for Cu plating (high adhesion with low tensile stress Cu deposit).

Solar cells implementing these passivating hetero-contacts define the silicon heterojunction technology (Si-HJT), with targeted cell efficiency levels >23.5% over full-area wafers using competitive production processes. This cell technology has the decisive advantages to combine high efficiency (potential for >21%

modules) with limited number of production steps (pre-requisite for keeping reduced costs). The technology exhibits a low temperature coefficient (< -0.3%/°C) as well as a high bifaciality (> 90%), triggering high energy yield for bifacial Si-HJT modules in the field. Calculations show that, with Si-HJT solar cells, the average levelized costs of energy could be below 4 €cts/kWh in sunny countries<sup>[1]</sup>. CSEM has developed a complete, performant and flexible platform covering all aspects of production and characterization of Si-HJT solar cells, from as-cut wafers to finished devices optimized for module integration. This technological platform allows CSEM conducting advanced R&D projects to develop new processes, materials, production and metrology equipment, as well as advanced concepts for improved performance, and/or reduced production costs; and also to provide services and small batch production for its customers. In 2017, CSEM engineered the heterocontacts materials and interfaces, so as to maintain high passivation properties while enabling for low-contact resistance and high transparency. Electron-selective and hole-selective contacts were further developed and integrated in silicon heterojunction (Si-HJT) solar cells, with efficiency demonstrated up to 23.9%.

Table 1: I-V parameters of CSEM best Si-HJT solar cell.

HJT cell CSEM	Voc mV	FF %	Jsc mA/cm <sup>2</sup>	EFF %
4 cm <sup>2</sup> Front emitter	728	81.2	40.47	<b>23.9</b>

Second, solutions for passivation of the contacts are developed to extend the learning curve of diffused c-Si cells production lines (in which gettering and hydrogenation of "dirty" silicon materials can be advantageous) with the integration of few additional process steps to limit the contacting recombination losses, by providing full-area passivating contact at the rear of the cells, as well as front-side passivated contacts under the fingers metallization. CSEM and EPFL developed electron and hole selective contacts, based on a thin oxide layer on which a silicon layer is deposited by PECVD, followed by dedicated thermal management. The contacts developed demonstrate high passivation and low contact resistance, with VOC = 727 mV and FF = 84% achieved by EPFL for a cell on a flat wafer implementing both hole- and electron-selective high temperature passivating contacts. Further developments are focusing on adapting such carrier selective junctions, for electrons and holes, to textured surfaces, and to achieve high transparency for front-side application.

• EPFL/IMT/PVLAB laboratory

[1] A. Descoedres, et al., Energy Procedia, 77, 508 (2015).

# Simple Processing of Back-contacted Silicon Heterojunction Solar Cells Based on Selective-area Nanocrystalline Silicon Growth

B. Paviet-Salomon, A. Tomasi<sup>•</sup>, D. Lachenal<sup>••</sup>, L. Barraud, A. Descoeuilles, G. Christmann, N. Badel, J. Geissbühler, A. Faes, B. Strahm<sup>••</sup>, S. Nicolay, C. Ballif, M. Despeisse

In collaboration with EPFL and Meyer Burger Research, CSEM is developing the next generation of back-contacted silicon heterojunction solar cells, aiming at demonstrating top-level conversion efficiencies with a cost-effective process flow.

Crystalline silicon solar cells implementing passivating contacts based on hydrogenated amorphous silicon and transparent conductive oxide layers demonstrate the key advantage of increased operating voltages, as demonstrated in CSEM silicon heterojunction solar cell (SHJ) platform. In addition, maximum optical performance can be achieved using an all back-contacted solar cell architecture, providing no metallization shadowing at the cell sunny-side. The back-contacted silicon heterojunction (BC-SHJ) architecture therefore represents one of the silicon solar cell approach with the highest efficiency potential, combining optimum electrical and optical performance. This was demonstrated in 2017 with the achievement by Kaneka, Japan, of the world-record conversion efficiency of 26.7% for a silicon solar cell using such BC-SHJ architecture. However, the successful industrial spread of BC-SHJ devices is impeded by their complex and delicate process flow, usually involving several costly photolithography steps, to realize the patterned rear contacts. In the frame of the European project "NextBase", CSEM, in close collaboration with EPFL and Meyer Burger Research, is developing the next generation of BC-SHJ devices, targeting high conversion efficiency along with a cost effective process flow.

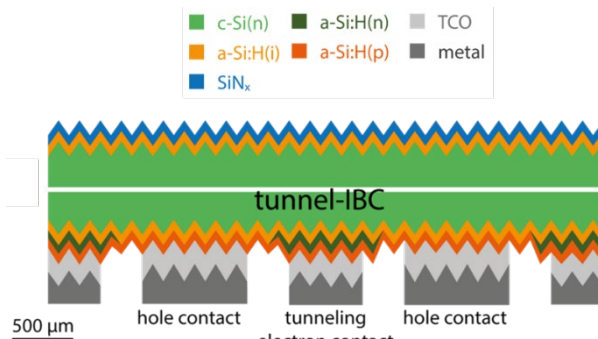


Figure 1: Schematic cross-section of the tunnel-IBC concept developed at CSEM.

CSEM developed and patented a novel BC-SHJ architecture, named "tunnel-IBC", featuring an interband silicon tunnel junction at the electron-collecting regions. In contrast to conventional BC-SHJ devices, where both the electron- and the hole-collecting fingers have to be patterned and aligned, in the tunnel-IBC concept only the electron collector is patterned. An overlaying full-area hole collector is then deposited. As a consequence, a tunnel junction is formed at the electron-collecting regions. Therefore, to work efficiently, the tunnel-IBC device requires an efficient carrier transport through the tunnel junction, and a low lateral conductance within the hole collector in order to avoid shunts between the electron- and hole-collecting regions. The key enablers of the tunnel-IBC technology are nanocrystalline silicon layers featuring anisotropic crystalline

growth, hence simultaneously fulfilling the two above-mentioned contrasting requirements. Our innovative tunnel-IBC architecture dramatically simplifies the process flow of BC-SHJ devices as it eliminates the hole collector patterning as well as its alignment to the electron collector. This novel design is thus a major step towards cost-effective processing of BC-SHJ devices.

As a major achievement, CSEM fabricated in 2017 a 23.9% efficient lab-scale tunnel-IBC solar cell ( $25\text{ cm}^2$ ). The current-voltage curve of this record device is plotted in Figure 2. Numerical simulations show that efficiency above 26% are reachable with the tunnel-IBC concept. These results demonstrate the high efficiency potential of the tunnel-IBC technology developed at CSEM.

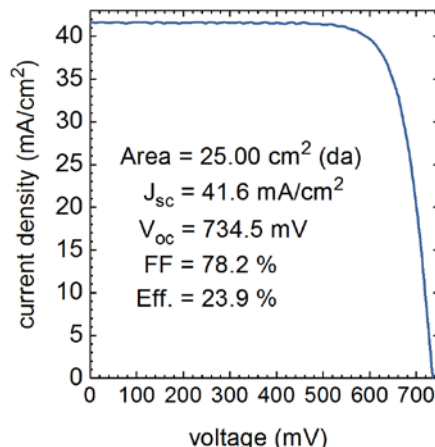


Figure 2: Current-voltage curve of the 23.9%-efficient record BC-HJT device jointly developed by CSEM, EPFL and Meyer Burger Research.

The upscaling of this process flow to full 6-in wafers devices is currently carried out at the Meyer Burger Research facilities. The first large area tunnel-IBC prototypes – obtained using mass production tools – demonstrated  $J_{sc} > 40\text{ mA/cm}^2$  and  $V_{oc} > 715\text{ mV}$ , hence showing that the tunnel-IBC technology has the potential for producing industrial BC-SHJ devices in a cost effective way in the coming years. Strong focus is now set to achieve higher performance by further reducing series resistance of the devices.

Future work also focuses on the metrology and on the integration of the developed solar cells. Dedicated contacting units are being developed, while a module architecture specifically designed for BC-SHJ devices, based on the Meyer Burger SmartWire® technology, is being developed to efficiently integrate the cell developments into the final product.

This work is funded by the European Union's Horizon 2020 Programme for research, technological development and demonstration under Grant Agreement no 727523.

• EPFL, IMT, PV-Lab

•• Meyer Burger Research

# Contacting Solutions for the Measurements of Next Generation Solar Cells

J. Levrat, J. Geissbühler, A. Faes, J. Champliaud, P. Häfliiger, V. Fakhfouri •, N. Bassi •, R. Ambigapathy •, C. Ballif, M. Despeisse

CSEM and PASAN have developed an innovative metrology solution for solar cell testing, called the PCBTOUCH. It allows measuring a large variety of silicon wafer-based solar cells, even those featuring complex metallic patterns, such as busbarless cells, metal wrap through (MWT) cells, interdigitated back contacted (IBC) cells, quarter or half cells, cells on ultra-thin wafers and any other type of bifacial cells. The contacting unit is based on a printed circuit board (PCB) optimized for each type of device, ensuring optimum electrical contact with the back of the cell, whereas the front contact is established with the already-existing GRIDTOUCH solution, i.e. a slightly bent bottom plate and featuring a grid of spring loaded wires.

The increasing pressure on photovoltaics cells and modules manufacturers regarding costs and efficiencies is considerably affecting the spectrum of cell and module technologies penetrating the market. The standard monofacial Al-BSF (Back Surface Field) cell is being gradually replaced by more advanced cell architectures such as PERL (Passivated Emitter Rear Locally Diffused), PERC (Passivated Emitter and Rear Cell) or heterojunction (HJT) but also cells featuring alternative designs, sizes or shapes, depending on the module technology, like shingling, half or quarter cells, and busbarless cells. The power rating of solar cells is facing new challenges that arise from these advanced designs. The most serious issue appears for bifacial devices featuring complex back metallization, such as busbarless, as well as for IBC (Interdigitated Back Contact) or MWT (Metal Wrap Through) cells. The standard multi-busbar IV probe station becomes more and more obsolete and a dedicated solution must be adapted for each individual cell design.

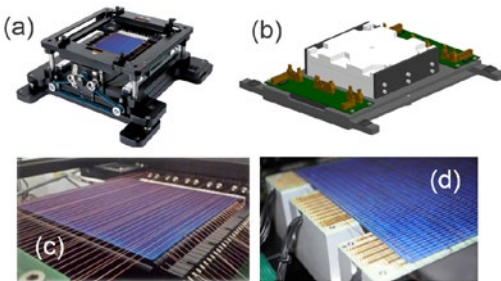


Figure 1: a) GridTOUCH frame; b) PCBTOUCH unit (lab version); c) Laboratory version of GridTOUCH unit, and d) production-line version of the PCBTOUCH.

To address these challenges, a new contacting solution called PCBTOUCH is presented. It is based on GridTOUCH (see Figures 1a and 1c), a bent station with spring loaded wires to contact the front side, and a custom printed circuit board (PCB) to contact the back side (see Figures 1b and 1d).

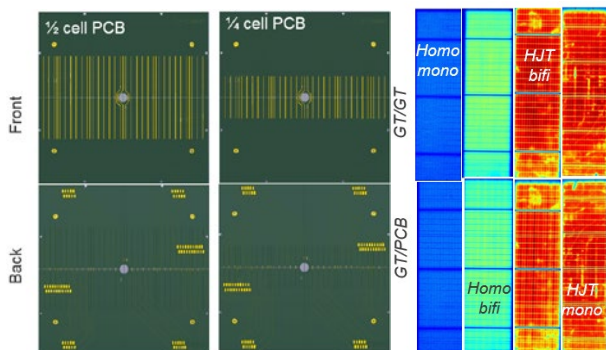


Figure 2: (Left) Front and back side of PCBs contacting half and quarter cells; (Right) EL measurements on homojunctions and heterojunctions cells featuring monofacial and bifacial ("bifi") collection designs.

The combination between these two patented innovations, developed by PASAN with the support of CSEM, offers flexible and reliable solution for the measurement of any cell design. The PCB at the rear replaces the back wires, ensuring a maximum compatibility with any type of cell metallization. An example is shown in Figure 2. These two PCBs allow the efficient contacting of half and quarter cells. Electroluminescence measurements (Figure 2, left) performed on various types of cells (monofacial and bifacials, homojunctions and heterojunctions) reveal the excellent homogeneity of the contacting.

The quality of the contacting and the high versatility of the PCB approach is evidenced by the contacting of IBC cells featuring an extremely small finger pitch (see Figures 3a and 3b). A one-to-one contacting and a non-repeatability on cell efficiency below 0.2% (0.5% are required to for qualification) is demonstrated with a very simple mechanical alignment procedure (see Figure 3c). A hole in the PCB allows an optical alignment check that can be used in production environment (see Figure 3d).

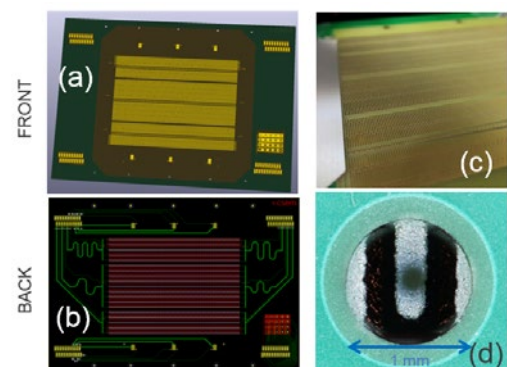


Figure 3: a) & b) Front and back side of the IBC PCB; c) & d) Mechanical and alignment procedure for cell measurement.

The success of the PCB approach for laboratory environment has been extended to industrial environment. Test PCBs have been designed with interruptions allowing their integration in production line. These interruptions allow the passage of conveyor belts.

The developed advanced contacting unit demonstrates therefore high reproducibility of contacting for varying and challenging cell designs, with the ultimate demonstration of high performance measurements for IBC solar cells, confirming the quality of the developed metrology concept. CSEM and PASAN therefore provide advanced characterization technologies to fulfill metrology needs for next generation silicon based solar cells.

This work was funded by the CTI in the frame of the COMET project.

# A PV Encapsulant Formulation Customized for Low-temperature Lamination Process

H.-Y. Li, J. Escarré, K. Söderström, L.-E. Perret, C. Ballif

A customized encapsulant formulation has been developed at CSEM to adapt the low-temperature lamination process of PV modules, addressing the specific needs of temperature sensitive PV technologies. This encapsulant has been validated to be processable at 85 °C in the standard PV laminator. The resulting glass-glass PV module shows superior creep resistance at up to 110 °C, strong encapsulant/glass peeling strength over 100 N/cm, negligible discoloration after 1000 hours of UV exposure (further tests ongoing). The UV cut-off wavelength can be adjusted up to 400 nm.

The lamination of PV modules is mostly carried out with a flat-bed vacuum-bag laminator. In the standard lamination process, the hot plate temperature is normally set at 140 to 170 °C in order to allow the melting or softening of the encapsulant so that sufficient viscoelastic property can be reached to ensure the quality of the lamination. In the case of conventional EVA (Ethylene-Vinyl Acetate)-based encapsulant, the lamination temperature needs to be sufficiently high to initiate the crosslinking reaction during the module lamination step. However, in recent years, the emerging cell or module technologies, e.g., dye-sensitized solar cells or perovskite cells, demand a low-temperature lamination process at temperature much lower than the standard and ideally at the temperature below 90 °C. Low-temperature lamination of PV modules have been shown to be possible at even room temperature by applying liquid-silicone-based encapsulant. However, this approach in most cases is not favored by the module manufacturer due to the additional investment in equipment and process development.

Here in this activity, the objective is to develop an encapsulant formulation that can be laminated at 90 °C in the standard flat-bed vacuum-bag laminator. The laminated module has to withstand the creeping test and the accelerated module degradation tests according to the specific PV and building norms. There exists a conflict on the desired encapsulant material viscoelastic property for the processability and the creeping resistance. The processability demands sufficiently low viscosity (high Tan Delta) in order to ensure enough flowability during the lamination process. However, as the creeping test takes place at the temperature of 90 to 110 °C, the viscoelastic property favored by the processability will cause poor material creeping resistance. This dilemma can only be conveniently solved by introducing crosslinking reaction in the encapsulant during or after the module lamination process.

The chemical crosslinking is normally implemented by means of peroxide curing, radiation curing, etc. As the radiation curing needs additional equipment and processing steps which complicate the module manufacturing process, it is not investigated in details here.

In the case of peroxide curing, the challenge is to identify a peroxide that can efficiently initiate the curing reaction in EVA at 90 °C. Subsequently, the peroxide needs to be compounded into the EVA base resin. At CSEM, a commercially available peroxide has been found to be able to initiate the crosslinking of EVA at 90 °C within one hour. The resulting glass/glass laminate can withstand the creeping test at 11 °C. The major issue with this solution is the high haziness of the film after lamination, which is an intrinsic problem of the peroxide selected. Besides that, the compounding process can be done with the twin-screw compounder in the lab scale. However the scorch-free extrusion process window is so narrow that practically it is highly challenging to implement this approach in production scale. The other way of compounding is via powder lamination, in which

case the additional equipment and processing step are unavoidable.

One PO (polyolefin)-based encapsulant formulation has been developed for this activity. The processability of this formulation has been validated at 90 °C within one hour lamination cycle time. The characteristics of the resulting laminates are as follows:

- No visual defect (bubble, discoloration).
- The peeling strength from the glass >100 N/cm.
- Creeping resistance 0 at temperature up to 110 °C; 0 at 85 °C and 85 RH%.
- Haze at 400 nm <10% before DH, <20% after 1000h DH.
- Yellowing after 1000 h QSUN < 5, invisible discoloration.

For certain cell/module technologies, the high UV cut-off wavelength is necessary for protecting the other components from UV degradation. In this activity, additives have been selected to reach the cut-off wavelength over 380 nm, as is shown in Figure 1. The cut-off wavelength can be adjusted from below 300 nm to close to 400 nm by the selection of different additives.

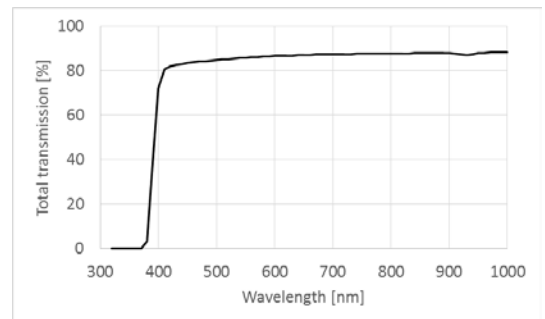


Figure 1: The total transmission of the developed PO encapsulant for low-T lamination process. Here the UV-cut off wavelength has been formulated to be above 380 nm.

The developed formulation is being upscaled for the production trials. This development can be used for particular cell technologies, as well as where additional module component needs to be laminated on a laminated module. As this second lamination step will take place at 90 °C or below, the module laminated with typical EVA encapsulant will not be influenced. A patent on this development is in preparation.

This development is a good example of the versatile functional encapsulant formulations that the CSEM compounding platform can offer to answer the needs of different applications.

# How Does a Substrate Plasma Pre-treatment influence electrical properties of a TCO Film?

I. Marozau, K. Vaideeswaran, G. Christmann, S. Nicolay, J. Dutson •, M. Hopkins ••, D. Allsopp ••, M. Dadras, O. Sereda

Within the current project CSEM has performed a detailed study of the microstructural evolution of the interface between doped ZnO layers grown on GaN substrate for LED applications. This microstructural investigation was combined with the pre-processing history, and electrical properties of the layers, yielding a detailed understanding on the interplay between the processing parameters, the microstructure and its effect on the electrical behavior of ZnO/GaN interfaces. The obtained results help to optimize the fabrication process of ZnO-based transparent conducting oxide layers.

Shortage of availability and increasing cost of indium impose a serious threat for electronic industry, which widely uses tin-doped indium oxide (ITO) as a transparent electrode for various areas of application. These include organic and inorganic light emitting diodes (LED), touch-screen displays, flexible electronics, and solar cells. Therefore, there is a growing demand in sustainable and low-cost alternatives to ITO for the abovementioned applications. The alternative materials shall exhibit similar functional properties (i.e. high transparency for visible light and low resistance) combined with high availability, low-market price, and reduced environmental impact in comparison to ITO.

Currently, among the high potential alternatives are ZnO doped with B or with Al (AZO), which have been shown to fulfil the required functional criteria<sup>[1]</sup>. Nevertheless, the integration of such a material with existing electronic devices remains a challenge owing to the high influence of the interface phenomena<sup>[2]</sup>. Specifically, in the case of GaN-based LEDs, the interfacial microstructure and properties can intervene heavily in the functional properties of the layer such as interfacial resistance and I-V characteristics. These properties may be modified by varying the deposition process parameters, as well as the pre-deposition treatment steps.

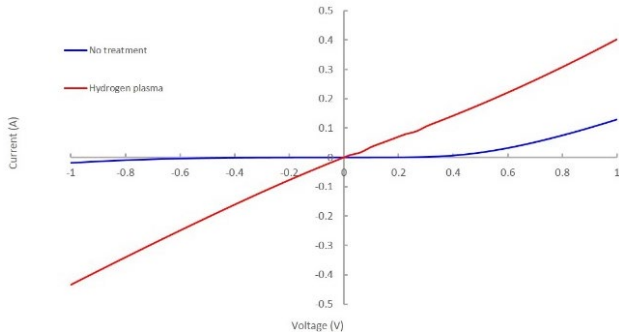


Figure 1: I-V characteristics of AZO/GaN interfaces with and without H<sub>2</sub>/N<sub>2</sub> plasma pre-treatment of GaN surface.

It was found that heterostructures composed of AZO layers grown on pre H<sub>2</sub>/N<sub>2</sub> plasma treated GaN surface present good ohmic contacts. Similar structures fabricated without the H<sub>2</sub>/N<sub>2</sub> plasma pre-treatment step exhibit poor contact characteristics (Figure 1). In order to understand the interplay between the

processing parameters and the electrical characteristics of the AZO/GaN contacts, CSEM has performed a detailed microstructural investigation of the corresponding interfaces by means of transmission electron microscopy (TEM). Figure 2 shows two typical micrographs of the AZO/GaN interfaces cross-section prepared by focused ion beam thinning technique and observed by TEM. The sample with H<sub>2</sub>/N<sub>2</sub> plasma pre-treatment exhibits a polycrystalline AZO layer with columnar crystallites that are nucleated on pyramidal bumps present at the GaN surface (Figure 2, left). These bumps are not observed in the sample without H<sub>2</sub>/N<sub>2</sub> plasma pre-treatment. As a result, the nucleation of AZO crystallites at the interface with GaN is suppressed leading to a different growth mode. In this case the formation of a ~50 nm thick layer of nanocrystalline material at the substrate surface before the development of the columnar microstructure is observed (Figure 2, right).

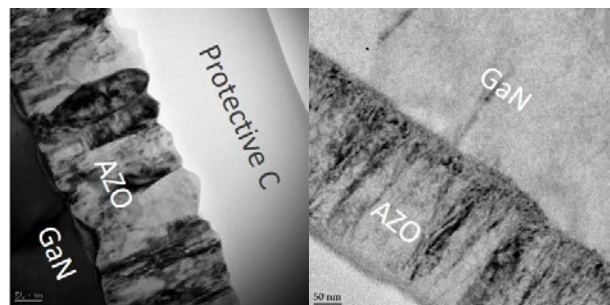


Figure 2: TEM cross-section of AZO / GaN interfaces for the samples deposited with (left) and without (right) H<sub>2</sub>/N<sub>2</sub> plasma pre-treatment of the substrate.

The microstructural differences at the AZO/GaN interface help to explain the role of H<sub>2</sub>/N<sub>2</sub> plasma pre-cleaning step for obtaining a good ohmic contact between the functional AZO layer and the substrate (Figure 1). In addition to surface "cleaning" from the possible organic residuals and contaminations, the plasma treatment also facilitates the formation of a thin nanocrystalline AZO layer at the interface with GaN, which enables easier electron transfer through the interface border. The obtained results are the key factor in further optimization of the fabrication procedure of ZnO-based transparent conducting oxide materials for LED applications.

- Plasma Quest Ltd, Unit 1B Rose Estate, Osborn Way, Hook, Hampshire, RG27 9UT, UK
- Department of Electronic and Electrical Engineering, University of Bath, Claverton Road, BA2 7AY, Bath, UK

[1] Y. S. Choi, et al., IEEE Transactions on Electron Devices; 2010, 57(1), 26-41.

[2] D. K. Hwang, et al., Applied Physics Letters; 2005, 86, 222101.

# NeuroCool—Smart Air Conditioning, Pay Less for a Better Comfort

Y. Stauffer, E. Olivero, E. Onillon

Smart control strategies can significantly lower operational expenses for heating, ventilation and air conditioning (HVAC) in buildings. Through the Neurocool CTI project, CSEM has developed a novel model predictive controller (MPC) which minimizes these operating costs while maintaining or improving user comfort. This controller has already been validated in regular office buildings.

Energy use for air conditioning and cooling is steadily increasing. Options to contain or reverse this trend include building refurbishment (long and costly), changes in user behavior (hard to engineer), and smart control of heating, ventilation and air conditioning (HVAC) systems. In that context, CSEM with its industrial partner Neurobat AG and research partner HEIG-VD initiated the Neurocool project with funding from the Swiss Commission for technology and innovation (CTI). This project consists in extending to ventilation and air conditioning the model predictive control (MPC) technology previously introduced by Neurobat for heating. The objective of this control technology is to reduce the energy consumption while maintaining or improving user comfort<sup>[1]</sup>.

There are two main differences in terms of control between heating and air conditioning. The first difference is in the number of control variables: only one for heating (the temperature of the circulating fluid), and up to three for air conditioning (the temperature, humidity and flow rate of the pulsed air). The second difference lies in the respective time constants of the systems: for heating they range from hours to days whereas for air conditioning they are between tens of minutes and hours.

To minimize the energy consumption of the HVAC unit while providing comfortable conditions to the user, we use an MPC approach. A self-learning thermal model of the building is at the heart of this approach. At each time step, future ambient conditions in the building are forecast, based on the current state of the building and forecast perturbations (e.g., weather), under various scenarios for the control variables. The optimal scenario is selected by looking for the minimal value of an objective function.

In this project, the objective function has two components, energy cost and user comfort, whose balance can be changed through a regularization parameter,  $\lambda$ . The optimized control variables are the temperature, humidity and flow rate of the pulsed air. Set constraints ensure compliance with operational requirements (comfort boundaries and system dynamics)<sup>[2]</sup>. Variations in cooling and dehumidification loads due to occupancy are treated as a perturbation by the optimizer.

After a successful validation in simulation, the Neurocool controller was deployed on three distinct sites. The first site is a climatic chamber in HEIG-VD. There, values of  $\lambda$  were manually varied between 0.0175 and 100 and the resulting comfort levels were monitored (Figure 1). In these experiments, the cooling load due to building occupancy was emulated. For low values of  $\lambda$  the

measured temperature/humidity in the room reaches the admissible boundaries, whereas for high values of  $\lambda$  a good comfort is obtained.

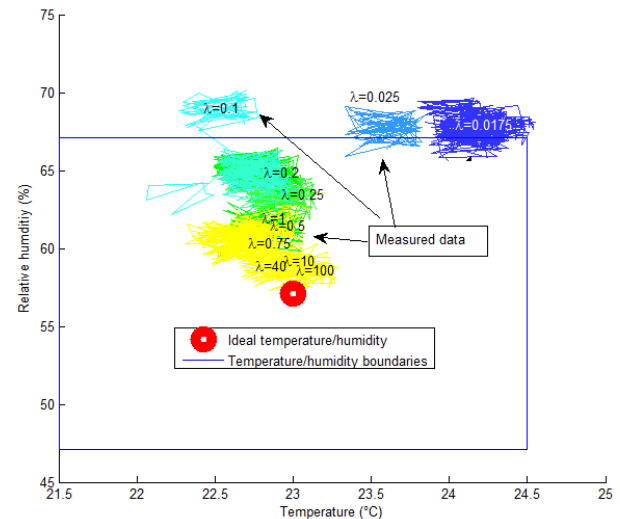


Figure 1: Measured trajectory of indoor temperature and humidity for various values of the regularization parameter,  $\lambda$  (dark blue: lowest; yellow: highest). The blue box corresponds to the comfort boundaries set as constraints.

The other two test sites were office buildings in Switzerland: one in Neuchâtel (CSEM headquarters) and one in Winterthur. In both cases, the Neurocool controller provided the expected comfort levels and proved robust against real user behavior, such as opening of windows and doors and variations in occupancy. The tests demonstrated energy savings between 12% (temperature control only) and 48% (temperature and flow-rate control) with at least the same level of user comfort. This dispersion in energy savings comes from two main reasons. First, the controllability of test sites varies; when it can act on the flow rate as well as on air temperature the MPC can find more energy-efficient solutions. Second, the accuracy of weather forecasts varies between sites, which directly affects the quality of the solution computed by the MPC<sup>[3]</sup>.

This project demonstrated that MPC can be successfully used for HVAC control thanks to a self-training thermal building model. With this distinctive model, deployment is simple and reliable since it does not require any manual adjustment. Neurobat AG is currently working on integrating the Neurocool features with the existing heating regulation in their product range.

[1] D. Lindelöf, Y. Stauffer, "De l'air frais à moindre frais", Bull. SEV-AES, pp. 27–30 (2017).

[2] Y. Stauffer, E. Olivero, S. Arberet, E. Onillon, L. Von Allmen, C. Mahomed, D. Lindelöf, "NeuroCool: an adaptive, model-predictive control algorithm for ventilation and air conditioning systems," Clima 2016 (2016).

[3] Y. Stauffer, E. Olivero, E. Onillon, C. Mahomed, D. Lindelöf, "NeuroCool: field tests of an adaptive, model-predictive controller for HVAC systems," Energy Procedia 122, 127–132 (2017) [doi:10.1016/j.egypro.2017.07.316].

# Management of District Heating and Cooling

E. Olivero, Y. Stauffer

*District heating and cooling systems are among the technologies with the highest potential of achieving EU climate and energy goals. Leveraging on its experience in model predictive control for thermal management of buildings, CSEM is working alongside its European partners for the development of novel management strategies to be deployed at district level.*

Space heating and domestic hot water production account for 79% of total final energy use in EU households, representing 192.5 Mtoe (million tons of oil equivalent) in 2016. In industries, around the same amount of energy (193.6 Mtoe) is used for space and industrial process heating. For comparison, the cooling demand in EU is rather small (24.5 Mtoe) even though trends show a significant growth. Today, only 16% of this energy is produced by renewable energy sources<sup>[1]</sup>.

District heating and district cooling have enjoyed increasing attention in the last years as one of the favored systems to achieve the ambitious EU's climate and energy goals<sup>[2]</sup>. In fact, district heating and cooling can benefit from waste heat produced in industrial processes or cogeneration plants, thus reducing the primary energy consumption needed for space conditioning. Generation systems located at district level reportedly have a lower primary resource factor (PRF i.e., ratio between the required energy from non-renewable resources to heat or cool a building and the final energy supplied) compared to systems located at building level<sup>[3]</sup>. Nevertheless, due to the high initial capital investment required, country-specific regulations, and legal and technical risks, district heating represents only 9% of heating in the EU<sup>[4]</sup>, while the share of district cooling is only 1%<sup>[5]</sup>. To reduce the energy consumption related to space conditioning in the short run, it is therefore important to act at building level, by boosting the retrofit of inefficient equipment and reducing waste thanks to smart management. At the same time, as the barriers to deployment of district heating and cooling are progressively lowered, we need to prepare for the future by leveraging our knowledge of building-related systems to develop novel technologies and control strategies that can further lower the district overall PRF and can improve the system reliability.

In line with this strategy, CSEM is focusing on the following topics:

- At building level – development of smart thermostats, gathering data from the environment and using the extracted information to optimally control the technical systems. In past projects such as Neurobat and Neurocool we have demonstrated that energy savings up to 28% can be achieved without degrading the occupants comfort for water-based heating systems<sup>[6]</sup>, while savings of 12% to 48% can

be achieved for air conditioning systems. In INDIGO, a H2020 project on district cooling technologies, we will expand our smart thermostats portfolio to include control of complex ventilation and air conditioning systems. A field demonstration in a hospital building in Spain will be performed in 2018.

- At building and district level – development of algorithms for real-time management of thermal energy at building and district levels ensuring an efficient balance between energy supply and demand. This is achieved at building level by leveraging the thermal storage potential of buildings through wall inertia and hot water tanks to absorb the production from renewable sources (Figure 1, local control). At district level, short-term storage in the distribution system, as well as in buildings, is used for thermal peak shaving to avoid the use of inefficient peak-load plants. Finally, forecasting algorithms are used to predict the cooling and heating demand and accordingly schedule the optimal operation of the production systems to minimize waste (Figure 1, DC system optimization and central control).

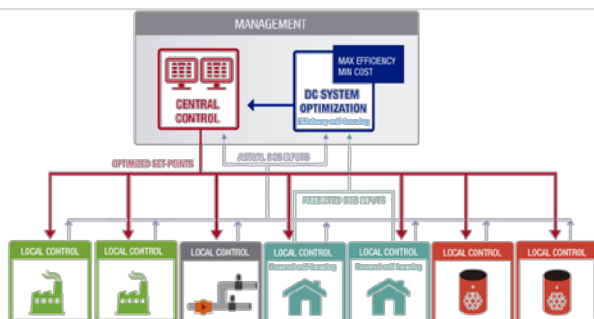


Figure 1: Management system for smart district cooling.

- At district level – seasonal (i.e., long-term) storage can be performed exploiting boreholes. In the frame of the Eurostar project DEBORAH, CSEM is developing a control software platform relying on advanced simulation models at building, district and plant level, cloud computing resources, and advanced algorithms to optimally control the use of such systems. This is mandatory to obtain energetic efficiency and maintain the borehole in its best operational range.

[1] "Heating and cooling," Eur. Comm. - Energy, <https://ec.europa.eu/energy/en/topics/energy-efficiency/heating-and-cooling>.

[2] European Commission, "A framework strategy for a resilient energy union with a forward-looking climate change policy," Communication COM(2015) 80 final, European Commission, Brussels (2015).

[3] Euroheat & Power's Task Force on eco-labelling, "Guidelines for assessing the efficiency of district heating and district cooling systems," Euroheat & Power, Brussels (2016).

[4] European Commission, "An EU strategy on heating and cooling," Communication COM(2016) 51 final, European Commission, Brussels (2016).

[5] A. Tvarne, H. Frohm, A. Rubenbag, "EU district cooling market and trends," RESCUE project (2013).

[6] D. Lindelöf, H. Afshari, M. Alisafaee, J. Biswas, M. Caban, X. Mocellin, J. Viaene, "Field tests of an adaptive, model-predictive heating controller for residential buildings," Energy Build. 99, 292–302 (2015) [doi:10.1016/j.enbuild.2015.04.029].

# Automated Quantification of PV Hosting Capacity

W. Martin, P.-J. Alet, A. Hutter

CSEM has developed a plugin for the grid simulation program Digsilent PowerFactory. This plugin rapidly and accurately computes the maximum allowable photovoltaic (PV) power in a low-voltage distribution network. Users can also define through this tool control strategies to be applied in the network, and quantify their effects on power quality and hosting capacity. This software solution supports both grid planning by distribution support operators, and technology development in relation to inverter control, demand response and distributed storage.

Distribution system operators (DSOs) see an increasing number of requests for connecting distributed photovoltaics (PV) to their networks. In combination with power quality issues related to the high penetration of PV, such as voltage rise and reverse power flows, this growth makes the task of these DSOs more complicated. Indeed, DSOs should go through strenuous impact studies before approving the installation of PV systems. Many of these companies avoid these procedures and choose instead a very conservative approach to authorizing PV connection and may mandate hardware upgrades to the grid. As a result, deployment of renewable energy sources is slowed down, costs are increased and electrical capabilities of the grid are underused.

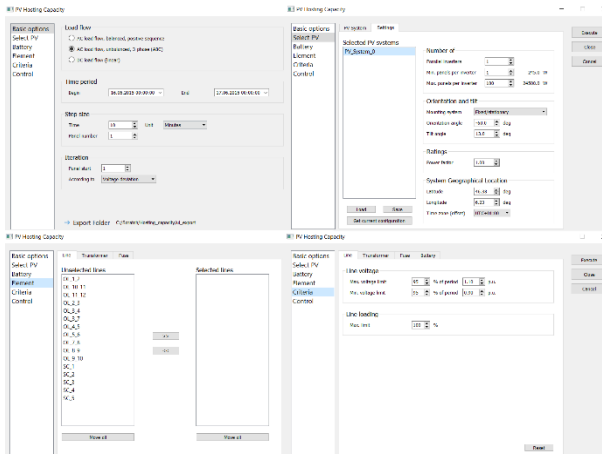


Figure 1: Graphical user interface of the PV hosting capacity computation plugin.

To address these difficulties, CSEM has developed a versatile tool for DSOs to rapidly evaluate the current state of their grid in terms of power quality under chosen PV configurations and to estimate the total PV hosting capacity of their network. The latter is defined as the maximum amount of PV that can be accommodated under existing control and infrastructure configurations before quality of service degrades beyond accepted levels. This tool (Figure 1) offers a seamless integration with Digsilent PowerFactory, a leading software package for grid simulation.

Tests were done on the CIGRE benchmark low-voltage microgrid network<sup>[1]</sup>, which we adapted by replacing all distributed generators replaced with PV (Figure 2).

The hosting capacity was calculated in six different cases: (1) under DACHZ rules, (2) under DACHZ rules relaxed to allow +10% voltage deviation between the transformer and customers' premises instead of 3%, and (3) under EN 50160 criteria. In cases (1) to (3) PV inverters operated at unity power factor (no control). Further simulations under EN 50160 criteria were then performed with various control methods. In (3.a) a smart

appliance scheduler aims at shifting electrical appliances to periods of solar production. Case (3.b) uses a smart inverter control strategy developed at CSEM and (3.c) combines both approaches.

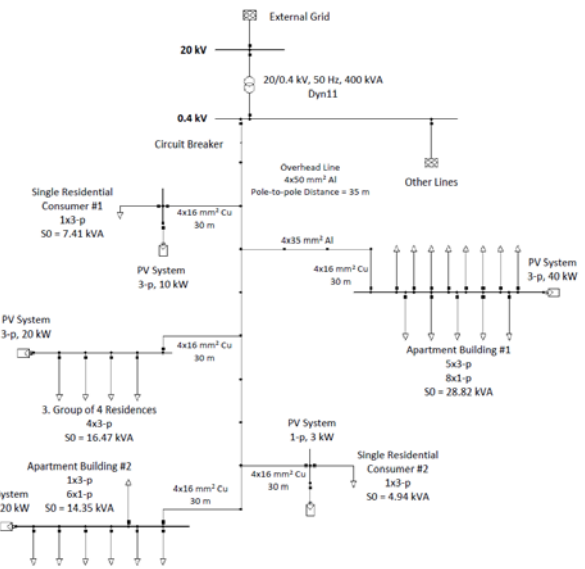


Figure 2: Single-line diagram of the benchmark low-voltage microgrid network in Digsilent PowerFactory.

The computation of the hosting capacity can be done under a few minutes depending on simulation settings. Results (Figure 3) show that standard rules can lead to significantly undersizing installed PV capacity for an entire feeder. Moreover, the developed tool has demonstrated that smart control strategies can yield an increase in PV hosting capacity of up to 57%.

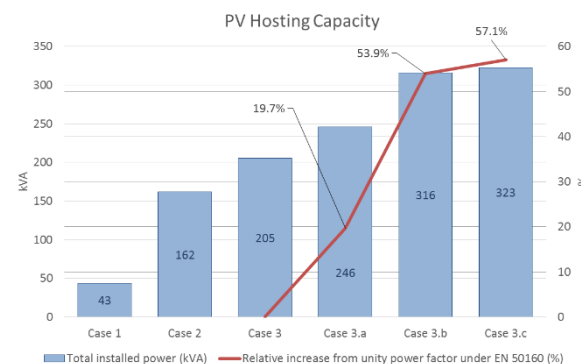


Figure 3: PVHC results for six different simulation cases.

This work was supported and funded by the European Union's Horizon 2020 research and innovation programme under grant agreement n°731211, project SABINA.

[1] S. Papathanassiou, N. Hatziargyriou, K. Strunz, et al., "A benchmark low voltage microgrid network," in Proc. CIGRE Symp. Power Syst. Dispersed Gener., pp. 1–8 (2005).

# Battery Modelling and Efficiency Estimation

V. Musolino, P.-J. Alet, A. Hutter, C. Ballif

CSEM is developing an integrated model for lithium-ion batteries. The model consists of three interconnected blocks: electric, thermal and aging models. In this project we have developed and validated the electric block to predict the battery terminal voltage, state of charge (SoC) and efficiency under arbitrary profiles of current and depth of discharge. The structure of the electric model is independent from the battery chemistry while the electric parameters are tuned for each specific battery technology. We validated the approach on lithium nickel oxide cells. The model, which is currently implemented in Matlab/Simulink, can be used for system engineering and for predictive control.

Batteries are complex, nonlinear systems. Performance indicators such as power and energy density, efficiency, and lifetime depend on factors including temperature, current profile, state of charge (SoC) and depth of discharge (DoD). Manufacturers' datasheets provide insufficient information to evaluate these indicators so they need to be complemented by a performance model.



Figure 1: Battery cells under test in a climatic chamber at the BFH-CSEM Energy Storage Research Center.

We used electrochemical impedance spectroscopy (EIS) as non-destructive technique to characterize the electrical properties of materials and their interfaces. The model is made of four impedance blocks connected in series (Figure 2) which respectively represent the internal high-frequency resistance, the charge transfer processes at the surface of the electrodes, the diffusion of charge carriers in the electrolyte, and the reflection of charge carriers in the crystalline structure of active materials. The model is valid at constant temperature and state of health of the battery in the frequency range from direct current to the kilohertz.

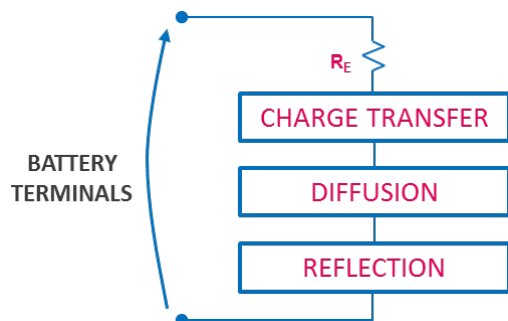


Figure 2: Electric model.

A complex situation when modelling battery performance is operations as primary control reserve (PCR), for which the current profile is determined by random fluctuations in grid frequency. When applied in this situation (Figure 3), the model predicts the terminal voltage with a high precision. Indeed, the root-mean-square (RMS) error over 24 h is only 20.64 mV (0.6%).

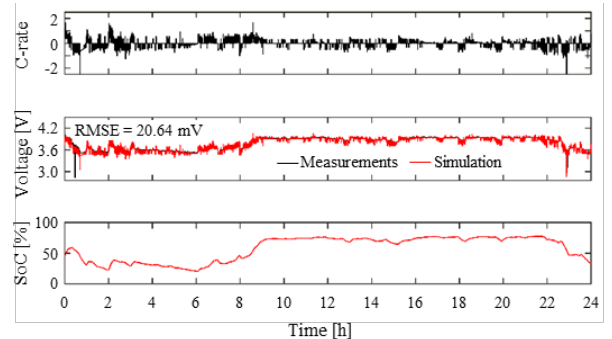


Figure 3: Simulated and measured voltage and estimated SoC of Boston-Power's Swing® 5300 cell under a current profile generated based on the primary control reserve (PCR) application.

The SoC estimation can be used to assess the effectiveness of the battery in a given application. For instance the model can be used to predict the unavailability of a battery system for PCR, due to the full charge or discharge. Table 1 reports the efficiency estimations different current rates and limits of SoC. The model performs much better when the battery is cycled between 20% and 80% of SoC. Close to 0% or 100% of SoC additional nonlinearities appear due to parasitic reactions, which are not taken into account in our model. The error is still lower than 2.2% in the SoC range of 0% to 100% and less than 0.5% in the SoC range of 20% to 80%.

Table 1: Measured and simulated efficiency of Boston-Power's Swing® 5300 cell under the PCR profile test for different current rates (C-rates) and limits of SoC.

C-rate	SoC range [%]	Efficiency [%]		Error [%]
		Measured	Simulated	
Max	Mean			
0.5	0.13	0 - 100	97.92%	97.74% 0.18%
1	0.26	0 - 100	96.15%	95.20% 0.95%
1	0.23	20 - 80	96.16%	96.35% 0.19%
2	0.47	0 - 100	91.24%	89.98% 1.26%
2	0.36	20 - 80	94.86%	94.45% 0.41%
3	0.62	0 - 100	88.00%	85.85% 2.15%
3	0.46	20 - 80	93.38%	92.87% 0.51%

The BFH-CSEM Energy Storage Research Center is a joint infrastructure of CSEM and the Bern University of Applied Sciences (BFH).

# Uncertainty Reduction in Predicting the Yield of Photovoltaic Power Stations

A. Tuomiranta, J. Levrat, P.-J. Alet

The trends that are currently transforming the markets of photovoltaic (PV) power generation also have an impact on the design practice of PV systems and their operation. Developments of PV plant performance models at CSEM PV-center aim at reducing the uncertainty involved in predicting the yield of PV power stations under both temperate and desert climates when integrating new technologies e.g., bifacial solar modules and batteries, and at improving operations and maintenance practices.

Digitalization trends in the photovoltaic (PV) sector encompass both system design and operations and maintenance activities<sup>[1]</sup>. Whether for value-driven design optimization of PV+storage power plants, or to optimize maintenance (e.g., cleaning) schedules, an accurate performance model of PV power plants is required. In this context, CSEM's developments aim in particular at integrating recent technological innovations (e.g., bifacial solar modules), changing design practices (e.g., increasing use of tracking systems in ground-mounted PV power plants), and climatic conditions in growing but previously under-researched regional PV markets (e.g., desert regions in the Middle East).

Whereas external costs and market conditions have a large impact on the economically optimal design of PV power plants, they do not carry technical uncertainties. We have therefore focused our efforts one reducing uncertainties in plant performance modelling i.e., yield prediction, which depend on modelling errors, ambient factor uncertainty, and the propagation of this uncertainty through the modelling steps. Our research efforts on the topic have been focused on improving the estimation of plant yield particularly in the areas of bifacial plane-of-array irradiance estimation, soiling impact modelling, and the estimation of electrical mismatch between cells, modules, and arrays.

The threefold objective of the activities related to bifacial plane-of-array irradiance estimation was to advance the state of the art in terms of accuracy, scope, and computational efficiency. As for accuracy, a modeling tool was developed to enable reliable estimation of cell mismatch loss considering both cell-specific ground shading, neighboring arrays, and variable ground reflectance. Compared to existing models, the capabilities of the tool were extended to arbitrarily dimensioned and spaced arrays, including single- and dual-axis tracking. The first version of the model, developed in the course of the COMET project, proved to outperform the previously proposed models in terms of estimation accuracy.

The starting point for modelling the performance of solar modules under real operating conditions is their characterization under the standard test conditions (STC) i.e., an irradiance of 1000 W/m<sup>2</sup> and a device temperature of 25°C. An important and complex deviation from the STC, which needs to be corrected in the model, comes from module soiling. This deviation especially influences the conversion of plane-of-array irradiance into cell current. The correction model being developed at CSEM can be integrated into an incidence angle modifier i.e., a correction factor which

captures the angular dependence of the reflectance of the module surface. We measured soiling losses (i.e., decrease in photocurrent generated in PV modules due to dust and other soiling sources) in a test site in the United Arab Emirates as a function of geometric and environmental parameters. The experimental data showed that soiling losses depend on the incidence angle of sunlight on the PV module. The relative impact of this incidence angle increased with higher soiling levels. Since state-of-the-art incidence angle modifiers do not include soiling correction, this phenomenon results in photocurrent being overestimated by a roughly linear function of the soiling level<sup>[2]</sup>. In addition, PV soiling losses were also shown to have a 3<sup>rd</sup>-degree polynomial dependence on module inclination angle as shown on Figure 1.

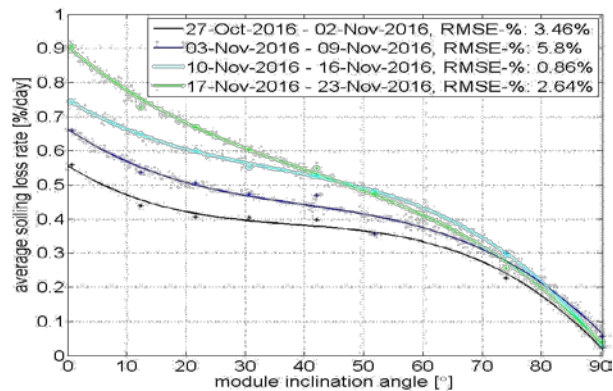


Figure 1: Dependence of PV soiling loss on module inclination in Abu Dhabi, United Arab Emirates.

With these enhanced plane-of-array irradiance estimator and incidence angle modifier, photocurrent in the PV devices can be estimated with a high-spatial resolution. To make use of this information, the cell and module mismatch resulting from the current variability between cells has to be accurately modelled. While the electrical description of this phenomenon is simple, computation of the operating point can be slow. We have therefore focused our efforts on improving the computational efficiency of the estimation of the current-voltage characteristics. Future work will extend this approach to the mismatch between arrays when losses in conductors and other balance-of-system (BOS) components are also taken into account.

Part of this work received funding from the Swiss Commission for Technology and Innovation (CTI) and Pasan SA under project Nr. 18445.1 PFIW-IW (COMET). CSEM thanks them for their support.

<sup>[1]</sup> SolarPower Europe Digitalisation & Solar Task Force, "Digitalisation & solar," SolarPower Europe, Brussels (2017).

<sup>[2]</sup> A. Tuomiranta, et al., "Correlation of solar module inclination and weather with soiling-induced power loss under hot desert conditions," Poster, Lausanne, Switzerland (2017).

# SYSTEMS

Jens Krauss

The activities of the SYSTEMS research program focus on system integration aspects of micro- and nano-technologies and aim at the coordination of expertise across multiple research programs in the fields of sensing and actuating, signal processing and control, high-precision mechanisms and instrumentation, low-power electronics, software, and biomedical engineering. The SYSTEMS research program is application driven and strongly user-oriented. Therefore, special consideration is given to such qualities as reliability, comfort, ease of maintenance, and convenience in operation. Our vision for the SYSTEMS research program is to promote innovations and new product concepts in the three application domains of (1) *Scientific Instrumentation*, (2) *Automation*, and (3) *Medical Device Technology*. During 2017 we have presented, for these application domains, more than 25 scientific and journal papers, participated in more than 30 conferences and workshops, and promoted our technologies during 5 exhibitions. Today, the SYSTEMS research program coordinates and maintains an IP portfolio of more than 50 patents, and last year we filed six new patents.

## Long-term objectives

**Automation:** Companies with manufacturing infrastructure in Switzerland (and Europe) continue to suffer from increased cost pressure, leading them to outsource production and thus lose know-how and innovation potential. Flexible and connected automation solutions with facilitated man-machine interaction enable an attractive total cost of ownership compared to a remote production site abroad, even for small to medium production volumes. Moreover, innovative Industry 4.0 solutions offer new, competitive production processes to preserve Swiss manufacturing, the Swiss Made brand, and the Swiss quality standards that come with it.

In the frame of the *Automation* research activity, we develop machine-learning techniques for automation and inspection tasks. We automate and interconnect complex manufacturing tasks, applying intelligent control and sensor fusion techniques. We aim to further extend our Industry 4.0 application software framework in order to easily deploy innovative solutions into different manufacturing and quality processes: with the benefits of self-aware, smart components (software/hardware), and supportive robots (so-called work companions), an optimum balance between flexibility, autonomy, and throughput is sought. Moreover, and in alignment with the MICROSYSTEMS research program's activities, we develop highly customized, integrated-sensing lab automation solutions.

**Scientific Instrumentation:** Rapid progress in material sciences and microtechnologies has led to rising ambitions in the field of (scientific) instrumentation and a quest for ever-smaller and smarter multi-technology systems. CSEM's *Scientific Instrumentation* research activity aims to meet coming demand in the fields of space exploration and watchmaking, as well as meteorology and industrial and medical instrumentation. Having originated in the watchmaking industry, CSEM continues to strive for remarkable watch technologies and new watchmaking materials and manufacturing processes, as well as groundbreaking new movements: with new escapements such

as the Genequand, mechanical watchmaking is in the midst of a renaissance—50 years after the quartz revolution.

CSEM flexure structure technologies are transforming the capabilities and costs of high-end instruments and have game-changing advantages over traditional rigid alternatives. And CSEM has leveraged its expertise in compliant and hybrid mechanisms with its long-standing expertise in MEMS and MOEMS. At term, sensors, actuators, and mechanism will be integrated at the process level, taking advantage of (metallic) additive manufacturing technologies to enable a new approach to complex instrument design. Apart from our considerable efforts in silicon flexure mechanisms (so-called Macro-MEMS), we aim—with our research activities in laser sources and laser stabilization—to reach unprecedented performance and miniaturization levels. Last but not least, we strive for new (industrial) applications for the Swiss miniature atomic clock (SMAC) concept, and ensure our European leadership in the field of miniaturized flash imaging LiDAR. Our competencies in multi-physics simulations are key to our expertise in the design of such complex, miniature, and fully integrated systems with limited available resources in terms of energy, computing power, and space.

**Medical Device Technology:** Today, the Western world is facing huge challenges in limiting the increasing costs of its healthcare system in the context of a steadily growing elderly population. The fourth industrial revolution, digitalization, is entering the healthcare domain to improve its efficiency and offer caregivers and patients new solutions, increasing the standard of care. Technology trends such as IoT and Big Data are further strengthening prevention, patient empowerment, and out-of-hospital care and the digital revolution will challenge and transform the entire healthcare industry.

At the same time, the era of digital personalized healthcare offers tremendous business opportunities. CSEM's *Medical Device* research activities with regard to placing human vital sensing and processing technologies into embedded, continuous on-body diagnostic systems drives global innovation toward new applications in the domains of rehabilitation, home care, in particular for elderly, healthcare and promotion, security, and eHealth. They allow patients to be inconspicuously monitored during their daily activities, such as work or sleep. And many more clinical and physiological studies in real conditions can now be envisaged thanks to services that offer more comprehensive information. Digital (health) data aspects directly connected with wearables, in particular related to data reliability and privacy, as well as to low-power devices guaranteeing data security, are also being addressed. Finally, thanks to work carried out at CSEM, doctors, insurers, and rescue teams will have more information related to occupational medicine, for instance in harsh environments. CSEM's medical device technology is certified according the standard ISO-13485, and aims to outperform existing commercial medical products with regard to comfort, precision, cost, and maintenance, and to convince with a seamless integration into the digital healthcare system.

## Highlights

Even if the SYSTEMS research program deployed major efforts with regard to its technology transfer activity in 2017, we have intensified further our collaboration with the center's other research programs

in the frame of CSEM's Multidisciplinary Integrated Projects (MIP) initiative. As a consequence, we can report further progress in the integration and characterization of low-power, portable human vital signs device chipsets with our colleagues from the ULP INTEGRATED SYSTEMS research program. In the joint program with the MICROSYSTEMS research programs, new concepts of (metallic) additive manufacturing techniques and topologies have been developed, and we highlight the creation of a series of innovative MacroMEMS components for the watch industry. Our collaboration with the PHOTOVOLTAICS & ENERGY MANAGEMENT research program focuses on key topics such as the integration of energy harvesting technologies into wearables, system design, and deep learning methods for smart grid applications. In the following, last year's scientific highlights per research activity shall be summarized:

**Scientific Instrumentation:** In 2017 we pursued our efforts in the domains of (i) laser systems and miniature atomic clocks (MACs), (ii) Macro-MEMS, and (iii) opto-mechanic precision systems (such as LiDARs). For this last topic, major efforts were deployed during the last reporting period to finalize CSEM's participation in the following three space missions: (1) CSEM's corner cube scanning mechanism (CCM) on EUMETSAT's Third Generation satellite (MTG), to be launched in 2019, helping scientists to better understand climate change; (2) CSEM's CLUPI focus mechanism, implemented on the drill of the Mars Rover in the frame of the ExoMars mission, to be launched in 2018; and (3) CSEM's flash LiDAR system, the so-called Vision-based Navigation sensor (VBN), in the frame of an on-orbit demonstration for autonomous space debris removal, to be launched by the satellite provider Surrey Space Technology Limited (SSTL) in 2018. For these large science mission projects, CSEM acts as a prime contractor, respecting its mission to provide Swiss SMEs, manufacturing entities, and local machine shops with the opportunity to participate through subcontracts and purchase orders. In the domain of Macro-MEMS, we have further reinforced our collaboration with CSEM's MICROSYSTEMS research program on the industrialization and manufacturing of compliant and hybrid Si-based watch mechanisms, and can report the filing of three new patents for watch components. Last but not least, we would like to highlight a scientific achievement in the domain of our activities in laser sources, stabilized lasers, cavity-stabilized continuous-wave lasers, and the optical frequency comb (stabilized mode-locked femtosecond laser): As reported in *Nature Photonics* (Aug. 2017) a paradigm-breaking approach to ultra-high repetition rate, ultra-short optical pulse generation has been developed by combining a novel optical fiber-based micro-photonic resonator with a pulsed laser source. This new approach is up to 100 times more efficient than previous efforts relying on continuous-wave lasers, and allows for easier control and stabilization with direct relevance to optical telecommunication and optical spectroscopy.

**Automation:** During the last reporting period the *Automation* research activities have put a special emphasis on innovative, interconnected, systemic Industry 4.0 solutions that collect and interpret data from several signal sources within an automation and/or manufacturing process to take decisions that optimize that process's overall performance. In the frame of the topics (i) machine learning and (ii) integrated measurement technologies, we can report a series of industrial developments for multi-sensor design solutions with interconnected data fusion,

analysis, and user feedback. Within the topic (iii) robotics and control system, we have tightened the links with the *Scientific Instrumentation* research activity by joining forces to progress on topics such as control strategies, real-time control, and embedded systems.

**Medical Device Technology:** In the frame of the research activities of the Medical Device Technology domain, we have further intensified our efforts regarding the research, development, and evaluation of innovative, medical-grade multi-sign monitoring wearables and are currently running half a dozen clinical studies according the ISO-13485 standard and in collaboration with our partners from the University Hospitals (CHUV, USZ, HNE, Inselspital, and HUG). During the last reporting period we made considerable progress regarding the further sensor electronics miniaturization of so-called cooperative sensor technology by integrating customized low-power chipsets as a result of the MIP project MiniNOB, in collaboration with our colleagues from the ULP research program. In 2017 we demonstrated—with a portable, wireless, 12-lead dry-electrode ECG Holter vest—the commercial potential of our proprietary cooperative sensor technology. Another key research topic into which we invested major effort during the last reporting period is the extension of our so-called oBPM™ technology (and IP) portfolio. Today, we have a series of prototypes in different form factors and for different body locations available to demonstrate our cuffless, continuous blood pressure monitoring technology. The focus during the next reporting period is to transfer the oBPM™ technology to industry, and we can confirm the interest of half a dozen commercial partners, from start-ups to traditional medical device technology companies. We would also like to draw attention to CSEM's digitalization initiative, in which context research into digital health and our cumulated health data will play a major role in the near future. Last but not least, we continue to enrich our algorithm portfolio—a portfolio based on the combination of inertial and PPG sensor signals—for different applications and in different wearable form factors (such as wrist-worn devices, textiles, and footwear), and can report an increasing number of license agreements.

We should also mention the best Swiss PhD in the biomedical engineering domain, authored by CSEM collaborator Dr. Martin Proen  a and entitled "Non-invasive hemodynamic monitoring by electrical impedance tomography". Proen  a was awarded the SSBE Research Award 2017 in recognition of his work, and it will pave the way to new (non-invasive) monitoring and processing techniques for pulmonary artery pressure (PAP). Another highlight of the *Medical Device Technology* research activity during the reporting period was the naming of AVA AG as the best Swiss start-up in 2017: AVA has collaborated closely with CSEM since the former's foundation, integrating and licensing CSEM's proprietary human vital signs monitoring technology into its fertility tracker wrist module.

# Robotic Platform Integrating Concurrent Manufacturing Processes for Construction of Large Multi-material Parts

F. Crivelli, A. Steinecker, P. A. Schmid

A hybrid-manufacturing machine for customized design, production, repair, and quality control of large, multi-material parts. An affordable and efficient solution that combines metal and non-metal 3D printing with subtractive manufacturing in an all-in-one, fully automated, robotic system. The large workspace associated with high manufacturing precision and a highly flexible kinematics will result in a powerful platform for construction and repair of complex, large volume components, and scale 1:1 prototypes.

The KRAKEN<sup>[1]</sup> concept was born after the successful conclusion of the MEGAROB<sup>[2,3]</sup> project, in which a robotic approach for machining and finishing of large parts (up to 20×6×3 m) was developed. The KRAKEN project will merge the subtracting manufacturing capability of the MEGAROB system together with high efficient metallic and novel non-metallic additive technologies. This will result in an affordable all-in-one machine for customized design, production, repair, and quality control of large functional parts made of aluminium, resin or both materials combined.

KRAKEN will combine a large workspace (from 0.1 till 20 m) with high manufacturing precision (tolerances below 0.3 mm and surface roughness below Ra 0.1 µm) and a fully automated approach. This will allow both SME and large industries to optimize the production of large customized parts and prototypes, decreasing both time (40%) and costs (30%), and increasing productivity (>25%). Additionally, by using a ceiling installation, floor space required could be reduced by 90%.

CSEM is collaborating within a consortium of 15 highly specialized partners selected for linking research results to technological necessities in the fields of software, monitoring, automation, materials, standardization, and end-users.

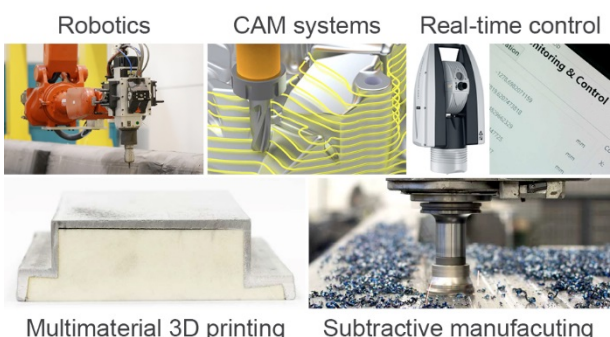


Figure 1: Features of the KRAKEN machine.

Main technological objectives of the project are: Development of new additive manufacturing approaches allowing high deposition rates (10 kg/h for aluminium and 180 kg/h for PU resin) and the use of combined metal and non-metal materials, development of new tools and high speed milling concept based on climb-up methodology (up to 2 mm depth and 25 cm/s speed), development of in-process geometry inspection and validation strategies to allow quality assessment and improvement of the produced parts, design and development of automatic controlling of the hybrid manufacturing process.

CSEM plays a key role in the last point, integrating the different components within the whole system and developing the algorithms to control the motion of the manufacturing tools during each required task.

The current KRAKEN machine includes: a three-axes overhead crane, a six-axes industrial robot arm (NJ130, Comau S.p.A., TO, Italy) mounted upside-down on the crane, a spindle for milling and polishing, and a laser tracker (AT960, Leica Geosystems AG, CH) for measuring the absolute pose of the manufacturing tool in real-time. The system will be further equipped with a set of tools for both metallic (aluminium) and non-metallic (PU resin) additive technologies, and a laser scanner for metrology and inspection. A dedicated software will complete the KRAKEN machine, allowing the operator to interact with the system in a user friendly and standardized manner. Direct interfacing with well-established CAD (computer-aided design) and CAM (computer-aided manufacturing) software will allow direct management of components characteristics and manufacturing approaches. Additionally, a metrology software will enable monitoring of the manufacturing processes and online quality inspection of the produced parts.

To achieve the required precision of 0.3 mm an external controller is being developed by CSEM to control the absolute pose of the robot tool based on the laser tracker's feedback. The controller runs on a linux-based real-time operative system with a sampling frequency of 1 kHz. The control software receives the 6D pose (3D position and 3D attitude) from the laser tracker and calculates a correction command to be sent to the robot controller to maintain the robot tool on the reference trajectory. This approach will allow high positioning accuracy of the manufacturing tool, independently from the motion performance of both the crane and the robot arm.

Different manufacturing process imply different control requirements: High position accuracy is required for milling, constant interaction force between the tool and the part is needed during finishing and polishing, while additive manufacturing requires a constant velocity in order to guarantee a homogeneous material deposition. Different control approaches are being implemented to allow each task of the hybrid manufacturing process to be optimally executed.

This project has received funding from the European Union's Horizon 2020 research and innovation programme under grant agreement No 723759. Their support is gratefully acknowledged.

[1] [www.krakenproject.eu](http://www.krakenproject.eu)

[2] [www.megarob.eu](http://www.megarob.eu)

[3] D. Boesel, P. Glocker, "Ultra-precision Manufacturing of XXL Parts", CSEM Scientific & Technical Report (2015), 92.

# Machine Learning Using Satellite Imaging for Agriculture and Forestry

I. Kastanis, J. Sun, P. A. Schmid

The recent availability of satellite imagery has created new opportunities for remote observation of the Earth. A growing field of applications is currently emerging in the landscape. Within agriculture classification methods enable the precise analysis of crop types. In forestry detection of alien species invasion can act as an early warning system for pre-emptive forest management. Health monitoring and damage assessment methods offer valuable information to environmental organizations and insurance companies. This report focuses on the use of machine learning for creating neural network models based on satellite imagery.

The launch of the Sentinel-2A satellite in 2015, as part of the Copernicus program, has signified a new era in Earth observation. Sentinel-2 joins the growing family of freely available satellite imaging instruments with an increased spatial and temporal resolution when compared to previous instruments like the LandSat program. The Sentinel-2 constellation consists of 2 identical satellites offering multi-spectral data with up to 10 m spatial resolution and a revisit time of 5 days. Further to that the European Space Agency, amongst other providers, offers currently a full historical archive of images. Image analysis benefits not only from the high temporal and spatial resolution, but also from the existence of the archives, that can be used to create process models based on previous years.



Figure 1: A region labelled with different crop types observed from the Copernicus Sentinel-2A satellite in 2016.

Traditionally image analysis of vegetation<sup>[1]</sup> has been based on indexes like the Normalized Difference Vegetation Index (NDVI) and the Fraction of Absorbed Photosynthetically Active Radiation (FAPAR). While they offer a concise way of measuring vegetation, they reduce the available information in an effort to simplify the analysis process.

Machine learning methods have the potential to learn directly from the data instead of using parametric models and thus reduce the need for manually adjusting the parameters of each model. In recent years deep learning, neural network models based on multiple layer architectures, have been gaining in popularity. Their success has been proven in a variety of applications, the most prominent being natural language processing and image classification, with performance comparable to humans and occasionally higher. Deep learning has demonstrated its capability to find correlations in complex

data sets. In the fields of agriculture and forestry the ability to find complex relations hidden deep in the data enables methods to use raw data instead of the previously mentioned indexes that are omitting potentially important information. CSEM has a long experience in the application of deep learning methods in computer vision and draws upon it to further extend the technology within new application domains.

The data sets obtained from satellite imaging instruments are high resolution in the spatial, temporal and spectral dimensions and can be classified as Big Data. While the problems of storage, transmission, and computational power are the ones most frequently discussed in Big Data problematic, data quality is of equal importance. In particular when discussing data driven approaches, such as machine learning, this issue becomes critical especially when creating a new model. The generation of a new model requires additional information such as the location of regions of interest and the type of vegetation. Collection of this data depends on human input and on this scale this cannot be easily considered completely reliable. In the real world this data will contain misplaced coordinates and incorrect labels. It is thus very important to provide methods for data consistency that eliminate irregularities from the data set, as well as having a learning algorithm that is capable of handling outliers.

Within the European project DataBio<sup>[2]</sup>, focusing on using Big Data for the bioeconomy, an initial study was performed. Satellite images together with geometric information and crop type were collected. A model for a specific crop was created and used for detecting whether an area contains this crop type or not. Preliminary experiments based on different conditions have shown promising results on crop type verification

The initial study performed demonstrates the potential of this approach. Using deep learning for detection and classification of vegetation types creates a new possibility in handling Big Data in the domain of Earth observation with a multitude of potential applications in the areas of precision and smart agriculture, pre-emptive forest management, health monitoring and damage assessment. This methodology provides an efficient and precise way of analyzing huge amounts of complex data and can have an impact on environmental issues in the national and global scale.

This project has received funding from the European Union's Horizon 2020 research and innovation programme under grant agreement No 732064.

<sup>[1]</sup> S. Valero, et al., "Production of a Dynamic Cropland Mask by Processing Remote Sensing Image Series at High Temporal and Spatial Resolutions", *Remote Sensing* (2016), 8(1), 55.

<sup>[2]</sup> <https://www.databio.eu>

# Collaborative Robot Intuitive Teaching by Single-hand Guidance

G. Gruener, A. Vardi •, P. A. Schmid

CSEM has developed a system that enables lay people to teach assembly tasks to a collaborative robot (cobot). Cobots are designed to work hand-in-hand with manual workers. With CSEM's system, lay people can now teach the cobot even complex assembly tasks by guiding the robot using a single hand. A trained robotics expert is no longer needed to reprogram the robot. The system shall ease cobots' entry barriers and offers a user-friendly, highly-flexible approach. In combination with CSEM's WP4C<sup>[1]</sup> system, it provides an advanced Industry 4.0 solution.

Recently, robot manufacturers have brought collaborative robots (cobots) to the market with moderate success. A cobot is an industrial robot that can share its workspace with a human without special safety equipment. To achieve the collaborative mode, cobots limit their maximum speed and acceleration. Some cobots are equipped with additional sensors to measure joint torques or end-effector contact forces and moments, which allow direct physical interaction with a user but make the robot more expensive. This results in a dilemma for the profitability of such systems.

Modern robot systems still require a skilled expert to program complex assembly tasks. Cobots have a niche in highly-flexible manual to semi-automated assembly lines. In this context, it is crucial that every line worker can re-teach the robot quickly. Guiding the robot by hand is the simplest way.

In this project, a Kuka LBR iiwa cobot is used to explore its advantages for small production lots. Each robot joint has a torque sensor providing contact feedback over the whole arm.

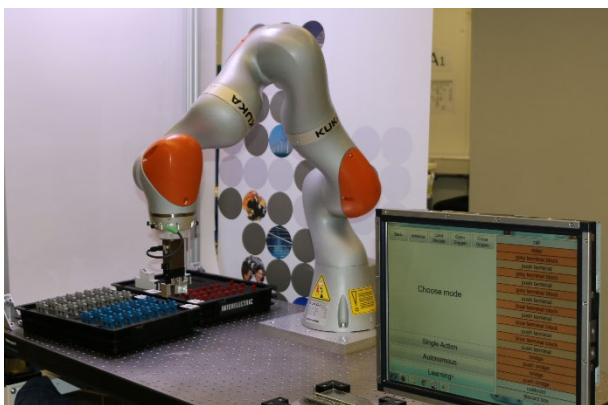


Figure 1: Kuka LBR iiwa at CSEM, no safety equipment is required.

CSEM's WP4C<sup>[1]</sup> assembly task was chosen for this study because it is representative of manual assembly involving complex contact operations requiring medium forces. This project concentrated on the assembly. Therefore, the parts were prepared for the robot to grasp with a custom-designed gripper. The assembly recipe is known. CSEM's VISARD was used to dynamically find the next part to be assembled.

The system has two different modes: **learning** and **working**.

In **learning** mode, the robot learns from a human operator how to perform the assembly one step at a time. The robot picks the appropriate part for the next assembly step according to the recipe and brings it near the assembly spot. The human then grabs the robot and guides it haptically through the assembly

motions and forces. Crucial for this mode is an optimized gravity compensation with smooth robot motion, enabling human guidance with low effort.



Figure 2: Cobot single-hand guidance of a complex assembly task.

Data from the robot's integrated joint encoder and torque sensors is monitored at 1 kHz and used to learn the assembly step. The motion and contact data is segmented, processed and reduced with a RDP algorithm<sup>[2]</sup>. The system learns the assembly step faithfully with one single guidance.

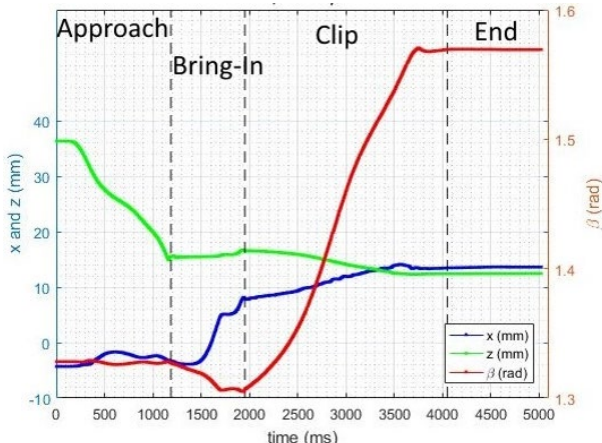


Figure 3: Phase segmentation of an assembly operation.

In **working** mode, the robot builds the complete assembly automatically by executing the learned assembly steps according to the recipe sequence (CSEM's YouTube channel<sup>[3]</sup>).

The implementation uses non-optimized assembly paths and forces: the robot also learns human flaws. Future work will optimize this maintaining the single teaching step goal.

CSEM would like to thank the Swiss Federation and the MCCS Micro Center Central Switzerland for their financial support.

• EPFL, Learning Algorithms and Systems Laboratory

<sup>[1]</sup> <https://youtu.be/zBao3QunnGY>

<sup>[2]</sup> [https://en.wikipedia.org/wiki/Ramer–Douglas–Peucker\\_algorithm](https://en.wikipedia.org/wiki/Ramer–Douglas–Peucker_algorithm)

<sup>[3]</sup> <https://youtu.be/8IE1DltHc5k>

# WiseRock—Wireless Sensor Network for Monitoring Rock and Slopes

C. Beyer, S. Bitterli, D. Piguet, B. Perrin, A. Kiser, R. Sigrist, R. Limacher

*There is an increasing demand and necessity for real-time monitoring of hazardous alpine areas. In collaboration with an industrial partner, CSEM developed a wireless sensor network for real-time monitoring of alpine hazardous areas. The system combines an ultra-low power ad-hoc communication network with low-cost sensor technology to provide long-term, autonomous monitoring capability while reducing the total cost of ownership by half compared to conventional wired sensor networks.*

The rising average temperature in the alpine area and the increased probability of extreme weather events caused by the climate change raises the instability of the slopes and rocks with increased occurrence of debris flow, landslides and rock fall. In order to preserve the safety of people and infrastructure, a continuous monitoring of hazard areas is necessary for timely alert and risk assessment. By default, wired sensor networks are installed today, which are complex and risk-prone to use. Their biggest weakness is the cabling itself, since, on the one hand, their installation is cumbersome and requires long presence of workers in the critical and hazardous area. On the other hand, the cables are prone to damages by rock falls or animals, which make part or totality of the system unavailable for dangerously long period of times and require risky human intervention.



Figure 1: Picture of the rock fall onto the Gotthard tracks in 2012.

CSEM developed in collaboration with a local SEM and the aid of CTI grants a novel wireless sensor network based on CSEM proprietary technology WiseNET. The system enables real-time monitoring of geological hazards in alpine areas and offers the advantage of a fast and flexible installation on site by linking ad-hoc individual sensor nodes (Figure 2). In case of a node failure, the network reorganizes autonomously to minimize information loss. Furthermore, the network can always be supplemented by additional nodes without much effort.



Figure 2: Picture of the developed sensor nodes together with commercial-of-the-shelf geological sensors.

Commercial-of-the-shelf geological sensors such as extensometers, crack meters, rip cords, strain gauge as well as

position and acceleration sensors are integrated in individual nodes for autonomous operation of at least 7 years (battery only). Certain nodes are additionally equipped with precise low-cost GNSS sensors to detect long-term relative position displacements with sub-cm resolution. These nodes are additionally powered by solar cells next to batteries.

The monitoring system enables a continuous risk assessment of the surveillance area by an intelligent combination of different measurement parameters. The network allows the timely detection and alerting of geological incidents, thus the network is suitable to monitor time-critical processes. The measurement protocol is dynamically adapted to the risk situation in order to optimize the life time of the network.

The development of a wireless sensor network designed for reliable operation in harsh environments for several years, places special demands on all system components. An optimal compromise had to be found between communication transmission robustness and latency, duration of operation and overall size / weight. A pilot network was successfully tested in an alpine hazardous area to evaluate and optimize the system performance (Figure 3).



Figure 3: Test network consisting of 7 nodes (#2-8) and one base station (#1), which is connected to cloud services via GPRS / GSM.

Key features of the new system are an autonomous, reliable operation of up to 7 years, a condition-based, automatic alerting in case of emergency and the integration of different sensors for an accurate determination of the threats. The estimated total cost of the new wireless sensor network is half of a conventional wired one, thus allowing to monitor more dangerous areas by the same means.

CSEM continues to support the local SME with the industrialization and knowledge transfer of the new system.

# A Wireless Solar Powered Pressure Pad for Aerodynamics Testing of Flexible Profiles

T. Burch, S. Bitterli, J. Kaufmann, E. Schaller

Based on CSEM's pressure strip technology a novel pressure pad for aerodynamics measurements on sails is being developed. The pressure pad integrates a MEMS pressure sensor, a low-noise signal acquisition chain, a Bluetooth wireless interface and a solar module in a thin and flexible pad. The self-adhesive pad can be permanently attached to sails to measure the airflow and find the optimal sail trim.

Knowing the effective pressure distribution over the sail plan is of great interest to sail designers for the aerodynamic and structural optimization of sails as well as to the sailing crew to find the optimal sail trim. Therefore, CSEM has matured the pressure measurement system developed for aerodynamicists and sail designers<sup>[1]</sup> towards a simple to use and easy to install instrumentation system for racing and leisure yachts.

On most sailboats, telltales are positioned on both sides of the leading edge of the jib. These small strips of yarn show how the air is flowing past the luff and indicate if the sail trim is good or not. However, telltales provide only suitable indication for close hauled trims and the visibility is not always easy for the helmsman in the back of the cockpit. The novel pressure pad system overcomes these limitations.

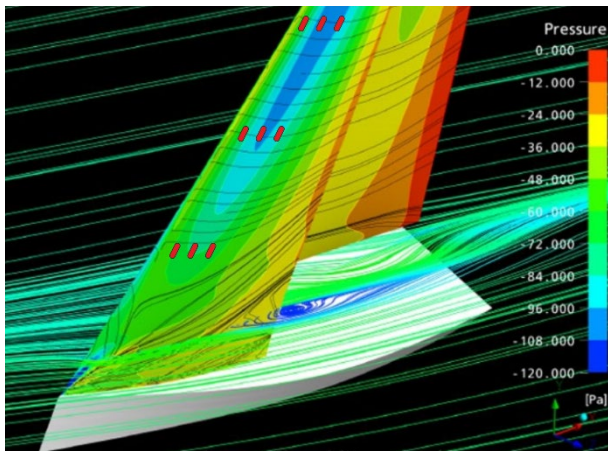


Figure 1: Illustration of pressure pads (red dots) attached to the areas on the jib with the highest differential pressure between lee and luv.

The system is based on nine self-adhesive pressure pads attached on three luff-sections of the sail (Figure 1). This is the area which generates the main propulsion due to highest pressure gradients. Each pad collects comprehensive pressure values and runs a data pre-processing cycle. Only the relevant information for indication of optimum sail trim is sent to the display in the cockpit. This allows to limit the wireless data traffic and saves energy. In order to distinguish between laminar and turbulent flow and to detect stall conditions the internal pressure sampling rate is much higher than the data up-date rate.

The dimension of the pad is 128 mm in length and 20 mm in width. The pad thickness is 0.8 mm at the measurement location, and 3 mm in the region of the electronics package (Figure 2). CSEM's patented micro-channel system is used to transmit the pressure from the thin measurement location to the embedded sensor. This ensures minimal intrusiveness and alteration of the flow.

A major improvement compared to earlier pressure strip applications is the micro-perforated hydrophobic membrane, placed at the pressure inlet, which prevents blockage of the micro-channels due to moisture or dust. The electronics is entirely solar powered without the need for a battery. A paper-thin flexible solar cell, placed on top of the pad, provides enough energy for the sensor electronics and the wireless interface, even in cloudy conditions. The integrated pressure sensors are a new generation of piezo-resistive differential low-pressure membranes with very high sensitivity. The key specification of the pressure pad is given in the table below.

## Key specification

- |                          |              |
|--------------------------|--------------|
| • FS pressure range      | 400 Pa       |
| • Measurement resolution | 0.025 % FS   |
| • Static accuracy        | 0.25 % FS    |
| • RF Interface           | Bluetooth LE |
| • Data up-date rate      | 0.5 – 2 Hz   |
| • Internal sampling rate | 10 – 50 Hz   |

Besides high sensitivity, robustness is of equal importance. The sensors need to withstand sail flogging and should be insensitive to stress produced by different sail bending curves. Advanced die bonding and packaging techniques have been developed to improve the robustness. The pressure sensors are bonded to a glass substrate buried in a cavity within the PCB. In addition, dedicated elastic layers decouple mechanical stress from the pad to the sensitive silicon membrane.

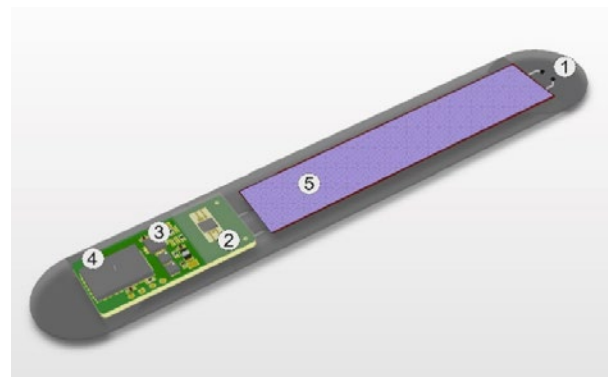


Figure 2: Pressure pad with pressure inlet (1), MEMS sensor (2), data acquisition electronics (3), Bluetooth interface (4) and solar cell (5).

The current pressure pad is clearly tailored to the sailing application, but has also potential for aerodynamics field-testing on any other object, for instance in the sports, automotive or aviation market.

CSEM would like to thank the Swiss Federation and the MCCS Micro Center Central Switzerland for their financial support.

[1] T. Burch, et al., "New System for Pressure Measurements on Yacht Sails", CSEM Scientific & Technical Report (2016), 97.

# Vision-based Detection and Classification of Particles in Fluids

J. Pierer, S. Widmer, N. Schmid, M. Höchemer, N. Blondiaux, G. Andreatta, E. Schaller

During the process of crude oil production, large amounts of produced water need to be cleaned before it can be released back to the ocean. Moreover, knowing the composition of the produced water within the processing chain it is possible to optimize the production cycle. The mostly employed manual sampling and testing are time consuming and take into account only a "snap shot" of the continuously running process. In close collaboration CSEM together with an industrial partner developed a video microscopy based system to fully automate the process and allow for continuous monitoring of the produced water.

Two main challenges were identified. First: the composition of the medium which contains besides oil droplets also solid particles such as sand, organic materials (e.g., algae) as well as air bubbles and chemical solvents. Second: The contamination of the optical windows by the medium and all of its ingredients.

The first challenge was addressed by application of a video microscopy system which allowed the quantification and classification of solid particles and oil droplets within the medium. The latter can be distinguished from the other materials using fluorescence imaging. A major obstacle with those fluorescence measurements are potentially fluorescent chemicals that might be present within the produced water and therewith influence common integrating instruments. During the project it was demonstrated that the proposed technology based upon a vision system is uncompromised by those chemicals.

To tackle the contamination issue, an investigation of several types of coatings and surface modifications was conducted resulting in mostly negative results. Primarily because of the variety of different ingredients as mentioned above. Finally a conceptually simple but in details complex constant flow of a protective water layer proved to be a sufficient way to avoid contamination of the optical windows.

The entire fluidic system was refined to finally allow the protective water layer and the sampling volume to be adapted to the optical system requirements. As the sampling volume per time is limited, a bypass system was implemented to allow for sufficiently fast exchange of the medium. The latter warranted that no large quantity of oil can bypass the detector without being sampled. The entire system was designed to allow control of all fluid movements towards and within the instrument.

The vision system in its basic functionality is comparable to an optical fluorescence microscope. Demands on its robustness and size, but overall a very long working distance, demanded a custom designed optical system. Besides standard optical components such as lenses and dichroic mirrors and an industrial CMOS camera, the entire illumination optic and electronic were integrated as well. The illumination works in both, transmissive and coaxial configuration. Core elements are several high-power UV LEDs as well as a visible one.

The entire system (Figure 1) including an industry PC, the LED driver, optics, temperature controller and a GSM modem, was implemented into a rugged housing which can be adapted for use in an explosive atmosphere. All of the fluidic sampling cell was attached to the side of this housing.

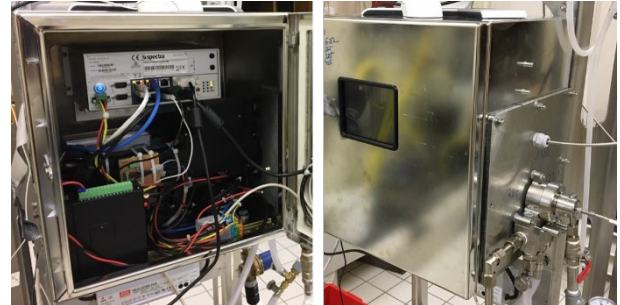


Figure 1: (Left) Inside of Instrument; (Right) Closed housing with fluidic system on its side.

The probably most important and complex part of the development were the software algorithms. Based upon the standard CSEM software framework called "Visard" a complex development and testing environment was set up. The software which controls all the instruments functions includes advanced, custom developed algorithms for detection and classification of the sampled media. Besides the development environment, an operational mode was implemented displaying the relevant information and status indicators to the onsite operator.

The instrument was calibrated with both synthetically mixed fluids with known fluorescence and other solid particles as well as real world samples, from oil treatment facilities. Qualification of the instruments functionality was conducted with both, synthetic samples as well as real world samples not used during the calibration process. Both times the measured oil content matched the real values within the expected uncertainty. Figure 2 shows a typical oil particle size distribution and the corresponding enhanced image.

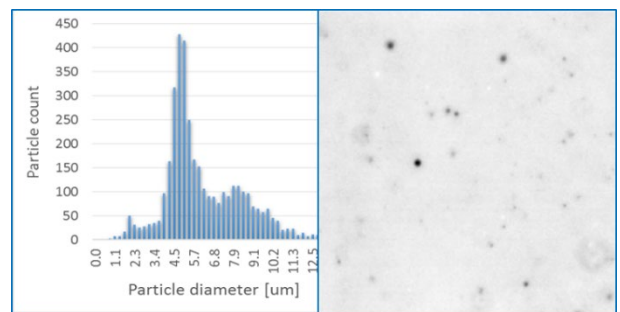


Figure 2: Measured particle size distribution and typical image (software enhanced).

The industrial partner is currently working on the transfer of the project results into an end-user product.

This work was partly funded by CTI. CSEM thanks them for their support.

# CLUPI Focus Mechanism—Close-up Imager for EXOMARS Mission

G. Perruchoud, A. Verhaeghe, P. Schwab, M. Gumi

Over the years CSEM has developed a particular expertise for high-precision opto-mechatronics systems used for space missions. CSEM developed several complex mechanisms for space and astrophysics missions, relying on compliant mechanisms. Based on that expertise, CSEM is in charge of the design and manufacturing the CLUPI Focus Mechanism.

In the frame of the ESA EXOMARS mission, ESA aims at landing a rover on the planet Mars, the ExoMars rover. Its goal is to collect evidence of previous life. A key instrument of the rover is its drill, equipped with an imager. CSEM developed and built the breadboard model of the CLUPI Focus Mechanism, based on flexure elements, which is part of the CLUPI imager. The breadboard is a first model, towards an EQM (Engineering Qualification Model) and two FMs (Flight Model) in the next project phases. The CLUPI imager development is under the responsibility of Thales Alenia Space Switzerland whereas the PI (Principal Investigator) activity is performed by the Space Exploration Institute. The EXOMARS rover is planned to be launched in 2020.



Figure 1: EXOMARS rover.

The CLUPI Focus Mechanism (CFM) will allow the frictionless adjustment of the focal distance of the imager, taking into account the launch mechanical loads (27 Grms). It will survive and operate in the harsh environment of Mars, especially the lower temperature (-120°C). The main challenges are the low mass requirement (<0.2 kg) together with the new development of a launch lock device.

The main performance requirements of the CFM are:

- Focal distance from 100 mm to  $\infty$  adjusted via a displacement of -4.3 mm to +4.3 mm.
- Position accuracy 5  $\mu\text{m}$  with a lateral deviation of 50  $\mu\text{m}$ .
- Operating temperature range from -55°C to +30°C.
- Non-operating Survival temp. range from -120°C to 50°C.
- Mass <0.2 kg.
- Number of cycles  $\geq 10'000$ .
- Operation in Mars atmosphere 6 mBar, 95% CO<sub>2</sub>.

The CLUPI Focus Mechanism (CFM) design is presented in the Figure 2.

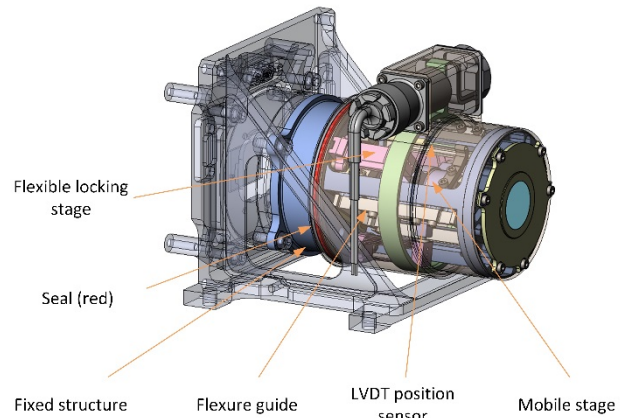


Figure 2: CFM (CLUPI Focus Mechanism).

A key element of the mechanism is the LVDT positioning sensor. It measures the mechanism position, and allows to drive the mechanism in closed loop. It is manufactured by Singer Instrument. Off-the-shelf units were qualified with minor customization following a preliminary test campaign.

The mechanism actuator is a voice coil actuator, off-the-shelf, manufactured by Moticont.

A key challenge was the development of the Launch Locking Device (LLD). It shall allow the mechanism to sustain launch. It relies on the Launch Locking Actuator (LLA) that is a commercial component based on a non-explosive mechanism using a link-wire.

During the first phase of the project, the tasks undertaken by CSEM included: design, manufacturing, and test of a new rotating LLD; design, manufacturing, and test of the Focus Mechanism Breadboard; thermal cycling test on the Voice Coil and the LVDT sensor (300 cycles @ -130°C to 80°C) and finally random vibration test on the complete Breadboard.

Figure 3 presents the integrated breadboard and associated measured guiding performances.

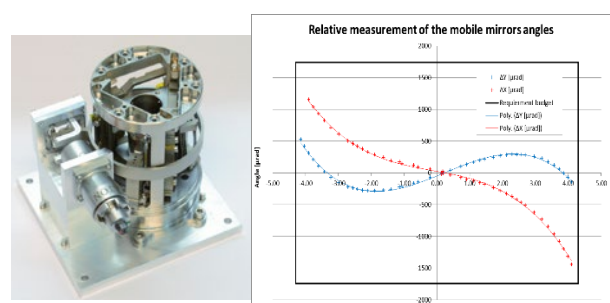


Figure 3: CFM breadboard mounted, guiding performance.

The next phase of the project will be the manufacturing, the testing and the delivery of the Engineering Qualification Model and of the Flight Models.

# Innovative Mechanical Design Based on Additive Manufacturing & Topology Optimization

L. Kiener, H. Saudan, D. Bommottet •, F. Cochet •

Additive Manufacturing (AM) is a major topic of interest for the manufacturing industries. While the common thinking is that everything can be done by AM – which is only partially true – it can be added that it cannot be done anyhow. The AM process needs to be well mastered as it introduces several new challenges which shall be taken into account already in the design phase. In parallel, reproducing by AM the same parts that are currently produced by traditional methods such as machining is usually of no interest. To ensure the highest added value (and lowest cost), the entire device – and not only the individual parts – shall be re-thought under a process oriented design perspective, including a system engineering vision. CSEM is investigating new capabilities of AM with the aim to help manufacturing industries to redesign their products according to this holistic approach.

The elaboration of products made by metallic Additive Manufacturing (AM) has been investigated at CSEM over several years, seeking at taking advantage of the new possibilities offered by AM technologies for newly designed as well as for re-engineered products with enhanced performances. The first step of this endeavor was to evaluate and to optimize all the processes involved with the aim to ensure the feasibility of complex parts, including 350 µm thick and 20 mm long flexure blades manufactured with AM, a typical geometry used at CSEM for the design of high precision mechanisms. Achieving such challenging geometries has required the identification, in-depth study and understanding of the critical AM process and post-processing parameters affecting the quality of the end product. This study was followed by specific in-house developments to master the complete AM chain, beginning with the design for AM, taking into account the new constraints of this technology, continued with the optimization of stainless steel and titanium materials fulfilling high-end mechanical performances. The post-processes such as machining, cleaning and thermal treatments have been extensively investigated. In parallel, the Topology Optimization was studied for complex structural parts to ensure the most efficient design taking into account multi-physics aspects.

Using AM technologies to reproduce a part whose design was driven by a conventional manufacturing techniques is often not advantageous, since it does not take into account the advantages offered by AM. For example, the complexity of the assembly can be reduced by designing a monolithic mechanism or by reducing the number of parts and combining the functions. The project AMAR (Additive Manufacturing of a slpring Assembly Rotor), in partnership with RUAG Space Switzerland Nyon and funded by the Swiss Space Office, is an example of a significantly improved production flow enabled by a smart combination of AM and post-processing techniques.

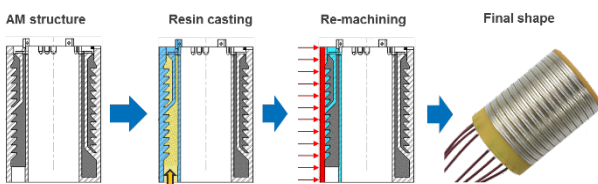


Figure 1: New process with additive manufactured parts (patent pending).

The new design developed in AMAR proposes to produce by AM a skeleton which comprises all the features, to cast it with insulating resin and to machine the final shape of the rotor. In comparison, the state-of-the-art production procedure is tedious,

implying a lot of machined parts with tight tolerances to be assembled in many successive steps.



Figure 2: Pictures of the first prototype built by AM.

To ensure an optimized redesign for AM, a system engineering approach allows understanding all the parameters pertaining to the mechanism and therefore being aware of all the key requirements to be considered during the design phase. In parallel, the design constraints associated with AM are to be deeply understood as well.

To further improve the design, the use of topology optimization software is actually the most efficient method to improve various properties of the parts designed for AM at the same time: e.g., mass reduction, eigen-frequencies tuning, thermal transfer optimization, thin-wall thickness optimization, etc. The optimization can be performed using multiple criteria at the same time, including combined multi-physics analysis; e.g., mechanical, thermal, magnetic, fluidic. Topology optimization requires to precisely define the most demanding load cases and therefore to deeply understand the mechanism and the entire system. This tool is the most powerful to successfully achieve a redesign for demanding applications such as high-precision mechanisms with complex structures for space applications. The competencies developed at CSEM on the whole AM process chain are applicable to any type of industry.



Figure 3: Example of topology optimization made at CSEM.

• RUAG Space Switzerland Nyon

# Sub-picosecond Mode-locked Semiconductor Laser for Space Applications

M. Krakowski • P. Resneau • M. Garcia • E. Vinet • Y. Robert • O. Parillaud • S. Kundermann, N. Torcheboef, D. L. Boiko

European Space Agency (ESA) considers Mode-Locked Semi-Conductor Laser (MLSCL) technology as a promising candidate for space applications in precision optical metrology systems. However very challenging performance requirements should be met. We address this challenge and realized two types of mode-locked multi-section edge emitting lasers in an on-going ESA project. In the next phase we will build a prototype that fulfills ESA requirements.

Mode-Locked Semi-Conductor Laser (MLSCL) technology is assessed for space applications in high precision optical metrology systems such as High Accuracy Absolute Long Distance Measurement (HAALDM). We report on the first iteration towards challenging performance requirements of the European Space Agency (ESA):

- Pulse duration <1 ps
- Pulse energy > 200 pJ
- Pulse Repetition Frequency (PRF) 1-3 GHz
- PRF stability <5·10<sup>-9</sup> at 1 second
- PRF tunability > 20 MHz.

The laser should be compact and robust against launch vibrations and have small power consumption. To address all these targets, we have realized two types of mode-locked (ML) multiple section edge emitting lasers: (1) very long (13.5 mm) monolithic tapered laser (Figure 1)<sup>[1]</sup>, and (2) inverse bow-tie external cavity (EC) laser<sup>[2]</sup> (Figure 2).

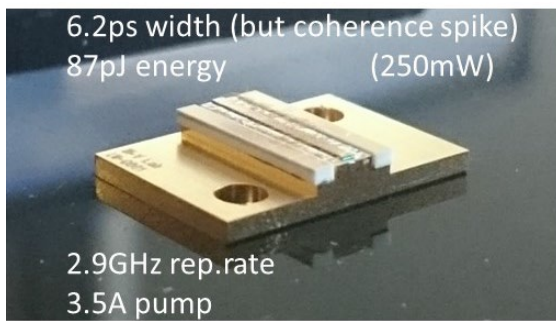


Figure 1: A very long (13.5 mm) monolithic tapered MLSCL.



Figure 2: Inverse bow-tie external cavity MLSCL.

Best performance is achieved with the second approach (Figure 2) which is selected for implementation in the final

MLSCL prototype of the project. To reach high energy pulses and to match the EC mode, the gain section has an inverse bow-tie geometry. Using a dedicated assembly of collimation lenses, the 80 mm long EC is closed with a flat mirror. The saturable electroabsorber section is at the back side of the gain chip for mode-locking at the fundamental EC frequency. We reach passive ML at 1.3 GHz, PRF with the pulse energy of 90 pJ, pulse width of 6.5 ps, and electric power consumption of 2.9 W. After a pulse compressor the pulse width is reduced down to 895 fs (Figure 3). By translation of the output coupling mirror, PRF was continuously tuned over 37 MHz range without additional adjustments. Active stabilization with a phase locking loop actuating on the driving current resulted in PRF relative stability at 2·10<sup>-10</sup> level on 10 s intervals (Figure 4).

These encouraging results of the first iteration run on sample design, fabrication and testing confirm feasibility of MLSCL technology for space-borne precision metrology.

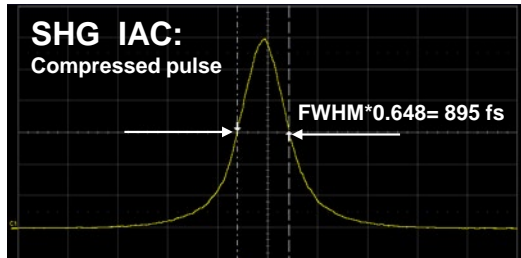


Figure 3: 2<sup>nd</sup>-order autocorrelation trace after a pulse compressor.

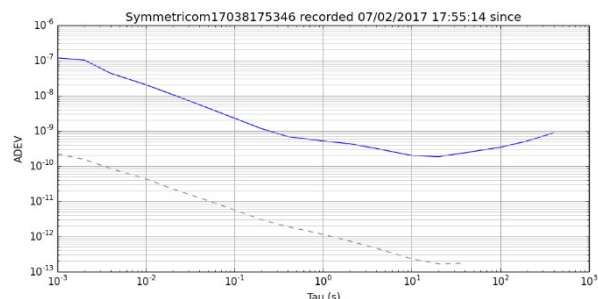


Figure 4: Allan variance of stabilized relative PRF.

Yet the pulse energy has to be doubled. We have already identified the limiting factors and proceeded to fabrication of the modified gain chips.

The project partner is III-V Lab. This work was partly funded by European Space Agency. CSEM thanks them for their support.

• III-V Lab, 91767 Palaiseau, France

<sup>[1]</sup> M. Krakowski, et al., "Lasing dynamics of very long (13.5mm) tapered laser emitting at 975 nm", SPIE-OPTO-2017-conference 10123 "Novel In-Plane Semiconductor Lasers XVI", paper 10123-13.

<sup>[2]</sup> M. Krakowski, et al., "High pulse energy passive mode locking of inverse bow-tie 975nm laser diode in external cavity", CLEO Europe 2017, paper cb-8-4.

# Landing on Mars with a Miniaturized Flash Imaging LiDAR

A. Pollini, C. Pache, J. Haesler, F. Droz

The LiDAR (Light Detection and Ranging) acronym was unknown to most of the public 9 years ago when CSEM built its first flash imaging LiDAR for the European Space Agency (ESA). Since then LiDAR has gained traction at least from advanced technologies fanatics as many derivatives of this type of sensor are considered to become omnipresent on future autonomous cars or on drones delivering parcels directly at home. This paper summarizes CSEM latest achievements and place them in perspective with the evolution of several potential markets.

Vehicles like cars and drones will be equipped with a LiDAR as a standard sensor in a mid-term perspective. Both markets are so large that hundreds of millions are raised regularly through the announcement of new start-ups or new products. How CSEM can keep pace in such an environment?

CSEM is a pioneer of flash LiDAR in Europe and is considered as a leading Research and Technology Organization (RTO) by ESA in this field. Several projects were completed during the last ten years and the (Swiss) industry is now becoming convinced by the maturity of the technology. The terminology "flash" comes to balance the wording "scanning" LiDAR. A scanning LiDAR measures ranges of one pixel after the other and assembles them afterward in a single 3D image. A flash LiDAR captures the same image, i.e. ranges for all pixels, in a single snapshot, in the same way as a standard camera. CSEM has focused its developments on flash LiDAR. The space market is not of direct interest for those active in the mass market. As a consequence, this is a perfect niche market that allowed to mature technologies. The Miniaturized Imaging Laser Altimeter (MILA) project<sup>[1]</sup> is a flagship activity recently completed. The main outcome of the project is a TRL4 prototype (Figure 1) delivered to ESA for its Guidance Navigation and Control (GNC) laboratory to be inaugurated before the end of the year.

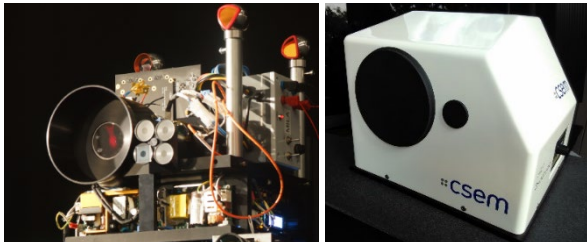


Figure 1: MILA TRL4 flash LiDAR prototype recently delivered to ESA.

Space applications have demanding requirements that are not easy to address altogether at the same time. The most challenging requirement for missions to Mars is the necessity to provide distance measurement at several kilometers and at the same time provide 3D maps with a few centimeters spatial and range resolution at closer ranges (down to a few meters). CSEM solution to this challenge is a flash LiDAR architecture with 3 modes of operation: altitude meter, attitude meter and imager. In altitude mode, the target is illuminated with a single low-divergence laser beam. The output is the range to the target. In attitude mode, the target is illuminated with a few low-divergence laser beams. The output is a set of ranges. Finally, in imager mode, the target is illuminated with a large-divergence laser beam. The output data is a full 3D image.

In MILA, CSEM successfully conducted open field tests (Figure 2). A spatial resolution of 20 cm and a range precision of 3.75 cm was demonstrated in imager mode with a target at 300 m. In altitude mode, a range precision of 3.75 cm has been demonstrated for up to 1100 m. This latter distance is not the limit of the instrument but the one of the test field.

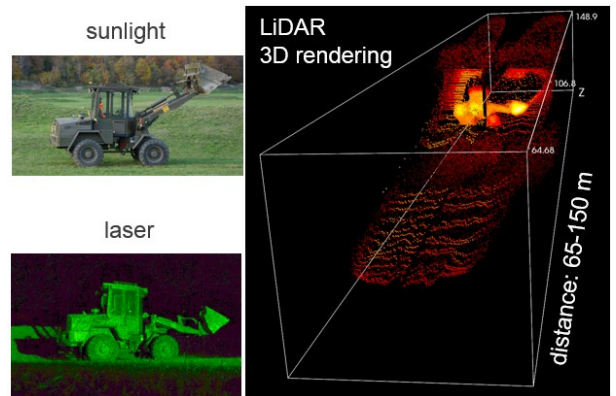


Figure 2: (Left) Target in the sunlight and illuminated by the MILA flash LiDAR prototype laser; (Right) Data cloud of a volume of 10 m by 10 m by 85 m (image generated in collaboration with HES-ARC).

While space remains a pillar for CSEM LiDAR developments, we are seeking to diversify the domains of application. Automotive and unmanned aerial vehicles markets are tempting but highly competition oriented. Looking into smaller markets, a niche where the MILA LiDAR architecture can be directly applied is bathymetry. This is a domain where LiDARs sound what is below a water surface. To assess the potential of the technology, the MILA prototype was installed to image a ship wreck in front of the Laténium Museum (Neuchâtel) with the support of the archeologist Fabien Leuenberger.

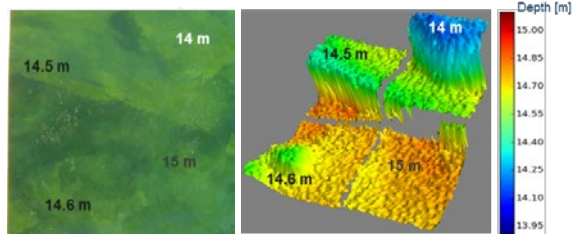


Figure 3: (Left) Picture of the wreck part; (Right) LiDAR data cloud.

The results are completely satisfactory. Details of the wreck were measured with a few centimeters resolution. CSEM is now building upon these exciting results and seeking partnership with actors of this domain. At the same time, CSEM pursues its effort to identify innovative solution for larger markets.

<sup>[1]</sup> ESA Contract No.4000112045/14/NL/HB

# Narrow-linewidth Low-RAM Semiconductor Lasers for Telecommunication and Metrology

S. Kundermann, J. O'Carroll •, D. Byrne •, L. Maigyte •, B. Kelly •, I. Kjelberg, S. Lecomte, R. Phelan •, D. L. Boiko

Modern coherent optical communication formats such as quadrature amplitude modulation (QAM) require narrow-linewidth lasers. In the framework of the Eurostars project HICOLA, narrow-linewidth lasers based on Eblana Photonics' discrete-mode technology have been developed. In addition light-emitting diode heaters have been integrated on-chip enabling a pure frequency modulation without introducing harmful residual amplitude modulation (RAM) in a simple and cost-effective way. This new technology is an enabling tool for other applications like gas spectroscopy, optical metrology, or atomic clocks.

Wavelength tunable lasers for 40G and 100G coherent optical communication systems need to meet stringent requirements on narrow linewidth emission across the entire tuning range, with typical values of 300 – 500 kHz required in commercial systems. Higher communication capacities can be achieved in next generation systems by applying higher order modulation formats such as 16QAM or 64QAM. However, such systems have even more stringent linewidth requirements<sup>[1]</sup>. For example, square 64QAM transmission at a data rate of 40 Gbit/s (the baud rate is 6.7G symbols / second) demands a laser with 1 kHz linewidth.

Eblana Photonics Ltd., CSEM partner in the Eurostars project HICOLA (E!8598), has a product line based on their proprietary Discrete Mode Laser Diodes (DMLD) technology<sup>[2]</sup>. Although linewidths as low as 70 kHz was demonstrated in free-running DMLD prior to the project, further linewidth reduction was required.

Laser design optimization was performed and free-running laser linewidth was reduced down to 50 kHz. For further linewidth reduction, an active stabilization of the DMLD onto an optical frequency reference was implemented. In the usual implementation, an external acousto-optic modulator (AOM) or the diode laser injection current is used for active frequency noise correction. This typically worsens significantly the intensity noise, which renders the laser unsuitable for QAM applications. We circumvented this problem with on-chip integrated frequency modulators based on Joule heating (see Figure 1) and showing zero residual amplitude modulation (RAM).

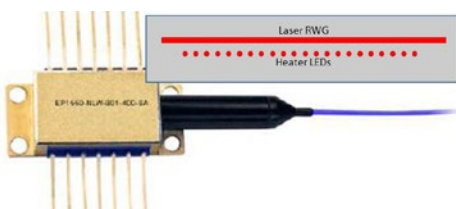


Figure 1: Schematic of the DMLD with laser ridge-waveguide (RWG) and the on-chip LED-based micro-heaters.

The integrated frequency modulator based on LED-heaters achieves above 10-kHz bandwidth. In Figure 2, the active reduction of DMLD frequency noise is illustrated for the case where the stabilization loop bandwidth is almost 200 kHz leading to a laser linewidth reduction down to 4 kHz. In Figure 3, the laser

relative intensity noise (RIN) is shown for the case of a free-running laser (black curve) and in the case of a frequency stabilized DMLD laser (red curve). The two curves coincide attesting that the RIN is not influenced and our new modulator is indeed characterized by zero RAM.

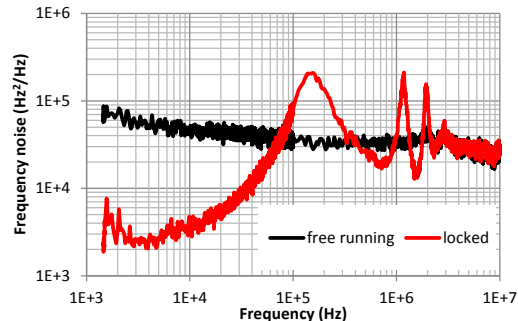


Figure 2: Frequency noise spectrum of the free running laser (black curve) and stabilized laser via on-chip heaters (red curve).

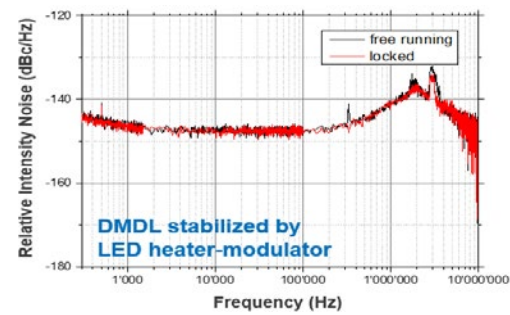


Figure 3: Relative intensity noise (RIN) spectrum of the free running laser (black curve) and stabilized laser via on-chip heaters (red curve) showing no RIN degradation.

In conclusion, DMLDs with integrated phase modulators are highly interesting for coherent optical communications and other applications demanding actively narrowed linewidth emission. The developed technology offers an economic approach compatible with high-volume production of monolithic compact semiconductor lasers. Other applications, related to gas spectroscopy, optical metrology, and atomic clocks will also take advantage of these new capabilities.

This work was funded by Eurostars program (project HICOLA E!8598) and the Canton of Neuchâtel. CSEM thanks them for their support.

• Eblana Photonics Ltd, Dublin 2, Ireland

<sup>[1]</sup> M. Seimetz, "Laser Linewidth Limitations for Optical Systems with High-Order Modulation Employing Feed Forward Digital Carrier Phase Estimation," in Optical Fiber communication conference, Los Angeles, (Feb. 2008).

<sup>[2]</sup> J. O'Carroll *et al.*, "Wide temperature range 0 < T < 85 °C narrow linewidth discrete mode laser diodes for coherent communications applications" Opt. Express, 19, no.26, pp B90-B95 (2011).

# Ultra-short Laser Pulses at 10 GHz Repetition Rate from an In-fiber Microresonator

E. Obrzud, V. Brasch, S. Lecomte, T. Herr

*Ultra-short laser pulses are the foundation of a wide range of applications including material processing, multi-photon microscopy, eye surgery, sensing of trace gases and pollutants as well as low noise microwave generation and optical clocks. Conventionally, ultra-short laser pulses are generated by so called mode-locked lasers at pulse repetition rates ranging from 100 MHz to 1 GHz. For some applications, such as optical data transfer or fast analog-to-digital conversion, even higher pulse repetition rates of 10 GHz or higher are desirable yet challenging to achieve. Here, a new efficient method for creating ultra-short laser pulses with high repetition rate is reported. The results have been achieved in a novel CSEM-designed optical microresonator that is based on and compatible with standard optical fiber components. Besides ultra-short pulse generation, the developed microresonator is suitable for laser linewidth narrowing and optical filtering.*

Ultra-short laser pulses concentrate optical energy into a small temporal interval. Among others, this enables accurate timing, as well as eye surgery or material processing without heat induced damage. Moreover, the high attainable optical peak powers give efficient access to nonlinear optical effects as used in multi-photon microscopy or super-continuum light sources. Generally, the ultra-short laser pulses are emitted periodically, which implies that the optical spectrum is composed of discrete, equidistant optical frequencies that are spaced by the pulse repetition rate. Such spectra are referred to as optical frequency combs and have gained significant importance as tools in optical precision metrology. While ultra-short laser pulse sources are to date rather bulky and expensive, it is expected that lower cost and miniaturization will in the future lead to widespread use in everyday application scenarios.

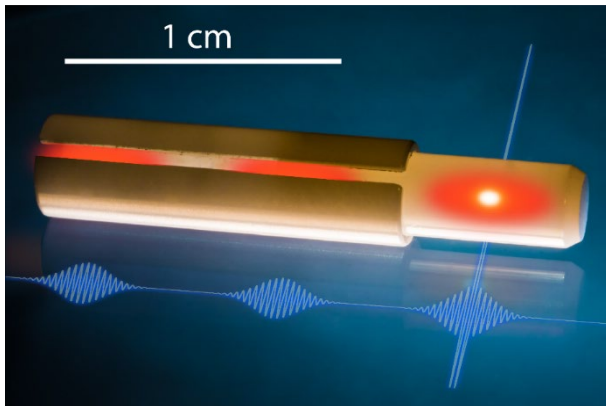


Figure 1: Illustration of soliton pulse formation in an in-fiber microresonator.

A particularly interesting application of ultra-short pulse laser is optical data transfer, which can help satisfying the rapidly increasing demand for higher bandwidth connectivity. An important laser characteristic in this context is the pulse repetition rate, which needs to be approximately 10 GHz or even higher (so that the spectral components of the frequency comb can be resolved and modulated to encode data). Such high repetition rates are challenging to achieve as they require a laser resonator not larger than approximately 1 cm. As a typical ultra-short pulsed laser resonators is comprised of several discrete

components, it is however extremely difficult or to build such lasers.

Recently, nonlinear optical microresonators have provided new opportunities for the generation of high repetition rate laser pulses relying on so called temporal cavity solitons. Such solitons are self-organizing pulses that can emerge and circulate in a microresonator when pumped by a continuous-wave laser beam. This microresonator technology has already proven itself in demonstration of optical data transfer and optical spectroscopy.

Major challenges for microresonator soliton technology are (i) power efficiency, (ii) reproducibility, and (iii) stabilization of the pulse generation mechanism. CSEM researchers in collaboration with the University of Geneva have now shown that these three challenges can be addressed by a novel microresonator design in conjunction with a paradigm breaking laser pumping scheme [1]. Figure 1 shows the new microresonator that consists of a 10 mm long optical fiber whose end facets have been coated by a dielectric coating. Enclosed in a ceramic ferrule, the microresonator is robust against mechanical perturbations. Moreover, the ferrule enables alignment-free connectivity to standard fiber-optic components (e.g., via the FC/PC standard). Importantly, the resonators only support are 'single-mode', which makes their optical properties predictable without requiring sample characterization and testing. The new laser pumping scheme uses electro-optically generated picosecond pulses instead of continuous-wave lasers. Owing to this, the soliton pulse generation is two orders of magnitude more power efficient and it can easily be controlled and stabilized. The generated pulses are in the femto-second regime and are generated with a repetition rate of 10 GHz. These results open entirely new perspectives for transferring microresonator technology from an academic to an applied setting where low cost, efficiency and robustness are key.

Based on the achievements described above, CSEM researchers are now exploring the potential of microresonators for optical data transfer, narrow linewidth lasers, low noise microwave generation as well as optical spectroscopy.

This work was funded by the Swiss National Science Foundation.

[1] S. Lecomte, T. Herr, "Temporal solitons in microresonators driven by optical pulses", Obrzud, Nature Photonics (2017)  
doi: 10.1038/NPHOTON.2017.140.

# High-speed Line Sensor for Optical Droplet Detection and Analysis

L. Hofer, S. Cattaneo, H.-R. Graf, C. Hofer, G. Orawetz, B. Schaffer

*QuadLine is a high-speed line sensor developed by CSEM for analyzing and optimizing fast motion processes. The purpose of this project was to evaluate if this sensor can be used for in-flight detection and analysis of liquid droplets and to build up a demonstrator to show the capabilities of the sensor. The QuadLine sensor has the potential to be a cheaper replacement of a high-speed camera and to offer FPGA-based online data analysis, thereby avoiding bottlenecks in data transmission to an external PC.*

The QuadLine [1] sensor has 64 rows (WRGB) $\times$ 320 columns. The pixels are 24 $\times$ 24  $\mu\text{m}$  in size and offer programmable full-well for a high and low sensitivity mode. 4 rows can be acquired simultaneously at full frame rate up to 200'000 fps. The exposure time can be configured from 0.5  $\mu\text{s}$  to 13 ms for each row independently. In addition to the high frame rate, a big advantage of the QuadLine sensor are the on-chip 10 bit ADCs (Figure 1).

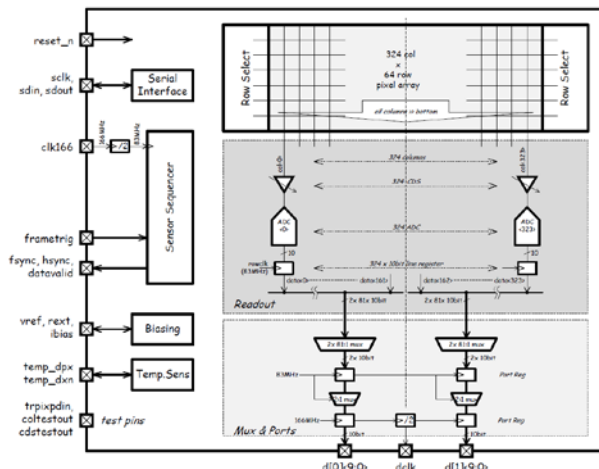


Figure 1: Block diagram of the QuadLine sensor.

Figure 2 shows the test setup for the detection of liquid droplets: A 1:1 telecentric lens with a white LED in-line illumination through a beam splitter is used to illuminate and image the droplets. For better contrast, a mirror is mounted on the opposite side of the lens to reflect the light back. Water droplets are generated by a peristaltic pump slowly pressing water through a syringe needle. A light barrier installed below the needle was used to generate a trigger signal for the data acquisition, making sure that the droplets are in the acquired frame sequence. Alternatively, one of the sensor lines could be used for triggering.

First test measurements were done with a chopper wheel to have a precisely controllable tool to verify the speed of the QuadLine sensor. A frame rate up to approximately 170'000 fps was successfully achieved with the current setup. The reason for not achieving the full sensor speed of 200'000 fps can be found in the electronics driving the sensor.

The same water droplet was acquired simultaneously by two sensor lines, which are separated by 744  $\mu\text{m}$  on the sensor to allow the droplet velocity measurement. For each line a sequence of 200 lines was recorded at a speed of 32'000 lines/s and an exposure time of 10  $\mu\text{s}$ . Figure 3 shows the acquired image for one of the two lines.

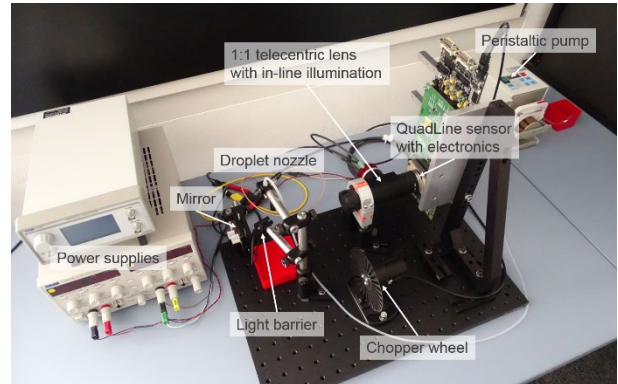


Figure 2: Test setup.

Performing edge detection (red dots) and fitting (green curve) allows an estimation of the droplet volume, under the assumption of rotational symmetry about the vertical axis and constant droplet velocity across the sensor. The droplet appears elliptical because the distance covered by the droplet per time unit is longer than the pixel height. For this measurement the mean droplet velocity can be estimated to approximately 1 m/s, the cross section is essentially circular with 2247 $\times$ 2290  $\mu\text{m}$  and the volume is estimated to 6.1  $\mu\text{l}$ .

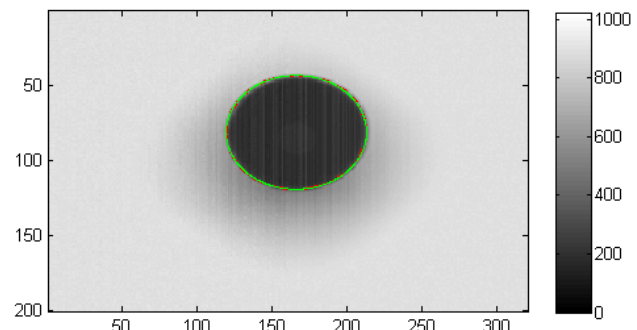


Figure 3: Measurement of a water droplet from a single sensor line.

We estimate that droplet volumes down to 1 nl should be detectable with the current setup. With larger magnification optics even smaller volumes could be measured. Also higher droplet velocities are feasible by using the full sensor speed.

Next, an algorithm performing line-by-line analysis will be developed, which can be done in real time on a FPGA. This would offer a unique advantage compared to the huge data volume generated by a 2D high-speed camera and subsequent image processing.

The QuadLine sensor was developed in collaboration with BOBST in the framework of a CTI-funded project.

[1] QuadLine Flyer (<http://www.csem.ch/Doc.aspx?id=35664>).

# SecureFLIM—Fluorescence Lifetime Imaging for Product and Brand Protection

S. Cattaneo, C. Hofer, J. Reinhardt •, R. Caviezel •, H.-R. Graf, B. Schaffer

Fluorescent security inks are well known features used to protect banknotes, documents and high-value products from counterfeiting. Currently these features are verified simply by inspecting their appearance (color and position) under a specific illumination. Fluorescence lifetime is an attractive parameter, which can drastically increase the security of current fluorescent tags and allows distinguishing tags that appears identical under a conventional fluorescent camera. Measuring fluorescence lifetime is however not straightforward and has traditionally required bulky, complex and expensive equipment. Here, we present a novel system based on a portable, cost-effective fluorescence lifetime imager and specially developed for lifetime-encoded tags, which has the potential to accelerate the uptake of fluorescence lifetime for anti-counterfeiting.

Counterfeiting is a globally increasing problem impacting companies, governments and consumers, causing every year estimated losses of more than \$ 200b worldwide. Of particular interest to counterfeiters are high-value products, such as pharmaceuticals, software, watches, and fashion goods. The problem is therefore particularly acute in Switzerland, with yearly losses estimated around CHF 2b. In response to this problem, anti-counterfeiting companies are constantly developing new and improved security features, in order to make valuable items harder to copy.

Fluorescent tags are well-known security elements, often encountered in banknotes, documents and luxury goods. Currently, fluorescent tags are checked simply by verifying their appearance (color, pattern) under a specific illumination (typically UV light), either by eye or with a fluorescence camera. Fluorescence Lifetime Imaging (FLIM) has recently attracted interest as an additional, hardly replicable covert feature. The adoption of the technology, however, has been severely hampered by the size, the high cost (60-100 kCHF), and the complexity of current FLIM systems, as well as by the lack of suitable materials for lifetime-encoded tags.

As reported previously, CSEM recently developed a compact, cost-effective reader for wide-field frequency-domain FLIM, including a MHz-modulated LED (460 nm), a CMOS-TOF imager (256×256 pixels), and dedicated FPGA electronics (Figure 1, left). The reader, originally developed for medical applications, yields a 2D map of fluorescent lifetimes with nanosecond resolution in a single shot.

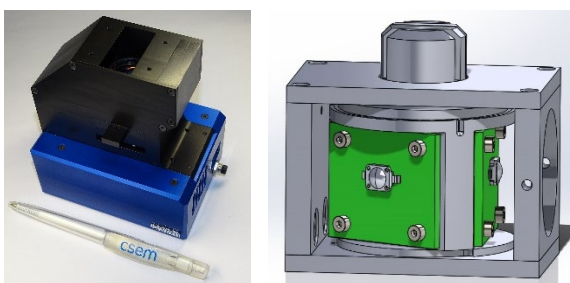


Figure 1: (Left) FLIM prototype with 465 nm excitation; (Right) Multi-wavelength illumination module with 3 LEDs (365 nm, 465 nm, 520 nm).

In collaboration with the Swiss company U-NICA, the FLIM reader was adapted for the specific needs of the anti-counterfeiting application. In particular, a multi-wavelength illumination module incorporating three LEDs (365 nm, 465 nm, and 520 nm) was developed (Figure 1, right), allowing the user

to select the optimum illumination wavelength for various security tags. The new module will allow measuring security tags based on UV inks, which represent the majority of the fluorescent tags currently used. The imaging optics of the reader was also redesigned, reducing the field of view from 6×6 mm to 4.8×4.8 mm, in favor of an improved spatial resolution.

For developing the fluorescent lifetime tags, a wide range of commercially available and proprietary fluorescent materials were tested. FLIM-encoded tags were produced by patterning fluorophores with specific lifetimes, or by mixing fluorophores in different ratios. Several suitable candidates for both short (<20 ns) and long (>50 ns) lifetimes were identified and thoroughly characterized. Figure 2 shows for example a compound sample with three different compounds (two short-lived, one longed-lived), imaged with the SecureFLIM prototype. As can be seen, very different lifetimes can be determined in a single image, enabling a completely new class of security features.

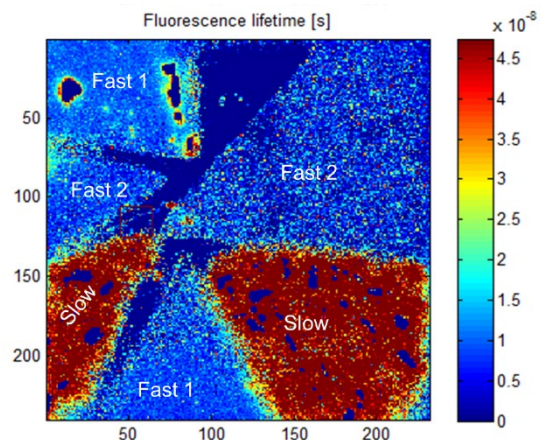


Figure 2: FLIM image of a compound sample, combining one slow (~45 ns) and two fast (<10 ns) fluorescent additives.

Next, the FLIM samples will be further refined to print patterns that can only be read in lifetime-mode. In parallel, polymer microparticles incorporating a lifetime-encoded barcode will be produced by UV polymerization in microfluidic channels. These advances will pave the way for a widespread application of FLIM in the domain of anti-counterfeiting.

This work was supported by Nano-Tera (projects FlusiTEx and FlusiTEx Gateway) and by the CTI (project SecureFLIM). We would like to thank them for their financial support.

• U-NICA Micronics AG, Malans

# **oBPM™—Optical Blood Pressure Monitoring: Performance in Anesthetized Patients**

J. Solà, F. Braun, M. Proença, R. Delgado-Gonzalo, D. Ferrario, M. Lemay, C. Verjus, M. Bertschi

The commercialization of smartwatches and smart bands is boosting the presence of optical sensors located at the wrist. Initially aimed at monitoring heart rate, such photoplethysmographic (PPG) sensors contain additional worthwhile information that is currently unexploited: in particular, concerning blood pressure. CSEM started ten years ago developing algorithms to extract cardiovascular information out of PPG signals. Initially at the chest, and later extended to other body locations, CSEM's optical blood pressure monitoring (oBPM™) solution offers a toolbox to enlarge the capabilities of PPG sensor devices, enabling breakthrough blood pressure (BP) monitoring functionalities. To differentiate from other competitors, CSEM is currently validating oBPM™ algorithms in a cohort of anesthetized patients including invasive reference means, and involving very challenging hemodynamic variations.

Several worldwide actors recently claimed methods to measure blood pressure (BP) from the analysis of photoplethysmographic (PPG) signals. To differentiate from such newcomers, CSEM positions itself in terms of reliable and clinically-supported results. In this context, CSEM focuses on providing performance figures of its proprietary optical blood pressure monitoring (oBPM™) solution in challenging environments, rather than biased and unrealistic laboratory experiments. An ongoing clinical study (NCT02651558) at CHUV, Lausanne University Hospital, currently assesses the accuracy of such oBPM™ algorithms when compared to invasive systolic BP measurements at the radial artery.

Figure 1 and Table 1 provide figures of merit for eight patients in the development dataset. The goal of the analysis is to demonstrate the performance of oBPM™ in detecting changes of BP induced by vasoactive anesthetic agents, compared to naïve predictions. In particular, concordance rate depicts the percentage of correctly-detected changes in BP trends,  $\Delta\text{BP}$  Error depicts the error in predicting the amount of such BP changes, and Accuracy  $\pm\Delta 20 \text{ mmHg}$  depicts the accuracy in detecting threatening changes of more than 20 mmHg.

## **Four quadrant plot analysis (N= 36)**

**Concordance Rate:** 97.2 %

**$\Delta\text{BP}$  Error:**  $0.3 \pm 7.7 \text{ mmHg}$

**$|\Delta\text{BP Error}| < 10 \text{ mmHg}$ :** 88.9 %

**Accuracy  $\pm\Delta 20 \text{ mmHg}$ :** 94.4 %

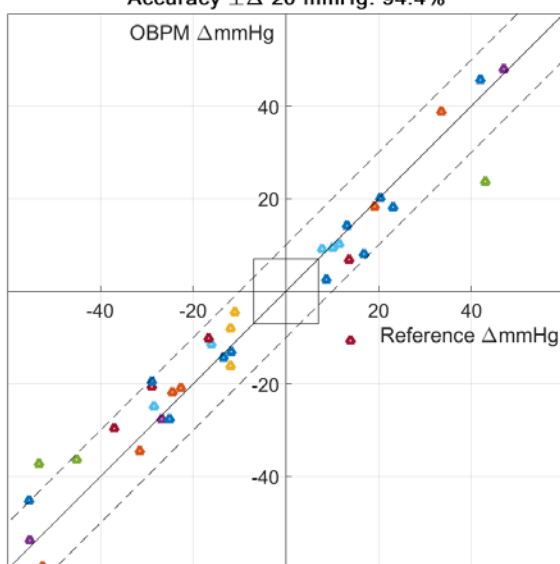


**Figure 1:** Performance of oBPM algorithms when applied to pulse oximeter signals of eight patients during anesthesia (N= 36 measurements). The reference are invasive systolic changes of BP.

**Table 1:** Performances of oBPM™ algorithms based on the analysis of PPG signals during anesthesia induction. PPG-HR depicts performance of an algorithm that estimates BP from heart rate changes. PPG-AMP depicts an algorithm that estimates BP from changes in amplitude of optical arterial pulsations.

	Concordance rate	$\Delta\text{BP}$ error (mmHg)	Accuracy $\pm\Delta 20 \text{ mmHg}$
<b>oBPM prediction</b>	97%	$0.3 \pm 7.7$	94%
<b>Benchmark 1: PPG-HR prediction</b>	56%	$6 \pm 22$	58%
<b>Benchmark 2: PPG-AMP prediction</b>	47%	$3 \pm 28$	50%

The tests performed on signals from pulse oximeters demonstrate the potential of oBPM™ in hemodynamic challenging conditions. CSEM prepares to transfer the oBPM™ technology to different commercial form factors (Table 2).

**Table 2:** Possible form factors of CSEM oBPM technology. TRL stands for Technology Readiness Level.

Location	Form factor	Application	TRL
		Continuous monitoring of BP trends during anesthesia	7
		Occasional ambulatory monitoring of BP via a smartphone camera	6
		Continuous ambulatory monitoring of BP via a smart bracelet	6
		Continuous ambulatory monitoring of BP via an armband	5

# Validation of a Multi-wavelength Photoplethysmogram Sensor to Measure Blood Pressure at Chest in Anesthetized Patients

A. Vybornova, J. Solà, F. Braun, M. Proença, D. Ferrario, C. Verjus, M. Bertschi, O. Chételat

For more than ten years, CSEM has been a pioneer in the development, implementation, and validation of novel solutions for non-invasive continuous blood pressure (BP) monitoring. One of the central devices in CSEM's catalog on BP-monitoring is a multi-wavelength reflective photoplethysmogram (PPG) sensor that allows to accurately estimate BP at the chest. As a part of the validation procedure to characterize the sensor's performances in an acute setting, CSEM is conducting a clinical trial on anesthetized patients in collaboration with the Lausanne University Hospital (CHUV). The results demonstrate that in the acute conditions a widely-used conventional single-wavelength approach remains unreliable, while the innovative multi-wavelength device considerably increases the BP-estimation performances.

CSEM multi-wavelength PPG sensor at chest<sup>[1,2]</sup> allows to estimate BP via a pulse wave velocity approach. The optical signal captures the pressure waves propagating from the aortic valve towards the chest vasculature. Both the velocity of those waves and the related time of propagation, i.e. pulse arrival time (PAT), provide a surrogate measure of BP<sup>[3]</sup>.

The biomedical community sees various advantages of PPG technology, in particular in ambulatory or sub-acute settings, for which form factors such as patches and/or wearable sensors are required. For these form factors PPG allows to measure BP continuously without interfering with the comfort of the patients. Unfortunately, there is only a limited number of studies investigating the performances of the PPG technology against invasive references during hemodynamic changes.

To perform a realistic validation of the multi-wavelength PPG sensor, CSEM is conducting a clinical trial (clinicaltrials.gov: NCT02651558) on 17 anesthetized patients in collaboration with Lausanne University Hospital (CHUV). This scenario involves the administration of the anesthetic drugs inducing considerable variations in the hemodynamic parameters that could not be induced in sub-acute studies. Under these conditions the performances of both the novel multi-channel and the conventional single-channel approaches were evaluated against invasive gold-standard BP reference measurements (radial-artery catheter).

The investigation revealed that the administration of anesthetic drugs may transiently compromise the PPG waveform. The results of Kruskal-Wallis statistical test suggest that the waveform alterations are induced by the extreme changes in hemodynamics parameters occurring during anesthesia. As illustrated in Figure 1, 60% of the patients showed significant ( $p < 0.05$ ) link between the amount of compromised waveforms and the changes in the hemodynamic parameters.

Furthermore, on the 17 patients processed, the PAT estimations from the single-wavelength sensors correlated with reference catheter-derived PAT values in 5, 4 and 6 patients for the green, red and infrared channel, respectively. Meanwhile, the novel

multi-wavelength approach allowed to obtain PAT estimates that correlated with the benchmark in 12 patients. PAT estimations were considered to correlate to benchmark if p-values smaller than 0.05 were measured. An illustrative example of one patient is reported in Figure 2.

The presented findings illustrate that in a setup where anesthetic drugs are administrated and no additional pressure is applied onto the optical probe, multi-wavelength reflective PPG sensors are required to obtain reliable hemodynamic measurements at the chest. The very low reliability of single-channel PPG sensors at the chest questions the feasibility of developments claimed by other groups.

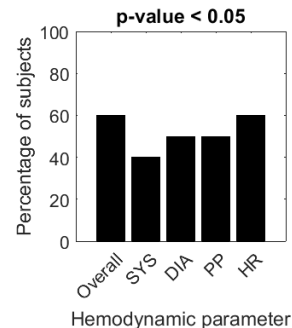


Figure 1: Percentage of patients in which the shape of the waveform was altered by one of the hemodynamic parameters, SYS, DIA, PP and HR stands for systolic, diastolic, pulse pressures and heart rate.

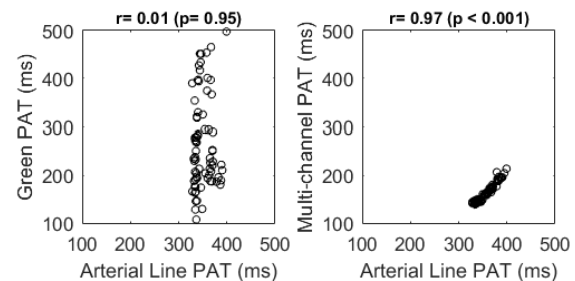


Figure 2: Example of the performances with a single-wavelength and a multi-wavelength reflective PPG approach.

[1] J. Sola, et al., "Chest Pulse-Wave Velocity: A Novel Approach to Assess Arterial Stiffness", doi : 10.1109/TBME.2010.2071385.

[2] J. Sola, et al., "Sensor device and method for measuring and determining a pulse arrival (pat) time", WO 2011120973 A1.

[3] R. Mukkamala, et al., "Toward Ubiquitous Blood Pressure Monitoring via Pulse Transit Time: Theory and Practice", doi: 10.1109/TBME.2015.2441951.

# ECG Quality Assessment of Dry-electrode Cooperative Sensors

O. Chételat, M. Rapin, D. Ferario, E. Haenni, S. Dasen, C. Meier, A. Falhi, J. Wacker, C. Pellaton •

*ECG has been routinely measured for many years with adhesive gel electrodes connected with shielded cables to a centralized ECG electronic device. One of the limitations that prevented alternative solutions which are better suited for wearables—such as textile electrodes—from replacing the classical technology was that the signal quality was not demonstrated as sufficient. In order to solve this issue, we developed and patented active dry electrodes called “cooperative sensors” embedded in a vest. Since cooperative sensors use a different type of transducer (dry instead of gel electrodes) and a different way of application (vest instead of adhesive), tests cannot be limited to compliance to medical standards (e.g., IEC60601-2-47 or IEC60601-2-25): a qualitative assessment in a real setting is necessary. This paper presents such assessment.*

The developed prototype (see Figure 1) measures 12 leads of ECG from cooperative sensors embedded in a vest. The sensors are located according to the Mason-Likar system and have stainless-steel dry electrodes. The cabling consists of a bus of two unshielded wires integrated in the vest. The vest is simply put on the skin (no skin preparation, no wetting) and zipped. The measured signals are streamed by Bluetooth from one of the sensors and displayed in real time on a computer or a smartphone where they are recorded for further analysis.

The assessment was performed on one healthy subject (so far). A commercial 12-lead ECG system (Schiller CS-200) was used as a reference (see Figure 2). The electrodes were placed at locations as close as possible to those of the cooperative sensors. The protocol was 1) a few minutes of resting (supine position), 2) exercise stress test on a bicycle (25 W steps, each 2 min long, from 50 W and up to subject's capability), 3) recovery.

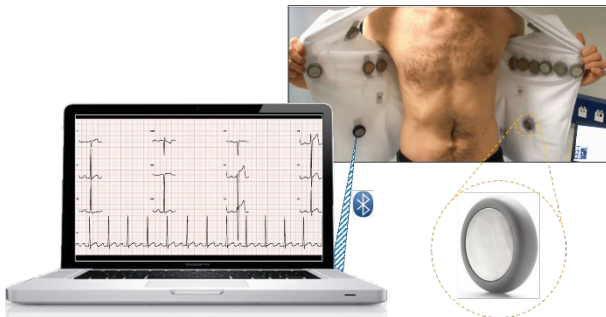


Figure 1: System under test made of dry-electrode cooperative sensors embedded in a vest.

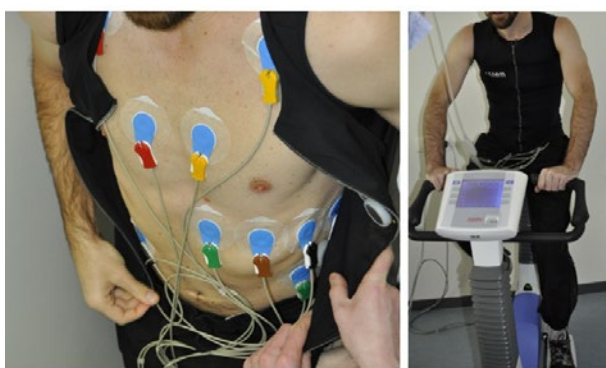


Figure 2: Test setup with reference sensor system (left) and subject performing the exercise stress test (right).

Figure 3 shows the signals obtained from the reference (black) and from the dry-electrode cooperative sensors (red) during the

exercise and resting phases of the protocol. The two signals are very similar. Note that they cannot be identical because the electrodes cannot be exactly at the same locations. However, when there is some 'noise' on the signals, a large part of it appears on both of them simultaneously, which means that the electrical artefact is present on the body.

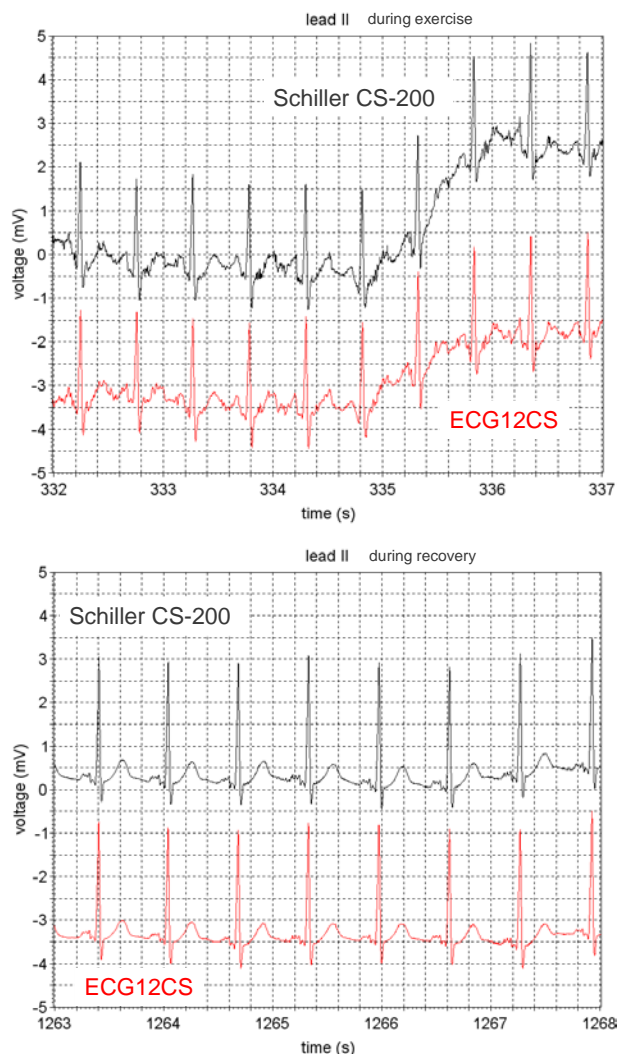


Figure 3: Typical ECG measured with reference (black) and cooperative sensors (red) during exercise (top) and recovery (bottom).

The performed assessment shows that at rest and during stress tests the quality of the signals measured with dry-electrode cooperative-sensor technology is at least equivalent to the signal quality of conventional 12-lead ECG systems.

• Service de cardiologie, Hôpital neuchâtelois

# Demonstration of a Proprietary Chip for Dry-electrode ECG and Impedance Measurements

P. Theurillat, M. Rapin, O. Chételat, P. Liechti

Classical approaches to make high-quality ECG measurements require the use of shielded cables connecting gel electrodes to a central unit. Moreover, impedance measurement requires at least two additional electrodes for current injection. CSEM has developed a concept based on dry-electrode sensors able to simultaneously measure ECG and thoracic impedance. Prototypes with discrete components were built to validate the correctness of CSEM approach<sup>[1]</sup>. Following this, an ASIC was realized in order to drastically reduce the system size. The small system size ( $56 \times 25 \times 5.5\text{ mm}^3$ ) and the simplicity of the cabling (only one unshielded and possibly uninsulated wire) make the system highly wearable and easy to integrate in a garment, thus improving the patient comfort. A demonstrator was realized in order to assess the ASIC performances in real life scenario. This paper presents the results of this development.

The developed demonstrator measures one ECG lead and impedance (real and imaginary components). Figure 1 (left) shows the typical sensor placement on a woman garment, whereas Figure 1 (right) shows the developed prototypes which contains the dedicated ASIC. The system is made of two sensors (active electrodes) connected together with one simple unshielded wire, each sensor having two dry-electrode contacts with the skin. With only two sensors, this patented technologies allows one to get ECG with a quality equivalent to three-electrode systems and impedance measured with the tetrapolar approach requiring four electrodes. The small and thin form factor allows one to wear the device under a simple garment. In order to further improve the patient comfort, the sensors were molded into soft silicon. Each sensor contains its own electronics (including the dedicated ASIC) and power supply (battery).



Figure 1: Sensors positions on the body.

In addition to ECG and impedance measurements, the system has additional sensing functionality, namely an inertial motion unit (IMU) for measuring body movements of the wearer.

The system includes a flash storage device allowing for the recording of the measured signals without any need of external device. Data can be downloaded afterward for further analysis. A Bluetooth 4 (BLE) connection integrated in the system allows transmitting in real time a set of signals to an external device for monitoring or post-processing purpose.

The final demonstrator dimensions are  $56 \times 25 \times 5.5\text{ mm}^3$ , including an 80 mAh battery. The battery allows a 24 hours of continuous measurement.

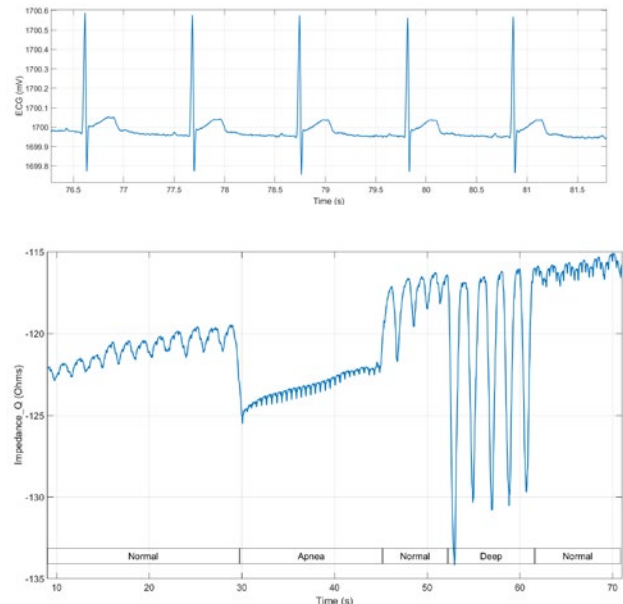


Figure 2: Typical ECG and impedance measurements.

The first tests conducted have shown good results of the system. The chip is fully operational. As shown in Figure 2, the ECG is clearly visible and complies with the medical standard for Holter devices, namely EN 60601-2-47.

The impedance signal shows that the respiration is visible during normal and deep respiration phases. Note that the impedance amplitude is much bigger during the deep phase, as expected.

The apnea phase shows that the signal is bound to the heart volume changes and/or pulmonary artery distension. This is interesting for devices able to measure cuff-less blood pressure. It can also be extracted during the other phases with appropriate signal processing.

This demonstrator shows that the developed ASIC can be implemented in products that are compliant with medical standards and that require one-lead ECG and impedance measured with dry electrodes and simplified cabling.

<sup>[1]</sup> O. Chételat, et al., "A Highly Integrated Wearable Multi-parameter Monitoring System for Athletes," 15th Nordic-Baltic Conference on Biomedical Engineering and Medical Physics, pp 148-151 (2011).

# A Novel Monitoring Solution to Reduce False Alarms in Neonatal Intensive Care Unit

M. Proen  a, F. Braun, D. Ferrario, A. Lemkadem, S. Dasen, V. Moser, O. Grossenbacher

The continuous monitoring of heart rate (HR), breathing rate (BR) and oxygen saturation ( $SpO_2$ ) in neonatal intensive care units (NICUs) poses a significant metrological challenge. Over the last years, CSEM has been developing contactless solutions for the estimation of HR and BR, which allows a gain in patient comfort and a reduction in false alarms caused by sensor detachment. In parallel, CSEM has developed a  $SpO_2$  monitoring solution robust against limb motion, the main cause of  $SpO_2$ -related false alarms in NICUs. These breakthroughs—carried out in the context of the Nano-Tera RTD project NewbornCare—are an answer to the strong clinical demand for reliable and patient-friendly monitoring solutions in NICUs.

False alarms in neonatal intensive care units (NICUs) lead to a strong overload for the medical staff and can—in the worst cases—lead to true alarms being missed. When monitoring the heart rate (HR) and the breathing rate (BR), the main cause of false alarms is the detachment of sensors, such as electrocardiographic electrodes. Regarding the monitoring of oxygen saturation ( $SpO_2$ ), false alarms are mainly induced by motion artifacts due to limb motion, as NICUs  $SpO_2$  probes are typically attached around the newborn's foot. In addition to being unsatisfying from a reliability viewpoint, the current monitoring setup in NICUs imposes a strong burden in terms of patient discomfort, thereby increasing the parents' anxiety. A patient-friendlier solution is strongly needed.

In the context of the Nano-Tera RTD project NewbornCare, CSEM has developed a solution—illustrated in Figure 1—aiming at filling the aforementioned loopholes of current NICUs systems. For HR and BR monitoring, CSEM's solution consists in replacing the standard wired sensors by two highly sensitive cameras allowing day (color) and night (near-infrared) vision, respectively. HR estimation is based on the analysis of pixel values in a region of interest (ROI) at the newborn's face<sup>[1]</sup>. BR estimation makes use of a motion estimation algorithm analyzing the movements of the chest ROI<sup>[2]</sup>. Both the face and chest ROIs are automatically obtained via a tracking algorithm. Regarding the monitoring of  $SpO_2$ , CSEM has developed a dedicated reflectance pulse oximeter to be positioned on the forehead, a location less prone to body motion than the limbs, and thereby less prone to false alarms.



Figure 1: CSEM's monitoring solution for NICUs.

The performance of the proposed monitoring solutions was evaluated on datasets recorded on healthy adults. Figures 2, 3 and 4 (top panel) show example estimations of the HR, BR, and  $SpO_2$  algorithms, respectively. The global performance on all subjects is provided in Table 1, and complies with the accuracy requirements targeted by the NewbornCare project. The final validation of the approach will be performed in an ongoing clinical trial on newborns in NICUs at the University Hospital Zurich. Preliminary results on  $SpO_2$  monitoring in a newborn patient are

shown in Figure 4 (bottom panel). Once validated, these monitoring solutions are expected to be a game changer for the reduction of false alarms in the future of NICUs.

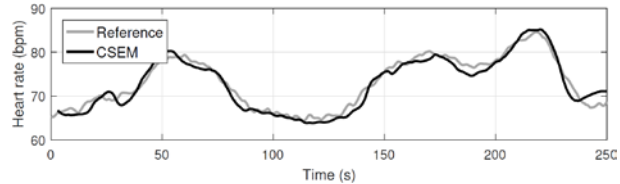


Figure 2: Example of HR validation.

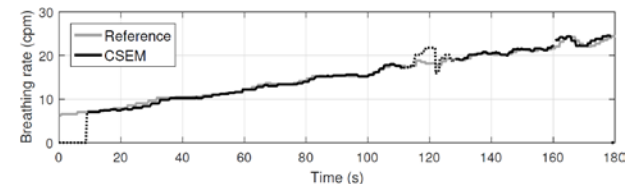


Figure 3: Example of BR validation. Dotted black lines are due to a low quality index during initialization or movement.

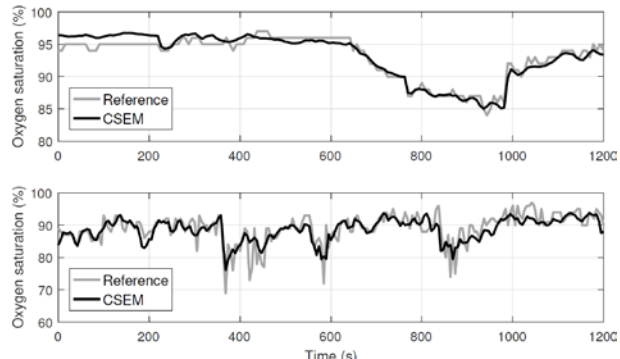


Figure 4: Example of  $SpO_2$  validation on a healthy adult (top) and on a newborn patient in NICUs (bottom).

Table 1: Performance of CSEM's monitoring solutions evaluated on datasets recorded on healthy adults.

Parameter (# of subjects)	Estimation error (mean $\pm$ SD)
Heart rate (n = 8)	0.70 $\pm$ 3.42 (bpm)
Breathing rate (n = 16)	0.20 $\pm$ 1.17 (cpm)
Oxygen saturation (n = 8)	0.07 $\pm$ 1.89 (% of $SpO_2$ )

This project was carried out in collaboration with EPFL (STI-JMV and LTS2 laboratories) and UZH (BORL laboratory and Neonatology Dept.). It was partly funded by Nano-Tera (RTD project NewbornCare).

[1] W. Wang, et al., IEEE TBME, 63(9), pp. 1974-1984, 2016.

[2] F. Braun, et al., Proc. of EMBC & NBC, pp. 567-570, 2017.

# A Wearable System Based on Cooperative Sensors for Multi-lead ECG Monitoring and Electrical Impedance Tomography Imaging

M. Rapin, F. Braun, J. Wacker, E. Haenni, J.-A. Porchet, A. Falhi, C. Meier, O. Chételat

Most of the currently available electrical impedance tomography (EIT) systems are limited by the number of electrodes. In view of overcoming this limitation we have developed a fully wearable EIT system based on cooperative sensors which allows for a variable number of electrodes. Another advantage of the proposed approach is that synchronous ECG is also recorded. Preliminary measurements on a healthy volunteer are presented.

The developed system is based on cooperative sensors (CS). CS are a measurement architecture based on active electrodes specially designed for acquiring bio-signals. In contrast to traditional approaches, CS neither require shielded or complex multi-conductor cables nor a central electronic unit. This advantage significantly simplifies their connection and integration in a garment. We have previously shown ambulatory ECG measurement with CS<sup>[1]</sup>. In this report, we show that our wearable CS system can also be used to simultaneously measure multi-lead ECG and multichannel bio-impedance signals for EIT imaging.

The electronic architecture enabling for this simultaneous measurement of ECG and EIT is detailed in<sup>[2]</sup>. Figure 1 shows an example of such a system when integrated in a vest. The system consists of one master sensor (black sensor) and an EIT belt with 16 CS (8 for current injections and 8 for voltage measurements). In the present configuration, 64 bio-impedance channels are measured at 80 frames per second and fully in parallel (via frequency-division multiplexing). In the current implementation, 4 CS were added on the thorax to measure additional ECG leads. Moreover, the master sensor has additional sensing functionalities, namely measuring body movements via an accelerometer and quantifying the blood oxygen saturation ( $\text{SpO}_2$ ) via an optical system<sup>[3]</sup>.



Figure 1: System under test made of dry-electrode CS embedded in a vest.

Figure 2 shows a typical ECG signal measured with CS, and Figure 3 shows a set of raw bio-impedance signals measured during normal breathing (four first cycles) and deep breathing (four last cycles). Raw bio-impedance signals can then be transformed into EIT images using a commonly used reconstruction algorithm such as GREIT<sup>[4]</sup>. Figure 4 shows an image sequence acquired during a normal breathing cycle. The size variation of the red regions representing the air volume variation in the lungs.

<sup>[1]</sup> M. Rapin, *et al.*, "Two-wire bus combining full duplex body-sensor network and multilead biopotential measurements," IEEE Transactions on Biomedical Engineering, (2017).

<sup>[2]</sup> M. Rapin, *et al.*, "A wearable EIT system based on cooperative sensors", Proc. Conf. EIT2017.

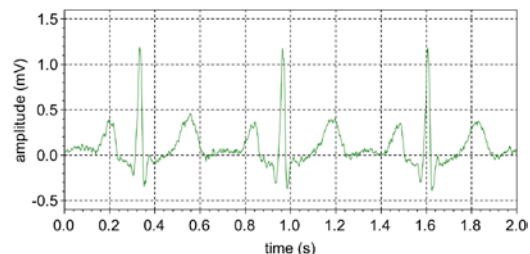


Figure 2: Typical ECG measured with CS.

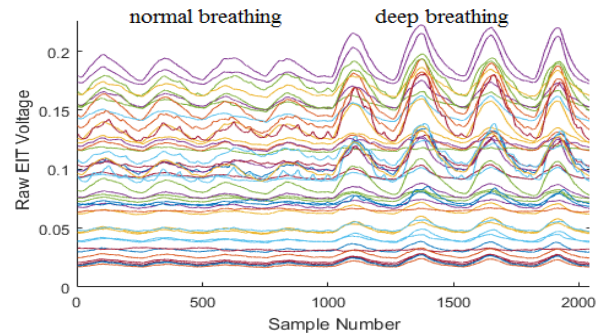


Figure 3: Raw bio-impedance signals measured with CS (8×8=64 bio-impedance signals).

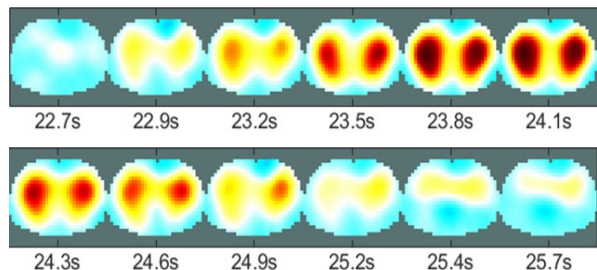


Figure 4: Typical EIT images sequence reconstructed during a normal breathing cycle.

In conclusion, this report shows a novel sensor system for ambulatory multi-channel bio-impedance and multi-lead ECG signal monitoring. The device is fully wearable thanks to the CSEM-patented CS technology, which allows connecting the sensors only with a bus of two unshielded wires, and does not require any central electronic unit. Such a system is able to synchronously measure multi-lead ECG and multichannel bio-impedance signals, paving the way towards a new generation of wearable EIT systems for non-invasive cardiovascular monitoring.

<sup>[3]</sup> J. Wacker, *et al.*, "Electrical and Mechanical Design of a Vest Measuring a Large Set of Physiological Signals," Proc. Conf. MobiHealth2014.

<sup>[4]</sup> A. Adler, *et al.*, "GREIT: A Unified Approach to 2D Linear EIT Reconstruction of Lung Images," Physiol. Meas., vol. 30, (2009).

# Sleep Phase Classification and Respiration Frequency Estimation Using a Wrist-worn Photoplethysmographic System

P. Renevey, R. Delgado-Gonzalo, A. Lemkadem, C. Verjus, M. Bertschi

*Sleep is important to ensure both physical and cognitive recovery. Disturbances in sleep patterns are indicators of underlying pathological conditions. For a proper analysis, polysomnography is the gold standard. However, it is obtrusive and requires medical supervision, which makes it not suitable for long-term studies or a large-scale implementation. CSEM is developing embedded systems to analyze the physiological variations observed during night based on wrist-worn photoplethysmographic measurements, which will enable unobtrusive and long-term monitoring of sleep.*

Sleep is a specific state of mind and body occurring with a periodicity of 24 hours in humans and most mammals (circadian rhythms). During sleep-time, recovery mechanisms take place to restore physical and cognitive abilities. The alteration of the normal sequence of these recovery phases can be the indication of underlying pathological conditions.

The reference system (gold standard) used to study sleep is polysomnography (PSG). PSG consists in the combination of different sensors used to record complementary physiological signals, including an electroencephalograph (EEG), an electrooculogram (EOG), an electromyogram (EMG), and an electrocardiogram (ECG). One of the outcomes of the analysis of PSG signals is the Hypnogram, consisting in the segmentation of sleep-time into different sleep phases. Hypnogram is determined from the visual inspection of PSG signals by a specialist. The resulting segmentation is partitioned into the following classes: REM (rapid eyes' movements) and NREM (non-REM). REM sleep, also designated as paradoxical sleep, corresponds to the phase where dreaming takes place and memory reinforcement occurs. NREM sleep is more related to the physical recovery and is subdivided into subclasses depending on the "deepness" of sleep: S1, S2, and S3.

PSG measurements are obtrusive due to the number of sensors and cables, require a medical supervision, and are therefore not suitable for the long-term analysis of sleep. CSEM is developing algorithms, based on the measurement of photoplethysmographic (PPG) and inertial signals at wrist, to analyze sleep. The proposed approach is based on the combination of the analysis of heart rate variability (HRV) with the analysis of body movements. It allows to estimate the respiration frequency and to segment the sleep phases<sup>[1]</sup>.

A first validation of the proposed approach has been implemented in the framework of CTI project 18842-2 with AVA AG<sup>[2]</sup>. The validation data has been recorded in controlled conditions using AVA's system in sleep lab facilities at the University of Fribourg. Ten female subjects, with four full nights per subject, have been involved in the creation of this medical database. The signals included in the data set are two PPG signals (left and right arms), PSG signals, and reference hypnograms obtained by visual annotation of the PSG signals. After the removal of problematic signals (electronic problem or human error) the validation data set contains sixty full night recordings.

Figure 1 depicts an example of the results obtained for the estimation of the breathing rate and for the classification of sleep

phases. Table 1 summarizes the results obtained for the estimation of the breathing rate (MAE is the mean absolute error and MAPE is the mean absolute percentage error). The results highlight that the proposed approach permits an accurate measurement of breathing rate during night.

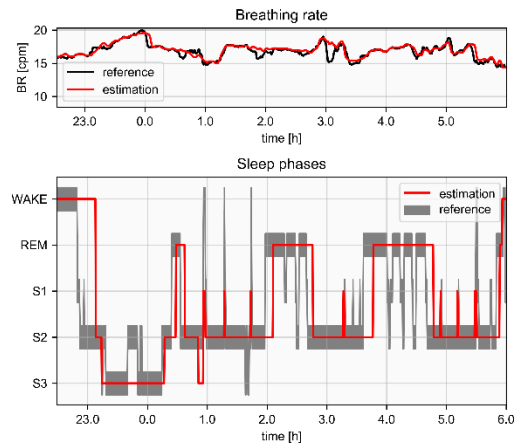


Figure 1: Example of the estimation of the breathing rate (top) and classification of sleep phase (bottom).

Table 1: Errors for the estimation of the breathing rate.

MAE [cpm]	MAPE [%]	MEAN [cpm]	STD [cpm]
$0.9 \pm 0.5$	$6.6 \pm 3.9$	$0.4 \pm 0.7$	$1.2 \pm 0.5$

Table 2 presents the results for sleep phase classification. The actual performances are strongly impacted by over-detection of REM sleep in a limited number of signals. Additional data have to be collected in order to modify the classification system without risking over-fitting. The current performances are promising and the algorithms are currently under an optimization process to improve the classification results.

Table 2: Sensitivity and specificity of sleep classification.

NREM Sens. [%]	NREM Spec. [%]	REM Sens. [%]	REM Spec. [%]	WAKE Sens. [%]	WAKE Spec.%]
$76 \pm 21$	$65 \pm 18$	$59 \pm 21$	$78 \pm 20$	$57 \pm 31$	$99 \pm 2$

The obtained results highlight that an unobtrusive wrist-worn device, such as a smartwatch or a fitness band, may be used as a substitute of PSG for large-scale long-term night analysis.

<sup>[1]</sup> P. Renevey, et al., "Optical Wrist-worn Device for Sleep Monitoring," Proc. EMBEC & NBC 2017, Tampere, Finland, 2017.

<sup>[2]</sup> <https://www.avawomen.com/>

# Swimming Performance with Wearable Inertial Sensors

R. Delgado-Gonzalo, A. Lemkadem, P. Renevey, E. Muntané Calvo, M. Lemay, K. Cox<sup>•</sup>, D. Ashby, J. Willardson, M. Bertschi

CSEM further expanded its physical activity profiling toolbox for smartwatches and fitness-bands by incorporating swimming analysis. The novel algorithm is capable of computing lap count, stroke count, time in lap, total swimming time, pace/speed per lap, total swim distance, and swimming efficiency (SWOLF). In addition, several swimming styles are automatically detected. The presented algorithm has been licensed to ICON Health & Fitness Inc. for their line of wearables under the brand iFit.

Swimming is considered one of the most complete physical activity, working most of body's muscles in a variety of ways and without major impacts. Its benefits are numerous and can be practiced by people across a broad range of ages and abilities (e.g., beginners, athlete, infant, elderly, over-weighted, injured, pregnant women). Like other sport activities, a precise real-time monitoring during the activity is of paramount importance to improve style and performance. However, swimming research has matured slowly due to difficulties caused by the use of new technologies into water.

CSEM extended its previously-published activity profiling algorithm<sup>[1]</sup> with results that provide swimming detection, style classification, lap and stroke count as well as SWOLF using a 3D accelerometer mounted on a wrist. This device is intended for sport and wellness applications, thus the accuracy of estimations is of importance regardless of the physical condition and training of the person.



Figure 1: Wrist device developed at CSEM for the monitoring of acceleration-related parameters.

A smart bracelet integrating a three-axial accelerometer and enough memory for 12 hours of continuous raw data recording was developed at CSEM and used to acquire raw acceleration signals at 25 Hz. The device, as shown in Figure 1, includes an LCD to display in real-time the parameters estimated with the embedded code and data-logging capabilities for offline analysis. The bracelet housing has a protection index of IP68 (6: Totally protected against dust 8: Protected against long periods of immersion under pressure). The device is capable of estimating fitness-related parameters real-time (e.g., activity classes, step count, and energy expenditure among others). Raw accelerometer data and estimated parameters can be stored and can be downloaded into a PC for further analysis.

During development, a total amount of 69 recordings were collected. The total number of laps adds up to 2679 combining

all swimming styles. An ensemble of 5 randomly-selected recordings were used to train the different sections of the algorithm during its development. For the scientific validation, references for swimming style and lap count have been notified by volunteers through a standardized form, while stroke count has been determined by manual annotations of the acceleration signals. The protocol conceived to validate the system and evaluate the accuracy of the algorithm was designed regardless of the swimming expertise of the user. Therefore, several elements of the protocol were decided by the user according to their capabilities. The user was free to choose between open turns, tumble turns, backwards flips, or stopping to catch the breath as well as the size of the swimming pool (50 m or 25 m).

The algorithm was implemented in fixed point for a low-power system. In particular, a system-on-chip was used with a microprocessor ARM® Cortex®-M0 with an average consumption of 13.9 µA and a memory footprint of 412 bytes of RAM and 2780 bytes of flash.

Table 1 shows the performance results of the lap. False positives make reference to the missed laps, and false negatives are usually related to two laps joined into a single one. Preliminary results on style classification and stroke count have been previously published<sup>[2]</sup>.

Table 1: Performance results of the lap detector.

	Lap count		
	Backstroke	Breaststroke	Front crawl
True positives	193	618	1854
False positives	0	4	5
False negatives	1	3	7
Precision	100.0%	99.36%	99.73%
Sensitivity	99.48%	99.52%	99.62%

Based on the presented and published results, the proposed model for swim analysis offers a high accuracy for swimming activities in the three main swimming styles. More precisely, we achieve precision and sensitivity values that are greater than 99% for lap detection and greater than 92% for style classification. Moreover, the stroke counter relative error is below 1.2% in the worst case. In view of these promising results, the suggested novel wrist sensor paves the way towards a new generation of affordable, comfortable, easy-to-use swimming monitor devices.

• ICON Health & Fitness Inc

<sup>[1]</sup> R. Delgado-Gonzalo, et al., "Physical Activity Profiling: Activity-specific Step Counting and Energy Expenditure Models Using 3D Wrist Acceleration", in Proc. EMBC '15, Milano, Italy, 2015.

<sup>[2]</sup> R. Delgado-Gonzalo, et al., "Real-time Monitoring of Swimming Performance", in Proc. IEEE EMBC'16, Orlando, USA, 2016.

# Validation Lung Phantoms

T. Parkel, N. Tscharner, S. Cattaneo

We report on the development of anthropomorphic lung model with inserted 3D-printed inner structures. The models can be driven with a programmable lab ventilator system and enable a thorough validation of radiotherapy treatments on lung tumors moving with the respiration cycles. A future goal is a completely 3D-printed flexible lung model making use of the latest printing technologies.

Recently CSEM has developed an anthropomorphic breathing validation phantom (LuCa) for the validation of new radio-treatment methods for lung cancer [1]. The scientific research in this field is focusing on reliable radio dose distribution on lung tumors moving with the respiration cycles. Besides featuring realistic anatomical properties, the phantom is capable of reproducing a patient's regular and irregular respiration pattern with a versatile and fully programmable lab ventilator system, also developed in house.

The LuCa system has provided a first validation for various treatment methods and so far is the only existing radio-treatment phantom system combining realistic material and anatomical motion properties. Next, the cancer treatment experts want to explore the radiation planning and arrival check under the influence of the inner lung structures motion. This interest triggered the request for generic LuCa lungs with more complex inner structures and the possibility of inserting 3D printed structures into the lung in a reproducible way.

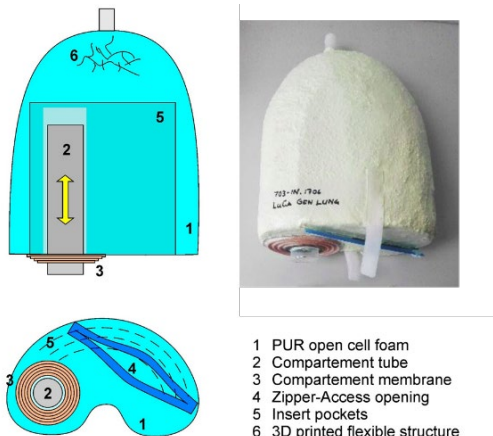


Figure 1: (Left) Schematic of the generic lung model with zipper access and compartment tube with SI motion; (Right) picture of the realized lung model.

As an intermediate solution, a generic lung with various access points to insert flexible 3D printed lung structures into fitted inner cavities was developed (Figure 1). The cavities are designed to hold the 3D printed structures in a predefined and reproducible way. The generic lung is fabricated from an ultra-low dense reticulated open soft cell polyurethane foam, which is used to stabilize fuel in large tanker airplanes. Flexible 3D printed lung structures were produced by selective laser sintering (SLS) (Figure 2). Various insert pockets were integrated in the lung, enabling the insertion of the inner structures at various depths and in different orientations. An integrated compartment tube enables inserting spheres or other specimens into the system

without any extra tools. The lung is driven by +14/-10mbar pressure range, resulting in 23 mm superior-inferior (SI) motion of the compartment tube and 3 mm anterior-posterior (AP) motion at the sternum.



Figure 2: 3D SLS printed flexible lung branch for insertion into the generic lung model.

The current lung is essentially handcrafted and therefore difficult to duplicate exactly. A completely 3D-printed flexible lung model making use of the latest printing technologies would be the next logical step. Despite being attractive, 3D-printing technologies currently cannot provide a good solution for flexible and hollow-printed organs. Currently, such parts can only be realized by removing physically the supporting material after the printing process.



Figure 3: Flexible 20 mm test spheres with inner structures.

In an effort towards a complete 3D-printed lung with inner structures, we started developing printing processes for producing hollow, flexible parts. First test results on flexible spheres with inner structures have shown very positive results (Figure 3). The mechanical behavior of the organ is influenced both by the material properties as well as by the design of the inner building structures. Next, we will focus on the development of a complete 3D-printing process to produce an entire lung with high flexibility with the requested motion during respiration cycles. This will open entire new possibilities in radiotherapy validation and other medical domains that could benefit from similar systems.

[1] S. Ehrbar, et al., "Respiratory motion-management in stereotactic body radiation therapy for lung cancer – A dosimetric comparison in an anthropomorphic lung phantom (LuCa)", Radiotherapy and oncology, 121 (2016) 328.



# ULTRA-LOW-POWER INTEGRATED SYSTEMS

Alain-Serge Porret

The ULTRA-LOW-POWER (ULP) INTEGRATED SYSTEMS program addresses the key challenges and technologies required to build very low power, (often) wirelessly interconnected, embedded smart systems or remote sensing nodes. The availability of such components is central to several global technological trends such as the Internet of Things (IoT) revolution, the advent of wearable technologies for wellness and medical applications (in line with the needs of an aging population), or the generalization of machine-to-machine (M2M) communications required by Industry 4.0.

It is generally recognized that the number of interconnected devices will continue to increase exponentially (as wearable items in our clothes or on our wrists, for implantable health monitors, at home in our appliances, to improve the security of our transport infrastructure, to track goods, etc.). Many of these applications need to pack extended functionalities into tiny, often almost disposable, wireless nodes, and at the same time to reduce power consumption in order to reach a battery life of years, or ultimately one that matches the life of the device. Efforts to achieve this goal can be helped by using harvesting to trickle charge the battery when the environment allows it. Additionally, many types of sensors generate an amount of raw data too large to be wirelessly streamed. Therefore, local processing is required to isolate the useful information from the noise. Local artificial intelligence will ultimately provide the tools necessary to efficiently achieve this goal.

The ULP program is engineered to help reach these goals, and can be summarized by the moniker "innovating to zero", meaning moving toward devices that consume zero power, require no batteries thanks to energy harvesting, occupy almost zero volume (are almost invisible), and asymptotically cost nothing (even for very complex functionalities), and that have virtually no exploitation hassle (smart, no configuration, no maintenance, secure, and exempt from privacy issues).

This vision still requires significant advances in a number of fields (see Figure 1), including energy storage (not studied here), energy harvesting (covered by the PV & ENERGY MANAGEMENT program), energy management, wireless communications, sensor interfaces, advanced embedded data processing, machine learning, and machine vision. This ambitious menu is approached with a judicious mix of hardware and software tools.

The trends mentioned above are largely made possible by today's mature IC technologies, which allow the packing of an incredible number of interfaces and of remarkable amounts of computational power in an ever-smaller volume, with constantly shrinking costs and lower power consumption. These trends are also clearly aligned with the so-called 'More than Moore' paradigm. Therefore, the development of ASICs (application-specific ICs) is a significant element of the program's activities, although COTS (commercial, off-the-shelf) solutions are used when suitable devices are available.

The markets covered by the program are very diverse, as the generic nature of Figure 1 suggests, and are growing in scope with the development of the Internet of Things (IoT) paradigm, which is also aligned with the global trends of "wireless everywhere" and "smart everything". Applications include:

- Consumer electronics (Bluetooth Smart devices, GPS-enabled devices, home automation and security systems, and image classification);
- Industrial systems (high-performance sensor interfaces, sensor networks for harsh environments, and optical quality control);
- Metrology (integrated measurement microsystems or optical encoders for various purposes);
- Medical and wellness (implants, vital sign monitoring, and electronic prostheses).



Needs, requirements, and solutions for modern IoT and wearable devices.

The circles highlighted in red ('ultra-low-power ASIC', 'ultra-low-power wireless', and 'machine learning') are some of the key challenges covered by the program.

The ULP INTEGRATED SYSTEMS program is divided into three research activities. The main areas of focus of each are summarized below.

**Wireless Systems:** (1) Reduction of the effective energy per bit required to send information through a realistic network, with realistic constraints. (2) Adaptation of advanced techniques used for standard “high-power” application to stringent ULP requirements. (3) Use of electromagnetic waves for ranging, localization, and remote sensing (for instance, vital sign monitoring).

**Vision Systems:** (1) Development of very-low-power imagers. (2) Development of machine learning algorithms with a special emphasis on embedded systems. (3) Design of specialized compact imagers—inside and outside of the visible spectrum—including multi/hyper-spectral capabilities. (4) 1D to 6D accurate position measurement through optical means.

**System-on-Chip:** (1) Mastering extremely low power (ELP) subthreshold logic design techniques. (2) Design of ELP mixed-signal sensing interfaces, with an emphasis on vital sign monitoring and timing devices. (3) Dedicated architectures suitable for ELP logic, including multi-core processors and dedicated accelerators. (4) Design of the power management circuits required by the above three focus points.

These activities resulted in many notable advances in 2017, some of which are highlighted below.

In *“Witness, an Autonomous Camera on a Sticker”*, an autonomous ultra-low-power image recording device integrated on a flexible palm-sized sticker is presented. Powered only by solar energy, it records still pictures of the environment based on a motion detection algorithm and stores them in a local memory for off-line use. The device is primarily used in surveillance applications, where a surveillance perimeter is created by placing units on walls and ceilings.

*“A Harvesting System with Adaptive Power Management Algorithm for Energy Autonomous Devices”* (page 144) describes a fully integrated energy harvesting unit controlled by a subthreshold processor. The system is able to seamlessly transfer power between a solar cell and a 3 V battery while powering external chips at 1.2 V. It manages the available energy optimally through a variety of embedded algorithms, including performing Maximum power point tracking (MPPT).

The companion paper *“A 0.5V Near Threshold Microcontroller Robust over PVT Variations”* (page 142) demonstrates a novel bulk biasing technique implemented with specific libraries designed in partnership with MIE Fujitsu Semiconductor Ltd for their deeply depleted channel (DDC) 55 nm process. The concept was fully validated by integrating a 32-bit RISC processor, proving stable operations at 0.5 V over a wide range of PVT (process, voltage, and temperature) variations. See also, on a related topic, the paper *“An Evaluation Tool for Standard Cell Libraries under PVT Variation: Application to Sub Threshold Design”* (page 140).

The core blocks of a robust 0.5 V low-power synthesizer operating at 2.4 GHz are described in *“A 500 $\mu$ W, 0.5V VCO and Fractional Divider for BTLE Robust over PVT Variations”* (page 132). This work extends the concept of body biasing to mixed-signal circuits and guarantees perfect operation over wide

variations of process, supply voltage (0.5 V  $\pm$  10%), and temperature (-40 °C to 85 °C).

*“A Power Management Unit for ULP SoC including BLE Radio”* (page 134) introduces a versatile power-management unit (PMU) dedicated to CSEM’s successful Bluetooth Low Energy (BLE) transceiver solution *icyTRX*. Some of the latest improvements to the *icyTRXIP* can also be found in *“Pre-Distortion Filter to increase Data Rate and/or Reduce Noise in Direct Frequency Synthesizer (G)FSK Modulators”* (page 131).

In *“High Performance Low Power Wireless Network for Water Distribution”* (page 130), a battery-operated wireless sensor network attached to hydrants is used to detect leaks in water distribution systems. The resultant solution is self-organizing and provides an accurate synchronization (+/- 1 ms) between nodes, as well as authentication, encryption, and the ability to perform over-the-air firmware updates.

*“Making Time Critical Cyber Physical Systems (CPS) Energy Efficient”* (page 128), explores a communication protocol that relies on concurrent transmissions generating constructive interferences. The study shows that this approach is more energy efficient than relying on collision avoidance. The solution has general applicability for CPS (e.g., aerospace, industrial process control, and robotics), infrastructure monitoring, and alarms.

Visually monitoring fast changing scenes and processes is a challenge for standard industrial camera systems, as smearing and rolling shutter effects impair the quality of the recorded images. These problems are addressed by the high-speed camera system as described in *“FastEye: A 1MP High-Speed Camera with Multiple ROI running at up to 64'000fps”* (page 139). The system is based on a CMOS image sensor with a global shutter, frame rates of up to 64,000 frames per second, and a user-friendly USB 3.0 interface.

In *“Single Detector for Multicolor Terahertz (THz) Imaging”* (page 15), an active multicolor terahertz (THz) imaging prototype is presented. The single pixel detector was integrated into a 0.18  $\mu$ m CMOS process and used to build a demonstrator for THz 2D imaging (using scanning). An improved version of the detector is being implemented in 55 nm CMOS technology.

Better interfacing life is also a growing trend. For instance, for in vivo measurements, a highly reconfigurable, ultra-low-power, 20-channel system on a chip (SoC) for biomedical signal acquisition is presented in *“Fully Integrated Low Power Bio Potential Acquisition Analog Front End IC”* (page 145). In vitro applications are also explored in *“Microelectrode Array (MEA) for Neural Interface”* (page 146), where a chip for electrophysiology measurements is described. The MEA features 4,096 full-duplex electrodes for sensing and stimulation, and is aimed at testing drugs on neurobiological models.

As a final highlight, the remote, contactless, radio frequency (RF) sensing of vital signs paves the way to unobtrusive, easy-to-use, continuous health monitoring in the home, at work, and in hospital environments. Such a vital sign RF sensing demonstrator is outlined in the paper *“Remote, Contactless RF Vital Signs Sensing”* (page 127).

# Remote, Contactless RF Vital Signs Sensing

E. Daskalaki, O. Vorobyov, E. Le Roux, J. R. Farserotu

*Remote, contactless, radio frequency (RF) sensing of vital signs paves the way towards unobtrusive, easy-to-use and continuous health monitoring at home, work and hospital environments. A vital signs RF-sensing demonstrator has been developed in the framework of the M3TERA H2020 project.*

Remote, contactless, RF vital signs (VS) sensing is an emerging technology with potential applications from health and wellness at home, to hospitals, safety and assisting living. RF sensing permits unobtrusive measurement of vital signs at longer distances and lower power compared to other solutions (e.g., vision). It can operate under any lighting conditions without the need for special clothing or devices. The broad application space includes self-monitoring of VS for better lifestyle control, monitoring of persons with sensitive skin (e.g., newborns, burn victims, elderly), safety (e.g., VS of drivers, pilots), as well as, multi-person VS monitoring in assisted living environments.

M3TERA is a H2020 project which targets the design and development of a highly-integrated, cost and energy efficient, reconfigurable sub mm-wave system<sup>[1]</sup>. In the framework of M3TERA, a RF-sensing demonstrator has been designed and developed for the remote measurement of heart rate (HR) and breath rate (BR). The RF-sensor is based on measurement of small displacements that occur when a person breathes and when the heart beats. The chest movement ranges from 0.6 to 1.2 mm due to the beating of the heart and from 1 to 2 cm due to respiration (refer to Figure 1). The displacement can be captured via the modulation of the power and phase of an RF signal reflected at the surface of the body. The target prototype is an FMCW radar operating at the 122.25-123 GHz or the 57-66 GHz band. As a first step, in order to investigate and demonstrate the principles of remote VS sensing, a continuous wave reflectometer was designed and developed based on a Software Defined Radio (SDR) platform. The use of the millimeter wave (mm-wave) frequency band offers increased displacement resolution as well as good skin reflectance.

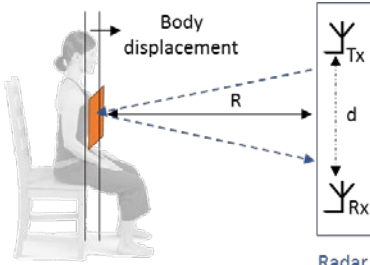


Figure 1: Radar-based VS measurement principle.

The laboratory system, which operates at 110 GHz, is comprised of a transmitter (Tx) and a receiver (Rx), as shown in Figure 1. The Tx signal is reflected by the body and the received (backscattered) signal is mixed with a Local Oscillator (LO). The intermediate frequency (IF) signal is IQ-demodulated in the digital domain. COTS components (RF generators, frequency

multipliers, harmonic mixer, amplifiers) were combined with the SDR which was used for the reception of the IF signal (Figure 2).

The SDR platform provides the software tools for the development of the RF digital signal processing (DSP) and the VS estimation algorithms. Novel, low-cost 3D printed mm-wave antennas were designed and developed, optimized for the VS demonstrator at CSEM<sup>[2]</sup>. Link budget analysis indicates that both HR and BR can be extracted at distances up to 10 m, given typical noise figure (12 dB) and phase noise specifications.

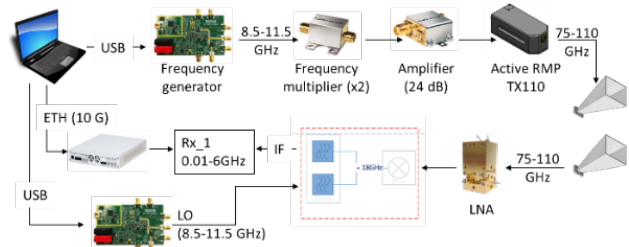


Figure 2: System setup.

Extraction of HR from the high-order BR harmonics is challenging and currently an open research problem. Various DSP algorithms were investigated for this purpose including wavelet decomposition, dynamic time wrapping, principle components analysis and dynamic harmonic notching. Figure 3 presents the results of the latter approach for the case of slow, sinusoidal-like breathing and fast, harmonic-heavy breathing. The effect of the breathing type on the quality of the HR estimation can be clearly observed.

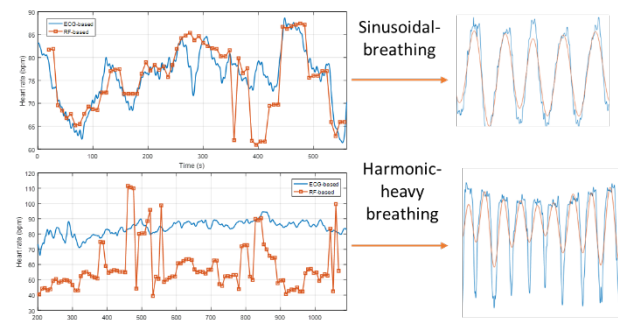


Figure 3: ECG-based (blue) and RF-based (orange) HR estimation during sinusoidal (top) and fast, harmonic-heavy (bottom) respiration.

The RF-sensing demonstrator has proven the feasibility of remote VS sensing. The next steps include the development of an FMCW radar which will provide the ability to track and monitor multiple persons in the same environment. Machine learning algorithms will be developed for the reliable separation of HR and BR. Further algorithmic development will target person tracking and compensation of motion artifacts.

<sup>[1]</sup> M3TERA (EU project under GA No 644039) [www.m3tera.eu](http://www.m3tera.eu).

<sup>[2]</sup> O. Vorobyov, J. R. Farserotu, J.-D. Decotignie, "3D printed antennas for Mm-wave-sensing applications", ISMICT Int. Symposium on Medical Inf. and Comm. Tech., (2017).

# Making Time-critical Cyber Physical Systems Energy Efficient

D. C. Rojas Quiros, J.-D. Decotignie

Wireless Sensor Networks (WSNs) promise breakthroughs in cyber physical systems (CPS). This study proposes a communication protocol for enabling WiseSkin (artificial skin for humans based on WSNs) to seamlessly convey tactile stimuli, thus addressing stringent adaptability, latency (<100 ms), reliability (>99%) and energy requirements. The protocol relies on concurrent transmissions enabled by constructive interference and this study shows that this approach is more energy efficient than the traditional one of avoiding concurrent transmissions. The solution has general applicability for WSNs in CPS (e.g., aerospace, industrial process control, robotics, etc.), infrastructure monitoring and alarms.

WiseSkin leverages WSNs to make possible a novel technology: artificial skin for humans capable of restoring tactile feeling<sup>[1]</sup> to those using prosthetic limbs. It consists of miniature nodes embedded in a polymer material that sense the pressure over the skin and transmit the data via a wireless multi-hop network to a control unit (CU), which transfers the stimuli to the nervous system (Figure 1, for additional details refer to<sup>[1]</sup>).

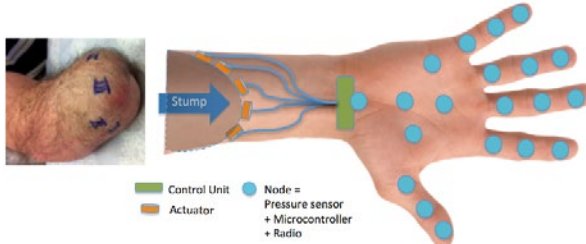


Figure 1: Schema of WiseSkin. A WSN embedded in a polymer senses the pressure over the skin, transmits the data via wireless multi-hop network to a CU, which transfers the stimuli to the nervous system of the user (source of the stump image: Lund University).

WiseSkin must convey the tactile stimuli in a manner that the user perceives as natural, which generates challenging requirements for the WSN: **adaptability** (to handle sporadic traffic surges), **responsiveness** (to ensure a worst-case end-to-end latency under 100 ms), **energy efficiency** (to maximize the lifetime of the nodes), and **reliability** (to maintain a packet delivery ratio over 99%).

The proposed protocol consists of two operating modes: low-traffic and high-traffic. The former aims at minimizing the energy consumption and the latter on conveying the tactile information when the skin is stimulated (extended report in<sup>[2]</sup>).

Both modes rely on simultaneous transmissions enabled by constructive interference at the symbol level<sup>[3]</sup>, which ensures state-of-the-art reliability and a fast transition between modes. This technology has traditionally been used for periodic traffic (e.g., Glossy<sup>[3]</sup>), while in this project we propose a modified version that caters to sporadic traffic surges (Modified-Glossy).

The protocol for WiseSkin, which leverages concurrent transmissions, was compared with ContikiMAC, which is based on the classical approach of avoiding concurrent transmissions. The evaluation used 10 nodes and monitored the end-to-end

latency (from the generation of the event until the arrival at the sink), energy consumption, and reliability. The results show that the Modified-Glossy protocol is more energy efficient, for targeting a given latency, while maintaining reliability over 99% (Figure 2). Moreover, the worst-case latency is highly predictable and the system naturally handles traffic surges (details in<sup>[2]</sup>).

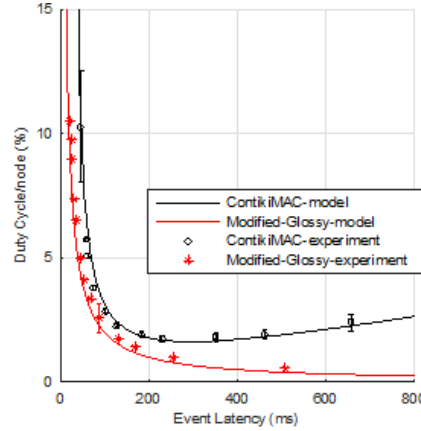


Figure 2: Duty cycle as a function of Latency. The Modified-Glossy protocol displays a lower duty-cycle in the entire range of latencies.

The proposed protocol has applications in multiple domains:

- **Cyber Physical Systems:** The high reliability and capability of providing predictable delays are ideal for enabling control loops in industrial processes, robotics or aerospace devices.
- **Monitoring:** The ability to accommodate traffic surges while also being energy efficient is ideal for networks that perform on-demand evaluations. For example, a WSN that can evaluate the water quality in an urban distribution network and that can reliably send the results of a requested analysis, while maintaining a battery life of several years.
- **Alarms:** The ability to seamlessly handle simultaneous transmissions ensures a reliable notification of an alarm even if multiple nodes aim to report it simultaneously. For example, a WSN that detects rocks falling on the train tracks can reliably convey an alarm triggered simultaneously by all the nodes, in case of a landslide.

Acknowledgement: This work was partially funded by NanoTera national research program under SNF grant No. 20NA21-143070.

[1] "WiseSkin" project: <http://www.nano-tera.ch/projects/353.php>

[2] C. Rojas, J.-D. Decotignie, "Artificial skin for human prostheses, enabled through wireless sensor networks", RTCSA IEEE Int. Conf. on Emb. and Real-Time Comp. Systems and Applic., (2017).

[3] F. Ferrari, et al., "Efficient network flooding and time synchronization with Glossy", IPSN Int. Conf. on Information Processing in Sensor Networks, (2011).

# Wireless Power Transfer for Wearable Applications

O. Vorobyov, V. Kopta, J. R. Farserotu

The proposed solution for Wireless Power Transfer provides a means of remote powering via guided propagation through a flexible, stretchable waveguide structure. The structure may be molded to conform to various different shapes (e.g., suited for wearable applications). In addition to low losses, the structure, without wires, also offers opportunities for improved reliability, lower production cost and ease of configuration.

Short distance wireless power transmission (WPT) is becoming increasingly popular as a means of remotely powering devices, towards batteryless operation. Potential applications include wearable devices, body area network (BAN) and consumer electronics applications, as well as, applications operating under constraints, or in environments, where conventional wired sources of power or batteries are either unsuitable or undesirable (e.g., extreme autonomy and miniaturization).

The proposed low loss, flexible waveguide (FWG) solution for WPT was developed in the course of the WiseSkin Nano-Tera project. WiseSkin targets the development of an artificial skin embedded with tactility sensors (pressure sensors) for restoration of a natural sense of touch in a prosthetics application. The proposed solution offers the following benefits:

- Batteryless operation – of nodes (e.g., sensor or actuator nodes) helps to reduce their footprint and lower their cost.
- Increased robustness / reliability – there are no wires or mechanical contacts (hard to implement and a first source of failure) to break, either for powering or communication.
- Easier to manufacture / lower cost – removal of the mechanical contacts eases manufacturing and reduces cost. Sensor and actuator devices may be placed anywhere within the FWG (not constrained by wires or connections).
- Ease of device placement – sensors and actuators can be placed almost anywhere within, as well as on, the structure.
- Scalability – to larger number of devices is readily possible as there are not contact or wires to connect.

An illustration of the concept for WPT<sup>[1,2]</sup> is shown in Figure 1.

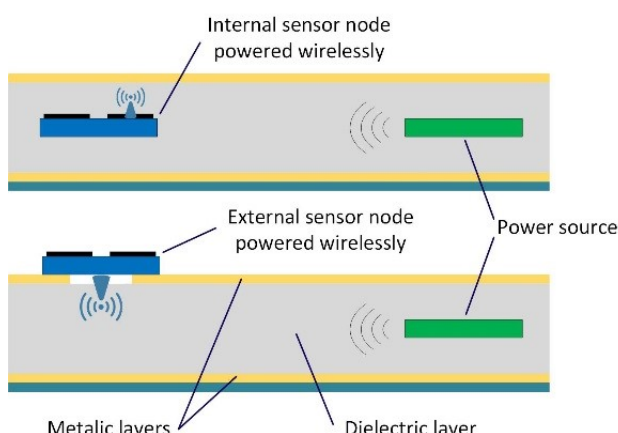


Figure 1: General concept of a sensor node remotely powered via RF energy harvested from a RF source and distributed via the FWG.

[1] V. Kopta, J. R. Farserotu, O. Vorobyov, "System and method for remote powering at least one sensor or actuator from a RF power source", May 3, 2017, EP Patent App. EP20,150,192,228; US Patent App. 15/336,955.

The sensor(s) or actuator(s) may be either inside or outside of the FWG structure. In this work, the antenna and the waveguide are optimized for operation in the 2.4 GHz ISM band. The use of other bands is also possible, in particular higher frequencies, which enable the antennas for the wireless sensor / actuator nodes to be further miniaturized.

In order to assess the performance of the proposed wireless power delivery system, several FWG prototypes were implemented. For the purpose of test and measurement, a compact capacitive loop antenna solution with top and bottom metallization was used (optimized for integration into the FWG at 2.4 GHz). The loop antenna is basically a rectifier-antenna combination (rectenna), i.e. without any integrated rectifier circuit. Antennas are inserted into both ends of the FWG (source and sink) and the received signal is measured and characterized in terms of S21-parameter of the waveguide.

The results are presented in Figure 2. The S21 parameter is equal to -4 dB at roughly 2.4 GHz, indicating that about 40% of the radiated power is available to power devices. The next step is to integrate ULP sensor nodes with the waveguide structure.

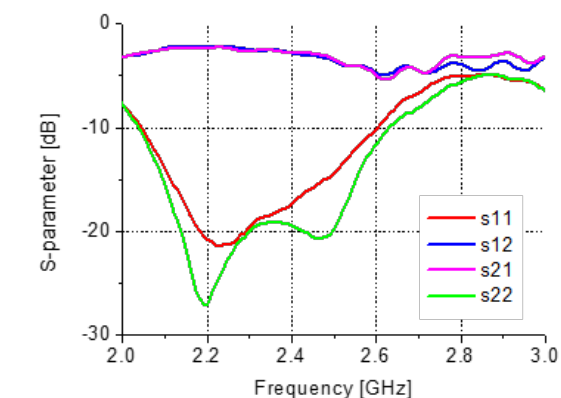
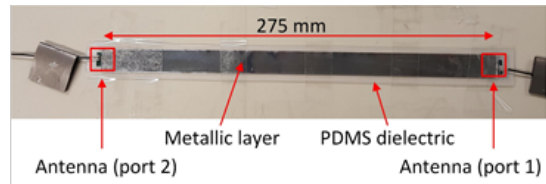


Figure 2: Sample of the waveguide under test (top) and its measured performance characteristics (bottom).

This work was partially funded by Nano-Tera national research program under SNF grant No. 20NA21-143070<sup>[3]</sup>. We would like to thank the Nano-Tera program and the SNF for their support.

[2] A. Vorobyov, et al., "Efficient through-waveguide wireless power transfer for body area networks", BIOCAS IEEE Biomedical Circuits and Systems Conf. (2017).

[3] "WiseSkin" project: <http://www.nano-tera.ch/projects/353.php>

# High Performance Low-power Wireless Network for Water Distribution

D. Piguet, B. Perrin, D. C. Rojas Quiros, J.-D. Decotignie, C. Hennemann, A. Restrepo-Zea, C. Kassapoglou-Faist, Y. Brunet

Hinni AG teamed up with CSEM and the Hochschule in Luzern to develop the third generation of the Lorno water monitoring wireless network. The project resulted in the realization of new high value added features such as self-organization, accurate synchronization ( $\pm 1$  ms) for leak localization ( $\pm 5$  m), authentication / encryption and the ability to perform over-the-air firmware updates.

CSEM developed and delivered an industrial grade wireless sensor network (WSN) for the monitoring of a water distribution network. To do so, CSEM relied on more than a decade of expertise in the domain in order to cope with particularly demanding, and sometimes conflicting, system requirements.

The solution implemented by CSEM is a self-organized, multi-hop wireless network. It exhibits state-of-the-art performance in energy conservation (up to 10 years lifetime on a single battery), low latency (alarms transmitted in less than one minute) and adaptability to both very short and long messages (from a few bytes to more than 4 kbytes). Upon request, the network can maintain very tight synchronization (1 ms) between the nodes, despite large temperature gradients. The solution is also secure and the node firmware can be updated over the air. Additionally, the architecture is versatile: depending on how they are combined, the same electronic boards can be used as relays, wireless sensors, cabled or cellular gateways or GPRS/3G sensor nodes in case of isolation from the WSN.

The customer, Hinni AG, is the Swiss market leader in the production, sales and maintenance of water hydrants and associated services. A decade ago, Hinni introduced the Lorno wireless monitoring system for the public water distribution network. The concept uses water hydrants as access points to the underground pipes. They are equipped with wireless sensors capable of measuring the status (opened / closed), temperature and pressure, as well as, a hydrophone for leak detection. The sensor measurements are transmitted to relays installed on street light posts and forwarded to a gateway connected to the internet, as illustrated by Figure 1.

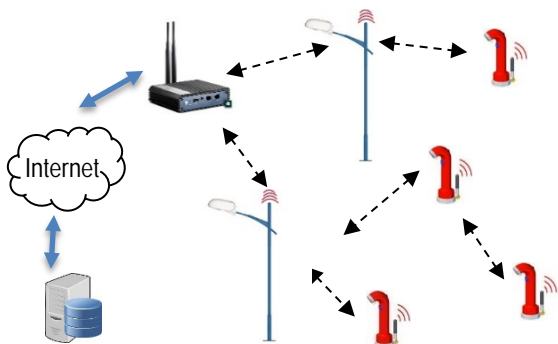


Figure 1: Lorno wireless water distribution network monitoring system.

In 2014, Hinni, CSEM and the Fachhochschule of Luzern teamed up to develop a new generation of the Lorno system aimed at general improvement the performance of the wireless network, implementation of additional features and enabling automatic localization of leaks. CSEM was tasked with the wireless network development, as well as the design of the electronic board.

The network relies upon the CSEM WiseNet solution operating with the ultra-low power WiseMAC medium access protocol. Among the new features, CSEM added a state-of-the-art routing protocol. This protocol enables the network to self-organize, allowing the customer to install or remove nodes without the need

for time and resource consuming network planning and manual configuration.

The new system's most innovative and advanced feature is the ability to localize water leaks automatically; whereas, the previous generations were limited to leak detection. The technique relies on the correlation of several hydrophone measurements taken at hydrants connected to the same pipe as the one that detected a leak. For an accurate correlation, it is essential that the measurements at each hydrant start simultaneously with a maximal difference of less than 1 ms (millisecond) between any pair of hydrants. For this purpose, CSEM developed a time synchronisation protocol with clock deviation estimate and compensation. Tests have shown that the clock compensation converges rapidly and that the error is below 1.2 ms in extreme conditions (-25 °C spray cooling). For the leak localization application, this translates into an accuracy of 5% of the length between the measurement points.

As the sensor nodes need to conserve energy, WSNs usually transport small blocks of information at a low data rate. To transport the audiograms recorded for leak localization, which have a significant size (several kbytes), CSEM implemented a transport layer with fragmentation and reassembly over multiple hops, between the sender and the base station. This feature takes advantage of the WiseMAC "more bit", an indication in uplink packets that allows a destination to stay awake for several consecutive packets, which results in a higher throughput without power consumption increase.

Additional enhancements brought by CSEM to the network are over-the-air firmware updates and security. Over the air firmware updates are important in order to reduce the maintenance costs because the transmission devices are not easily accessible, as they are either locked inside hydrants or high up in the light posts. The over-the-air firmware update protocol made by CSEM uses compression based on the difference between the new and the old version and a reliable data dissemination protocol.

Additionally, data authentication and encryption based on AES were added to protect the wireless network against attacks and data corruption. Security is of especially high importance for wireless networks attached to critical resources and infrastructure.

CSEM continues to support Hinni with respect to new product industrialization and certification. Moreover, CSEM is currently developing a compatibility layer that will allow relays of the new Lorno generation to communicate with hydrants equipped with the first and second Lorno generations.

# Pre-Distortion Filter to increase Data Rate and/or Reduce Noise in Direct Frequency Synthesizer (G)FSK Modulators

A. Vouilloz, N. Scolari

A pre-distortion filter implemented in the most recent versions of icyTRX is presented here. The filter reduces the PLL bandwidth of the direct frequency fractional frequency synthesizer modulator enabling the data rate to be increased and/or the adjacent noise/spurs to be reduced at the existing rate.

The new Bluetooth Low-Energy 5 specification adds a 2 Mbps data rate option to the existing 1 Mbps data rate. To address the higher data rate in the icyTRX direct frequency synthesis (G)FSK architecture, it is necessary to increase the Phase Lock Loop (PLL) bandwidth in proportion to the data rate in order to preserve the bandwidth of the modulating signal. This bandwidth, without calibration, must be oversized in order to ensure that there is sufficient margin to address the data rate when the following parameters are varied:

- The temperature.
- The frequency versus voltage gain of the voltage controlled oscillator (VCO).
- The silicon chip-to-chip variations (loop filter passives, bias currents, etc.).

The variation of these parameters acts to either reduce or increase the PLL bandwidth, depending on their values.

In a direct frequency synthesizer modulator, if the PLL bandwidth is too narrow compared to the bandwidth required by the data rate, the inter-symbol interference (ISI) is increased, which introduces more errors in the receiver. On the other hand, an over-sized PLL bandwidth results in increased phase noise and more parasitic spurs radiated in transmit (TX) mode because these unwanted signals are not as efficiently filtered by the PLL. An over-sized PLL bandwidth makes it therefore more difficult to comply with regulatory guidelines concerning e.g., adjacent channel power (ACP), as well as, some FCC rules.

The idea presented here is to use a simple solution that allows us to significantly reduce the PLL closed-loop bandwidth used in icyTRX in the TX mode for direct (G)FSK modulation. Specifically, a digital compensation filter is added in order to keep the data rate constant, while reducing the PLL bandwidth. The benefits of reducing the closed-loop PLL bandwidth with such a compensation filter are better ISI performance, reduced phase noise and improved spurs rejection outside the closed-loop bandwidth of the PLL.

In the direct frequency synthesis (G)FSK modulator architecture, the bandwidth of the modulation signal is determined by the following parameters:

- Phase frequency detector (PFD) phase gain.
- Charge-pump current gain versus phase.
- VCO frequency gain versus control voltage.
- Passive loop filter.
- The programmable divider with a division factor N.

Some of these parameters are readily determined, such as the division factor N and the phase gain of the PFD. But the charge-pump gain variation is mainly correlated to the bias current source variation, which is sensitive to the temperature if a bias current source proportional to the absolute temperature

(PTAT) is used. Further, the VCO gain is sensitive to the tuning voltage settled by the PLL and also to the variation of fabrication parameters (process corners). The passive loop filter is programmable, but it is also sensitive to the process corners. The PLL frequency response in closed loop range – i.e. the range where the modulation signal is low-pass filtered in direct modulation principle – is fully defined by the previously mentioned parameters. There are no (or just a few) parameters that may be freely adjusted to change the shape of the frequency response of the modulated signal.

Our approach is to add a numerical "pre-distortion filter" in the digital path of the modulation signal that may be used to directly modulate the fractional frequency synthesizer via the  $\Sigma\Delta$ . This provides a degree of freedom, which is necessary to adjust the initial "analog" closed-loop frequency response of the PLL e.g., to flatten the amplitude and the group delay frequency responses in the modulation signal path. The result is that the frequency response of the modulated signal is *different* than the "analog" PLL frequency response. The amplitude and phase (group delay) frequency responses are compensated via a pre-accentuation digital filter. Figure 1 shows the eye-diagram of a 1 Mbps (G)FSK signal without pre-distortion and Figure 2 shows the results with pre-distortion applied to the same PLL bandwidth.

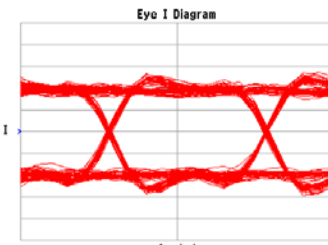


Figure 1: Eye-diagram without pre-distortion filter applied.

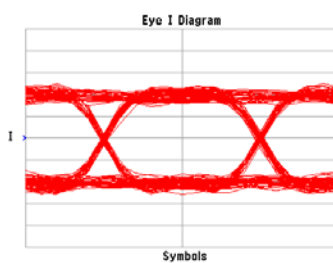


Figure 2: Eye-diagram with pre-distortion filter applied.

The advantage of the proposed pre-distortion filter in the path of the modulation signal is about 4 to 5 dB more with respect to the rejection of unwanted fractional/references spurs and phase noise outside of the PLL bandwidth. Put differently, this is equivalent to multiplying the (G)FSK data-rate by a factor of 1.6 to 1.8, while keeping the "analog" PLL bandwidth constant.

# A 500 $\mu$ W, 0.5 V VCO and Fractional Divider for BTLE Robust over PVT Variations

C. A. Salazar Gutierrez, P. Persechini, E. Pérez Serna, D. Ruffieux, H. Kurata •

*A low-power VCO and fractional divider robust with respect to process, voltage and temperature variations has been developed for IoT and energy harvesting applications. Integrated in a 55 nm deeply-depleted channel (DDC) technology, the body biasing feedback based circuit compensates the transistor drain-to-source IDS current and guarantees full functionality over three process corners (TT, SS and FF), at 0.5 V  $\pm$  10% supply voltage and over a temperature range between -40°C and 85°C.*

Lowering the voltage is a promising solution to reduce the digital dynamic power consumption and extend the system lifetime of IoT and energy harvesting applications. The frequency synthesizer and, more specifically, the VCO and the fractional divider are power hungry blocks that can take advantage of the lower voltage to reduce transceiver power consumption. However, this strategy comes at a cost in terms of large transistor drain-to-source current (IDS) variability over process, voltage and temperature (PVT) variations due to its near/sub-threshold operation, making the design of these critical blocks more challenging.

This work proposes a 2.8 GHz VCO and a dynamic fractional frequency divider that is highly robust to PVT variations; made possible through the use of a body bias feedback technique. The proposed solution consumes 500  $\mu$ W from a nominal 0.5 V supply voltage.

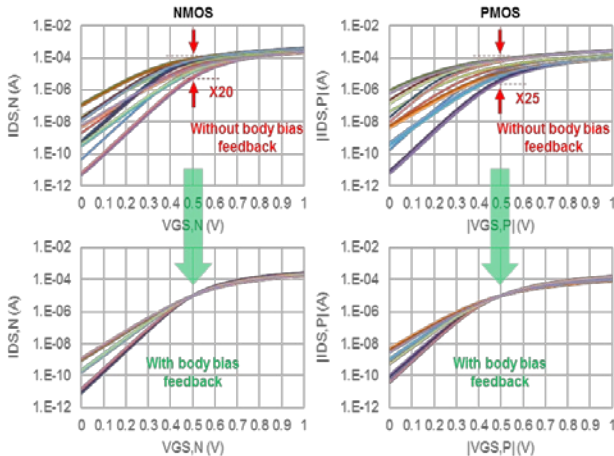


Figure 1: IDS vs VGS characteristic for an ULL NMOS and PMOS transistor with and without body bias feedback across PVT corners.

Figure 1 shows the IDS versus gate-to-source voltage (VGS) characteristic for ultra-low leakage (ULL) NMOS (left) and PMOS (right) transistors, with and without the proposed body bias feedback across PVT corners. When no bulk biasing is applied ( $V_{BS} = 0$  V), the current variation across PVT is increased as VGS is reduced. The proposed adaptive body feedback loop generates the required bulk voltage to enable the transistor to

deliver a constant current independently from PVT variations. As a result, the 20 times PVT current dispersion observed at  $V_{GS} = 0.5$  V is compensated for a given 10  $\mu$ A reference current (see Figure 1).

The circuit has been integrated using a 55 nm DDC CMOS technology from Mie Fujitsu Semiconductor. It is composed of a NMOS cross coupled VCO with a body feedback current control loop, a dynamic frequency divider (by four), a 5-stage cascaded 2/3 dual-modulus divider and a second order delta sigma mesh modulator. Four bulk biasing sections composed of low, standard and high threshold voltage transistors are used among the VCO and divider chain in order to cover the large frequency range of operation. The layout of the proposed circuit is depicted in Figure 2.

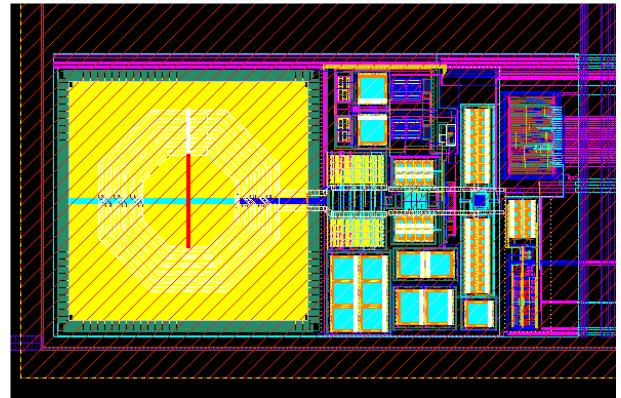


Figure 2: VCO and fractional frequency divider layout.

The results of simulations show full functionality of the circuit across three process corners (typical, slow and fast) from a 0.5 V supply, over a temperature range of -40 to 85°C. The VCO provides 10% frequency tuning centered at 2.8 GHz and consumes 400  $\mu$ W of power. The dynamic frequency divider provides fractional frequency divisions in the range of 8 to 252, with a nominal power consumption of 100  $\mu$ W.

This work has demonstrated how bulk biasing can be used for low voltage and low power applications covering a large range of frequencies, while offering more than 35% power reduction compared to the previous state-of-the-art [1,2,3].

• Mie Fujitsu Semiconductor Limited

[1] V. K. Chillara, et al., "An 860  $\mu$ W 2.1-to-2.7 GHz all-digital PLL-based frequency modulator with a DTC-assisted snapshot TDC for WPAN (Bluetooth Smart and ZigBee) applications," Dig. Tech. Papers IEEE ISSCC Int. Solid-State Circuits Conf. (2014) 172.

[2] A. Paidimarri, et al., "A 0.68 V 0.68 mW 2.4 GHz PLL for ultra-low power RF systems," Proc. IEEE RFIC Radio Frequency Integrated Circuits Symposium (2015) 397.

[3] J. Silver, et al., "An ultra-low-voltage all-digital PLL for energy harvesting applications," Proc. ESSCIRC European Solid-State Circuits Conf. (2014) 91.

# Fully Integrated, Low-power FM-UWB Transceiver for Short-range, High-density Wireless Sensor Networks

V. Kopta

The FM-UWB radio presented in this report was developed within the WiseSkin project. The target is to provide ultra-low power wireless connectivity between the nodes inside of an artificial skin developed for use with prosthetic limbs and haptic applications. The radio exploits the short distance between the nodes; trading receiver sensitivity for very low-power consumption. At the same time, it provides for sub-carrier FDMA; enabling up to four nodes to transmit simultaneously in the same RF band; effectively reducing network latency.

The WiseSkin project aims at the restoration of a natural sense of touch to people using prosthetic limbs. This is achieved by embedding a large number of sensor nodes (with pressure sensors) into an artificial skin. Pressure data from sensors is conveyed to the central unit, which uses this information to drive the actuators (vibrating electromotors) used for stimulation of the amputee's residual limb, enabling sensory feedback and control of the prosthesis. In order to improve the adaptability and robustness of the communication protocol as well as the scalability, flexibility and manufacturability of the sensor skin, wireless communication is used between sensor nodes. The short distance between nodes (e.g., a few cm), enables us to trade receiver sensitivity for power consumption.

A simplified block diagram of the transceiver is shown in Figure 1. The large Frequency Modulation Ultra-Wide Band (FM-UWB) signal bandwidth of 500 MHz relaxes constraints on both transmit and receive oscillators, enabling the use of free-running ring oscillators for carrier generation. These are periodically calibrated using an on-chip Successive Approximation (SAR) Frequency Lock Loop (FLL) to compensate for drift due to temperature variations. The transmitter uses direct digital synthesis to produce the triangular sub-carrier that controls the VCO and subsequently generates the FM-UWB signal. The transmitter consumes 583  $\mu$ W from a 1 V supply, while radiating a -11.4 dBm FM-UWB signal. The power amplifier with a fully integrated matching network, achieves an average efficiency of 18%.

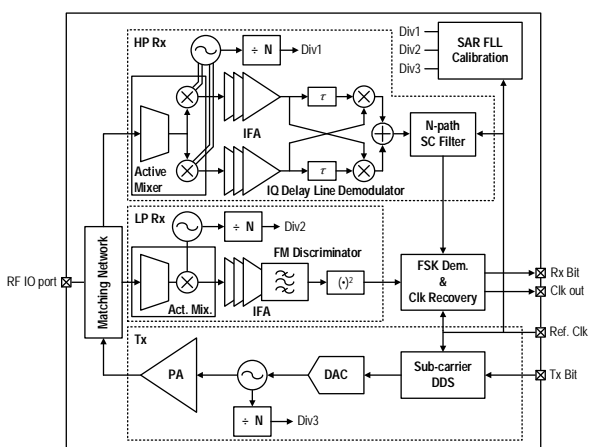


Figure 1: FM-UWB transceiver block diagram.

[1] V. Kopta, et al., "An approximate zero IF FM-UWB receiver for high density wireless sensor networks", IEEE TMTT Transactions on Microwave Theory and Techniques, 65 (207) 374.

Two receivers have been implemented providing different modes of operation in terms of power consumption, sensitivity and number of channels. The "high-power" (HP) receiver consumes 550  $\mu$ W, and allows up to 4 nodes to transmit at once in the same RF band. This is achieved using different sub-channels<sup>[1]</sup> (SC-FDMA). For a single user, the sensitivity is around -68 dBm. The sensitivity degrades slightly with the increasing number of users and/or their power (Figure 2).

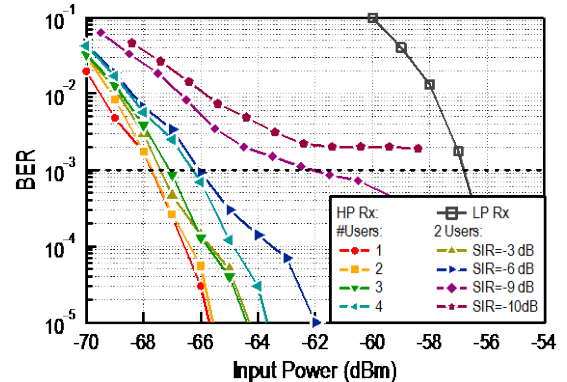


Figure 2: BER curves for the two receivers.

The integrated FSK demodulator and clock recovery circuit enable correct operation at a reference clock offset of up to 8000 ppm. With the state-of-the-art on-chip RC oscillators providing roughly 2100 ppm variation over the operating temperature range, the integrated transceiver demonstrates the feasibility to completely remove of all of the off-chip components; reducing the size and cost of sensor nodes.

Another property of the selected receiver architecture is its robustness to out of band narrow-band (NB) interferers. Both the HP and LP receivers can still demodulate data with a 3 dBm NB interferer present at 2.4 GHz (58 dB stronger signal for the LP and 66 dB stronger signal for the HP receiver). This NB signal could be used to power the sensor node (assuming rectifier efficiency >50%); enabling a fully wireless solution, offering enhanced robustness to the sensor skin<sup>[2]</sup>.

This work was partially funded by Nano-Tera national research program under SNF grant No. 20NA21-143070.

[2] V. Kopta, et al., "System and method for remote powering at least one sensor or actuator from a RF power source", US and EU Patent Application (2016).

# A Power Management Unit for ULP SoC including BLE Radio

F. X. Pengg, N. Scolari, A. Vouilloz, E. Le Roux, N. Raemy, R. Godinho Caseiro, P.-A. Beuchat

The Bluetooth Low-Energy (BLE) transceiver icyTRX<sup>[1]</sup> has been successfully promoted as low-power and low supply-voltage IP over the last years. To render this IP even more attractive, the present project aims at optimizing the overall power consumption by adding a dedicated yet versatile power management unit (PMU).

In general the optimum operating voltage of a circuit integrated in an advanced CMOS technology does not coincide with the output voltage level of the available power supply. This is particularly true for most battery operated systems, where e.g., a lithium coin-cell with an output voltage in the range of 3.0 V to 2.4 V supplies a circuit operating around 1 V. An inductive or capacitive DC-DC converter makes the charge required to supply the system available at a level closer to its operating voltage thus avoiding the otherwise dissipative voltage drop.

The system PMU is developed as service block for the icyTRX transceiver while maintaining versatility for a wide range of systems on chip (SoC). Figure 1 presents a block diagram of the icyTRX transceiver co-integration with the PMU. The latter has three sub-units, one for the DC-DC conversion including its digital control, one for the icyTRX transceiver and one to manage a "customer" part of the IC. The following characteristics make the present development an attractive solution for a wide range of applications:

- High efficiency DC-DC conversion.
- Optimized power cycling of different parts of the circuit.
- Good isolation between individual circuit blocks.
- Very-low power standby mode.
- Reduced external component count.

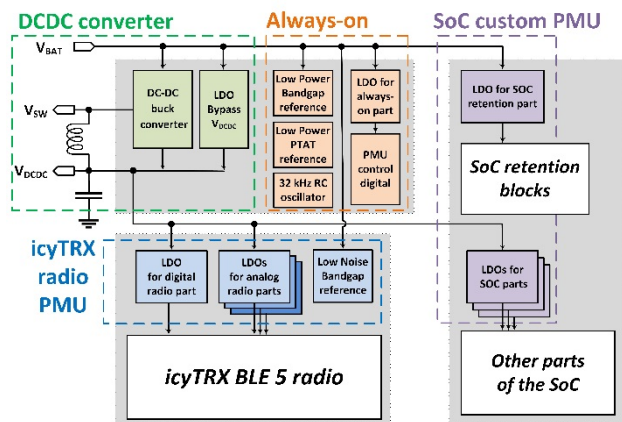


Figure 1: Block diagram of the integrated icyTRX with PMU.

The PMU can be operated in SLEEP-mode, when a minimum of low-power blocks is maintained operational, in LDO-mode, when the full system is operational but consumes low currents and in

BUCK-mode, when some high current consumption operation is activated. In BUCK-mode an inductive DC-DC converter, nominally operated in pulse-width-modulation, converts a supply range between 1.7 V and 3.6 V down to an adjustable output between 1.2 V and 1.8 V (where the output has to be at least 0.3 V lower than the input). The switching frequency is configurable between 1 MHz for low noise operation during RF activity and 8 MHz when high efficiency is required. The converter quiescent current is about 300  $\mu$ A. In LDO-mode a low drop-out linear regulator (LDO) with a quiescent current of only 10  $\mu$ A replaces the buck converter. If needed, this LDO can also deliver more than 20 mA. In SLEEP-mode the only blocks still active are the digital PMU control which is supplied by an always-on low power LDO, a low-power 32 kHz RC oscillator for time-keeping and low-power voltage and current-references which reduces the overall current consumption to 500 nA.

Fast switching "cap-less" LDOs regulate the DCDC output voltage down to the different supply voltages of the respective circuit blocks. The icyTRX transceiver is partitioned into four power domains (analog, power amplifier, frequency synthesis and digital) for good isolation and optimized individual on-off timing. Figure 2 compares the current consumption of the receiver (RX) in LDO- and BUCK-mode respectively, which reduces from 6.1 mA to 3.2 mA while degrading the sensitivity by only 0.5 dB from -97 dBm to -96.5 dBm.

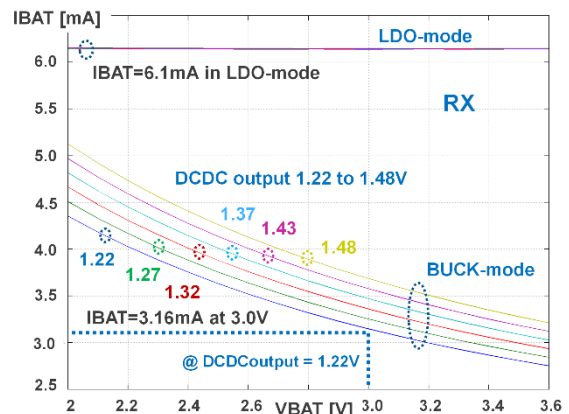


Figure 2: RX current consumption versus supply voltage.

In transmit mode (TX) the current reduces from 9.5 mA to 4.7 mA for an output power of 0.5 dBm.

[1] <https://www.csem.ch/Doc.aspx?id=41379&name=flyer-icytrx-2017.pdf>

# Photovoltaic Cell Antenna

O. Vorobyov, C. Hennemann, P. Dallemande, J.-D. Decotignie

Photovoltaic (PV) cells are now common place in home appliances and consumer devices, such as wearable electronics, as a primary or alternative energy source. The metallic PV cell components can also be used as (parts of) an antenna for a radio frequency (RF) transceivers. In this work, both functions are combined to realize a novel PV cell antenna for increased compactness and reduced weight and cost.

It is typically desirable for miniature, low-power wireless systems to be compact and lightweight. This is particularly true in the case of e.g., wearables and aerospace applications. In such applications, combining the PV cell and the antenna offers potential advantages in terms of size and weight. However, the technical constraints of the PV cell on the one hand and wide range of different antenna solutions on the other hand poses significant challenges to their effective integration.

Most of the solutions published in the literature use an additional antenna element placed above the PV cell or integrated in the PV cell structure to radiate and/or receive electromagnetic (EM) waves in support of wireless communications. Many solutions use perforated metallic structures placed on top of the PV cell. Such solutions have shown low efficiency and are complex to implement. Furthermore, they may adversely impact the efficiency of the PV cell.

The solution proposed by CSEM leverages the direct current (DC) lines available in PV cells of all types and shapes. The PV cell is used as is, without any physical modification (e.g., additional MS lines, ground planes). The DC lines can be seen as microstrip (MS) or coplanar waveguide (CPW) lines. Attached to the DC lines, the PV cell elements act as an antenna, which can be seen as load or a parasitic antenna element. Usually, Radio Frequency (RF) devices have a 50 ohm input / output circuit impedance. However, the length and shape of the PV cell impacts the impedance which influences the antenna resonance frequency. Consequently, fine tuning of the impedance matching circuit is essential.

A potential limitation of the proposed approach is that it leads to a relatively narrowband antenna. This is due to the matching circuit and the specific DC line topology. However, the antenna bandwidth limitation can be bypassed in the case of a PV cell array (e.g., PV cell elements not connected to antenna can be used as passive antenna components to improve the operational bandwidth).

In the context of an internal R&D project<sup>[1]</sup>, a small flexible PV cell was used to test the resonance performance of the PV cell and evaluate the potential of using the cell as an antenna for wireless communication, as well as, a source for energy harvesting. The PV cell under test is depicted in Figure 1.

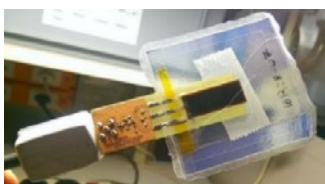


Figure 1: Solar cell element antenna prototype.

<sup>[1]</sup> C. Hennemann, et al., "GWAPO—Generic wireless autonomous conformable patch with display", CSEM Scientific & Technical Report (2016), 14.

An important advantage of the proposed solution is that no physical modification of the PV cell is required. A detailed block diagram of the photovoltaic cell antenna combined with a wireless transceiver is presented in Figure 2. In this block diagram, the PV energy harvesting is combined together with the RF communication. The harvested energy both from the PV cell and RF are stored in the battery to ensure stable wireless transceiver operation.

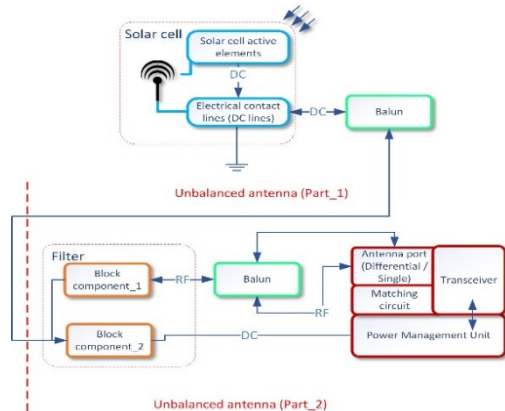


Figure 2: Block diagram of the proposed antenna system solution.

Current lab tests show that the PV cell can be used as an RF antenna together with a transceiver. Proposed antenna exhibits almost omnidirectional radiation and has an operational bandwidth of about 30 MHz (i.e., when matched from 1.7 to 2.45 GHz) (Figure 3). The results demonstrate the potential for the integration of the antenna and the PV cell into a multi-functional hybrid PV/RF module: energy harvesting via the PV cell, RF communication (e.g., short range wireless, satellite, drones, smart straps), and device location estimation etc.

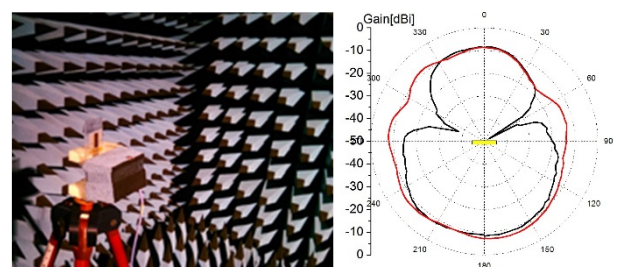


Figure 3: Antenna under test: radiation pattern measurements (CSEM anechoic chamber).

Such multi-function modules with integrated PV cell antennas are ideally suited to support sensing, actuation and remote management of autonomous devices in the future Internet of Things. Potential applications include e.g., connected cars, smart homes, wearables, security systems, and GPS, etc.

# Biowave—a Biometric Watch Activated by Veins

E. Grenet, P.-A. Beuchat, B. Dunan, C. Gimkiewicz, A. Luu-Dinh, P. Nussbaum, C. Hennemann, S. Pochon, G. Basset

*Located in a watch buckle, the Biowave is an ID-wearable replacing passwords and cards. Identified by their unique wrist vein pattern, the Biowave owner can gain access to devices (computer...), services (banking, medical, transport...), and premises (work, home, car...) securely and reliably. The device is only 5.5 mm thick and has two weeks battery life. A smartwatch version of the Biowave is currently also being commercialized.*

The vein pattern on our wrist is a unique biometric signature that can be used for personal identification. CSEM developed a complete hardware solution for the startup Biowatch SA, allowing the integration of a biometric recognition system in a watch buckle for identification. The system consists of a flat vision system with near-infrared active illumination, biometric processing capabilities and two communication schemes, Near-Field Communication (NFC) and Bluetooth Low Energy (BLE). Once identified thanks to his/her unique vein pattern, the owner can authenticate securely and proceed to banking transactions, get access to a computer, a building or a car. No pins, passwords, cards or keys are required anymore.

The user performs his/her identification once a day by taking an image of their wrist with the watch buckle deployed (Figure 1). An active infrared illumination enhances the contrast of the veins on the skin. The embedded biometric algorithm is then performed on the wrist image, delivering the identification if the vein pattern image matches with the one stored in the device. This stored image is acquired in a unique enrolment procedure done at the first use of the device. The watch then is closed, and the user identification is kept as long as it remains closed. A proximity sensor ensures that if the buckle moves away from the skin, the identification is lost, as well as if the mechanical clasp of the buckle is opened.

Once identified, the user can securely connect to a device using a simple gesture to authorize a service like unlocking an access to a car, an office, a computer or a transport network, or authorizing a sensitive transaction like a bank transfer. This authentication to services, devices and premises is performed contactless either by NFC or BLE.

The challenges for such a wearable were multiple: it must be highly secured, reliable, low power, and extremely slim.

- The security of the device relies on several aspects: a False Acceptance Rate (FAR) lower than 0.001%, an embedded processing, an NFC chip including a secure element allowing secured data storage and data encryption, a mechanical clasp and a proximity sensor.
- The reliability of the device is shown by a False Rejection Rate (FRR) lower than 1%.
- The autonomy of the device is due to hardware and firmware optimizations. The BLE supervises the incoming events (accelerometer, button or NFC/BLE signals) while keeping unused components in deep sleep modes, to achieve a lifetime of two weeks before a device recharge.
- The ergonomics of the device was reached by a drastic reduction of the thickness thanks to a complete redesign of the optical system (selection of the most convenient imager and design of a wafer scale custom optics). The complete optical system achieves 1.8 mm thickness (imager + optics).

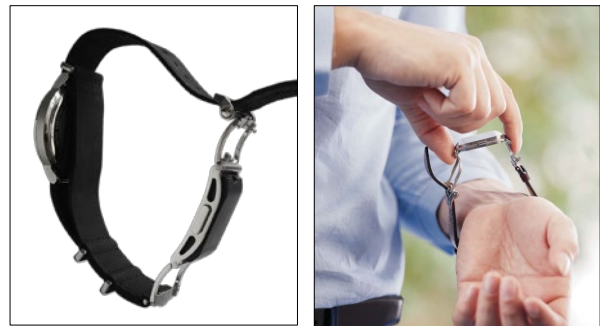


Figure 1: Biowatch buckle (left) and identification process (right).

The Biowave system was designed through a meticulous choice for the target components, allowing the implementation of all the use cases of the Biowatch business (banking, access control, online authentication, etc.) to bring maximum benefit to its customers. The system has been implemented on an 8-layers printed circuit board with chip-scale packages for all components (imager, microcontroller, flash memory, BLE, NFC, secure element, accelerometer, colour LEDs for feedback). Custom antennas have been designed for BLE and NFC communications. The flat optics has been prototyped thanks to CSEM replication technology expertise, providing high quality veins images (Figure 2). A custom battery supplies 44 mAh capacity enabling two weeks autonomy. The final module reaches the expected volume of 30×17×5.5 mm.

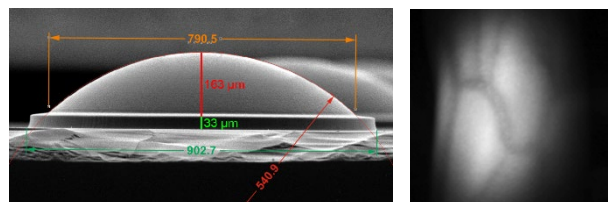


Figure 2: Wafer scale custom lens (left) and veins imaging (right).

The Biowave system has been implemented in a smartwatch form factor first, allowing Biowatch to quickly deliver its early customers with fully functional prototypes – from the biometric recognition to the personal authentication activation (Figure 3). Further improvements are underway to increase the level of security, by integrating a heart rate detection (liveness) and the resilience to presentation attacks (spoofing tentative).

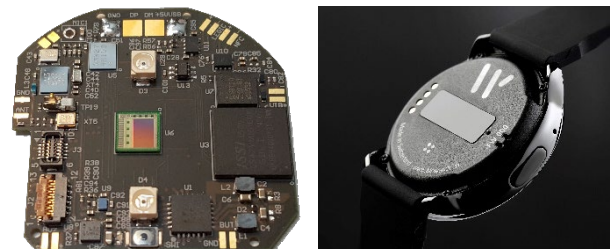


Figure 3: The Biowave smartwatch board (left) and prototype (right).

# X-Ray Photon Counting Chip with Backside Detector

R. Quaglia, P.-F. Ruedi, Y. Zha, A. Bischof, M. Despont, P. Niedermann

CSEM has developed an integrated circuit for single X-ray photon counting. The circuit is coupled with an X-ray absorber material for a new generation of X-ray imaging detectors for applications in various fields from medical imaging to physics experiments. The proposed solution has potential advantages in terms of cost, reliability and modularity compared to the state of the art.

X-ray photon counting with energy discrimination opens the door to X-ray color imaging, offering advantages in term of tissue or material discrimination. Furthermore, the use of direct X-ray detection provides for sharper images, as well as reduced X-ray dose, compared to indirect detection based on a scintillator coupled to an image sensor. The state-of-the-art direct detectors exploit silicon (Si) or cadmium telluride (CdTe) absorbers bump bonded to a readout circuit. Here we present an alternative approach that relies on a germanium (Ge) as the absorber material on the backside of a readout chip. The absorber is formed from germanium pillars grown on a p-type wafer. The absorber is subsequently covalently bonded by a low-temperature process to the backside of a readout chip (n-type wafer) thinned down to a thickness of 15  $\mu\text{m}$ . This forms a heterojunction at the interface between the readout and absorber wafers. A schematic cross section of the detector is shown in Figure 1. When an X-ray photon is absorbed, electron-hole pairs are created and the holes are then collected at the common cathode and the electrons are collected by the pixel anode. Since the total charge collected at the anode is proportional to the energy released by the incident photon, a proper circuit can be placed inside each pixel in order to count (photon counting) the number of incoming photons exceeding one or more given thresholds.

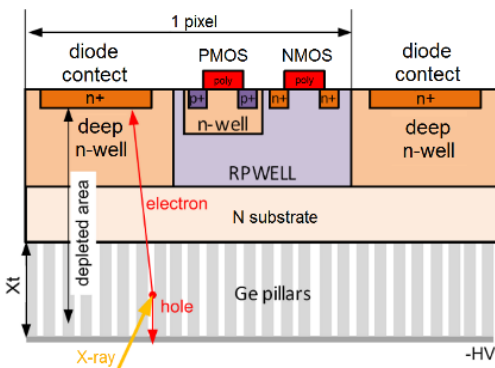


Figure 1: Lateral view of the pixel.

As germanium has a higher absorption coefficient than Silicon, an absorber made of germanium has the great advantage of a wider energy range of applications (e.g., 20-80 keV) whereas traditional silicon absorbers have comparatively low efficiency. The higher efficiency of a germanium absorber is also advantageous for low-energy X-ray medical imaging (e.g., mammography) because a smaller total ionizing dose is required. However, the unconventional diode formation and smaller bandgap material (0.67 eV of Ge vs 1.12 eV of Si) in these

germanium absorbers result in a higher leakage current (expected in the mA/cm<sup>2</sup> range) that needs to be compensated for by the analog front end.

A photon counting chip with an array of 16×16 pixel has been realized in a 150 nm process<sup>[1]</sup>. Figure 2 shows a microphotograph of the chip.

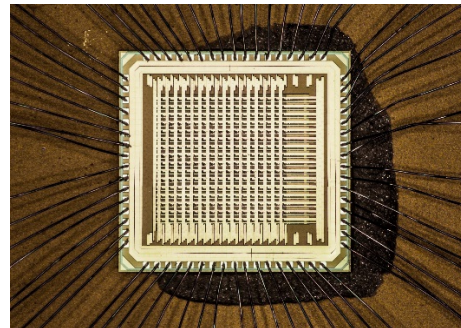


Figure 2: Microphotograph of the chip.

First trials have been done with a silicon absorber instead of a germanium absorber, with an X-ray source of 50 keV. As the active area of the chip is very small (1.6×1.6 mm), and in order to acquire large images, we mounted the target sample on an x-y-z micromanipulator acquiring images in different positions along the x and z axis combining the single acquisitions. A reconstructed image is shown in Figure 3. The number of photons counted per pixel during the exposure time is color encoded.

The next step will be to use a detector with a germanium absorber.

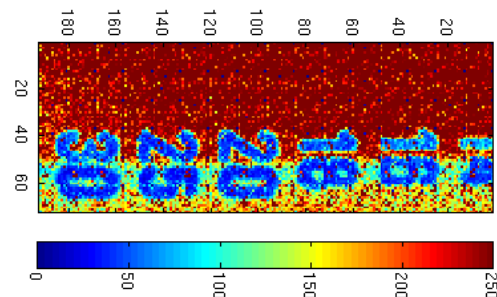


Figure 3: Reconstructed image of X-ray detection using silicon as an absorber material in the place of germanium.

The project partners are G-ray, EMPA, and ETH Zurich. This work was partly funded by the Swiss National Science Foundation (SNSF). CSEM thanks them for their support.

[1] R. Quaglia, et al., "An integrated circuit for future X-ray imaging detectors based on a Ge pillars absorption layer", CSEM Scientific & Technical Report (2016), 109.

# Image Sensor with Stacked Photodiode

P.-F. Ruedi, P. Heim, J. W. Schüttauf, J. Bailat

An image sensor with stacked amorphous photodiodes over the pixel has been developed. It offers 100% fill factor while freeing place in the pixel enabling either to reduce the pixel size or to increase the complexity of the in-pixel processing for dedicated applications.

Natural visual scenes have a very wide illumination dynamic range, making it difficult to render a good image quality in challenging illumination conditions. CSEM previously developed a time-to-saturation pixel with in-pixel digital memory offering an intra-scene dynamic range in excess of 120 dB without parameter adjustment. However, this high intra-scene dynamic range and ease-of-use have to be paid for in terms of fill factor. To remedy the low fill factor (~ 20%), one solution consists in depositing the photodiode on top of the pixel instead of being part of the pixel. This enables close to 100% fill factor and also the whole pixel area can be used for circuitry.

Taking advantage of CSEM's know-how and skills in the field of amorphous photovoltaic solar cells, we have deposited on top of non-passivated chips a layer stack of amorphous silicon (a-Si:H). In each pixel, the a-Si:H layer stack is connected to the pixel circuitry through the top metal layer, as illustrated in Figure 1. A layer of ITO (Indium Tin Oxide) deposited on top of the a-Si:H forming a transparent counter electrode. The ITO layer is subsequently removed from the pad areas by laser engraving. The remaining ITO serves as a mask for etching the a-Si:H. Finally, a gold pad is deposited on top of the ITO to enable it to be biased.

An existing CSEM image sensor test chip<sup>[1]</sup> with a pixel pitch of 14 µm has been modified to accommodate the a-Si:H layer. It contains pixels with n-well to p-substrate photodiodes with a fill factor of 20% and pixels with a-Si:H photodiodes, with 100% fill factor, with different metal contacting areas on the same chip for comparison purpose. Two types of junctions have been deposited: i-p and n-i-p.

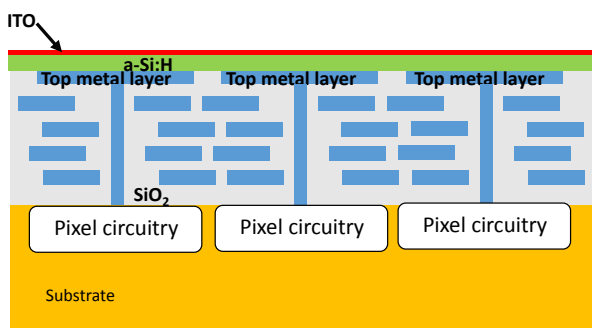


Figure 1: Image sensor module principle.

Figure 2 shows a microphotograph of the chip covered with a-Si:H and ITO. The different metal contacting areas are visible; the top part shows the unmodified sensor with in pixel photodiodes, the bottom part of the pixel array with 3x3 rectangles shows the 100% fill factor through stacked amorphous silicon.

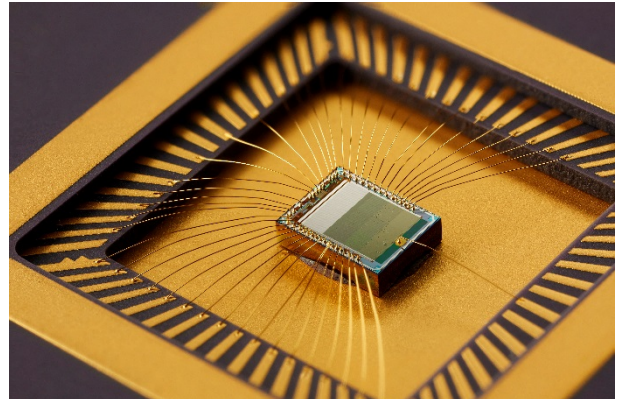


Figure 2: Microphotograph of the chip with top part of the chip unmodified and the lower part (3x3 square array) showing the amorphous photodiodes with 100% fill factor.

Figure 3 shows an image acquired with the test chip. It illustrates the difference of sensitivity between in-pixel n-well-substrate photodiodes and stacked a-Si:H photodiodes. The top part of the image is obtained with standard pixels with in-pixel n-well-p-substrate photodiodes, while the rest of the image is obtained with stacked a-Si:H photodiodes. The sensitivity is more than 6x higher with the stacked photodiodes compared to in-pixel photodiodes. The leakage current at room temperature is between 0.2 and 0.3 nA/cm<sup>2</sup> and does not vary by more than 3%/V as a function of the reverse bias applied.

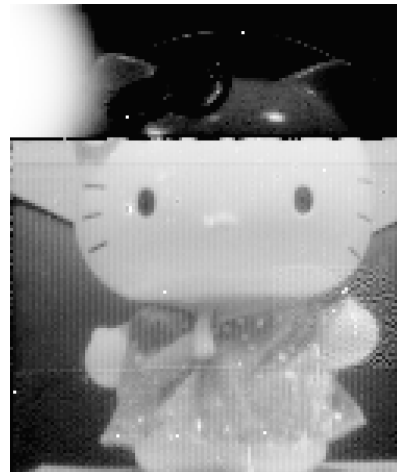


Figure 3: Sample image acquired with the test chip.

In addition to offering 100% fill factor, the proposed approach also enables electron imaging, such as in image intensifier systems based on a photocathode, vacuum imaging of particles, electron microscopy, beam imaging and X-ray applications.

[1] P. Heim, F. Kaess, P.-F. Ruedi, "High dynamic range versatile front-end for vision systems", CSEM Scientific & Technical Report (2007), 25.

# FastEye—A 1 MP High-speed Camera with Multiple ROI running at up to 64'000 fps

P. Jokic, B. Schaffer, H.-R. Graf, S. Emery

Visually monitoring fast-changing scenes and processes is a challenge for standard industrial camera systems as smearing and rolling-shutter effects impair the quality of the recorded images. To address these problems, the FastEye high-speed camera system was developed. It features a CMOS image sensor with global shutter, frame rates of up to 64'000 frames per second and a user-friendly USB 3.0 interface.

Capturing fast moving objects with a minimum of smearing effects and other artifacts is one of the main challenges with respect to high-speed camera design. High frame rates, short exposure times and low noise levels are therefore crucial elements for high quality imaging of rapidly changing scenes. Here, we present the FastEye high-speed camera, featuring a 1024×1280 pixel image sensor, which was developed at CSEM. Multiple regions of interest (ROI) can be set, with exposure times down to 500 ns, enabling frame rates of up to 64'000 frames per second (fps). A USB 3.0 interface provides connectivity to a computer, where the sensor and the acquisition logic can easily be controlled via Matlab.

Figure 1 shows the implemented VIA1M imaging sensor. It features 12 µm pixel pitch, full well capacity of > 150 ke- and achieves a SNR of > 52 dB. A row readout time of 1 µs combined with parallel top-half and bottom-half sampling allows frame rates of up to 2'000 frames per second at full resolution. By reducing the number of active rows, the time for reading out a frame is linearly reduced, making 32 x higher frame rates possible at the minimum resolution (32×1120 pixel).

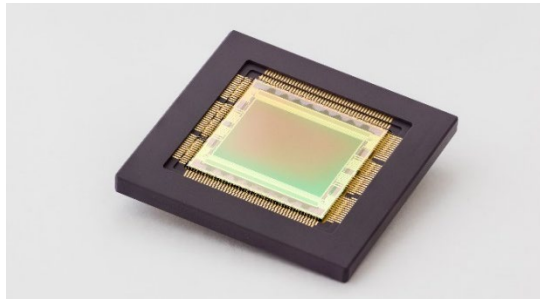


Figure 1: VIA1M image sensor.

A Xilinx Kintex-7 FPGA is used for interfacing the image sensor, making it possible to achieve the high data rates and bus widths required for reading out the parallel image data. The FPGA controls the sensor timing and functionality. It translates commands received via USB into sensor signals and buffers the captured images in on-board RAM before streaming them out to the connected PC. Firmware can be loaded through the USB interface, enabling simple updates of both the FPGA and the sensor firmware. Pixels are sorted in real-time inside the programmable logic, reducing image reconstruction time in software. For specific applications, further pre-processing capabilities, such as computer vision algorithms or object detectors, could be configured within the available FPGA logic, simplifying post-processing of the images. The Matlab script provides abstracted commands for controlling the sensor settings like the exposure time or frame periods. Additionally, it allows different customised settings to be stored in a user-friendly format such that image-acquisition sequences can be easily set up.

The camera features an input for external trigger sources, allowing events to be captured automatically without any human interaction required. In order to support a large number of objectives, which might be necessary for certain applications, the

camera is equipped with a standardized Nikon F mount or alternatively with a Nikon C mount. Figure 2 shows the FastEye system with a normal 50 mm objective mounted.



Figure 2: FastEye camera.

The FastEye camera can be used for a wide range of applications where rapid movements need to be captured:

- Testing—Crash tests for mechanical qualification processes.
- Security—Surveillance of fast changing environments or mounted on moving platforms.
- Industrial—Monitoring moving parts of machines to detect anomalies and predict failures.
- Automotive—Obstacle detection within limited reaction time.

In Figure 3, a frame from a 2 kfps video is displayed showing the impact of a water droplet during the camera tests.



Figure 3: Screenshot from a test video recorded with FastEye.

Here we have shown a user friendly high-speed camera, offering 500 ns exposure times with 1 MP resolution for industrial applications.

# An Evaluation Tool for Standard Cell Libraries under PVT Variation: Application to Sub-threshold Design

T. C. Müller, J.-L. Nagel, M. Pons Solé, D. Séverac, K. Hashiba <sup>•</sup>, S. Sawada <sup>•</sup>, K. Miyatake <sup>•</sup>, S. Emery, A. Burg <sup>••</sup>

A tool has been developed to compare standard cell libraries in different operating conditions, i.e. different sets of supply voltage, temperature, process corner, and bias voltages. The approach has then been applied to a 0.5 V sub-threshold cell library developed by CSEM to evaluate the effectiveness of adaptive body bias compensation in the Mie Fujitsu 55 nm DDC process [1].

For a digital designer, the relative speed difference between different processes is a useful figure to solve commonly asked questions: First, it allows the designer to estimate the achievable performance of the circuit for a given yield target. Second, knowing the range of variation across anticipated operating conditions is important to decide for a realistic set of constraints for the CAD tools during implementation which has a large influence on the tool runtimes as well as on the achievable performance of the design. Finally when using methods like adaptive voltage scaling or adaptive body biasing there is a need for the designer to evaluate the effectiveness of the chosen compensation approach.

The evaluation is done in three steps: First, the library files are parsed. Second the delay tables are resampled using bivariate spline interpolation across corners to a common load index and a corner specific transition index. The latter one is derived by exploiting the high gain of CMOS circuits: As shown in Figure 1 a buffer chain is constructed, with the same load on each node. An input transition is applied and throughout the chain quickly converges to a characteristic transition which only depends on the operating corner and the chosen load. The implementation is a simple iterative table lookup in the transition tables of the library files which is repeated once for each value from the load index to construct the transition index.

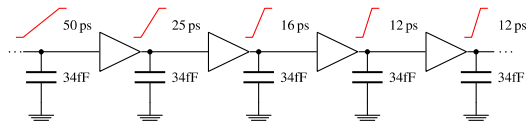


Figure 1: Buffer chain illustrating the converging transition time for a given load.

Finally, after these normalization steps, each delay table entry—in the following called realization  $r = \{\text{cell, input transition, output load, logic inputs, ...}\}$ —of the operating corner  $OC_i$  is normalized with the entry of the corresponding realization in a reference corner  $OC_{ref}$ , resulting in a relative delay factor  $\alpha_r$ :

$$\alpha_r = t_{pd}(r, OC_i) / t_{pd}(r, OC_{ref})$$

In this work a sub-threshold cell library developed by CSEM for the Mie Fujitsu 55 nm DDC process was targeted for analysis, with the goal to evaluate the effectiveness of adaptive body biasing for process, voltage and temperature (PVT) compensation. The body bias voltages have been set based on the result of spice simulations with the goal to achieve an identical drive current across the corners. A commercial library characterization tool was used to derive non-linear delay model

<sup>•</sup> Mie Fujitsu Semiconductor Ltd. Yokohama, Kanagawa, Japan

<sup>••</sup> EPFL, Switzerland

(NLDM) representations utilizing the Liberty format across the PVT range with and without compensation.

When analyzing the resulting normalized relative delays  $\alpha$  for all realizations without compensation, we observe a wide distribution of the median delay (blue line in the boxes of Figure 2, top). The worst case median exceeds a delay factor of 20 in regard to the reference corner with outliers (black crosses) nearly reaching to a factor of 80. After compensation (Figure 2, bottom) the median delay is pushed back, achieving values close to one. Still, even after compensation, some outliers remain with up to the extreme of 4.3 times the reference delay. These outliers however are rare and for a typical critical path we may only expect a few of them, if at all, which limits their potential effect on the overall timing.

In conclusion, the analysis tool was able to demonstrate the effectiveness of the adaptive body bias compensation approach, illustrating the capability of pushing the corners close together.

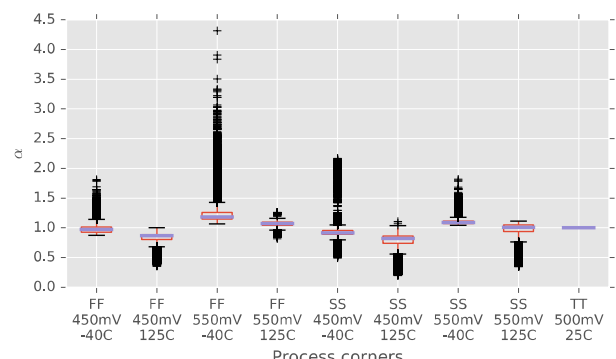
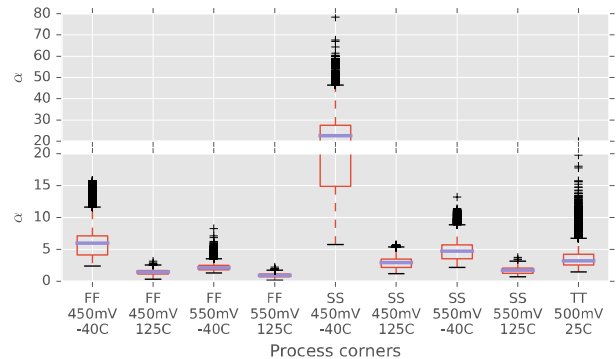


Figure 2: Tukey boxplots of the normalized relative delay  $\alpha$  before (top) and after (bottom) compensation. The compensated TT corner has been chosen as  $OC_{ref}$  to allow for direct comparability between both plots.

[1] T. C. Müller, et al., "PVT compensation in Mie Fujitsu 55nm DDC: a standard-cell library based compensation", IEEEES3S The IEEE SOI 3D Subthreshold Microelectr. Techn. Unified Conf. (2017).

# SoC Estimator—A Fast Exploration Tool for Different Architectural Choices in SoCs

E. Azarkhish, S. Emery

The level of complexity of the integrated circuits (IC) is growing exponentially. Modern system-on-chips (SoC) are composed of several subcomponents with a wide range of functionalities. Sensors, amplifiers, processors, and voltage converters are just a few examples of components which can be integrated into a modern SoC. Today, the component-based design approach is widely adopted, in order to prune the design space and deal with the ever-increasing complexity of the ICs. This allows for selecting pre-designed and pre-validated IPs and integrating them to build a system depending on the required functionality and characteristics. To this end, having an early design exploration platform providing a fast estimation of power, area, and cost is highly desirable. In this report, we present SoC-Estimator and briefly introduce its capabilities.

A typical embedded SoC consists of different components provided by external/internal IP providers. For example, a random-access-memory (RAM) block can come directly from the fab or from an IP provider with a wide range of parameters (e.g., technology options, supply voltage, memory size). Figure 1 shows a simple SoC composed of components such as filters, data converters, power managers, and processors. When designing such system it is desirable to be able to perform comparisons between off-the-shelf IP components in terms of power consumption and silicon area, and to choose one from a unified library of components. It is then useful to perform a fast evaluation of the system-level power consumption, area, and cost. This can help designers with the choice of the IP blocks and guide them through the subsequent steps.

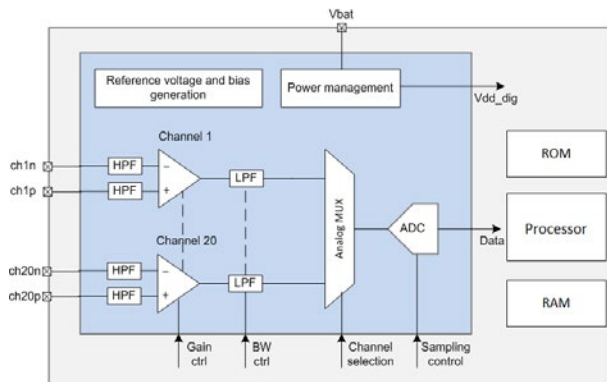


Figure 1: A simple system-on-chip (SoC) with different components.

Commercial platforms exist for system-level power estimation and exploration. Docea Power<sup>[1]</sup> (acquired by Intel in 2015) provides Aceplorer for power modeling and AceThermalModeler for thermal modeling. InCyte<sup>[2]</sup> by Cadence does a similar job, however, it has been recently discontinued. Also, many other industrial and academic platforms exist for system level explorations. Most of these platforms follow different methodologies and are not easy to learn, integrate, and use. One simple way to obtain early estimates is to use Excel sheets. Excel sheets are easy to work with, but tedious to modify and extend. Formulas, also, are not self-explanatory, and are difficult to remember and modify later:

```
=IF($C$7="Typical",VLOOKUP($C$4:$AA$120:$AT$147;3);
```

We propose SoC-Estimator, a python-based environment capable of parsing self-explanatory models, with enough flexibility to support new components.

[1] Intel Docea Power: <https://www.intel.com/content/www/us/en/system-modeling-and-simulation/docea/overview.html>.



Figure 2: An overview of the SoC-Estimator framework.

An overview of the SoC-Estimator environment is shown in Figure 2. It receives inputs in CSV representation format and allows for defining typed parameters. It supports a wide range of units (e.g., Watts, Amperes, Volts), and allows for combining them (e.g.  $\mu\text{A}/\text{MHz}$ ,  $\mu\text{W}/\text{MHz}/\text{mm}^2$ ). It automatically performs unit conversion and checks for errors and inconsistencies. Complex expressions and formulas are supported, as well:

param	$I_{\text{total}}$	uA	$(I_{\text{ampbase}} + I_{\text{amp}} * N_{\text{ch}} * f_{\text{H}} + I_{\text{adcbase}} + I_{\text{adc}} * \text{SampleRate} + I_{\text{lvds}} + I_{\text{imm}} + I_{\text{temp}} + (\text{Naux}+1) * I_{\text{aux}})$
output	power	mW	$(I_{\text{total}} * VDD)$

Apart from the expression of nested and dependent formulas, SoC-Estimator also allows for defining characterization tables:

entry	word	io	mux	area	readc	writec	leakage
entry	128	16	4	7357.838	5.656	5.121	0.093
entry	128	32	4	11870.65	10.081	8.928	0.154
entry	128	48	4	16383.47	14.507	12.734	0.214
entry	128	64	4	20896.29	18.932	16.541	0.275
entry	128	80	4	25409.1	23.357	20.347	0.336
entry	128	96	4	29921.92	27.783	24.154	0.396

Assertions are easily specified as well, allowing for consistency and range checks:

22	assert	$(-40 \leq \text{temperature} \leq 80)$
23	assert	$(1.0 \leq \text{VDDA} \leq 1.32)$
24	assert	$(1.0 \leq \text{VDDPA} \leq 1.65)$
25	assert	$(0.9 \leq \text{VDDD} \leq 1.1)$

Finally, SoC-Estimator allows for hierarchical instantiation of components. This way, a SoC platform can be built easily from the existing components and model. As an example, a complete bio-sensor interface and SoC (see Figure 1) was modeled and compared against its specifications.

In this report, an early exploration tool for different architectural choices in SoC platforms is presented. Several components have been modeled using this platform and validated versus their datasheets. SoC-Estimator is easy to learn and adopt, and its component library can be easily extended to be used for future explorations.

[2] Cadence InCyte: <https://www.design-reuse.com/news/19019/power-analysis-pre-rtl-exploration.html>.

# A 0.5 V Near-threshold Microcontroller Robust over PVT Variations

D. Séverac, D. Ruffieux, M. Pons Solé, J.-L. Nagel, D. Sigg, J. Deng, C. A. Salazar Gutierrez, P. Persechini, R. Caseiro Godinho, C. Monneron, Y. Liechti, T. C. Müller, A.-S. Porret, D. Manic, S. Emery

In this work, performed in close collaboration with Mie Fujitsu Semiconductor Limited (MIFS), specific libraries using a novel bulk biasing technique have been developed. To validate the concept, a circuit based on an icyflex2 processor has been integrated and characterized over PVT (Process, Voltage and Temperature) variations. The results demonstrate the advantage of the MIFS 55 nm DDC technology for low-power integrated circuits operated in the near threshold domain (0.5 V).

Ultra-Low Leakage (ULL) transistors available with MIFS DDC technology have been specifically engineered to operate at 0.5 V, with a reduced leakage current, so as to minimize the dynamic power consumption. This is achieved owing to a large body effect and a specific bulk doping profile, leading to improved matching. Working in the near threshold voltage region, rather than at a typical nominal voltage of 0.9 V, has two main negative consequences that need to be addressed: 1) the reduction of the speed of the transistor, and 2) the larger performance spread and mismatch among transistors.

After having taken into account various different trade-offs, such as speed, power, leakage, matching and tunability, a complete set of logic cells was designed using an optimally sized MOS transistor geometry. Having all transistors with the same dimensions yields a better matching with respect to their currents and hence control of their speed over the entirety of bulk biasing voltage range.

Thanks to the wide current tuning capability of the DDC technology due to its high impedance bulk terminal, the decrease in speed and the performance variation between the different operating conditions can be partially compensated in a lower power way. The left hand side of Figure 1 shows that a factor 10'000 of transistor current variations between best (BC) and worst (WC) case PVT conditions is obtained at 0.5 V without compensation. With compensation (right hand side of Figure 1), the large variation is reduced to below a factor of two.

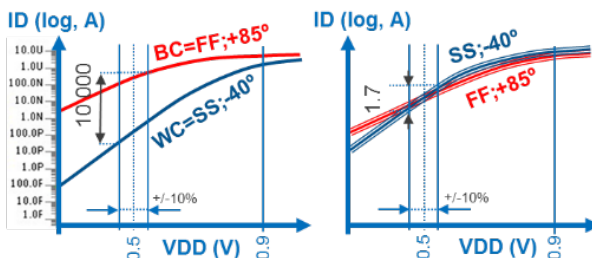


Figure 1: Transistor current variation for worst and best cases without (left) and with (right) the compensation mechanism.

A specifically designed voltage regulator continuously adapts the bulk bias to the PVT conditions; it allows, as shown in the right side of Figure 1, a reduction of the variation from an initial factor of 10'000 to less than a factor of 2. Moreover, by choosing the reference current ( $I_{ref}$ ), one can tune the transistor strength, hence the system speed.

Using the standard cells that were developed, a test vehicle circuit containing 50 different ring oscillators using most diverse types of cells as well as a 32-bit processor system was manufactured. The frequency measurements of compensated rings over various PVT conditions (Slow-SS, Fast-FF and Typical-TT) are shown in Figure 2, given  $I_{ref}$  set for maximum speed and normalizing the values to the case of 0.5 V and 25°C.

Overall, the frequency variation is within +/- 30% over PVT range of PVT conditions considered.

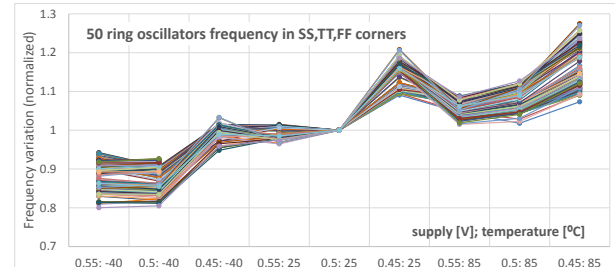


Figure 2: Normalized frequency of diverse rings measured over PVT.

Applying the same compensation methodology to the icyflex2 32-bit processor yields the results presented in Figure 3. Dashed lines show the maximum measured frequency for all extreme corners over the given temperature range [-40 °C...125 °C] and the range of supply voltages [0.45 V...0.55 V], at an  $I_{ref}$  of 100  $\mu$ A. Over the PVT conditions considered, a difference between the min and max frequency of only a factor of 2 was found. This is a drastic improvement compared to the 10 K variation of Figure 1.

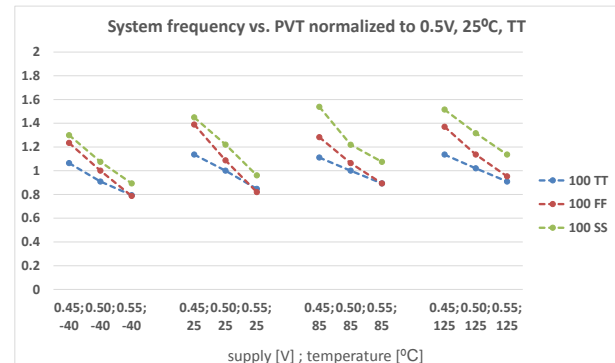


Figure 3: icyflex2 maximum frequencies in PVT with  $I_{ref}=100$  Ma.

These results demonstrate that Adaptive Bulk Biasing can successfully be applied to compensate for PVT variations of 0.5 V near-threshold logic circuits implemented with MIFS C55DDC technology while maintaining a good processor performance. Moreover, Bulk Biasing provides an additional knob allowing to tune the performance of the circuit at runtime, without changing the power supply; hence preserving low dynamic power consumption. This enables us to define several modes of operation, where speed and leakage current (fast mode, slow mode, retention) may be traded depending on the required overall performance. As such, MIFS C55DDC technology is found to be a very good process particularly suited to implement ULP wireless sensor nodes that are needed for the IoT era.

# Implementation and Benchmarking of RISC-V Microprocessors

H.-R. Graf, J.-L. Nagel, S. Emery

CSEM has evaluated two RISC-V microprocessor architectures which are freely available and suitable for integration on low-power System-On-Chips. Both RISC-V cores were synthesized and mapped to a Field-Programmable-Gate-Array (FPGA) and benchmarked using CoreMark. As a RISC-V Foundation member, CSEM complements its actual offer of low-power microprocessors for the industry with RISC-V cores.

RISC-V (pronounced "risk-five") is a new instruction set architecture (ISA) originally developed for research and education at the University of California, Berkeley. It is now set to become a standard open architecture for industry implementations.



Figure 1: The RISC-V logo.

The RISC-V Foundation<sup>[1]</sup>, a non-profit corporation controlled by its members, directs the future development and drives the adoption of the RISC-V ISA. CSEM is (together with numerous companies such as AMD, Google, HP, IBM, NVidia, NXP and Qualcomm) a registered member of the RISC-V Foundation.

The goal of RISC-V is to provide a completely open ISA that is freely available to academia and industry. The ISA avoids "over-architecting" for a particular microarchitecture style or implementation technology.

The base integer ISA is available for 32-bit, 64-bit or even 128-bit architectures. Standard ISA extensions exists e.g., for hardware multiplication and division; atomic instructions; IEEE-compliant floating-point arithmetic with single or double precision; compressed 16-bit instructions (to reduce code size).

In addition to supporting standard general-purpose software development, another goal of RISC-V is to provide a basis for non-standard extensions for custom instructions or application-specific hardware accelerators.

The University of California, Berkeley, not only provides and maintains a GNU based open-source toolchain (including compiler, standard-library, debugger and simulator), but also a configurable reference RISC-V system, the "Rocket Chip", available completely free as synthesizable RTL source-code<sup>[2]</sup>.

The Rocket has a single-issue in-order 5-stage pipeline and its 64-bit core implements the RISC-V basic ISA and all standard extensions, including double-precision floating point arithmetic and compressed instructions.

In 2016, the ETH Zurich and the University of Bologna have together released an open-source RISC-V core called "RI5CY" as part of their Parallel Ultra-Low power processing Platform (PULPino)<sup>[3]</sup>.

The RI5CY has a single-issue in-order 4-stage pipeline and implements the 32-bit base integer architecture, the compressed instructions extension and several proprietary ISA extensions

such as: hardware loops, post-incrementing load and store instructions, SIMD and MAC operations.

At CSEM, we have used Xilinx Vivado to synthesize and map both RISC-V cores on a FPGA (Xilinx ZYNQ 7020) at 25 MHz. A low-cost FPGA development board "ZedBoard" was used to debug, assess and benchmark the cores.

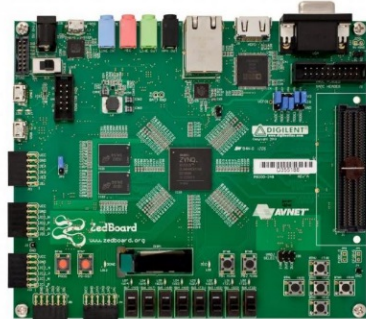


Figure 2: ZedBoard with a Xilinx ZYNQ 7020 FPGA.

When not taking into account the size of the optional floating point unit (FPU), the Rocket core is smaller, although it implements a 64-bit architecture and has a deeper pipeline.

The EEMBC CoreMark<sup>[4]</sup> is the leading industry-standard benchmark for CPU cores. CoreMark is capable of testing a processor's basic pipeline structure, basic read/write, 32-bit integer and control operations. We have compiled the source-code (using gcc -O3) to benchmark the performance of both RISC-V FPGA implementations. Obviously, the RI5CY benefits clearly from its proprietary ISA extensions, while the Rocket's additional features (64-bit architecture and FPU) bring (as expected) no advantage for CoreMark.

Table 1: FPGA synthesis and benchmark results.

Core	Architecture	MHz	Size (cells, w/o FPU)	CoreMark /MHz
Rocket	Rocket Chip	25	6900	2.16
RI5CY	PULPino	25	9660	2.84

As RISC-V Foundation member, CSEM wants to provide RISC-V cores for the industry and complements its actual offer of low-power microprocessors. In this initial study, we have proven that these two freely available open-source cores are indeed ready to use. CSEM is working on architectural improvements, adding customized instructions and hardware accelerators, to integrate RISC-V cores in low-power System-On-Chip on real silicon (ASIC).

[1] <https://riscv.org/risc-v-foundation>

[2] <https://github.com/riscv>

[3] <https://github.com/pulp-platform/pulpino>

[4] <http://www.eembc.org/coremark/index.php>

# An Harvesting System with Adaptive Power Management Algorithm for Energy Autonomous Devices

L. Zahnd, J. Deng, Y. Zha, J.-L. Nagel, C. Arm, M. Pons Solé, P. Persechini, D. Ruffieux, C. Monneron, R. Godinho Caseiro, Y. Liechti, S. Emery

A fully-integrated energy harvesting and transfer unit controlled by a sub-VT MCU has been implemented. The system is able to seamlessly transfer power between a solar cell and a 2.5-3 V battery while energizing external chips at 1.2 V. It manages the available energy optimally thanks to control algorithms such as hill-climbing, hysteresis regulation, Pulse Width Modulation for Maximum Power Point Tracking (MPPT) and output regulation.

Many modern electronic systems (i.e. wearable devices, connected sensors for the IoT) would greatly benefit from being able to harvest their own energy so as to eliminate wiring, daily recharge, maintenance or the need for oversized batteries. Energy autonomous operation for such devices requires combining in a low cost, compact system: 1) energy harvesting, 2) power conversion, and 3) storage functions. In addition, the awareness of the energy available at any time is a must for an optimum management of the application which could switch between different power modes contextually.

The smart fully-integrated powering unit, whose layout is pictured in Figure 1, is a System-on-Chip (SoC) that has been designed in 65-nm CMOS to provide an effective such solution for energy-autonomous connected nodes. It features two icyflex2-MCUs operating in sub-threshold and whose frequency can be changed dynamically for both minimum and scalable energy consumption. The MCUs control on the one hand an integrated energy harvester/transfer unit in the way described above and are able thanks to standard digital interfaces to interact with off-the-shelf components (COTS), process and manage related data to be transmitted wirelessly.

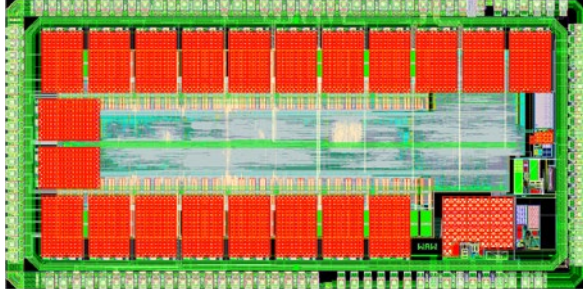


Figure 1: Smart powering unit SoC layout comprising a fully-integrated switched-capacitor based harvester, two MCU cores, 32 KB SRAM, 8 KB ROM, standard peripherals and interfaces.

The block diagram of the proposed adaptive energy harvesting system used with a photovoltaic (PV) cell is shown in Figure 2.

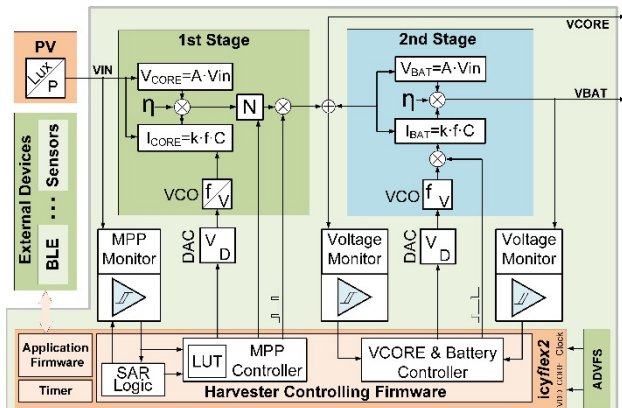


Figure 2: Block diagram of the dual stage energy harvesting unit.

The system consists of a dual stage energy conversion path and three control loops: one for MPPT and two for output voltages regulation. The 1<sup>st</sup> stage boosts the PV output voltage to a VCORE of ~1.2 V, suitable to power the SoC and an external wireless transmitter. The surplus (or missing) energy is transferred to (or taken from) a 2.5-3 V LiMn battery (or supercap) via the bidirectional 2<sup>nd</sup> stage charge pump. The higher standard voltage is used to power and interface COTS. To achieve maximum power transfer, a dynamic MPPT algorithm was implemented. It is able to:

- Detect changes of illumination via the level-crossing ADC.
- Search the PV-cell maximum power point with a SAR ADC.
- Control the 1<sup>st</sup> stage configuration to tune the current load.

To minimize the hardware complexity and power consumption, the MPP monitor is power-cycled and reconfigurable as either level-crossing ADC or SAR ADC. MPP open-circuit voltage method is used for calculating the optimized PV-cell voltage. Then, an energy-efficient hill-climbing algorithm is executed on the MCU to reach the targeted PV-cell voltage after configuring the 2D charge pump (CP) network (1×1 to 4×21) and its operating frequency for voltage gain and load setting. When illumination is weak, a PWM scheme (periodically turning on and off part of CP units) is applied to the 1<sup>st</sup> stage. With this approach a wide range of input currents spanning several decades ( $\mu$ W-mW) can be harvested with >50% efficiency.

To set the 1<sup>st</sup> stage output voltage, a control loop based hysteresis regulation is applied. By comparing VCORE using the voltage monitor, the regulation scheme turns off and on the 2<sup>nd</sup> stage. Thus the 1<sup>st</sup> stage is over or under loaded for a limited period, which creates a saw-tooth shape waveform within a predefined range (i.e.  $\pm 50$  mV) around the target voltage. The hysteresis regulation is also applied to the output of the 2<sup>nd</sup> stage to prevent over-charging or over-draining the battery.

Figure 3 shows a measurement of the powering SoC when the illumination is changed (between indoor and outdoor). It demonstrates that the system can adapt the PV-cell voltage to the MPP and maintain VCORE within a predefined range.

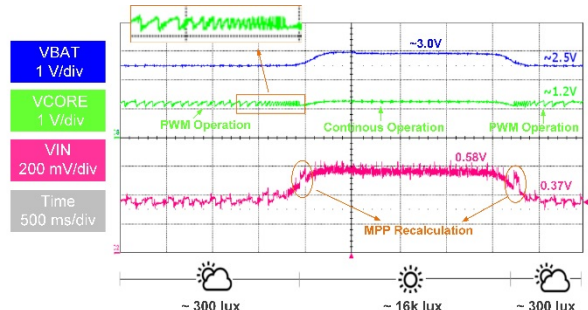


Figure 3: SoC measurement when varying the illumination condition.

# Fully Integrated Low-power Bio-potential Acquisition Analog Front-end IC

M. Augustyniak, Y. Zha, J. Deng, A. Bischof, M. Pons Solé, C. Monneron, R. Godinho Caseiro, S. Emery

A highly reconfigurable, ultra-low power, 20-channel system-on-a-chip (SoC) for biomedical signal acquisition is presented. It is designed to acquire electro-encephalo, -cardio and -myogram (ExG) signals having an amplitude spanning from 1  $\mu$ V to 10 mV in a frequency range from sub-Hz to 10 kHz.

Personalized healthcare solutions for 24/7 monitoring of an aging but connected population hold the promises to move the point of care from hospitals to the home reducing costs.

To meet that goal, low-cost, miniaturized, lightweight and unobtrusive wearable or implantable systems able to measure and monitor vital signs have to be developed to improve patients comfort and ease adoption. System-on-chips have a great potential to fulfill the above requirements by co-integrating sensing, data processing and transmission functions on a single miniature die that can be mass-produced at low cost.

A variety of physiological signals can be recorded with electrode-based measurements such as EEG, ECG and EMG, hence potentially with a single, generic ExG monitoring circuit. However, high reconfigurability is required to acquire such various electrical signals having voltages spanning from 1  $\mu$ V to 10 mV in a frequency range from sub-Hz to 10 kHz as illustrated in Figure 1.

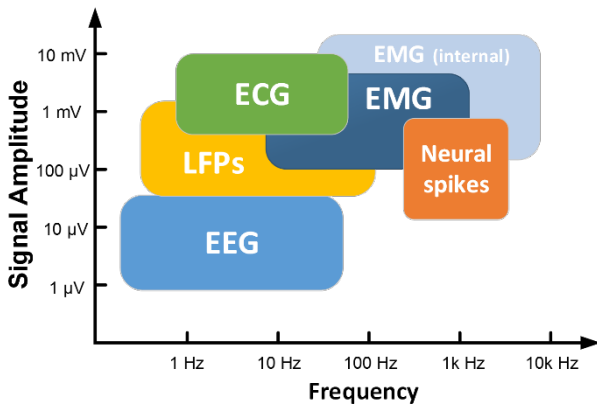


Figure 1: Physiological signals recording: frequency and voltage range.

Figure 2 shows the architecture of a circuit designed to meet such challenges. Featuring twenty ultra-low power parallel channels, the Analog-Front-End (AFE) that is configured digitally performs tailored filtering and amplification depending on the type of signals being recorded. Channels are then multiplexed before optimally amplified signals are digitized sequentially at a rate of 1 MSPS with a  $\pm 0.9$  V full scale 12-bit SAR ADC.

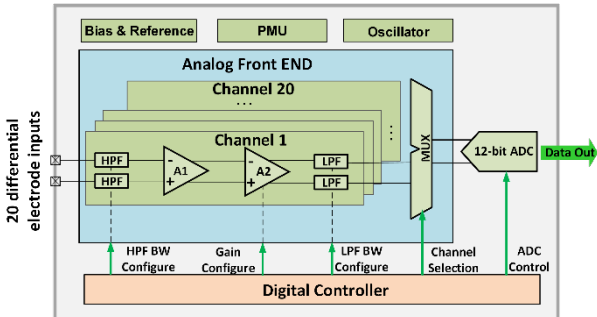


Figure 2: Block diagram of the 20-channel bio-potential acquisition system.

There are several design challenges associated with the acquisition of such signals. Firstly, the contact between electrode and skin is a metal-to-electrolyte interface, which superimposes a DC half-cell potential to the biomedical signal of interest. It results in a time-varying offset voltage which can exceed the tiny signal amplitude by more than four orders of magnitude. This requires a high-gain, low-noise AFE which is robust to differential offset drift and has a high input impedance and high Common-Mode Rejection Ratio (CMRR).

Another major challenge is the trade-off between power, noise, linearity, area and the input impedance. Considering these difficulties, an RC High-Pass Filter (HPF) is implemented using a temperature compensated pseudo resistor and on-chip capacitor. A two-stage amplification path is used with a proper optimized value of the input transistor size for obtaining higher gain, linearity, output swing, while achieving lower noise and consuming less power. Each amplifier has a configurable high-pass-filter characteristic for offset elimination, high CMRR (ca. 85 dB) and noise filtering. A Chebyshev gm-C low-pass filter (LPF) with on-the-fly autonomous calibration is implemented for band limitation and further noise reduction.

In order to perform on-chip processing of the digitized data so as to e.g., suppress motion-induced artefacts or extract higher level features for surveillance, a pre-processing accelerator complemented with a 32 b icyflex2 RISC processor, 256 kB SRAM, 64 kB ROM, a programmable sequencer, 8 timers, 16 GPIOs, I<sup>2</sup>C, SPI, JTAG, UART) are co-integrated forming a compact vital sign monitoring SoC suitable for applications based on ExG measurements.

The AFE consumes only 24  $\mu$ W per channel while maintaining large gain and bandwidth configurability. The MCU and accelerators are designed to run at 150 MHz. A picture of the layout of the SoC, which is currently being manufactured, is shown in Figure 3.

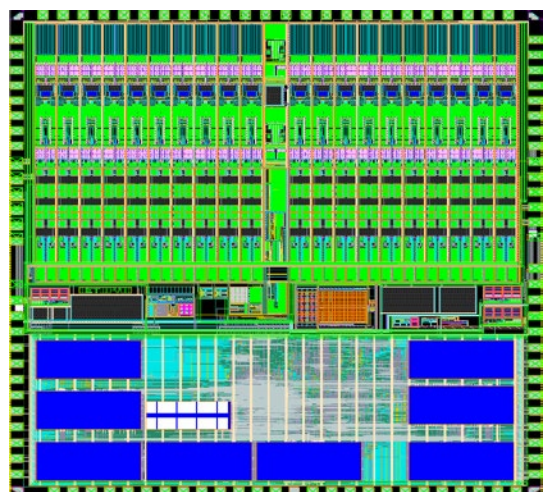


Figure 3: Layout of the SoC designed for ExG signal acquisition applications.

# Microelectrode Array for Neural Interface

A. Bischof, Y. Zha, P.-F. Rüedi

A microelectrode array (MEA) chip for in-vitro electrophysiology measurements was integrated in 0.35  $\mu$  CMOS technology. The MEA features 4096 full-duplex electrodes for sensing and stimulation, and is embedded in a multi-well system. This enables to run in parallel multiple experiments for testing drugs on neurobiological models.

In vitro neurobiological models are the most valuable tools to validate brain drug efficacy and toxicity before clinical trials. Pharma companies have a great need to access new technologies to improve the read-outs from in vitro screenings. Conventional patch clamp or MEA MEMS-based technologies can simultaneously access signals, but from a few cells only. This significantly limits the understanding of the collective behavior of neuronal circuits. Conversely, CMOS-based electrical biosensors (also termed High Density MEA or HD-MEA) integrate thousands of electrical sensors on chip, which drastically increases the experimental capability of sensing large neuronal networks. It allows the simultaneous measurement of the signals generated by thousands of neuronal cells, which enables the study of the electrical activity of neuronal circuits at network level. As a result, it is possible to record the electrical signatures of a network of cells to assess functional (healthy) or dysfunctional (diseased) states, and most importantly, to track the pharmacological response to a drug.

A CMOS chip with a 64 $\times$ 64 pixel array has been developed. Each pixel of 60 $\times$ 60  $\mu\text{m}^2$  features a flat electrode made in the top metal layer of the process, in-pixel voltage amplification and filtering to amplify with a gain of 100 the small biopotential signal present at the interface between the metal plate and the living tissue. In addition to sensing, each electrode can also be used individually for voltage stimulation, thus enabling to generate fine stimulation patterns and observe how the biological cell tissue reacts. Figure 1 shows a microphotograph of the chip encapsulated in the reservoir which holds the living tissue.



Figure 1: Microphotograph of the chip in its container.

Using through silicon via technology avoids bonding wires and enables a flat area extending on all sides of the chip to improve the quality of contact between the tissue and chip and therefore maximize tissue recording quality.

With 4096 electrodes able to both record and stimulate, it offers the highest number of stimulation sites available on the market, and also the largest active area. The characteristics of the microelectrode array chip are summarized in Table 1.

The device will be incorporated in a multi-well microtiter plates architecture for parallelized and semi-automated drug screening.

Table 1: Characteristics of the chip.

Parameter	Value
Resolution	64 $\times$ 64 pixels
Pixel pitch	60 $\mu\text{m}$
Active area	3.9 $\times$ 3.9 $\text{mm}^2$
Gain	10 - 1600
Frame rate	18 kfps
Maximum stimulation voltage	5 V
Electrode input common mode	0 - 400 mV
Electrode input signal (high gain)	+/- 2 mV
Power consumption	350 mW

Figure 2 shows neuronal spike activity of hippocampal neuronal cells seeded on a microelectrode chip, recorded by a single channel. Neuronal spikes are clearly visible.

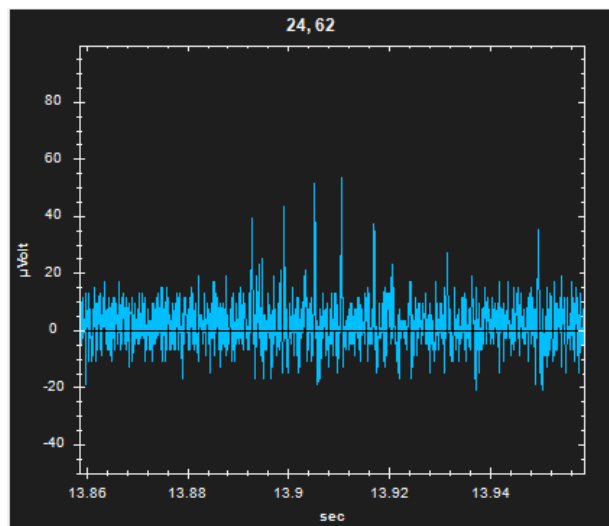


Figure 2: Output of a single channel.

This work, performed in collaboration with 3Brain, was partly funded by the Swiss Commission for Technology and Innovation CTI (project no. 18760.1 PFNM-NM) CSEM thanks them for their support.

# ANNEXES

## Publications

- [1] S. Barcellona, L. Piegari, V. Musolino, C. Ballif, "Economic viability for residential battery storage systems in grid-connected PV plants", IET Renewable Power Generation, August 2017
- [2] M. Boegli, Y. Stauffer, "SVR based PV models for MPC based energy flow management", Energy Procedia, 122, September 2017, 133-138
- [3] D. L. Boiko, A. V. Antonov, D. I. Kuritsyn, A. N. Yablonskiy, S. M. Sergeev, E. E. Orlova, V. V. Vaks, "Mid-infrared two photon absorption sensitivity of commercial detectors", Applied Physics Letters , 111 (17), October 2017, 171102
- [4] F. Braun, A. Lemkadem, V. Moser, S. Dasen, O. Grossenbacher, M. Bertschi, "Contactless Respiration Monitoring in Real-Time via a Video Camera", June 2017
- [5] F. Braun, M. Proen  , J. Sol  , J.-P. Thiran, A. Adler, "A Versatile Noise Performance Metric for Electrical Impedance Tomography Algorithms", IEEE Transactions on Biomedical Engineering, 64 (10), October 2017, 2321-2330
- [6] C. Brivio, V. Musolino, P.-J. Alet, M. Merlo, A. Hutter, C. Ballif, "Analysis of lithium-ion cells performance, through novel test protocol for stationary applications", 2017 6th International Conference on Clean Electrical Power (ICCEP) , June 2017, 410-415
- [7] L. Duempelmann, J. A. M  ller, F. L  tolf, B. Gallinet, R. Ferrini, L. Novotny, "Controlling the Color of Plasmonic Substrates with Inkjet Printing", Advanced Optical Materials, 5 (17), September 2017
- [8] O. El Baradai, J. Schleuniger, S. Fricke, C. Bosshard, "Printed and Bio-sourced Lithium Ion Batteries for Wearable Technologies", Battery Power online, (9828), October 2017
- [9] A. Faes, A. Lachowicz, N. Badel1, J. Geissb  hler, J. Champliaud, J. Levrat, L. Curvat, J. Horzel, F. Debrot, L.-L. Senaud, B. Paviet-Salomon, S. Martin de Nicolas, A. Descoeuadres, C. Alleb  , N. Badel, L. Barraud, P.-J. Alet, M. Despeisse, et al., "Multi-wire interconnection", November 2017
- [10] H. Gao, S. Generelli, F. Heitger, "Online Monitoring the Water Contaminations with", Proceedings, 2017, 1, September 2017, 522-525
- [11] L. Gasparini, B. Bessire, M. Untern  hrer, A. Stefanov, D. L. Boiko, M. Perenzoni, D. Stoppa, "Novel CMOS sensors for improved quantum imaging", SPIE Newsroom, April 2017, 10.1117/2.1201701.006847
- [12] S. Karlen, J. Gobet, T. Overstolz, J. Haesler, S. Lecomte, "Lifetime assessment of RbN3-filled MEMS atomic vapor cells with Al2O3 coating", Optics Express, 25 (3), February 2017, 2187
- [13] S. Karlen, J. Gobet, T. Overstolz, J. Haesler, S. Lecomte, "Quantitative micro-Raman spectroscopy for partial pressure measurement in small volumes", Applied Spectroscopy, 71 (12), September 2017, 2707-2713
- [14] C. Kirsch, S. Altazin, R. Hiestand, T. Beierlein, R. Ferrini, T. Offermans, L. Penninck, B. Ruhstaller, "Electrothermal Simulation of Large-Area Semiconductor Devices", International Journal of Multiphysics, 11 (2), February 2017, 127-136
- [15] I. Kjelberg, E. D. Rode, S. A. Marinello, L. Schaerer, "Monitoring Induced Seismicity", ERD  L ERDGAS KOHLE, Heft 2, February 2017, 65-73
- [16] M. S. Krzemnicki, C. S. Hanser, V. Revol, "Simultaneous X-ray Radiography, Phase-Contrast and Darkfield Imaging to Separate Natural from Cultured Pearls", The Journal of Gemmology, 35 (7), September 2017
- [17] D. Lindel  f, Y. Stauffer, "Intelligent geregelte Raumlufttechnik: NeuroCool – f  r mehr Komfort bei tieferen Kosten", bulletin.ch, August 2017, 23-30
- [18] N. Marjanovic, "Printed electronic components for hybrid integration; case study – sun sensor", November 2017
- [19] N. Marjanovic, "Flexible Hybrid Electronics; case studies", September 2017
- [20] W. Martin, Y. Stauffer, C. Ballif, A. Hutter, P.-J. Alet (2017), U. Betancourt, T. Ackermann (Eds.), Darmstadt, Germany: Energynautics GmbH, ISBN:978-3-9816549-5-0
- [21] J. Mayer, B. Gallinet, T. Offermans, I. Zhurinsky, R. Ferrini, "Self-contained optical enhancement film for printed photovoltaics", Solar Energy Materials and Solar Cells, 163, April 2017, 51-57
- [22] S.-J. Moon, L. L  fgren, A. Walter, B. Kamino, D. Sacchetto, F. Sahli, J. Werner, M. Br  uninger, B. Niesen, J. Bailat, S. Nicolay and C. Ballif, "Highly Efficient Organometallic Halide Perovskite mini-modules through a full laser patterning process", May 2017
- [23] C. Moufawad El Achkar, R. Carrillo, A. Hutter, "Unsupervised detection and classification of multiple refrigeration units in a commercial environment", November 2017

- [24] E. Obrzud, S. Lecomte, T. Herr, "Temporal solitons in microresonators driven by", *Nature Photonics*, 11, September 2017, 600-607
- [25] L.-E. Perret-Aebi, H. Li, "Assessment of Photovoltaic Module Failures in the Field", *Photovoltaic Power Systems Programme*, (Report IEA-PVPS T13-09:2017), May 2017
- [26] L.-E. Perret-Aebi, "Profiter encore plus du soleil", *bulletin.ch*, (10/2017), October 2017, 10-19
- [27] M. Proen  a, F. Braun, J. Sol  , J.-P. Thiran, M. Lemay, "Noninvasive pulmonary artery pressure monitoring by EIT: a model-based feasibility study", *Medical & Biological Engineering & Computing*, 55 (6), June 2017, 949-963
- [28] B. M. Quant, F. Braun, D. Ferrario, R. M. Rossi, A. Scheel-Sailer, M. Wolf, G.-L. Bona, R. Hufenus, L. J. Scherer, L. F. Boesel, "Body-monitoring with photonic textiles: a reflective heartbeat sensor based on polymer optical fibres", *Journal of The Royal Society Interface*, 14 (128), March 2017
- [29] B. M. Quant, R. Hufenus, B. Weisse, F. Braun, M. Wolf, A. Scheel-Sailer, G.-L. Bona, R. M. Rossi, L. F. Boesel, "Optimization of novel melt-extruded polymer optical fibers designed for pressure sensor applications", *European Polymer Journal*, 88, March 2017, 44-55
- [30] G. Quaranta, G. Basset, O. J. F. Martin, B. Gallinet, "Color-Selective and Versatile Light Steering with up-Scalable Subwavelength Planar Optics", *ACS Photonics*, 4 (5), May 2017, 1060-1066
- [31] M. Rapin, F. Braun, J. Wacker, O. Ch  telat, "A Wearable System For Multichannel Bioimpedance And Multilead ECG Monitoring", August 2017
- [32] M. Rapin, J. Wacker, O. Ch  telat, "Two-Wire Bus Combining Full Duplex Body-Sensor Network and Multilead Biopotential Measurements", *IEEE Trans Biomed Eng*. 2018 Jan;65(1):113-122. doi: 10.1109/TBME.2017.2696051
- [33] Y. Stauffer, E. Olivero, E. Onillon, C. Mahomed, D. Lindel  f, "NeuroCool: field tests of an adaptive, model-predictive controller for HVAC systems", *Energy Procedia*, September 2017, 127-132
- [34] N. Torcheboeuf, G. Buchs, S. Kundermann, E. Portuondo-Campa, J. Benn  s, S. Lecomte, "Repetition rate stabilization of an optical frequency comb based on solid-state laser technology with an intra-cavity electro-optic modulator", *Optics Express*, 25 (3), February 2017, 2215-2220
- [35] C. Trepte, C. Philips, J. Sol  , A. Adler, B. Saugel, S. Haas, S. Bohm, D. Reuter, "Electrical impedance tomography for non-invasive assessment of stroke volume variation in health and experimental lung injury", *Br J Anaesth.*, 118 (1), January 2017, 68-76
- [36] L. von Allmen, G. Bailleul, T. Becker, J.-D. Decotignie, M. E. Kiziroglou, C. Leroux, P. D. Mitcheson, J. M  ller, D. Piguet, T. T. Toh, A. Weisser, S. W. Wright, E. M. Yeatman, "Aircraft Strain WSN Powered by Heat Storage Harversting", *IEEE Transactions on Industrial Electronics*, 64 (9), September 2017, 7284-7292
- [37] N. N. Vukovic, J. Radovanovic, V. Milanovic, D. L. Boiko, "Low-Threshold RNGH Instabilities in Quantum Cascade Lasers", *IEEE Journal of Selected Topics in Quantum Electronics*, 23 (6), May 2017, 1200616

## Proceedings

- [1] A. Adler, M. Proen  a, F. Braun, J. X. Brunner, J. Sol  , "Origins of Cardiosynchronous Signals in EIT", *EIT 2017*, Dartmouth (US), 21-24 June 2017, 73
- [2] A. Adler, A. Bolye, F. Braun, M. G. Crabb, B. Grychtol, W. R. B. Lionheart, H. F. J. Tregidgo, R. Yerworth, "EIDORS Version 3.9", *EIT 2017*, Dartmouth (US), 21-24 June 2017, 63
- [3] A. Antonov, D. Kuritsyn, A. Gajic, E. Orlova, J. Radovanovic, V. Vaks, D. Boiko, "Tailoring Risken-Nummedal-Graham-Haken Instability in Quantum Cascade Lasers", *CLEO/Europe-EQEC 2017*, Munich (DE), 25 June 2017
- [4] P. B  guery, M. Petit-Pierre, H. Obara, R. Brunet, S. Marat, M. Boegli, "Building energy simulation coupled with real data for enhanced monitoring analysis", *Building Simulation 2017*, San Francisco (US), 7-9 August 2017
- [5] J. Bjurstr  m, H. L  fgren, M. Gunnarsson, G. Gruener, H.-R. Graf, T. M  ller, "A Miniaturized Motion Controller Customization for Exploration", *14th Symposium on Advanced Space Technologies in Robotics and Automation (ASTRA2017)*, Leiden (NL), 20-22 June 2017

- [6] N. Blondiaux, R. Pugin, "Ice Phobic Coating Associated to Low Power Electromechanical Deicers", EU Aviation Icing Workshop - FP7 STORM, Brussels (BE), 29-30 March 2017
- [7] D. L. Boiko, "On a question about quantumness in superradiance", XV International Conference on Quantum Optics and Quantum Information - ICQOQI'2017, Minsk (BY), November 2017
- [8] G. Borque Gallego, L. Rossini, E. Onillon, A. Karimi, "Linear Parameter-Varying Kalman Filter for Angular Velocity Estimation of a Reaction Sphere Actuator for Satellite Attitude Control", Advanced Intelligent Mechatronics - AIM2017, Munich (DE), 03-07 July 2017, 352-357
- [9] R. Delgado-Gonzalo, J. Hubbard, P. Renevey, A. Lemkadem, Q. Vellinga, D. Ashby, J. Willardson, M. Bertschi, "Real-time Gait Analysis with Accelerometer-based Smart Shoes", EMBC2017 - 39th Annual International Conference of the IEEE Engineering in Medicine and Biology Society, Jeju Island (FI), 11-15 July 2017
- [10] M. Despeisse, *et al.*, "Heterojunction Technologies and beyond: How to reach Top Efficiencies at Competitive Prices", Intersolar, Munich (DE), 4 May 2017
- [11] L. Gasparini, B. Bessire, M. Unternährer, A. Stefanov, D. Boiko, M. Perenzoni, D. Stoppa, "SUPERTWIN: towards 100kpixel CMOS quantum image sensors for quantum optics applications", SPIE OPTO, San Francisco (US), 27 January 2017, 101112L
- [12] J. González-Chávarri, E. Hammes, L. Parellada, I. Castro-Hurtado, E. Castaño, I. Ayerdi, H. F. Knapp, G. G. Mandayo, "Multisensor platform for indoor air quality measurements", 11th Spanish Conference on Electron Devices, Barcelona (ES), 8-10 February 2017
- [13] J. Haesler, K. Kautio, L. Balet, S. Karlen, T. Overstolz, B. Gallinet, "Ceramic based flat form factor miniature atomic clock physics package (C-MAC)", 2017 European Frequency and Time Forum & International Frequency Control Symposium (EFTF-IFCS) , Besançon (FR), July 2017
- [14] P. Heinstein, "Photovoltaik & Architektur", 15. Österreichische Photovoltaik Tagung, Vienna (AU), 13 November 2017
- [15] S. Karlen, G. Buchs, T. Overstolz, N. Torcheboeuf, E. Onillon, J. Haesler and D. Boiko, "MEMS atomic vapor cells for gyroscope applications", 2017 European Frequency and Time Forum & International Frequency Control Symposium (EFTF-IFCS), Besançon (FR), July 2017
- [16] S. Karlen, J. Haesler, T. Overstolz, G. Bergonzi, S. Lecomte, "MEMS atomic vapor cells sealed by Cu-Cu thermocompression bonding", 2017 European Frequency and Time Forum & International Frequency Control Symposium (EFTF-IFCS)
- [17] I. Karuseichyk, A. Mikhalychev, D. Mogilevtsev, G. Y. Slepyan, G. Buchs, D. L. Boiko, A. Boag, "Shaping field correlations with entangled quantum antennas", IV International Conference on Quantum Technologies (ICQT), Moscow (RU), July 2017
- [18] L. Kiener, H. Saudan, G. Perruchoud, M. M. Dadras, K. Vaideeswaran, "Additive Manufacturing: from elementary flexible structures to compliant mechanisms", Metallic Materials and Processes MMP2017, Deauville (FR), 25 October 2017
- [19] M. Krakowski, P. Resneau, M. Garcia, E. Vinet, Y. Robert, O. Parillaud, D. L. Boiko, "High pulse energy passive mode locking of inverse bow-tie 975 nm laser diode in external cavity", CLEO/Europe-EQEC 2017, Munich (DE), June 2017
- [20] M. Krakowski, P. Resneau, M. Garcia, E. Vinet, Y. Robert, M. Lecomte, O. Parillaud, B. Gerard, S. Kundermann, N. Torcheboeuf, D. L. Boiko, "High pulse energy stabilized passively mode-locked external cavity inverse bow-tie 990nm laser diode for space applications", European Semiconductor Laser Workshop ESLW 2017, Copenhagen (DK), 15 September 2017
- [21] M. Krakowski, P. Resneau, M. Garcia, E. Vinet, Y. Robert, M. Lecomte, O. Parillaud, B. Gerard, D. L. Boiko, "Lasing dynamics of very long (13.5mm) tapered laser emitting at 975 nm ", SPIE OPTO 2017, San Francisco (US), 20 February 2017, 101230E
- [22] S. Kundermann, J. O'Carroll, D. Byrne, L. Maigyte, B. Kelly, I. Kjelberg, S. Lecomte, R. Phelan, D. L. Boiko, "On-chip integrated zero-RAM frequency modulator for noise reduction and linewidth narrowing in discrete-mode lasers", CLEO/Europe-EQEC 2017, Munich (DE), 25 June 2017
- [23] A. Lemkadem, M. Proençā, R. Delgado-Gonzalo, P. Renevey, I. Oei, G. Montano, J. A. Martínez-Heras, A. Donati, M. Bertschi, M. Lemay, "An Autonomous Medical Monitoring System - Validation on Arrhythmia Detection", EMBC2017 - 39th Annual International Conference of the IEEE Engineering in Medicine and Biology Society, Jeju Island (KO), 11-15 July 2017

- [24] C. Manzoni, A. Carrard, E. Fontana, M. Lemay, M. Bertschi, R. Delgado-Gonzalo, "Towards VO2 Monitoring - Validation of a Heart Rate Based Algorithm", EMBC2017 - 39th Annual International Conference of the IEEE Engineering in Medicine and Biology Society, Jeju Island (KO), 11-15 July 2017
- [25] N. Marjanović, "Hybrid Integration; Case Study with Sun Sensor for Cube Satellites", Additive Manufacturing for Products and Applications Conference 2017, Zürich (CH), 13-15 September 2017
- [26] N. Marjanović, "Hybrid sun sensors for pico satellite", International Conference and Exhibition on Integration Issues of Miniaturized Systems, Cork (IR), 8-9 March 2017
- [27] N. Marjanović, J. Disser, F. Zanella, J. Schleuniger, A. Mustaccio, R. Ferrini, M. Schnieper, E. Assaf, "Hybrid integration; case study with sun sensor for cube satellites", Industrializing Additive Manufacturing – Proceedings of Additive Manufacturing in Products and Applications - AMPA2017, Zürich (CH), 13-15 September 2017, 264-272
- [28] V. Mitev, L. Gasparini, D. Stoppa, C. Piemonte, F. Acerbi, A. Stefanov, L. Balet, T. Herr, D. Boiko, "SiPM in g(2) measurements", Quantum Information and Measurement (QIM) 2017, Paris (FR), 05 April 2017, QT6A.46
- [29] D. Mogilevtsev, A. Mikhalychev, I. Karuseichyk, G. Buchs, D. Boiko, G. Slepyan, A. Boag, "Shaping field correlation with entangled quantum antennas", IEEE Conference on Microwaves, Communications, Antennas and Electronic Systems (IEEE COMCAS 2017), Tel Aviv (IL), November 2017
- [30] S.-J. Moon, L. Löfgren, A. Walter, B. A. Kamino, D. Sacchetto, F. Sahli, J. Werner, M. Bräuninger, B. Niesen, J. Bailat, S. Nicolay, C. Ballif, "Highly Efficient Organometallic Halide Perovskite mini-modules through a full laser patterning process", International Conference on Hybrid and Organic Photovoltaics 2017, Lausanne (CH), 21-24 May 2017
- [31] T. C. Müller, J.-L. Nagel, M. Pons, D. Séverac, K. Hashibaz, S. Sawadaz, K. Miyatakez, S. Emery, A. Burg, "PVT Compensation in Mie Fujitsu 55 nm DDC: A Standard-Cell Library Based Comparison", IEEE SOI-3D-Subthreshold Microelectronics Technology Unified Conference, San Francisco (US), 16-19 October 2017
- [32] V. Musolino, C. Rod, P.-J. Alet, A. Hutter, C. Ballif, "Improved Ramp-Rate and Self Consumption Ratio In A Renewable-Energy-Based DC Micro-Grid", 2017 Second IEEE International Conference, Nuremberg (DE), 27-29 June 2017
- [33] G. Quaranta, G. Basset, O. J. F. Martin, B. Gallinet, "Steering and filtering white light with resonant waveguide gratings", SPIE Nanoengineering: Fabrication, Properties, Optics, and Devices XIV, San Diego (US), 31 August 2017, 1035408
- [34] M. Rapin, D. Ferrario, E. Haenni, J. Wacker, A. Falhi, C. Meier, J.-A. Porchet, O. Chételat, "Electromagnetic Disturbances Rejection with Single Skin Contact in the Context of ECG Measurements with Cooperative Sensors", The 39th Annual International Conference of the IEEE Engineering in Medicine and Biology Society (EMBC2017), Jeju Island (KO), 11-15 July 2017
- [35] M. Rapin, F. Braun, J. Wacker, O. Chételat, "A wearable EIT system based on cooperative sensors", 18th int. conf. on biomed. applications of Electrical Impedance Tomography (EIT2017), Hanover, New Hampshire (US), 21.24 June 2017, 24-24
- [36] M. Rapin, D. Ferrario, C. Pellaton, E. Haenni, S. Dasen, O. Chételat, "ECG quality assessment of dry-electrode cooperative sensors", 4th European Congress on eCardiology and eHealth, Berlin (DE), 8-10 November 2017
- [37] P. Renevey, R. Delgado-Gonzalo, A. Lemkadem, M. Proença, M. Lemay, J. Solà, A. Tarniceriu, M. Bertschi, "Optical Wrist-worn Device for Sleep Monitoring", EMBEC2017 - European Medical and Biological Engineering Conference 2017, Tampere (FI), 11-15 June 2017, 615-618
- [38] C. Rojas, J-D. Decotignie, "Artificial Skin for Human Prostheses, Enabled Through Wireless Sensor Networks", 23rd IEEE International Conference on Embedded and Real-Time Computing Systems and Applications, Hsinchu (TW), 16-18 August 2017
- [39] P.-F. Rüedi, A. Bishop, M. K. Augustyniak, P. Persechini, J.-L. Nagel, M. Pons, S. Emery, O. Chételat, "Ultra low power microelectronics for wearable and medical devices", Desing, Automation and Test in Europe, Lausanne (CH), 27-31 March 2017, 1426-1431
- [40] J. Schleuniger, O. El Baradai, S. Fricke, "Printed Batteries - towards eco- and cost friendly mass production", European Coating Symposium ECS, Fribourg (CH), 8-10 November 2017

- [41] J. Solà, M. Proença, F. Braun, R. Delgado-Gonzalo, D. Ferrario, P. Renevey, C. Verjus, M. Lemay, O. Chételat, M. Bertschi, J. Krauss, "A systematic classification of cuffless blood pressure monitoring techniques: the three-layer framework", EMBC2017 - 39th Annual International Conference of the IEEE Engineering in Medicine and Biology Society, Jeju Island (KO), July 2017
- [42] J. Solà, A. Vybornova, F. Braun, M. Proença, R. Delgado-Gonzalo, D. Ferrario, C. Verjus, M. Bertschi, N. Pierrel, Y. Degiorgis, P. Schoettker, "Cuffless blood pressure monitoring at the chest: single-channel reflective PPG sensors are inaccurate", EMBC2017 - 39th Annual International Conference of the IEEE Engineering in Medicine and Biology Society, Jeju Island (KO), July 2017
- [43] J. Solà, A. Vybornova, F. Braun, M. Proença, R. Delgado-Gonzalo, D. Ferrario, C. Verjus, M. Bertschi, N. Pierrel, P. Schoettker, "Performance of Systolic Blood Pressure estimation from radial Pulse Arrival time (PAT) in anesthetized patients", EMBEC2017 - European Medical and Biological Engineering Conference 2017, Tampere (FI), 11 June 2017, 294
- [44] Y. Stauffer, E. Olivero, E. Onillon, D. Lindelöf, C. Mahomed, "NeuroCool: field tests of a model-predictive controller for VAC systems", Energy for Sustainability International Conference, Funchal (PT), 8-10 February 2017
- [45] B. Timotijevic, M. Luetzelschwab, D. Z. Bayat, Y. Petremand, L. Aebi, M. Tormen, "Compact optical MEMS accelerometers and temperature sensors", Photonics West, San Francisco (US), 28-02 January 2017
- [46] O. Vorobyov, V. Kopta, J. R. Farserotu, C. C. Enz, "Efficient Through-Waveguide Wireless Power Transfer for Body Area Networks", Biomedical Circuits and Systems - BIOCAS, Turin (I), October 2017

## Conferences and Workshops

J. Bailat, D. Dominé, P. Häfliger, J. Brossard, P. Kohler, M. Benkhaira, G. Cattaneo, N. Badel, C. Denizot, L. Löfgren, J.-W. Schüttauf, M. Crettaz, P. Liechti, M. Correvon, L. Zhou, R. Gentsch, J. M. Koller, N. Blondiaux, A. Bionaz, J. Kaufmann, *et al.*, "L'effet photovoltaïque au service de la montre-bracelet", Journée d'étude, Montreux (CH), 14 September 2017

L. Barraud, A. Descoedres, *et al.*, "Defect equilibration in Silicon Heterojunction solar cells", Silicon PV 2017, Freiburg (DE), 3 April 2017

D. L. Boiko, "Risken-Nummedal-Graham-Haken Instability in Quantum Cascade Lasers", Self-Generation of Optical Frequency Comb in Semiconductor Lasers, Turin (IT), 26 October 2017

C. Bosshard, "Sensor surfaces: from technology to market", Innovation Landscape Micro & Nano, Reinach (CH), 25 January 2017

C. Bosshard, "Smart implants: from sensing to stimulation", 13th Bernd-Spliessl Symposium, Basel (CH), 17 June 2017

M. Despeisse, C. Allebé, *et al.*, "Si-based dual junction solar cells enabling 1-sun efficiency above 30%", SiliconPV 2017, Freiburg (DE), 3 April 2017

A. Faes, A. Lachowicz, N. Badel, J. Geissbühler, J. Champliaud, J. Levrat, L. Curvat, J. Horzel, F. Debrot, L.-L. Senaud, B. Paviet-Salomon, S. Martin de Nicolas, A. Descoedres, C. Allebé, N. Badel, L. Barraud, P.-J. Alet, M. Despeisse, "R&D plating line for advanced silicon solar cells metallization", Swiss PV-Days, Lausanne (CH), 23-24 March 2017

A. Faes, M. Despeisse, J. Levrat, J. Champliaud, A. Lachowicz, N. Badel, J. Geissbühler, T. Söderström, Y. Yao, J. Ufheil, P. Papet, B. Strahm, J. Hermans, A. Tomasi, J. Fleischer, P.V. Fleischer, T. Takahashi, C. Ballif, "Multi-wire interconnection of back-contacted silicon heterojunction solar cells", 7th Metallization Workshop, Konstanz (DE), 23-24 October 2017

M. Fretz, R. J. James, A. Steinecker, "Optical Hearing - A new Approach for Cochlear Implants", 14. Dortmunder MST Konferenz, Dortmund (DE), 05 July 2017

M. Fretz, "Miniaturized Hermetic Packages in Glass and Sapphire", Swissphotonics Workshop on Miniaturized Photonic Packaging, Alpnach (CH), 16 May 2017

S. Fricke, "Printed Sensors Technology: Design, Manufacturing Process and Applications", Annual Manufacturing Forum 2017 - Innovating with Flexible Hybrid Electronics, Singapore (SG), 27 July 2017

S. Fricke, "Druckbare Sensoren für Food Packaging", ICT-Agri-Food Symposium - Intelligente Sensoren für Landwirtschaft und Nahrungsmittelbranche, Tänikon (CH), 5 September 2017

G. García Mandayo, J. González de Chávarri Ostolaza, E. A. Hammes, L. Parellada Monreal, I. Castro Hurtado, E. Castaño Carmona, I. Ayerdi Olaizola, H. F. Knapp, "Multisensor platform for indoor air quality", 11th Spanish Conference on Electron Devices, Barcelona (ES), 8-10 February 2017

- J. Haesler, K. Kautio, L. Balet, S. Karlen, T. Overstolz, B. Gallinet, "Ceramic based flat form factor miniature atomic clock physics package (C-MAC)", ESA Workshop on Microwave Technology and Techniques (MTT), Noordwijk (NL), April 2017
- S. Heub, R. Ischer, A. Grivel, R. Pugin, G. Weder, "Non-invasive measurement of oxygen and carbon dioxide in microscope biochamber", Nanobiootech Conference, Montreux (CH), 13-15 November 2017
- S. Karlen, J. Haesler, T. Overstolz, G. Bergonzi, S. Lecomte, "Cu-Cu thermocompression bonding as an innovative sealing method for MEMS atomic vapor cells", ESA Workshop on Microwave Technology and Techniques (MTT), Noordwijk (NL), April 2017
- S. Karlen, G. Buchs, T. Overstolz, N. Torcheboeuf, E. Onillon, J. Haesler, D. L. Boiko, "Nuclear spin decoherence time in MEMS atomic vapor cells for applications in quantum technologies", Fourth International Conference on Quantum Technologies (ICQT), Moscow (RU), July 2017
- I. Kastanis, "Machine learning for predictive maintenance or machine health monitoring", 2. F&E Konferenz zu Industrie 4.0 von «Industrie 2025», Winterthur (CH), 11 January 2017
- I. Kastanis, "Digitalisierte Handarbeit und kooperative Robotik", Fachveranstaltung Robotics & Collaborative Robots, Cham (CH), 30 May 2017
- I. Kastanis, "Satelliten Bild-Datenverarbeitung – DataBio", Intelligente Sensoren für Landwirtschaft und Nahrungsmittelbranche, Tänikon (CH), 5 September 2017
- I. Kjelberg, "La Microtechnique et l'Astronomie", cours dans le cadre de la formation EPFL Microtechnique 4e semestre, Lausanne (CH), 1 March 2017
- I. Kjelberg, "Thermo optical design aspects", ESA SOIDT Space Optics Instrument Design & Technology, Polzu Quatu, Sardinia (IT), May 2017
- H. F. Knapp, "Facing challenges in miniaturized sample handling", Swiss Symposium on Lab Automation 2017, Rapperswil (CH), 16 March 2017
- M. Krieger, "Vision & Wireless embedded Systems Program Overview", medela Technology Scouting Day 2017, Baar (CH), 19 December 2017
- M. Krieger, S. Generelli, N. Glaser, J. Dissier, N. Marjanovic, S. Emery, M. Schnieper, J. Bailat, C. Bosshard, D. Ulrich, "Bricks for autonomous IoT edge nodes", Industrie 2025 F&E Konferenz, Winterthur (CH), 11 January 2017
- M. Krieger, "Contactless vision & RF technology for human physical condition monitoring", medela Technology Scouting Day 2017, Baar (CH), 10 July 2017
- M. Krieger, "Sensors and the Internet of Things - Status and Future Outlook", Sensors - Key Elements in the new world of digitalization, Basel (CH), 14 November 2017
- M. Krieger, S. Generelli, "Bodensensorik Nährstoffe", Intelligente Sensoren für Landwirtschaft und Nahrungsmittelbranche, Tänikon (CH), 5 September 2017
- M. Krieger, M. Bertschi, "Vitalparametermessung bei Mensch und Tier", Intelligente Sensoren für Landwirtschaft und Nahrungsmittelbranche, Tänikon (CH), 5 September 2017
- A. Lachowicz, J. Geissbühler, A. Faes, *et al.*, "Reliable Copper Plating Process for Heterojunction Solar Cells", 7th Metallization Workshop, Konstanz (DE), 23-24 October 2017
- W. Martin, A. Hutter, C. Ballif, P.-J. Alet, "Automated quantification of PV hosting capacity in distribution networks under user-defined control and optimisation procedures", 7th Solar Integration Workshop, Berlin (DE), 24-25 October 2017
- S. Mohrdiek, "Packaging solutions for long-term active implants", Micronarc Alpine Meeting 2017, Villars-sur-Ollon (CH), 6-7 February 2017
- B. Paviet-Salomon, "Interdigitated back-contacted silicon heterojunction solar cells featuring an interband tunnel junction enabling simplified processing", BC workshop 2017, Freiburg im Breisgau (DE), 21-22 November 2017
- V. Revol, S. Senck, B. Planck, T. Stadelmann, M. Scheerer, J. Kastner, "Industrial application of X-ray Talbot-Lau grating interferometry in aeronautics and aerospace", X-ray and neutron imaging with gratings, Villigen (CH), 15 September 2017
- D. Sacchetto, S. Nicolay, *et al.*, "MoO<sub>x</sub> and TiO<sub>2</sub> carrier selective contacts for dopant-free SHJs", Silicon PV 2017, Freiburg (DE), 5 April 2017
- P. A. E. Schmid, "The WorkPlace 4.0 Companion – A system for smart manual assembly", 2. F&E Konferenz zu Industrie 4.0 von «Industrie 2025», Winterthur (CH), 11 January 2017
- P. A. E. Schmid, "Digitalisierung der Handarbeit mit dem WorkPlace 4.0 Companion (WP4C)", Swiss Mechatronics Day 2017, Zürich (CH), 29 June 2017
- P. A. E. Schmid, "Industrie 4.0 Impulsreferat Kollaborierende Automation", Praxiszirkel Industrie 4.0: Kollaborierende Automation, Brugg (CH), 16 March 2017
- P. A. E. Schmid, "Visual testing and quality control with neuronal networks and 3D lightfield imaging", EPIC Workshop on Automation for Fabrication and Testing of Optoelectronics, Achim (DE), 10-11 May 2017
- P. Schmid, I. Kastanis, M. Höchemer, A. Steinecker, "Application of advanced data analysis in industrial environment", EPoSS Annual Forum 2017, Graz (AT), 18-20 October 2017

P. A. E. Schmid, "Bildgebende Verfahren in Unkrautbekämpfung", Intelligente Sensoren für Landwirtschaft und Nahrungsmittelbranche, Tänikon (CH), 5 September 2017

A. Steinecker, "Sensoren - Daten - Algorithmen", Megatrend Digitalisierung, Arth-Goldau (CH), 23 August 2017

F. Zanella, G. Basset, B. Gallinet, C. Schneider, A. Luu-Dinh, S. Fricke, M. Schnieper, M. Zahir, "Microlenses for improved space imagers", CMOS Image Sensors for High Performance Applications, Toulouse (FR), 21 November 2017

## Publicly Funded Projects

Canton de Neuchâtel	NECAN – Développement de solutions PV pour le bâtiment
CCEM – Electricity	CONNECT-PV – Conductive transparent electrodes: a competence cluster for highly efficient thin film photovoltaics
Eurostars	ALBIREO – Low-power impulse-radio ultra-wideband module for remote control and keyless access
Eurostars	CIT-MSA – Disposable sensor array for bioprocess monitoring in disposable bioreactors
Eurostars	DEBORAH – Optimization of design and control of district level thermal energy systems
Eurostars	HICOLA – Highly coherent laser for coherent communication and sensing
Eurostars	LAMMIC – Production of laminin-521™ coated microcarriers for stem cell expansion
Eurostars	MDFD – Medical device for measuring electro-mechanical properties of skeletal muscles
Eurostars	PERISCOPE – NILM for Industrial and Public Buildings
Eurostars	POLYOMINO – All-in-one platform for the design and the production of customized free-form OPV modules
Eurostars	SWIRSENSE – Short-wavelength infrared tunable laser for sensing applications
Eurostars	WBPS – Wearable blood pressure system
Forschung Aargau	SECTEX – Development of hidden, shape and colour encoded micro flakes for robust textile authentication
Forschung Aargau	SENSORSURFACE – Colorimetric sensor structures on COP polymer foils for bioassays
Interreg	HARISSA – Fabrication de pièces plastiques 3D microstructurées par injection plastiques : applications dentaires, médicales et horlogères
Ligue Pulmonaire Suisse	OXYSMART – Validation of portable SpO2 sensor by reflective means
Nano-Tera	FLUSISAFE – Fluorescence lifetime encoding for anti-counterfeiting
Nano-Tera	FLUSITEX – Developing a wound dressing with an integrated sensing layer for non-invasive wound monitoring using fluorescence lifetime detection
Nano-Tera	FLUSIGATE – Development of a ratiometric textile sensor for pH
Nano-Tera	HEARRESTORE – Image-guided micro surgery for hearing aid implantation
Nano-Tera	ICYSOC – Inexact sub-near-threshold systems for ultra-low power devices
Nano-Tera	MINIHOLTER – Photoplethysmography-based ambulatory heart rate monitor device embedded into a smart watch
Nano-Tera	NAMB – Night ambulatory monitoring of blood pressure
Nano-Tera	NAMBPGATE – Transfer of NAMB blood pressure technology into AVA product
Nano-Tera	NEWBORNCARE – Reducing the false alarms of neonate vital sign monitoring via a computer vision-based approach to accurately measure heart and respiratory rates in a contactless way
Nano-Tera	OBESENSE – Monitoring the consequences of obesity

Nano-Tera	OBESENSEGATE – Improvement of commercial FieldWiz system with cardiac monitoring add-on
Nano-Tera	PARATEX – Novel smart textile to non-invasively monitor pressure, oxygenation and perfusion of tissue to prevent pressure ulcers in paraplegics
Nano-Tera	RASECAN – A new tool for rapid sensing of cancer by parallel AFM
Nano-Tera	SHINE – Solar to hydrogen integrated nano-electrolysis
Nano-Tera	SPINERPAIR – Hybrid CMOS-polymer neural interfaces for restoration of sensorimotor function after spinal cord injury
Nano-Tera	SYNERGY – Realizing photovoltaic energy harvesting systems based on tandem solar cells with efficncty beyond that achievable with state-of-the-art industrial single-junction cells
Nano-Tera	WISESKIN – Wise Skin for tactile prosthetics
SATW	IMMOCOATING – Sensor coating for immobilisation of colorimetric bioassays on absorbance enhancing nano-gratings
SATW	META-SURFACES – Meta-surfaces-large-area metasurfaces for planar light management
SNI – Nanoargovia	NFOPTICS – Uniaxilly oriented anisotropic electrospun nano-fibrous layers for optical applications
SNI – Nanoargovia	PLASMORETARDER – Plasmonic nanoscale retarder controlled with liquid crystals
SNSF	ACTIVE INTERFACES – Holistic strategy to simplify standards, assessments and certifications for building integrated photovoltaics
SNSF	CELLSTRATES – Smart engineered substrates for high throughput mechanobiology
SNSF	EOCOMB – Broadband optical frequency comb source based on electro-optic modulation for resolved comb line precision spectroscopy
SNSF	FASTIQ – Ultrafast infrared emitter on a quantum cascade
SNSF	FILINE – Bridge Proof of Concept awarded to Victor Brasch
SNSF	HEMODYNAMEIT – Subject-adapted 3D dynamic bio-impedance models: application to blood pressure monitoring
SNSF	MAXIN – Hybrid PVT collector
SNSF	MUSCLELAB – Silicon elastomer structures to measure mechanical properties of muscle models
SNSF	NOVIPIX – Novel integrated pixel X-ray detectors
SNSF / program NRP 70	PV2050 – Novel generation perovskite devices
SNSF / program NRP 70	PV2050 – Photovoltaics into the built environment: from semi-transparent PV glazing to high efficiency roof integrated solutions
Swiss Federal Office of Energy (SFOE)	DCSMART – Distribution en courant continu dans les réseaux intelligents
Swiss Federal Office of Energy (SFOE)	Démonstration d'une toiture PV terra-cotta sur une ferme traditionnelle
Swiss Federal Office of Energy (SFOE)	PROSUMER-LAB – Einfluss neuartiger Strategien und Komponenten des Energiemanagements von netzintegrierten, intelligenten Gebäuden auf die Stabilität und Qualität des Haus- und Verteilnetzes
Swiss Federal Office of Energy (SFOE)	Lokale Vorhersage der Sonneneinstrahlung
Swiss Federal Office of Energy SFOE	BRUTTEN – PV-Gebäudehülle mit warmem Erscheinungsbild im Wohnquartier

Swiss Federal Office of Energy SFOE PVLIFE – Neuchâtel, musée suisse de l'architecture solaire à ciel ouvert

Swiss Space Office AMAR – MdP2016 Additive Manufacturing of an SRA Rotor

Swiss Space Office E-GRIP2 – Einstein gravitational red-shift probe mission study

## Swiss Commission for Technology and Innovation (CTI)

18101.1 PFNM-NM	3D NANOMET	Surface micro-nanostructuring of metallic surfaces for improved tribological performances
18616.1 PFNM-NM	ALSCN	High volume process for AlScN thin film deposition
25701.1 PFNM-NM	AMTI	Additive manufacturing of Ti based alloy for aerospace application
25714.1 PFNM-NM	AUTOMIA	Automated bovine milk analysis by push-button identification and characterization of somatic cells
25559.1 PFIW-IW	BINPICK	Flexibles, hochmodulares und innovatives Zuführsystem für Kleinsteile
18623.1 PFNM-NM	BIOWAVE	Realisation of the BIOWAVE pre-product, a BIometric Watch Activated by VEins
18473.2 PFNM-NM	BUBBLES	Fluid sensor with acoustical pattern analysis of physical properties and IoT integration
27049.1	CBM	Deep learning for condition based monitoring on railway vehicles
26001.2 PFNM-NM	CLEAN-WAVE	Development of materials, processes and technologies for the manufacturing of cost effective self-cleaning solar reflectors
17623.1 PFNM-NM	CNT-SENSE	Surface enhanced Raman scattering sensor for airborne carbon nanotubes in workplaces
17863.2 PFLS-LS	COCO	Sustainable intensification of agricultural cropping systems supported by smart swiss ICT-AGRI solutions
18445.1 PFIW-IW	COMET	Contacting and metrology for advanced photovoltaic cells and modules technologies
18894.1 PFNM-NM	CORIBO	MEMS-based micro-Coriolis density and flow sensor bonding
25171.1 INNO-NM	COSTO	Feasibility study : Fingerprint of gemstones
18314.1 PFIW-IW	COTM	KU-KA frontend : Additive-manufactured Satcom user terminal frontend for connectivity on the move applications in Ku and Ka band
18888.1 PFES-ES	CUBIC 2	The world's lowest-power platform to wirelessly exchange information peer-to-peer
16692.2 PFIW-IW	CUMAPRO	Massenproduktion von kundenspezifischen PV-Modulen für die Gebäudeintegration, Customised Mass Production
17266.2 PFIW-IW	DEFIA	Development of novel electrode foil solution for solar cells interconnected with smartwire connection technology applied in the glass-glass module configuration
25600.1 PFNM-NM	DENSXO	Gas density sensors based on adaptive oscillators
18421.1 PFIW-IW	DLC ABB	Improved DLC electrically active layer for high power bipolar silicon semiconductor
25726.2 PFNM-NM	DORES	Mirrored force resonance with double balance wheel for watches

25739.1 PFNM-NM	DSC-GLUE	Development of an adhesive formulation for durable dye-sensitive glass-modules for building integrated photovoltaic power generation
18633.1 PFNM-NM	DUALCOMB	Dual comb mid IR source technology
25374.1 PFNM-NM	ECHOPAD	Flexible pad-based ultrasound system for continuous heart monitoring
17708.1 PFNM-NM	ELECTROLUMINATI	Electro-illumination of dive watches through mechanical power generation
25790.1 PFIW-IW	EMAILLE	Oberflächeninspektion für grossflächige Emaillekörper
25365.1 PFNM-NM	EMIRS 2.0	Development of new infrared light sources for gas detection application.
18003.1 PFNM-NM	FASTOBS	Dynamic nanoindentation enabling fast observation, high stain rate, fatigue testing and multiaxial loading and force measurements
18481.1 PFNM-NM	FEMTOPOWER	Femtopower will develop ultrahigh power ultrashort pulse femtosecond laser source for highspeed industrial micromachining
25799.2 PFIW-IW	GMD	Predictive maintenance for mill drive power train systems
19288.1 PFNM-NM	HIFILL	Industrial fabrication of ultra-high fill factor microlenses
25138.1 PFNM-NM	HI-MU-LENS	Wafer-scale integration of high-refractive index microlenses on III-IV semiconductor photodiodes
18099.1 PFNM-NM	HIPERSTEER	High performance beam steering unit
18307.1 PFIW-IW	HOT-WINDOWS	Heated aircraft windshields- development of a transparent and more reliable heating for the production of aircraft windshiled series
18421.1 PFIW-IW	IDEAL	Improved DLC electrically active layer for high power bipolar silicon semiconductor edge passivation.
25137.1 PFNM-NM	INDIFUSEHOLDER	Ultra-low energy voltage indicator for new type of fuses
27100.1 PFLS-LS	INTUBSENS	Development of a pressure sensor for medical applications
17142.2 PFEN-NM	IOTLOC	Development of a network for advanced low power localization using LoRa technology
18737.1 PFNM-NM	LAOSS	Large area organic semiconductor software for photovoltaic and light emitting devices (LAOSS)
16871.1 PFNM-NM	LIDTDOS	LIDT und Degradations Prüftechnik für industrielle Anwendungen
18458.1 PFNM-NM	LIGHTHARVFOILS-FEASIBILITY	Foils for transparent and colour-free solar energy harvesting
18959.1 PFIW-IW	MAXIMAL	Modular radial and axial active magnetic bearing for maxon motors
25480.1 PFNM-NM	MCII	Surface treatment of materials by new multi-charged ion implantation unit: Process development and optimization for industrialization of turnkey equipment.
18559.1 PFLS-LS	MEMO-MAB	Banking of human antibody repertoires for therapeutic use
18325.1 PFNM-NM	MULTISENSOR	Development of a module integrating an optical temperature sensor and two optical accelerometer
18088.1 PFNM-NM	NANOWHITE	Process development and reliability of white solar module for BIPV
18760.1 PFNM-NM	NEURUG	Multi-well biosensor for drug screening applications

18808.2 PFIW-IW	OCTOPLUS	Development of a smart manufacturing Octopus cluster platform for thin film depositions on both sides of a substrate without breaking vacuum and without external substrate handling
17896.1 PFIW-IW	OILGUARD	Oil in water monitoring
18646.2 PFNM-NM	OPTINCLINO	Optical inclinometer: Development of a fully packaged MEMS inclinometer with remote optical readout for Structural Health Monitoring
18755.1PFNM-NM	OPTOGAS	CO <sub>2</sub> /O <sub>2</sub> gas mixing and sensing for life sciences
18327.1 PFNM-NM	OPTOREC	Development of high-end optical reference cavities for laser stabilization
18267.1 PFNM-NM	ORCA	On-reed camera array
18419.1 PFIW-IW	PEARLSCAN	Automatic assessment and measurement of pearl necklaces
18352.1 PFNM-NM	PIFPAF II	Pipetting system with flowsensor and microelement for passive flow control
17244.1 PFLS-LS	POSBONE	Compact and flexible system for total knee replacement surgery
18926.2 PFNM-NM	PRINT-BAT	Feasibility study: Flexible printed batteries
18748.1 PFNM-NM	PRISM	High resolution multi-color detection system with adaptive algorithms for parallelized gene sequencing systems
18082.1 PFNM-NM	PROMISES	Perovskite photovoltaic material screening for enhanced stability
25422.2 PFIW-IW	PUMPOMAT	Robotergesteuerter Präzisionsmontagearbeitsplatz
17705.1 PFNM-NM	PUNCH	Production-ready, next generation back-contacted silicon heterojunction solar cells and modules
26290.1 INNO-NM	PV TILES	Research and development of a terracotta coloured integrated solar roof tile
26116.1 PFES-ES	RAILCHECK	RailCheck with fingerprinting
14782.1 PFLS-LS	SARENAPATCH	Micro patch portable pour l'injection en continu d'insuline
18465.1 PFNM-NM	SECUREFLIM	Fluorescence lifetime imaging microscopy (FLIM) for the product and brand protection market
18462.1 PFNM-NM	SILICON EYE	Design of a vision for positioning systems
16584.1 PFEN-IW	SILVERLINE 2	Next generation production processes and quality controls for watch batteries
26824.1 PFIW-IW	SMINTEBI	SMart INDividual TEnant BILLing (SMINTEBI) feasibility study
16694.2 PFIW-IW	STABILITY	Dynamische Lageregelung für Hydraulikmodule demonstriert an einem Stelzentraktor im Rebberg
17518.1 PFEN-NM	SUPERTC	SuPeRTC, a super high performance temperature compensated miniature real time clock module
18679.2 PFIW-IW	SWISSHOLO	Security 1st and 2nd level features provide (hidden) unique identifying structures for trademark protection of titanium implants
1799.1 PFNM-NM	SWW	OEM module and new algorithms (speed, sleep)
18939.1PFNM-NM	TEXAS	New casting tool for textured hydrogel surfaces for 3D cell culture

18130.1 PFIW-IW	TORS	Tribological optimization of spinning traveler and ring for spinning and twisting
18539.1 PFLS-LS	TRACTEUR	Development of an automated seed drill for the site-specific reseeding of grassland
18741.1 PFNM-NM	TRUEAIRSPEED	Pressure measurement system for paragliders
17324.1 PFLS-LS	U4P	Using physiological parameters measured with a wrist-worn device to predict ovulation, detect pregnancy, and monitor gestation
18612.1 PFNM-NM	VALIPLATE-II	High-accuracy calorimetric tool for validating the liquid volume dispensed by liquid handling instruments
18621.1 PFEN-NM	WATT.CH	Smart wristband powered by PV cells
25990.1 PFNM-NM	WAVEZ-F	Feasibility study for OBPM monitoring
18091.1 PFEN-NM	WISEROCK	Low-cost WSN with GNSS capability for long-term landslide monitoring
18394.1 PFLS-LS	ZEPTOTRACK	Real-time surgical instruments positioning with reference integrated in surgical lamp

## European Commission Projects

H2020 – NMBP 2016	ACENANO	Analytical and characterization excellence in nanomaterial risk assessment: A tiered approach
FP7 – ICT	ACTION	Active Implant for optoacoustic natural sound enhancement
H2020 – IOT 2016	ACTIVAGE	ACTivating InnoVative IoT smart living environments for AGEing well
FP7 – TRANSPORT	AEROMUCO -COMPLEMENT	AEROdynamic Surfaces by advanced MUltifunctional Coatings
FP7 – NMP	AMBASSADOR	Autonomous management system developed for building and district
H2020 – LCE 2016	AMPERE	Automated photovoltaic cell and module industrial production to regain and secure European renewable energy market
H2020 – ICT 2016	BIOCDX	A miniature bio-photonics companion diagnostics platform for reliable cancer diagnosis and treatment monitoring
FP7 – ICT	BIOFOS	Microring resonator-based biophotonic platform for food analysis
H2020 – LCE 2015	CHEOPS	Production technology to achieve low cost and highly efficient photovoltaic perovskite solar cells
H2020 – IND CE	CITCOM	Complimentary inspection technique based on computer tomography and plenoptic camera for MEMS components
FP7 – ICT	COLAE-COMPLEMENT	Commercialization clusters of OLAE (flexible, organic and large area electronics and photonics)
H2020 – ICT 2016	DATABIO	Data-driven bioeconomy
H2020 – ICT 2015	DETOP	Dexterous transradial osseointegrated prosthesis with neural control and sensory feedback
H2020 – LCE 2016	DISC	Double-side contacted cells with innovative carrier-selective contacts
FP7 – ICT	D-LIVER COMPLEMENT	Monitoring of patients with liver diseases
FP7 – SPACE	ELSA-COMPLEMENT	European levitated spherical actuator

FP7 – TRANSPORT	EVITA-COMPLEMENT	Non-destructive evaluation, inspection and testing of primary aeronautical composite structures using phase contrast X-ray imaging
H2020 – ICT 2016	FLAIR	FLying ultrA-broadband single-shot Infra-Red sensor
FP7 – ICT	FLEX-O-FAB -COMPLEMENT	Pilot-scale hybrid roll to roll/sheet to sheet manufacturing chain for flexible OLEDs
H2020 – MSCA-ITN 2016	FoodSmartPhone	Smartphone analyzers for on-site testing of food quality and safety
FP7 – SPACE	FOSTERNAV -COMPLEMENT	Flash optical sensor for terrain relative robotic navigation
H2020 – MG 2014	FUTURESKY	Smart, green and integrated transport
H2020 – ICT 2014	GATEONE	Innovation service for European smartization by SMEs
FP7 – ICT	GO4TIME-COMPLEMENT	Global, flexible, on-demand and resourceful timing IC & MEMS encapsulated system
FP7 – NMP	GREENANOFILMS	Development and application of ultra-high resolution nano-organized films by self-assembly of plant-based materials for next generation opto- and bio-electronics
FP7 – HEALTH	HEMIBIO COMPLEMENT	Hepatic microfluidic bioreactor
FP7 – ENERGY	HERCULES COMPLEMENT	High efficiency rear contact solar cells and ultra-powerful modules
H2020 – EEB 2017	HYBUILD	Innovative compact hybrid electrical/thermal storage systems for low energy buildings
H2020 – EE 2015	INDIGO	New generation of intelligent and efficient district cooling systems
FP7 – SECURITY	INGRESS	Innovative technology for fingerprint live scanners
FP7 – NMP	INNOVABONE COMPLEMENT	Novel biomimetic strategy for bone regeneration
H2020 – SC5 2014	INREP	Towards Indium free TCOs
H2020 – ICT 2016	INSPEX	Integrated smart spatial exploration system
FP7 – ENVIRONMENT	INTASENSE-COMPLEMENT	Integrated air quality sensor for energy efficient environment control
H2020 – FOF 2016	KRAKEN	Hybrid automated machine integrating concurrent manufacturing processes, increasing the production volume of functional on-demand using high multi-material deposition rates
FP7 – ICT	LASSIE-FP7	Large area solid state intelligent efficient luminaires
H2020 – MG 2014	LYNCEUS2MARKET	Safer and more efficient waterborne operations through new technologies and smarter traffic management
H2020 – ICT 2014	M3TERA	Micromachined terahertz systems -a new heterogeneous integration platform enabling the commercialization of the THz frequency spectrum
H2020 – ICT 2014	MEDILIGHT	Miniaturized smart system for light stimulation and monitoring of wound healing
H2020 – ICT 2015	MIRPHAB	MidInfraRed PHotonics devices fABrication for chemical sensing and spectroscopic applications
H202 – SESAR 2015	NAVISAS	Navigation of airborne vehicle with integrated space and atomic signals

H2020 – LCE 2016	NEXTBASE	Next-generation interdigitated back-contacted silicon heterojunction solar cells and modules by design and process innovations
FP7 – ICT	PASTA-COMPLEMENT	Integrating platform for advanced smart textile applications
FP7 – ICT	PEGASO	Personalised guidance services for optimizing lifestyle management in teen-agers through awareness, motivation and engagement
H2020 – LCE 2016	PENTAGON	Unlocking European grid local flexibility through augmented energy conversion capabilities at district-level
FP7 – SPACE	PHASER	High-speed, high-frequency electro-photonic ADC for space enabled routers
FP7 – NMP	PLIANT	Process line implementation for applied surface nanotechnologies
H2020 – ICT 2014	RAWFIE	Road-, air- and water-based future internet experimentation
FP7 – SPACE	REMOVE-DEBRIS	A low cost active debris removal demonstration mission
H2020 – SEC 2016 - 2017	ROBORDER	Autonomous swarm of heterogeneous robots for border surveillance
FP7 – SECURITY	SAVE-MED	Tackling counterfeit medicines and related criminal networks
FP7 – ICT	SEMIAH	Scalable multi-criteria energy management infrastructure for aggregation of households
H2020 – ICT 2014	SMARTER-SI	Smart access to manufacturing for systems integration
FP7 – NMP	SMARTRONICS COMPLEMENT	Development of smart machines, tools and processes for the precision synthesis of nanomaterials with tailored properties for organic electronics
FP7 – ICT	SPLENDID COMPLEMENT	Personalized guide for eating and activity behavior for the prevention of obesity and eating disorders
FP7 – ENVIRONMENT	STRATOCLIM	Stratospheric and upper tropospheric processes for better climate predictions
FP7 – ICT	SUNFLOWER	Sustainable novel flexible organic watts efficiently reliable
H2020 – FETOPEN 2014/15	SUPERTWIN 3	All solid-state super-twinning photon microscope
FP7 – ICT	SWAN-iCare	Smart wearable and autonomous negative pressure device for wound monitoring and therapy
H2020 – EEB 2016	THERMOSS	Building and district thermal retrofit and management solutions
FP7 – NMP	TRIBUTE	Take the energy bill back to the promised building performance
FP7 – ICT	VIAMOS	Vertically integrated array-type Mirau-based OCT system for early detection of skin pathologies – Small or medium-scale focused research project (STREP)
FP7 – ICT	WELCOME	Wearable sensing and smart cloud computing for integrated care to COPD patients with comorbidities
FP7 – ICT	WISERBAN-COMPLEMENT	Smart miniature low-power wireless microsystem for body area networks

# European Space Agency (ESA), Swiss Space Office and CNES Projects

## ESA Projects

AMIGO	Autonomous medical monitoring and diagnostics
CCM-MTG	Development and manufacture of corner cube mechanisms for MTG satellite
CECILE	LiDAR integrating compressive sensing
CLUPI	CLUPI instrument for Exomars
C-MAC	Ceramic miniature atomic clock physics package – C-MAC PP
CS4SPACE	Compressive sensing
DANOE	High-dynamic absolute nanometric optical encoder technology assessment for space phase II
DELIAN	Detrous lightweight arm for exploration
ENRUM	Space and energy resources utilisation mapping (EnRUM)
EUSO-B2	Extreme universe space observatory – Phase B2
FGU	Micro-optoelectronic frequency generation unit (FGU)
HOPP	Photodiode development
HOPWELL	Space validation of glass lid soldering techniques to hermetically seal small size optoelectronic parts
ITI-SiC	Silicon carbide sensors for harsh space environments
LAFP	Develop a large angle flex pivot for space applications
LIDISOR	LIDAR for Inter-satellite optical ranging
MACAREW	Magnetic characterization of reaction wheels
MCC-X	Miniaturised motion controller customisation for exploration
MEMS GC-MS	MEMS-based gas chromatograph and mass spectrometer
MEMS-REAL	MEMS reliability assessment
ML-BI-CIS	Microlenses deposition for backside illuminated imagers
MLSCL	Sub-picosecond model-locked semiconductor laser for space missions
MONALISA PHASE 1	Laser for LISA mission
MTS	Miniature timing source (mTS): miniature atomic clock, MEMS vapor cells, ASIC specifications
NIRS	NIR immersed grating in transmission for high resolution spectroscopy
NPI BEARING	Miniature magnetic bearings for space actuators
NPI-CELL	PhD on fabrication of miniature atomic cells
NPI-EIT	Wearable physiological sensor network – non-invasive and non-occlusive blood pressure (BP) measurement based on Electrical Impedance Tomography (EIT)
OEO	Ultra-low phase noise reference oscillator
OSRC	Digital stabilisation electronics for lasers
STAR	Lidar for Wavefront distortion
STIFS	Definition for optical atomic clock
SWIRS	New generation SWIR immersed grating (Phase1)
WALES-PLUS	Wafer level encapsulation for microsystems-PLUS

## Swiss Space Office Projects

SPACEXCT      X-ray techniques for NDT and damage characterization for space materials and components / Austrian Space Applications Programme

## CNES Projects

BlazedGratSpher      Blazed grating on spherical substrate

## Swiss Space Center Projects

T-BEAR      Measurement method for active magnetic bearing

## Industrial Property

### Patent portfolio

In 2017, 20 invention reports were submitted internally for examination which have led to 18 patent applications filed in 2017 (15 regular applications and 3 provisional applications). The patent portfolio has been further enhanced by the extension of different countries of 13 patent files based on prior patent applications.

## Collaboration with Research Institutes and Universities

<i>University</i>	<i>Institute</i>	<i>Professor</i>	<i>Field of collaboration</i>
AO Research Institute Davos	Biomaterials & tissue engineering program	M. Alini	Intervertebral disc biomechanics
Aristotle University of Thessaloniki	Laboratory of Medical Informatics	N. Maglaveras	Collection of large set of physiological signals
Bern University of Applied Sciences (BFH)	Institute for Energy and Mobility Research	A. Vezzini	Energy Storage Research Center
Bern University of Applied Sciences (BFH)	Micro- and Medicaltechnology	G. Gruener	WP4C – WorkPlace 4.0 Companion / Y-Delta
Bern University of Applied Sciences (BFH)	MSE	V. Koch	Sensory processing prosthetics
Brown University	School of Engineering	A. V. Nurmikko	Integrated circuits for brain implants
Carleton University	Systems and Computer Engineering	A. Adler	Electrical-impedance tomography
CEA-LETI	Capteurs et Actionneurs	M. Le Prado	Atomic gyroscopes
Christian-Albrechts-Universität zu Kiel	Klinik für Anästhesiologie und Operative Intensivmedizin	I. Frerichs	Electrical-impedance tomography
CHUV	Service de cardiologie	E. Pruvot	Cardiac arrhythmias
CHUV	Département Anesthésiologie	P. Schoettker	Blood pressure
Croydon Healthcare NHS Trust	Trust R&D	J. Chang	Clinical validation
Empa	Laboratory for functional polymers	F. Nüesch	Transparent PV
Empa	Laboratory for Air Pollution / Environmental Technology	L. Emmenegger	Optical gas spectroscopy
Empa	Department of advanced materials and surfaces	P. Görning	X-ray read out circuits
Empa	Swiss federal laboratories for materials science and technology	P. Hoffmann	Solid state lighting

<i>University</i>	<i>Institute</i>	<i>Professor</i>	<i>Field of collaboration</i>
EPF Lausanne	TCL Telecommunications Circuits Laboratory	A. P. Burg	Good enough circuits, ultra-low power and sub-threshold design
EPF Lausanne	IMT/PVLAB	C. Ballif	Photovoltaics
EPF Lausanne	ICLAB Integrated Circuits Laboratory	C. C. Enz	Approximate arithmetic, ULP Radio and protocol for WiseSkin
EPF Lausanne	Embedded Systems Laboratory	D. Atienza	ECG monitoring
EPF Lausanne	Laboratoire de métallurgie thermomécanique	E. Boillat	Additive Manufacturing
EPF Lausanne	SCI STI JMV Group	J.-M. Vesin	Newborn vital signs monitoring based on multiple vision sensors
EPF Lausanne	Laboratory of advanced semiconductors for photonics and electronics	N. Grandjean	GaN-based semiconductor lasers / Solid state lighting
EPF Lausanne	Hemodynamics and Cardiovascular Technology Laboratory	N. Stergiopoulos	Cardiac output monitoring
EPF Lausanne	LAP Processor Architecture Laboratory	P. lenne	Embedded systems
EPF Lausanne	Signal Processing Laboratory 2	P. Vandergheynst	Newborn vital signs monitoring based on multiple vision sensors / Signal Processing
EPF Lausanne	Instant Lab Laboratory	S. Henein	Flexure guides
EPF Lausanne	LSBI Foundation Bertarelli Chair in Neuroprosthetic Technology	S. Lacour	Artificial skin, restore spinal connections
EPF Lausanne	Laboratory of Photonics and Quantum Measurements	T. J. Kippenberg	Optical microresonators and frequency combs
EPF Lausanne	Microtechnique	D. Briand	Printed Electronics
EPF Lausanne	Medtronic Chair in Neuroengineering	D. Ghezzi	Printed Platinum electrodes
EPF Lausanne	Advanced Quantum Architecture Laboratory	E. Charbon	Micro-optics
EPF Lausanne	Powder Technology Laboratory	H. Hofmann	Mesoporous Sol-Gel Films
EPF Lausanne	Microsystems Laboratory	J. Brugger	Printed Optics
EPF Lausanne	LESO	J.-L. Scartezzini	Human Centric Lighting
EPF Lausanne	Applied Signal Processing	J.-M. Vesin	Signal Processing
EPF Lausanne	Signal Processing Laboratory 5	J.-P. Thiran	Electrical-impedance tomography
EPF Lausanne	LIPID	M. Andersen	Human Centric Lighting
ETH Zurich	Department of Chemistry and Applied Biosciences	A. De Mello	Microfluidics / Fluorescence lifetime imaging
ETH Zurich	Laboratory for solid state physics	H. von Känel	X-ray read out circuits
ETH Zurich	Integrated Systems Laboratory	L. Benini	Sub-Near-Threshold Multicore
ETH Zurich	Department of Chemistry and Applied Biosciences	M. Kovalenko	Fluorescent quantum dots

<i>University</i>	<i>Institute</i>	<i>Professor</i>	<i>Field of collaboration</i>
ETH Zurich	Lebensm.- u. Ernährungstoxikologie	S. Sturla	Aptamer-based assays for food safety
Haute Ecole d'Ingénierie et de Gestion du Canton de Vaud (HEIG-VD)	Institut d'Automation Industrielle	D. Maillefer	Design of Test Bench
Hôpital neuchâtelois, HNE	Département de médecine	C. Pellaton	Multiple collaboration including a clinical investigation on non-invasive blood pressure
Hôpitaux Universitaire de Genève	Département d'Urgences Pédiatriques	A. Gervaix	Monitoring de pneumonie
IPC-Oyonnax-France	Innovation Plasturgy Composites	L. Tenchine, S. Dessors	Injection Molding
Lund University	Department of Biomedical Engineering	C. Antfolk	Prosthetics
National Institute of Standards and Technology (NIST)	Optical Frequency Measurements group	S. A. Diddams	Optical frequency combs and their applications
NREL, USA	NREL	A. Tamboli	Multi-junction devices
ONERA-France	Modane-Avrieux Center	M. Lyonnet, Y. Michou	Pressure Sensitive Painting
ONERA-France	Meudon Center	M.-C. Mérienne	Pressure Sensitive Painting
Osaka Institute of Technology	Faculty of Information Science and Technology	K. Oshima	Routing in wireless sensor networks
Paul Scherrer Institute PSI	Laboratory for Micro- and Nanotechnology	Y. Ekinci	Plasmonic retarders for imaging
Politecnico di Milano	Department of Energy	M. Merlo, A. Casalegno	Battery modelling
SUPSI	IDSIA Dalle Molle Institute for Artificial Intelligence	L. M. Gambardella	Machine learning
Technical University of Kaiserslautern	Chair of real-time systems	G. Fohler	Real-time networking
University Hospital Inselspital Bern	Department ENT Surgery	M. Caversaccio	Image-guided micro surgery for hearing aid implantation
University Hospital Inselspital Bern	Cardiovascular Department	S. F. Rimoldi	Blood Pressure
University Hospital Inselspital Bern	Department of Sleep	S. Ott	Sleep analysis
University Hospital Inselspital Bern	Department of Pulmonary Disease	T. Geiser	Oxygen therapy
University Hospital Zurich	Division of Neonatology	J.-C. Fauchère	Newborn vital signs monitoring based on multiple vision sensors
University Hospital Zurich	Biomedical optics research laboratory	M. Wolf	Newborn vital signs monitoring based on multiple vision sensors
University Hospital Zurich	Clinic of Neonatology	M. Wolf	Neonate monitoring
University Hospital Zurich	Planungs- und Baubegleitendes Facility Management	S. Caravatti	Localisation and tracking for asset Management

<i>University</i>	<i>Institute</i>	<i>Professor</i>	<i>Field of collaboration</i>
University of Applied Sciences and Arts (FHNW)	Institut für Nanotechnische Kunststoffanwendungen	M. Kristiansen	Micro and nano structuring
University of Applied Sciences and Arts (FHNW)	Institute for Medical and Analytical Technologies	Michael de Wild	Imprint of nanostructures
University of Applied Sciences and Arts (FHNW)	Hochschule für Life Sciences	U. Pieles	Biology and sensing
University of Applied Sciences and Arts, Lucerne (HSLU)	CC Electronics	E. Niederberger	Solid state lighting
University of Applied Sciences and Arts, Lucerne (HSLU)	CC Aerospace biomedical science & technology / CC Mechanische Systeme / CC Electronics	M. Egli	Fluidic feeding system
University of Applied Sciences and Arts, Lucerne (HSLU)	Institute of Mechanical Engineering and Energy Technology IME	R. Legrand	Smartgripper
University of Applied Sciences HTW Chur	Departement Angewandte Zukunftstechnologien, Institut für Photonics und ICT IPI	U. Hauser-Ehninger	Solid state lighting
University of Applied Sciences, Zurich (ZHAW)	Institute of Computational Physics	B. Ruhstaller	Electrode design for PV & Solid state lighting
University of Athens	Dept. of Informatics & Telecommunications	S. Hadjiefthymiades	Wireless infrastructures, location based services, unmanned vehicles
University of Basel	Psychiatry Hospital / Center for Chronobiology	C. Cajochen	Human Centric Lighting / Chronobiology
University of Basel	Dept. of Physics	C. Schöneberger	Development of light management optics for solar cells
University of Basel	Department of Chemistry	E. Constable	Photo-Electrochemistry
University of Bern	Quantum Optics Lab	A. Stefanov	Entangled photons / quantum optics
University of Bern	ARTORG Organs-on-Chip Technologies	O. T. Guenat	Cellulosic material for in-vitro tissue models
University of Bern	ARTORG Center for Biomedical Engineering	S. Weber	Guided surgery
University of Bern	ARTORG Center for Biomedical Engineering	S. Weber	Image-guided micro surgery for hearing aid implantation
University of Geneva	Exoplanetary Systems	F. Pepe	Instrument for exoplanet search
University of Geneva	Department of Physical Chemistry	T. Bürgi	Surface-enhanced Raman scattering
University of Geneva	Computer vision and multimedia laboratory	T. Pun	Obstacle detection for the elderly based on stereo vision
University of Neuchâtel	Laboratoire Temps-Fréquence	G. Miletí	Cell-based atomic clocks
Wyss Center	Bio and Neuro Engineering	C. Clément	Integrated circuits for brain implants

## Teaching

	<i>Title of lecture</i>	<i>Context</i>	<i>Location</i>
J.-D. Decotignie	Informatique du Temps Réel	Bachelor Informatique	EPF Lausanne
	Real Time Networks	Master Computer and Communication Systems	EPF Lausanne
M. Despont	Packaging and hybridization, the valorization of MEMS technologies	Micro- 534 Advanced MEMS 2017 (D. Briand)	EPF Lausanne
J. R. Farserotu	Satellite Communication Systems and Networks	Master degree course under Communication systems and space technology	EPF Lausanne
I. Kjelberg	La Microtechnique et l'Astronomie	Cours EPFL Microtechnique 4e semestre	EPF Lausanne
	Thermo-Mechanical Design For Space Optics	Space Optics Instruments Design – Cours for professionals 2017 (ESA)	Poltu Quatu (IT)
J. Kruis	Secondary mirror design for the Stratospheric Observatory for infrared Astronomy (SOFIA)	Mechanism design II	EPF Lausanne
G. Nisato, N. Marjanović, F. Zanella	MICRO-505 Printed Systems & Large Area Manufacturing	Master course with Prof. D. Briand	EPF Lausanne

## Theses

### PhD Degrees Awarded in 2017

<i>Name</i>	<i>University</i>	<i>Title</i>
S. Cloix	UNI Genève	Sparse multi-view 3D computer vision – application to embedded assistive technologies
J. Mayer	University of Basel	Light management films for enhanced harvesting in printable photovoltaics
M. Proença	EPF Lausanne	Estimation of hemodynamics via electrical impedance tomography
J. Sun	ETH Zürich	A quality inspection system for precision machinery based on generative modeling

### CSEM Employees carrying out a PhD

<i>Name</i>	<i>Professor / University</i>	<i>Theme / CSEM Unit</i>	<i>Start year</i>
M. Auchlin	V. Gass / EPF Lausanne	Electrical engineering topic / Micro&Nano Systems	2017
L. Driencourt	E. Constable / University of Basel	Optical plasmonic nano-structures for enhanced photochemistry / Center Muttenz	2017
L. Dümpelmann	L. Novotny / University of Basel	Deep-subwavelength plasmonic nanostructures for light harvesting / Center Muttenz	2013
T. Frei	EPF Lausanne	Thermal management of microsystem in harsh environment / Micro&Nano Systems	2017
Z. Hejazi	A. De Mello / ETHZ	Miniaturized fluid sample preparation for water quality monitoring / Center Alpnach	2017
S. Jafari	S. Sturla / ETH Zürich	Aptamer-based assays for food safety / Center Landquart	2017

<i>Name</i>	<i>Professor / University</i>	<i>Theme / CSEM Unit</i>	<i>Start year</i>
P. Jokic	L. Benini / ETH Zurich	Embedded Machine Learning / Integrated and Wireless Systems	2017
V. Kopta	C. C. Enz / EPF Lausanne	FM-UWB Radio for High-Density Wireless Sensor Networks / Integrated and Wireless	2013
J. Mayer	C. Schönenberger / University of Basel	Light management and harvesting for photovoltaic and sensing applications / Center Muttenz	2014
T. C. Müller	A. P. Brug / EPF Lausanne	Variation-aware digital design / Integrated and Wireless Systems	2016
E. Obrzud	F. PEPE / University of Geneva	Optical frequency comb for spectrograph calibration / Systems	2016
D. C. Rojas Quiros	J.-D. Decotignie / EPF Lausanne	Development of MAC and routing protocols for dense wireless sensor networks / Integrated and Wireless Systems	2014
L.-L. Senaud	C. Ballif / EPF Lausanne	Photovoltaics	2017
F. Sorba	H. Shea / EPF Lausanne	Development of an integrated device for cell stiffness measurement / Micro&Nano Systems	2015
A. Tuomiranta	C. Ballif / EPF Lausanne	Optimal design and operations of photovoltaic power plants / Photovoltaics	2015

#### PhD Funded by CSEM

<i>Name</i>	<i>Professor / University</i>	<i>Theme / CSEM Unit</i>	<i>Start year</i>
T. Aderneuer	C. Cajochen / University of Basel	Free form micro optics for human centric lighting / Center Muttenz	2017
G. Borque Gallego	Y. Perriard / EPF Lausanne	Mignature magnetic bearing reaction wheel / Systems	2017
F. Braun	J.-P. Thiran / EPF Lausanne	Estimation of hemodynamics via electrical impedance / Systems	2013
F. Chicco	C. C. Enz / EPF Lausanne	Low-power RADAR topic / Integrated and Wireless Systems	2017
S. Karlen	G. Miletí / University of Neuchâtel	MEMS cells for atomic clocks / Systems	2014
G. Quaranta	O.J.F. Martin / EPF Lausanne	Resonant waveguide gratings for spectrometry / Center Muttenz	2015
M. Rapin	J. Snedeker / ETH Zurich	Wearable EIT system / Systems	2013
Y. Tang	O. T. Guenat / University of Bern	Cellulosic material for sensing applications / Center Landquart	2017

## Commissions and Committees

P.-J. Alet	Advisory board of European project MIGRATE European Technology and Innovation Platform Photovoltaics: member of the steering committee, member of the executive committee, leader of the grid integration working group Jury member for Intersolar Photovoltaics Award
F. Amez-Droz	CSEM Representative, Swiss Association of Science Journalism
C. Bosshard	BaselArea.Swiss: Member of Advisory Board and Technology Field Leader Micro, Nano & Materials Managing Director of the Swissphotonics NTN
S. Cattaneo	Expert for W.A. de Vigier Foundation
P. Dallemagne	Secretary and Swiss representative of Technical Committee 5 "Information Technology Applications", International Federation for Information Processing (IFIP)
J.-D. Decotignie	Advisory board member, DREAMS - Distributed REal-time Architecture for Mixed criticality Systems, EU project ISO TC 65 Swiss Committee ISO TC 65C, WG16 convenor, Wireless Industrial Communication Standardization Program Committee, Conf. on Embedded & Real-Time Computing Systems & Applications (RTCSA), Hsinchu, Taiwan Program Committee, Euromicro Conference of Real-Time Systems, Dubrovnik, Croatia Program Committee, IEEE Int. Conf. on Wireless for Space and Extreme Environments (WISEE), Huntsville, USA Program Committee, Real-Time Networks and Systems, Grenoble, France Program Committee, Workshop on Factory Communication Systems, Trondheim, Norway Program Committee, Workshop on Real-Time Networks, Dubrovnik, Croatia
M. Despont	Board member of the Swiss-MNT network Chairman of the IEEE International Conference on Micro ElectroMechanical Systems (MEMS), Belfast, UK, 2018 CSEM and HTA representative at the Micro- and Nano- Technology Workgroup, European Spatial Agency (ESA) External Expert at PhD Thesis, EPFL Member of the editorial board of Microelectronic Engineering Journal (Elsevier) Member of the executive board of the Swiss research program NanoTera Member of the Executive Technical Program Committee of Transudcers 2017, June 18-22, 2017, Kaohsiung, Taiwan Member of the Industrial Advisory Board, Nanotechnology Program, Prof H. Bahaskaran, Oxford University, UK Member of the Int'l Steering Committee of the Micro- and NanoEngineering (MNE) conference Senior Member of the IEEE Society
M. El-Khoury	CNCI Chambre Neuchâteloise du Commerce et de l'Industrie, Neuchâtel Concours International de Chronométrie, Le Locle, Membre du Comité d'honneur Member of the Swiss Academy of Engineering Sciences SATW
S. Emery	Member of the Technical Committee of the IEEE SOI-3D-Subthreshold (S3S) Conference

J. R. Farserotu	Chair and Research Co-ordinator The Hermes Partnership Chair of ETSI Technical Committee Smart Body Area Networks (TC SmartBAN) Member of the Steering Committee, IEEE International Symposium on Medical Information and Communication Technology 2017 (ISMICT 2017)
R. Ferrini	Chair of the Swissphotonics Solid State Lighting (SSSL) – Swiss National Laboratory for Solid State Lighting
S. Fricke	Member of IEC Technical Committee 119 Program Committee Member and Session Chair of SPIE Conference on Microtechnologies
E. Györvary	Extended Board Member CSEM Brasil Extended Board Member of the Heterogeneous Technology Alliance (alliance federating the Fraunhofer (microelectronics), VTT, CEA-Tech, and CSEM) Member of EARTO Working Group on Emerging Technologies for Healthcare Member of the Finnish Chamber of Commerce Member of the Latin American Chamber of Commerce Steering board member of Innovation Group Digitalization at Swiss Food Research
H. Heinzelmann	Member of the Begleitgruppe „Aktionsplan synthetische Nanomaterialien“ 2017, Federal Office of Public Health FOPH Program Committee, MNE Micro Nano Engineering 2017, Braga Program Committee, SSI Smart Systems Integration 2017, Cork Steering Committee, CCMX Competence Center for Materials Science and Technology Strategic Commission, Institut Carnot iC LAAS CNRS, Toulouse VP Nanotechnology, Swiss Society for Optics and Microscopy SSOM
C. Julia-Schmutz	Communication Coordinator within the Heterogeneous Technology Alliance (HTA) CSEM Representative, BioAlps
H. F. Knapp	Board member for NTN INARTIS Board of Directors member for cluster initiative Toolpoint for Lab Science Executive Board member of biotechnet, Switzerland Jury member for Zinno Ideenscheck Pre-jury member for Swiss Technology Award
G. Kotrotsios	IEEE Subcommittee on Computer Vision and Human-Machine Interaction in Industrial and Factory Automation IEEE Subcommittee on Human-Machine in Manufacturing Environment Member of the Board of Directors of CSEM Brasil Member of the Board of the Heterogeneous Technology Alliance (alliance federating the Fraunhofer (microelectronics), VTT, CEA-Tech and CSEM) Member of the Executive Board of EARTO, the European Association of Research and Technology Organisations Member of the Executive Board of EREA (the European Association of Aeronautics Research Centers) Member of the Swiss Academy of Engineering Sciences SATW Micronarc, member of the Group of Experts

M. Krieger	CSEM Representative Greater Zurich Area (GZA) CSEM Representative Manufuture.ch association CSEM Representative SEMI global semiconductor industry association CSEM Representative Zürcher Handelskammer (ZHK) CSEM Representative, Advanced Factory Automation workgroup of Swissmem (AFA) International Advisory Board IPAS Precision Assembly Seminar Chamonix 2018
S. Lecomte	European Time and Frequency Forum (EFTF) scientific committee member
A. Madrigal	Chair person of the Advisory Board of the new Space exhibition of the Museum of Transport of Lucerne CSEM Representative, General Forum Clean Sky CSEM Representative, Network of European Research Organisations on ESA Issues (NERO) CSEM Representative, Swiss Aeronautics Security and Defense Division of Swissmem (Swiss ASD) CSEM Representative, Swiss Space Industries Group of Swissmem (SSIG) Expert for the evaluation of H2020 proposals in the Space Work Programme of the European Commission Member of the General Assembly of EREA (Association of European Establishments in Aeronautics) and CSEM Delegate in the Aviation and Security Research Groups of the Association Member of the Strategic Committee of the Swiss Aeropole
N. Marjanovic	Swiss ePrint Conference 2017 Organizing committee
S. Mohrdiek	Member of Phonotics21 Work Group 6 – Design and Manufacturing of Components and Systems Swissphotonics, Head of Swiss Photonic Packaging Laboratory
J.-L. Nagel	Member of the Editorial Board of the "Journal of Low Power Electronics" (JOLPE)
R. Pugin	Member of the Expert Committee of the Association NTN Innovative Surfaces Member of the Scientific Committee of the 2017 World Congress on Micro and Nano Manufacturing Member of the Scientific Committee of the 4M Micro-Nano Manufacturing Association
D. Ruffieux	Member of the International Technical Program Committee of the European Solid State Circuit Conference (ESSCIRC) in the RF and mmWave Building Blocks
E. Schaller	Member of the Executive Board of sensors.ch, Switzerland
P. Schmid	CSEM Representative Swiss Mechatronics Cluster
P. Steiert	Advisory Board Member for Institute für Chemistry and Biological Chemistry at the ZHAW Advisory Council for cluster initiative Toolpoint for Lab Science Member of the Executive Board for microPark Pilatus

## Prizes and Awards

- April 2017 The real-time embedded face recognition VIP (Vision-In-Package) system receives the gold medal of the 2017 Innovators Award from the Vision Systems Design magazine (Chicago, USA).
- June 2017 A joint development from Witschi Electronic AG and CSEM wins the Grand Prix des Exposants of the the EPHJ trade fair 2017. The fruit of this successful collaboration—the WisioScope S—monitors oscillator amplitude and frequency with photodetectors that measure the flicker of laser light reflected off a balance wheel (Geneva, CH).
- June 2017 The Best Student Paper Award is presented to CSEM and EPFL at the IEEE PVSC 2017. The team was rewarded for its joint work, entitled, "Perovskite/Silicon Tandem Solar Cells: Challenges Towards High-Efficiency in 4-Terminal and Monolithic Devices" (Washington, USA).
- June 2017 Stephanie Essig and coworkers (a CSEM–EPFL–NREL collaboration) win the IEEE PVSC 2017 Award for Most Outstanding Technical Contribution, for their work entitled "32% Efficient III-V/Si Dual-junction Solar Cells and their Challenging Path Towards Cost Competitiveness" (Washington, USA).
- September 2017 Martin Proen a receives the 2017 SSBE Research Award for the work he performed during his PhD thesis, entitled "Non-invasive Hemodynamic Monitoring by Electrical Impedance Tomography" (Winterthur, CH).
- September 2017 The Swiss company AVA is designated best start-up 2017. The potential of this fertility wristband—developed in a technological partnership with CSEM—won over the experts who had the task of identifying the most promising and innovative companies in Switzerland (Zurich, CH).
- September 2017 CSEM is rewarded for its technological excellence with a Herm s Innovation Prize. This award is given each year by the Club de Paris des Directeurs de l'innovation and the European Institute for Creative Strategies and Innovation (Paris, FR).
- September 2017 Matthieu Despeisse and coworkers (a CSEM–EPFL–NREL collaboration) receive the Best Poster Award at the EU PVSEC 2017 for their work on ">32% Efficient III-V/Si Multi-junction Solar Cells" (Brussels, BE).
- November 2017 During the MRS Fall Meeting 2017 in Boston (USA), CSEM and EPFL are awarded first place in the Science in Video competition organized by the Material Research Society, for their movie "Let There Be Light" (Boston, USA).
- December 2017 The scientist Josep Sol  i C ros is the recipient of the Neode Prize 2017. This award is in recognition of his development—together with his team at CSEM—of a new solution for measuring blood pressure continuously and without a cuff (Neuch tel, CH).



**CSEM SA**  
Jaquet-Droz 1  
CH-2002 Neuchâtel

**CENTER ALPNACH**  
Untere Gründlistrasse 1  
CH-6055 Alpnach

**CENTER LANDQUART**  
Bahnhofstrasse 1  
CH-7302 Landquart

**CENTER MUTTENZ**  
Tramstrasse 99  
CH-4132 Muttenz

**ZÜRICH OFFICE**  
Technoparkstrasse 1  
CH-8005 Zurich



**CONTACT**  
[www.csem.ch](http://www.csem.ch)  
[info@csem.ch](mailto:info@csem.ch)  
[jobs@csem.ch](mailto:jobs@csem.ch)